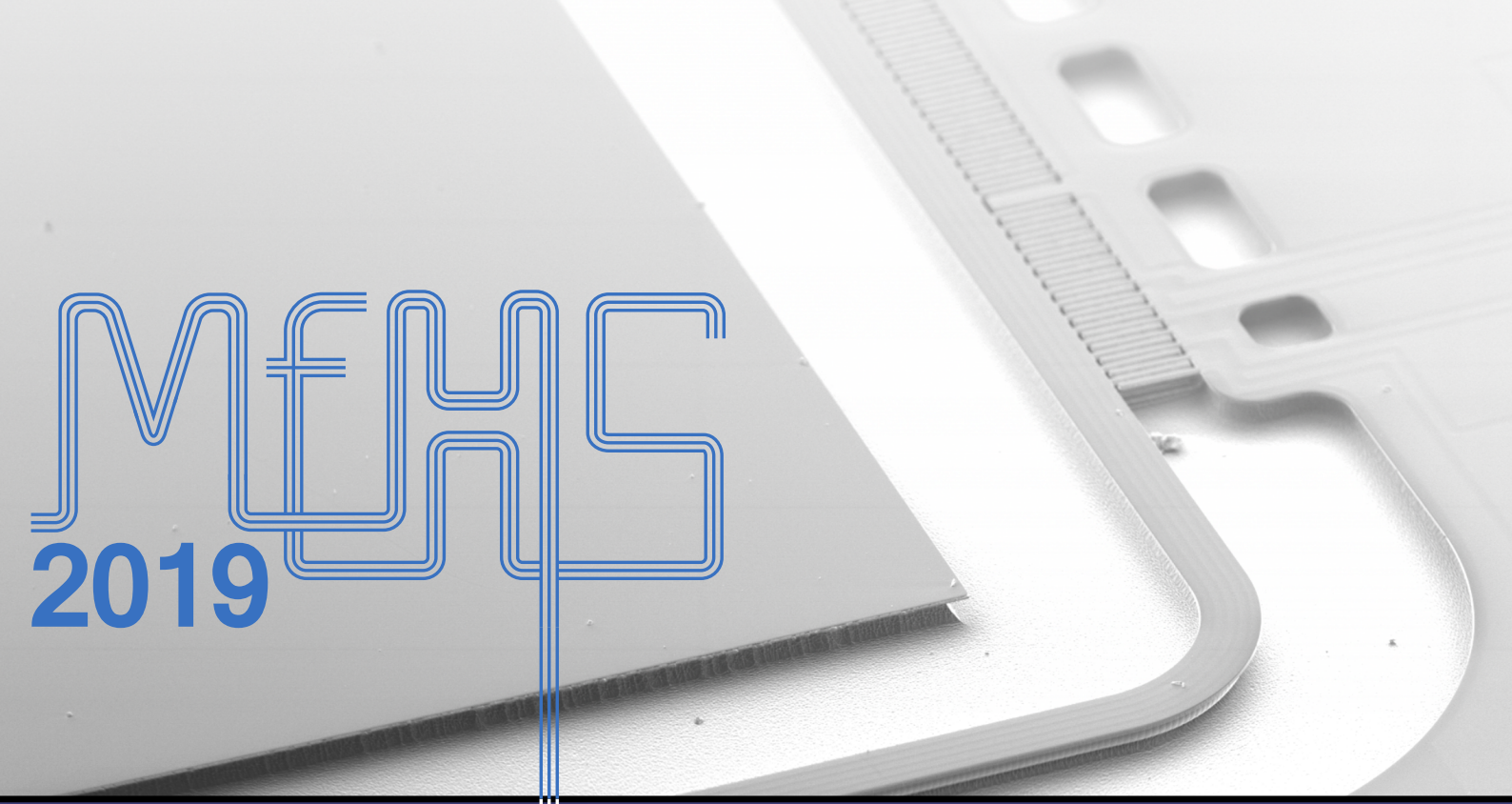

MFHS 2019

Conference Proceedings

The 4th Conference on MicroFluidic Handling Systems

2-4 October 2019

Enschede
The Netherlands

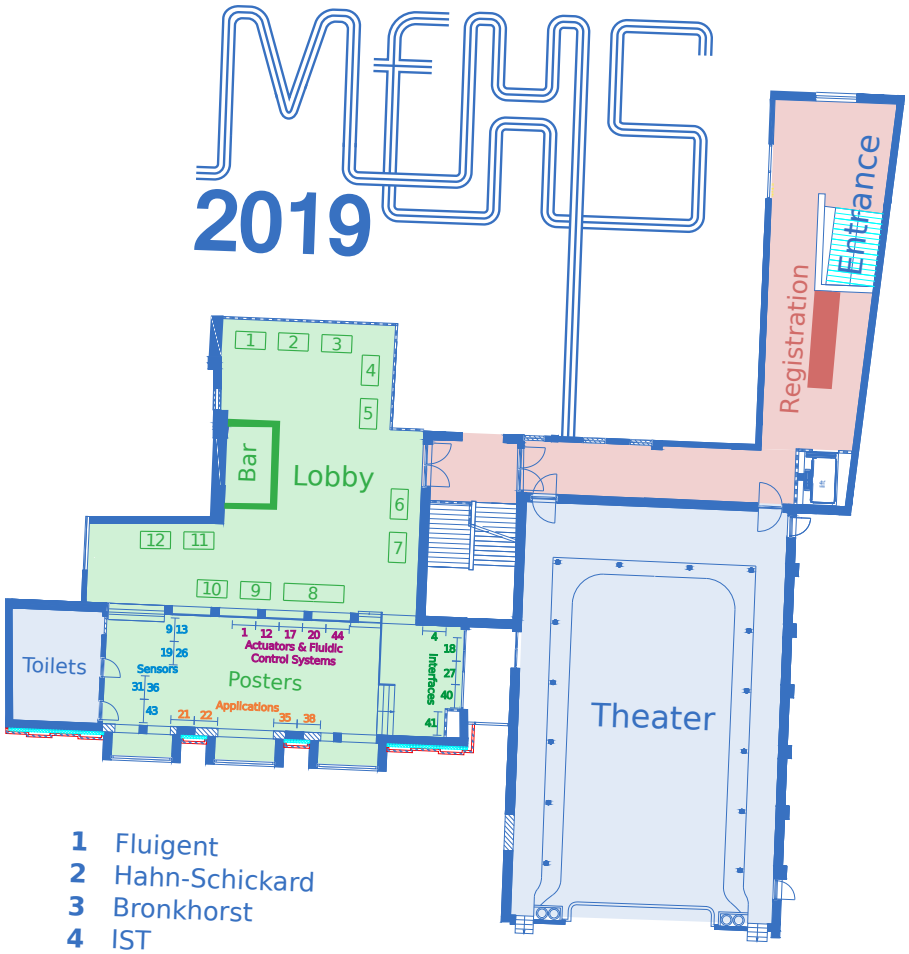

1 Fluigent
2 Hahn-Schickard
3 Bronkhorst
4 IST
5 Kloé
6 Salland Engineering
7 Shaw Mountain Technology
8 Bürkert
9 BioFluidiX
10 TrueDyne
11 Convergence
12 HNP Mikrosysteme

Conference: The 4th Conference on MicroFluidic Handling Systems (MFHS 2019).
Dates: 2-4 October 2019.
Chairs: Joost Lötters and Gerald Urban.
Technical program committee: Jens Ducrée, Bernhard Jakoby, Florian Krogmann, Shuichi Shoji, Peter Koltay, Jankees Hogendoorn, Andreas Ernst, Peter Müllner, Sabeth Verpoorte, Luis Fernandez, Loes Segerink, Remco Wiegerink and Niels Tas.
Sponsors: Bürkert, Fluigent, Krohne, MDPI Micromachines, Bronkhorst, Innovative Sensor Technology, Kloé, Salland Engineering, TNO, Shaw Mountain Technology, BioFluidiX, Hahn-Schickard, MESA+, Truedyne, Convergence Industry, HNP Mikrosysteme, University of Twente, Micronit and Axetris.
Location: De Kleine Willem, Langestraat 45, 7511 HB Enschede, The Netherlands.
Organization: Remco Wiegerink, Susan Janse, Dennis Alveringh. Jarno Groenesteijn, Henk-Willem Veltkamp, Yiyuan Zhao, Remco Sanders, Yaxiang Zeng, Qihui Yu, Mahdieh Yariesbouei, Thomas Schut and Sabrine Mejri.
Proceedings: Dennis Alveringh.

Welcome to the 4th International Conference on MicroFluidic Handling Systems

From 2 - 4 October 2019, the 4th International Conference on Microfluidic Handling Systems (MFHS 2017) will be held in Enschede, in the picturesque setting of former theatre De Kleine Willem, as a follow-up to the successful first three conferences in Enschede in 2012 and 2017, and in Freiburg in 2014.

Worldwide, accurate handling - i.e. analysis, dosage, measurement and control - of small and extremely small mass flow rates of both gases and liquids is becoming more and more important, driven by numerous applications. In 2020, the market for microfluidic devices may grow to $10 - $20 billion, according to Yole (2017), however, all depending on finding the next "killer application". Examples of economically and societally relevant applications are e.g. personalised medicine, improvement of medical infusion pump systems, high-pressure liquid chromatography (HPLC) and mass-spectrometry (MS), nutrition supply and waste drainage in organ-on-a-chip systems, research on catalysts and recipes for effectively extracting oil from wells (enhanced oil recovery), energy content measurement (calorific value or Wobbe Index) of natural gas and bio-gas, monitoring of ground water pollution, production of pharmaceuticals and specialty baby food with high nutritional value by means of flow chemistry, production of solar cell panels with CVD and ALD processes, and dosage systems for accurately dosing additives like e.g. vitamins to food and beverages.

Whether in analytical instrumentation, flow chemistry, energy, semiconductor industry, food and beverage or life sciences - microfluidic handling systems are facing four major trends: (1) a need for accurate measurement and calibration facilities; (2) a need for complete functional systems rather than for the individual components; (3) commercialisation of academic research results, and (4) standardisation of fabrication technology & materials, modules & connections, and quality assurance & test equipment. In the future, the impact of this field of research may become bigger and potentially large target markets may arise, especially when spin-off companies start manufacturing and selling their products, systems or pilot plants.

The MFHS 2019 focuses mainly on the technology, components, devices and systems that enable the application in microfluidic systems. It provides an excellent opportunity to bring together scientists and engineers from academia, research institutes and companies to present and discuss the latest results in the field of microfluidic handling systems. The conference goals are to stimulate interaction and knowledge exchange between the delegates in a friendly atmosphere. The most recent academic and industrial developments in the field of microfluidic sensors, actuators, interfaces, fluidic control systems and applications will be presented in 5 oral sessions and 1 poster session.

We are looking forward to seeing you at the MFHS 2019 conference!

Prof. Joost Lötters
Conference Co-chair

Prof. Gerald Urban
Conference Co-chair

Sponsors

Platinum

bürkert
FLUID CONTROL SYSTEMS

Gold

FLUIGENT
SMART MICROFLUIDICS

KROHNE

micromachines
an open access journal by MDPI

Bronkhorst®
Flow Technology

iST Innovative Sensor Technology
physical. chemical. biological.

KLOÉ

SALLAND Engineering
Test Technology Center

TNO innovation for life

SMT Shaw Mountain Technology

BioFluidiX

Hahn Schickard

MESA+
INSTITUTE FOR NANOTECHNOLOGY

truedyne

convergence
Accurate · Automated · Awesome

HNP M
HNP Mikrosysteme

UNIVERSITY
OF TWENTE.

Silver

micronit
microtechnologies

axetris

Conference committee

Chairs

Prof. dr. ir. Joost Lötters
MESA+ Institute for Nanotechnology, University of Twente, Enschede, the Netherlands
Bronkhorst High-Tech BV, Ruurlo, the Netherlands

Prof. dr. Gerald Urban
Institüt für Mikrosystemtechnik (IMTEK), Albert-Ludwigs-Universität
Freiburg, Germany

Technical program committee

Prof. dr. Jens Ducrée
School of Physical Sciences, Dublin City University
Dublin, Ireland

Prof. dr. Bernhard Jakoby
Institute for Microelectronics and Microsensors, Johannes Kepler University
Linz, Austria

Dr. Florian Krogmann
Chief Research & Development Officer, Innovative Sensor Technology IST AG
Ebnat-Kappel, Switzerland

Prof. dr. Shuichi Shoji
Department of Electronic and Physical Systems, Waseda University
Tokyo, Japan

Dr. Peter Koltay
Institüt für Mikrosystemtechnik (IMTEK), Albert-Ludwigs-Universität
Freiburg, Germany

Dr. ir. Jankees Hogendoorn
KROHNE Nederland B.V.
Dordrecht, the Netherlands

Dr. Andreas Ernst
BioFluidiX GmbH
Freiburg, Germany

Prof. dr. Peter Müllner
Boise State University, Boise, Idaho, USA
Shaw Mountain Technology, Nampa, Idaho, USA

Prof. dr. Sabeth Verpoorte
Rijksuniversiteit Groningen
Groningen, The Netherlands

Dr. ir. Luis Fernandez
University of Zaragoza
Zaragoza, Spain

Dr. ir. Loes Segerink
The BIOS Lab-on-a-Chip Group, University of Twente
Enschede, The Netherlands

Dr. ir. Remco Wiegerink
MESA+ Institute for Nanotechnology, University of Twente
Enschede, the Netherlands

Dr. ir. Niels Tas
MESA+ Institute for Nanotechnology, University of Twente
Enschede, the Netherlands

Program

Wednesday, 2nd of October

17:00 – 19:00	Registration & welcome reception	Lobby

Thursday, 3rd of October

8:00 – 8:45	Registration	Lobby
8:45 – 9:00	Opening & announcements	Theater
9:00 – 9:30	Invited talk 1: “Flow chemistry & chemical sensors”	Theater
9:30 – 10:50	Session 1: Sensors	Theater
10:50 – 11:20	Coffee break & exhibition	Lobby
11:20 – 12:40	Session 2: Actuators & Fluidic Control Systems	Theater
12:40 – 13:40	Lunch & exhibition	Lobby
13:40 – 14:10	Invited talk 2: “Energy transition”	Theater
14:10 – 15:30	Session 3: Industrial Sensors & Fluidic Control Systems	Theater
15:30 – 16:00	Coffee break & exhibition	Lobby
16:00 – 17:45	Poster session & exhibition	Lobby
18:00 – 20:00	Conference dinner	Wilmink
20:00 – 22:00	Evening show	Theater

Friday, 4th of October

8:00 – 8:45	Registration	Lobby
8:45 – 9:00	Opening & announcements	Theater
9:00 – 9:30	Invited talk 3: “Biopharmaceuticals”	Theater
9:30 – 10:00	Invited talk 4: “Flow control for organ on a chip”	Theater
10:00 – 10:40	Session 4: Applications	Theater
10:40 – 11:10	Coffee break & exhibition	Lobby
11:10 – 12:30	Session 5: Industrial Applications	Theater
12:30 – 13:00	Closing session & awards ceremony	Theater
13:00 – 14:00	Lunch & exhibition	Lobby
14:30 – 16:00	Optional lab tour	University

Invited talks

Prof. Maarten Honing
Maastricht University
Flow chemistry & chemical sensors
Development & validation of universal MS based sensing technologies in (micro)fluidic chemical reactors.

Dr. ir. René Peters
TNO
Energy transition
Energy transition and the energy gasses of the future.

Prof. dr. ing. Michel Eppink
Synthon Biopharmaceuticals BV / Wageningen University & Research
Biopharmaceuticals
Microfluidics as a tool in the development of biopharmaceutical proteins.

Pim de Haan, MSc
University of Groningen / TI-COAST
Flow control for organ on a chip
A highly stable, pressure-driven flow control system for organs-on-chips based on Coriolis mass flow sensors.

Session 1: Sensors

Thursday, 3rd of October, 9:30 – 10:50
Chairs: Loes Segerink & Joost Lötters

Session 2: Actuators & Fluidic Control Systems

Thursday, 3rd of October, 11:20 – 12:40
Chairs: Peter Koltay & Niels Tas

Session 3: Industrial Sensors

Thursday, 3rd of October, 14:10 – 15:30
Chairs: Jankees Hogendoorn & Florian Krogmann

Session 4: Applications

Friday, 4th of October, 9:30 – 10:40
Chairs: Peter Mullner & Remco Wiegerink

Session 5: Industrial Applications

Friday, 4th of October, 11:10 – 12:30
Chairs: Stefan Schork & Florian Krogmann

Poster session

Thursday, 3rd of October, 16:00 – 17:45

Sensors

Applications

Actuators & Fluidic Control Systems

Interfaces

Development & validation of universal MS based sensing technologies in (micro)fluidic chemical reactors.

*Erik de Lange[a], Jonah Norbury[a], Nils Robbertson[a], Alex Yang[a], Darya Hadavi[a], Marc Escriba-Gelonch[b], Volker Hessel[c], Maarten Honing[a]**

a. *M4I Institute for multi-modal molecular imaging, Faculty of Health, Medicine & Life Sciences, Maastricht University, Universiteitssingel 50, 6229 ER, Maastricht, the Netherlands.*
b. **Laboratoire de Génie des Procédés Catalytiques**, *Ecole d'Ingénieurs en Chimie et Sciences du Numérique, CPE Lyon, boulevard du 11 Novembre 1918 Villeurbanne, France.*
c. *EC&MS Research, The University of Adelaide, Adelaide, South Australia 5005 Australia.*
m.honing@maastrichtuniversity.nl

INTRODUCTION

The continuous search for greener and cost-effective syntheses of small molecules is an essential activity of process chemists in Pharma R&D. Likewise, and based on the "continuous manufacturing" guideline of the FDA [1], the necessary transformation from batch to flow chemistry in getting increasingly important in this industry. Yet, it requires a more fundamental and deeper understanding of synthesis under dynamic conditions. Most importantly, it is anticipated that the use of continuous-flow processing will improve product quality. Quality, or better Quality by Design (QbD), go hand in hand with the need for novel "process analytical technologies" (PAT) [2].
These encompass technologies detecting physical parameters such as Temperature or viscosity and a variety of chemical detection approaches. Amongst others these can be NMR, IR/NIR, Light Scattering (flow cytometry) or MS. It must be mentioned, that NIR and other spectroscopic technologies, are the most frequently applied technology in chemical and polymer industry. Main criteria for the successful introduction of these technologies are robustness (hazardous conditions = high temperature, acidic), sensitivity and large dynamic ranges (linearity), universal detection or specificity, the ability to measure real time resolved on- or in-line. Moreover, changes in the ratio between different reagents from different compartments are expected to lead to changes in the physical conditions and thus chemistry and continuous monitoring of T, P and viscosity is needed. In summary, novel PAT technologies are needed. The should be able to real-time monitoring of chemical conversions, being on/in, creating a more fundamental understanding of the kinetics, identification of "by" products and in some cases the "structural configuration" of the product molecules [3,4].
More and more, ufluidic flow-reactors, are coupled to NMR, UV, IR and physical detectors. Albeit its robustness and widespread use in industry, IR/NIR/ MIR or even Raman is not universal, a clear advantage of NMR despite its relative "insensitivity". Likewise, with its "ultimate" sensitivity [3], mass spectrometry with the so-called ESI interface is not able to differentiate between structural isomers, and the interface by its nature is not considered "universal". Novel technologies, like Ion Mobility Spectrometry (IMS) integrated in MS and equipped with Atmospheric pressure Photon Ionisation is expected to leverage this gap.
We are researching 'typical" Diels-Alder (See reaction Scheme) and the photo induced chemical conversion of provitamin D to Vitamin D3 [3], using the off/on-line coupling with ESI/APPI-IMS-MS/MS for the detection of structural isomers (cis/trans, R/S). With this approach we were able to assign reaction kinetics, detect "by-products", identify and assign the structural isomers within a 200-millisecond time frame. In this poster presentation, the experimental set-ups, the data and the potentials of this approach will be discussed.

REFERENCES

1. US FDA Center for Drug Evaluation and Research, Draft guidance in "Quality considerations for continuous manufacturing, Feb 2019.
2. Thayer, A.M., Real-time monitoring; Although process Analytical Technologies is finding a home in drug manufacturing, progress is slow, CEN.ACS.ORG 2014 8 – 12.
3. G.A. Price, D. Mallik, M.G. Organ, Process Analytical tools for flow analysis: A perspective. J. Flow Chem., 7 (2017) 82 – 86.
4. M.Escriba – Gelonch, E. Shahbazali, M. Honing and V. Hessel, Quality-in(process)Line (QuIProLi) process intensification for a micro-flow UV-photo synthesis enabled by online UPLC analysis, Tetrahedron, 74(2018) 3143-3151.
5. A. Ray, T. Bristow, Ch. Whitmore, J. Mosely, On-line reaction monitoring by mass spectrometry, modern approaches for the analysis of chemical reactions, Mass Spectrom. Rev., 37 (2018) 565 - 579.

Microfluidics as a tool in the development of biopharmaceutical proteins

Production and development of biopharmaceutical proteins (e.g. monoclonal antibodies) is mainly performed in eukaryotic organisms such as Chinese Hamster Ovary (CHO) cells. The process development of these biotherapeutic proteins includes the expression/fermentation (Upstream Processing) and purification (Downstream Processing). During the Downstream Processing the protein of interest is purified according a chain of purification steps. Especially the chromatographic steps need quite some development time. To improve the speed of development, high-throughput screening microfluidics technologies should be implemented.
In this presentation a high-throughput microfluidics method will be explained which can rapidly screen washing and elution conditions of a specific chromatographic purification step. An imaging surface plasmon resonance (iSPR) platform is used in real-time and label-free.

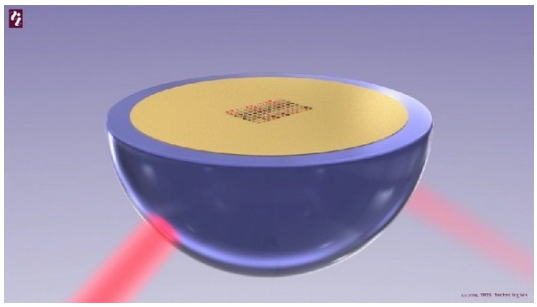

Figure 1: snapshot of a microfluidics iSPR chip

A HIGHLY STABLE, PRESSURE-DRIVEN FLOW CONTROL SYSTEM FOR ORGANS-ON-CHIPS BASED ON CORIOLIS MASS FLOW SENSORS

P. de Haan[1,2], J.P.S.H. Mulder[1], J.C. Lötters[3,4], and E. Verpoorte[1]
[1] University of Groningen, Groningen Research Institute of Pharmacy, Pharmaceutical Analysis, The Netherlands
[2] TI-COAST, Amsterdam, The Netherlands
[3] University of Twente, Integrated Devices and Systems, Enschede, The Netherlands
[4] Bronkhorst High-Tech BV, Ruurlo, The Netherlands

Organs-on-chips have risen to prominence over the last decade, to be used as novel models for drug and toxicology testing or as tools for personalized medicine. These miniaturized models of human organs or organ systems are based on a minute piece of human tissue or living human cells. Microfluidic channels allow the cells to be supplied with cell medium or other liquids and gases. These flows are usually generated by syringe pumps, which depend on a syringe slowly being emptied by mechanical force, applied to the plunger of the syringe by a stepper motor. These stepper motors generate pulsations when used at low flow rates. There is, therefore, a trade-off when using syringe pumps: a narrower syringe would lead to a more stable flow, with less pulsations; but this leads to a low available volume and thus a short experiment time. Exchanging syringes brings the risk of infecting the cell culture with microbes, as well as the introduction of air bubbles, so this should be avoided if possible.

In this work, we present the development of a new flow control system, based on pressurized liquid containers of any size, which are pressurized with a gas (Figure 1). This creates a pressure-driven flow, which is measured and controlled by downstream mass flow sensors and integrated valves (Bronkhorst High-Tech, Ruurlo, The Netherlands). These miniaturized mass flow sensors are based on a vibrating tube, through which the liquid flows. Because of this vibration, the velocity of the mass changes, resulting in a Coriolis force that can be detected in this system [1]. An integrated proportional control valve corrects for deviations from the set mass flow point [2]. We show the functionality of this flow control system with three examples (Figure 2). First, we demonstrate that this system can be used to manipulate complex biological liquids in a continuous-flow, miniaturized model of the multi-organ human digestive tract (Figure 3) [3]. In this system, artificial versions of saliva, gastric juice and intestinal juice were continuously mixed with samples, to expose these samples to digestive enzymes contained in the juices.

Second, we cultured living human intestinal cells in a gut-on-a-chip, a miniaturized model for the human intestinal tract (Figure 4) [4]. In this device, Caco-2 cells are grown on a porous membrane, separating the apical (top) and basolateral (bottom) channels. After pre-treatment by the juices of the digestive tract, drugs may be added to the apical compartment, to study their uptake into the body. Two flows of cell medium were used to supply the cells with nutrients and oxygen, at 0.5 mg/min for more than a week.

Lastly, we demonstrate that the output of the Coriolis-based flow control system is independent of the liquid used, by mixing ethanol and water at different ratios in a micromixer and measuring the density of the effluent with a third flow sensor.

In the future, we will combine the first two elements of this work in a fully integrated gut-on-a-chip for drug and toxicology testing.

Word Count: 495

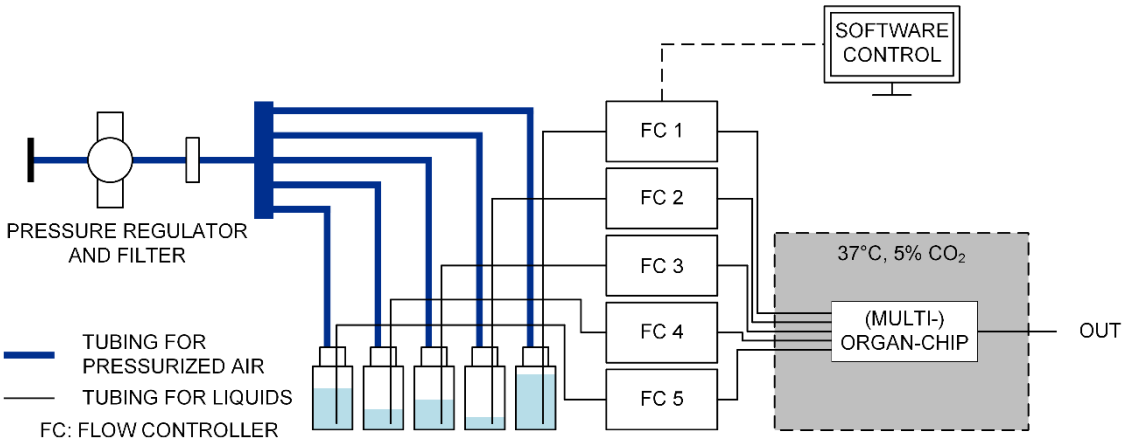

Figure 1. Schematic of the flow control system. Five individual liquid containers are pressurized with air (1 bar), which causes a flow to the mass flow controllers (FC 1–5). The flow controllers contain a Coriolis-based mass flow sensor and a proportional control valve, after which the liquids flow to the multi-organ-chip in an incubator.

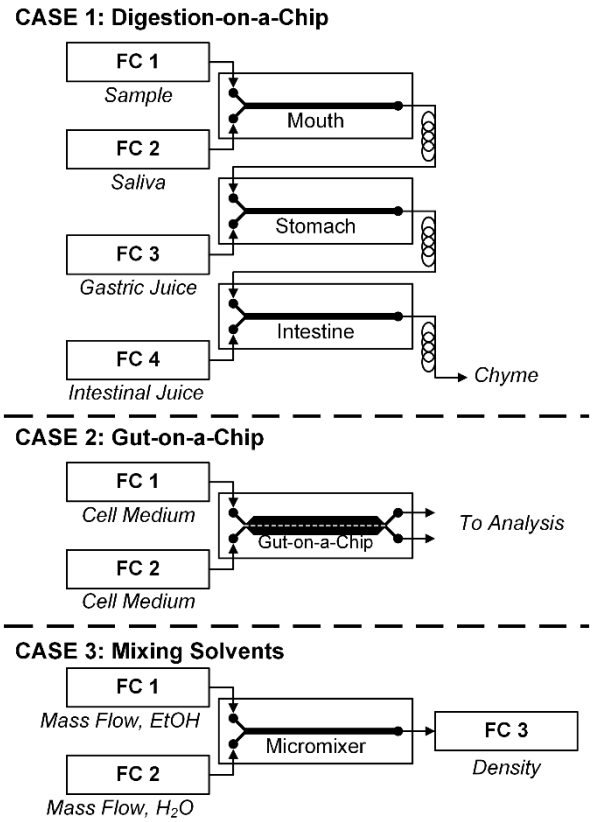

Figure 2. Three cases are presented to demonstrate the flow control system. In case 1, samples were continuously mixed with artificial digestive juices in micromixers and sample incubation loops. In case 2, gut epithelial cells were cultured inside a gut-on-a-chip microdevice for more than 4 days. In case 3, ethanol and water were mixed at varying ratios and the density of the effluent was measured in a third flow controller. FC: Flow controller.

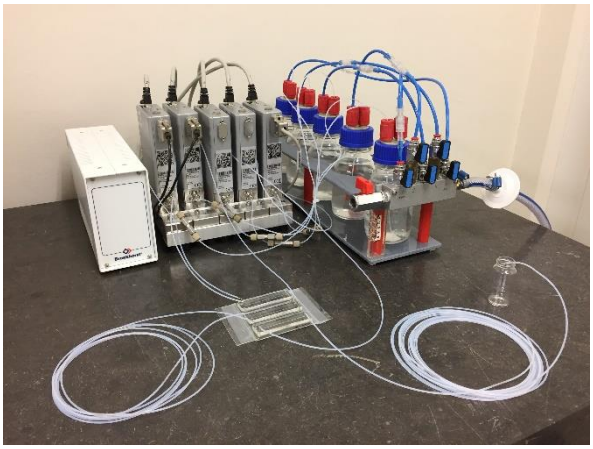

Figure 3. Photograph of the digestive system in case 1, with the Coriolis-based mass flow sensors at the back, liquid reservoirs at the right (blue/red caps), and the three micromixers with incubation loops in the front.

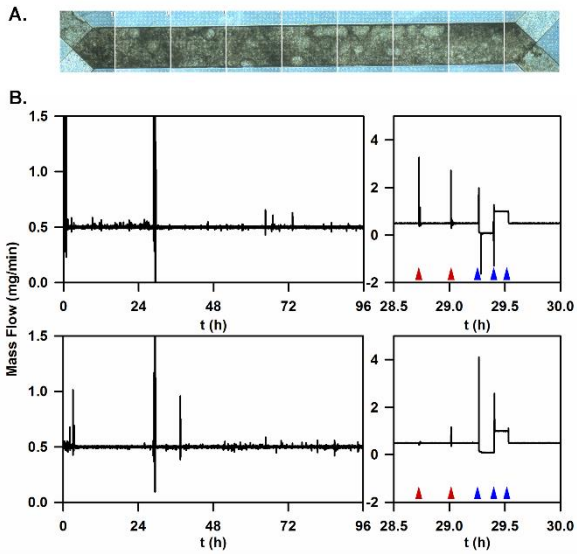

Figure 4. A) Micrographs of the cells grown in the gut-on-a-chip (channel width = 1 mm). B) Plots of the mass flow over time over four days, showing long-term stability. The peaks around 29 h were caused by external factors and by adjusting the flow rates (inserts on the right).

CONTACT

Pim de Haan – pim.de.haan@rug.nl

REFERENCES

[1] J. Haneveld, T.S.J. Lammerink, M.J. de Boer, *et al*. "Modeling, design, fabrication and characterization of a micro Coriolis mass flow sensor". J. Micromech. Microeng., 20(12). p. 125001, 2010.

[2] W. Sparreboom, J. van de Geest, M. Katerberg, *et al*. "Compact mass flow meter based on a micro coriolis flow sensor". Micromachines, 4(1). pp. 22-33, 2013.

[3] P. de Haan, M.A. Ianovska, K. Mathwig, *et al*. "Digestion-on-a-chip: a continuous-flow modular microsystem recreating enzymatic digestion in the gastrointestinal tract". Lab Chip, 19(9). pp. 1599-1609, 2019.

[4] D. Huh, H.J. Kim, J.P. Fraser *et al*. "Microfabrication of human organs-on-chips". Nat. Protoc. 8(11). pp. 2135-2157, 2013.

A UNIVERSAL FLOWMETER FOR MICROFLUIDICS

C.Cavaniol[1,2], W.Cesar[2], S.Descroix[1], & J-L. Viovy[1,2]
[1] PSL Research University, Institut Curie, CNRS UMR 168, Paris, France
[2] Fluigent SA, Kremlin-Bicêtre, France

ABSTRACT

We recently developed a new microfluidic approach to measure flow rate based on viscous dissipation at the solid/liquid interface and that requires no calibration step. In particular, we have conceived a sensor able to measure flow rate in the µL/min to hundreds of µL/min range. The core sensing element is a wheel, obtained by Stop Flow Lithography, that can freely rotate around an axle in a Hele-Shaw microchannel. We demonstrate that the sensor response is linear with flow rate and its slope doesn't depend on the viscosity of the liquid.

KEYWORDS

Microfluidic, Sensor, Flowrate, Calibration

INTRODUCTION

In the last 2 decades, Microfluidics has provided a better understanding and control of liquid flows at microscale. A fundamental step in these microfluidic applications (in hydrodynamics[1], chemistry[2] or biology[3-4]) is to reliably control and monitor the flow in microchannels. With this aim, several types of flow sensors have been proposed[5-6]. Currently, the most common flow sensor commercially available relies on the heating diffusion/convection profile in the flowing liquid to measure accurately the flow rate. Unfortunately, this method requires a calibration step for each fluid in order to take into account the specific fluid heating characteristics.

To overcome these limitations, and based on physical assumptions we developped a flow sensor independent on the fluid characteristics. The core element is a wheel positionned around an axle (Fig 1a). Indeed, due to low Reynolds number at this scale, flows surrounding the wheel follow Stokes equations - inertia being negligible. No wheel translation is permitted thanks to the presence of the axle. To provide a net torque, the wheel is set in an asymmetric position in the channel (Fig1b). The torque L is found by integrating the shear stress tensor σ_t multiplied by the momentum arm r on the surface of the wheel (Eq.1):

$$L = \int_{S_c} \sigma_{\mathbf{t}}(\mathbf{r})\mathbf{dS}.r \qquad (1)$$

$$\text{and} \quad \sigma_{t,ij} = \eta\left(\frac{\partial u_i}{\partial x_j} + \frac{\partial u_j}{\partial x_i}\right) \qquad (2)$$

with $\sigma_{t,ij}$ its component and η the fluid viscosity.

Due to the Stokes equation linearity, the wheel rotational speed should be linear with the flow rate. Moreover at steady state, the total torque on the wheel is equal to 0. Its movement should be viscous-free as the shear stress is linearly dependent on the viscosity (Eq.2). To confirm these assumptions, we tested two wheel radii (R=100 and 150 µm) keeping other geometrical parameters constant (see Fig.1b) with fluids of various viscosities (ranging from 10 to 10^2 mPas).

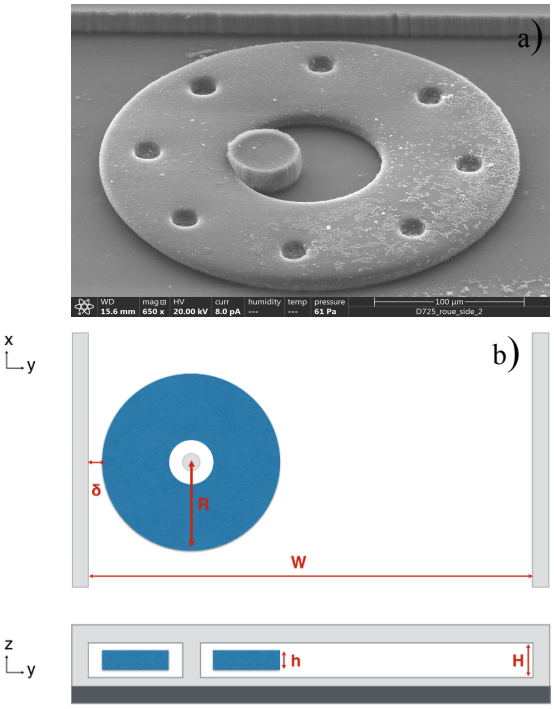

Figure 1: a) Scanning electron microscopy of the wheel (R=150 µm) b) Geometry of the Chip (top view and cross-section). Full PDMS chip (light grey) on a glass slide (dark grey). The wheel is in PEGDA 250 Mn (blue), positioned asymmetrically in the channel (H=20±1 µm; h=14.3±1 µm.; δ=11±3 µm; W-D= 422±3 µm; R= 100 and 150 µm; ±1)

MATERIAL & METHODS

Photopolymerization Setup

This core element is obtained by an in-situ photo-polymerization process called Stop Flow Lithography[7]. A flowing stream of photosensitive polymeric liquid is stopped in a PDMS microfluidic chip and then photopolymerized. It requires the use of an accurate pressure controller (MFCS 2 bar, Fluigent), to monitor the flow of the photosensitive

liquid composed of Poly(ethylene glycol) (250) diacrylate (PEG-DA, Sigma Aldrich) mixed with a 10%(V/V) photoinitiator solution (Darocur 1173, Sigma Aldrich). The UV exposure (375nm) is performed thanks to a contactless and maskless photolithography system (Primo, Alveole) paired with a microscope (Eclipse Ti, Nikon).

Sensor Experimental Setup

To study the response of our sensor to flowrate, syringe pump (Nemesys, Cetoni) or pressure controller (MFCS 7 bar, Fluigent) coupled with a reference thermal flowmeter (Flow Unit M, Fluigent) were used. PEGDA 250 and PEGDA 700 of respective viscosity η_{250} = 15mPa.s and η_{700} = 110 mPa.s were flown in the chip.

The rotation of the wheel is recorded thanks to a fast CCD Camera (Phantom V4.2, Vision Research) and analysed with a homemade tracking Matlab script.

RESULTS & DISCUSSION

Wheel Characterization

Stop Flow Lithography allows to photopolymerized objects free in solution. Indeed, the PDMS permeability to gas combined with the quenching of free radical polymerization by O_2 prevent photopolymerized particle from sticking to the channel wall. As described by Dendukuri et al.[8], for a given set of parameters (photoinitiator concentration, light intensity, O_2 diffusion coefficient, channel height,…), a critical time of exposure is required to convert enough double bonds to achieve a proper photopolymerization. This critical time of exposure correspond to the knee of the particle height versus exposure time curves (Figure 2)

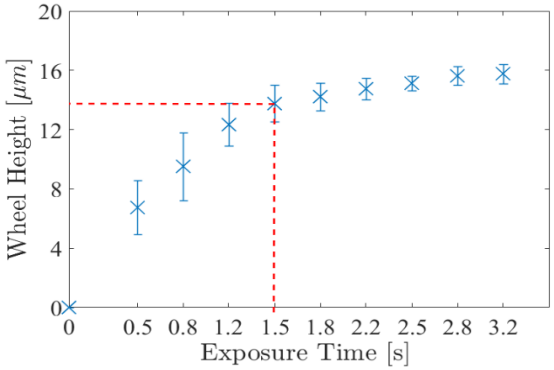

Figure 2: Wheel height depending on the exposure time. The red lines correspond to critical values for times and height: 1.5s and 13.7±1μm

In our case, the laser power density is 20 ±0.5 mJ/mm2 at 375nm with a 20x objective and a channel height H=20±1 µm. We choose an exposure time over the critical one but not too high to avoid overpolymerization: t_{exp} = 1.8s with h=14.3±1 µm.

Rotational Speed

To confirm our initial assumptions, we tested two wheel radii (R=100 and 150 µm) with liquid (PEG-DA 250 and 700 of varying viscosities). First, experimentally we observe (Figure 1) that the wheel rotates and its average speed is linear with the flow rate for all (R_i, η_i) combinations (for η_{250} R^2=0.971 and for η_{700} R^2=0.998). Moreover, as expected, for both viscosities the slope coefficient is similar (for η_{250}: 9.808 and for η_{700}: 9.498) showing our sensor independency regarding fluid viscosity.

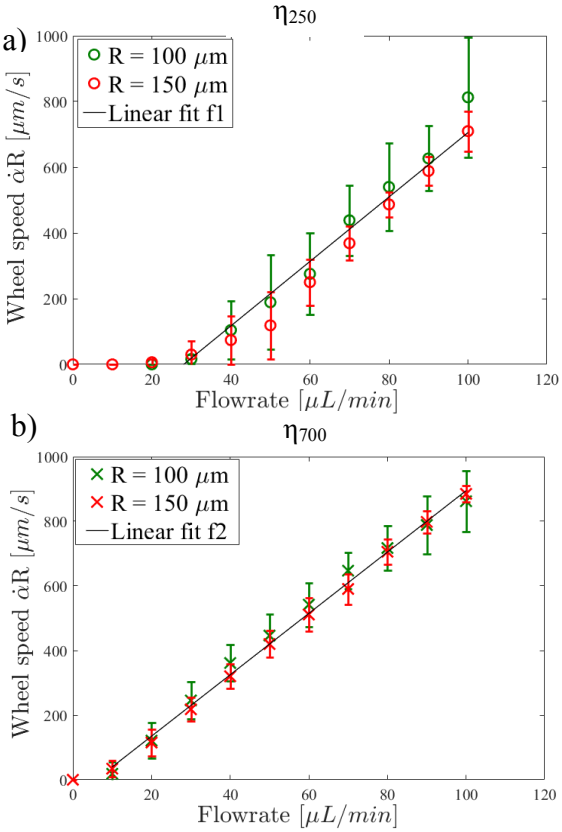

Figure 3: Wheel speed as function of the flow rate : the wheel speed equal to the measured rotational speed time the radius for a viscosity : a) η_{250} =15 mPa.s. The linear fit f1: y=9,808.x-275,3 (R^2=0,971) b) η_{700} =110 mPa.s. The linear fit f2: y=9,498. x-54,96 (R^2=0,998). They are both calculated without considering threshold data.

For all the operating conditions, a certain flow rate is required to rotate the wheel. This threshold flow rate seems dependent on the fluid viscosity. But, even for a given couple (R_i, η_i) threshold discrepancies have been observed. Eventually, we can extract a dependency from the radius (R) between the flow rate (Q) and the rotational speed ($\dot{\alpha}$):

$$\dot{\alpha} \propto \frac{Q}{R} \qquad (3)$$

Besides, we also observed that the instantaneous angular velocity is not constant over a revolution (see Figure 4.a), but its pattern is the same for all periods.

Therefore, all periods (respectively angular velocity of a revolution) are equal to the average period (respectively average angular velocity). To investigate on possible reasons for non-uniform velocity, we first test our initial hypothesis of laminar and steady state flow.

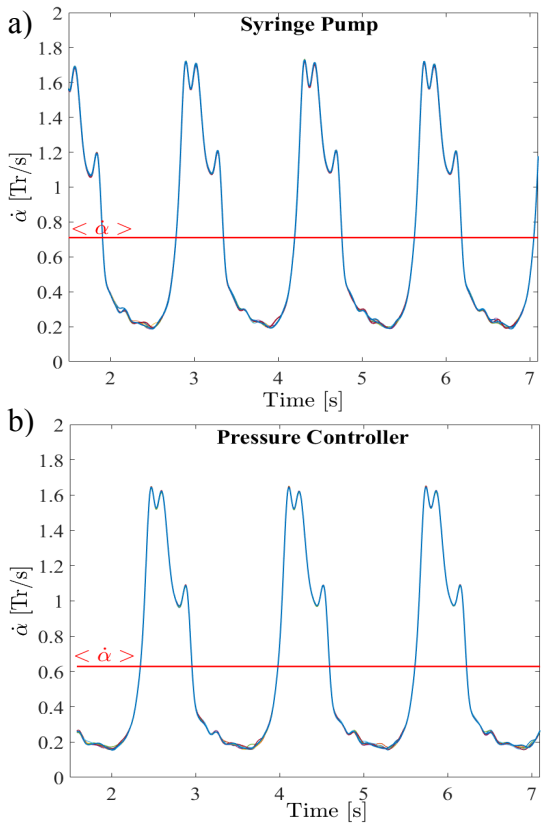

Figure 4: Wheel angular speed (R=150µm) as function of time with PEG-DA 250 for: a) actuation with syringe pump Q = 50µL/min and b) actuation in pressure ΔP = 850mbar and Q ~ 50µL/min on the calibrated reference flow unit.

We can estimate an upper limit for Reynolds number Re_{max} in our experimental conditions by taking the maximum flow rate for liquid of the lowest viscosity. The flow velocity U is estimated in a Hele-Shaw channel through:

$$U = \frac{3.Q}{2.W.H} \qquad (4)$$

In our geometry U (Q=100µL/min) ~ 0.17 m/s giving a Re_{max} ~ 0.19. This Reynolds number is substantially below values of non-laminar effect, which confirms our initial hypothesis. Moreover, fluid velocity U is approximately 2 orders of magnitude higher than the speed of the wheel validating steady state flow hypothesis. Another possible reason of this non uniform wheel velocity could be fluctuations in the fluid actuation. However, it is unlikely that the fluctuations due to syringe pump would be synchronized with the angular speed of the wheel. To fully discard this assumption, we also performed similar experiments using pressure controller instead of a syringe pump. As shown in Figure 3, we confirm that the pattern of angular velocity as a function of time doesn't depend on the actuation format. Eventually, a possible reason for these variations could be imperfections in the process of fabrication in the wheel resulting in changes of boundaries conditions leading to non-uniform torque.

Another interesting characteristic of our sensor comes from the PDMS elastomeric properties (E=1-3 MPa). Indeed, as described by Gervais et al., PDMS chip is expected to deform linearly with the pressure inside the chip [9].

Influence of the channel deformation

In our previous experiments, the difference in viscosity should radically affect the chip deformation for a given flow rate.

However, this dependency on the viscosity doesn't seem to influence our sensor response. To confirm these observations, we first characterize the deformation of the chip under pressure for two configurations with the same total hydraulic resistance but with different positions for the sensor chip in the fluidic circuit.

The first configuration is similar to the previous conditions where the chip is set after the flow unit at the end of the fluidic circuit (called Config LD). In the second configuration, our sensor is set before the flow unit (called Config HD). In the letter case, the output pressure of the sensor is no longer the atmospheric pressure due to added pressure difference from the reference flowmeter. Consequently, the deformation should be different with the same flow rate.

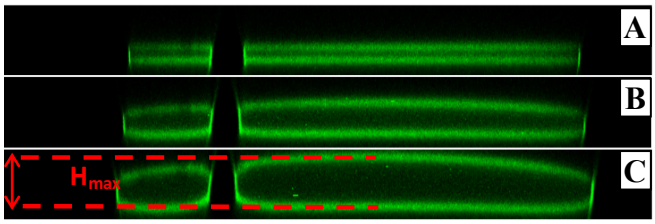

Figure 5: Confocal images of the chip under pressure performed with a mix of water and glycerol (20/80% (W/W)) + BSA Alexa Fluo (C=5µg/mL). A) Fluidic system under ΔP=0mbar B) ΔP=2500 mbar C) ΔP=5000 mbar. In red, Hmax is the height of the chip measured at its center.

To study the channel deformation, we performed confocal microscopy imaging (Figure 5) In particular, we characterized this deformation by measuring H_{max} as the maximum of height deformation in the perpendicular plan of the axel location.

We thus define the rate of deformation $\%H_{max}(\Delta P)$ for a certain pressure difference ΔP as:

$$\%H_{max}(\Delta P) = 100 \cdot \frac{H_{max}(\Delta P) - H_{max}(0)}{H_{max}(0)} \quad (5)$$

In Figure 6.a), we clearly observe an higher deformation rate for the HD configuration. Moreover, the linear deformation for both cases is consistent with the description reported by Gervais et al. [9]. Then, we studied the wheel angular speed for both configurations. These experiments were performed for a given radius and viscosity (R=150µm and η_{250}) in the range of [0;5bar] (respectively ~ [0;500µL/min]). The results presented in Figure 6.b show that the deformation of the channel height does not influence the angular speed of the wheel.

Consequently, our sensor is able to properly work under high range of pressure and could be set everywhere in a fluidic circuit without changing its response, which was not obvious with a PDMS chip.

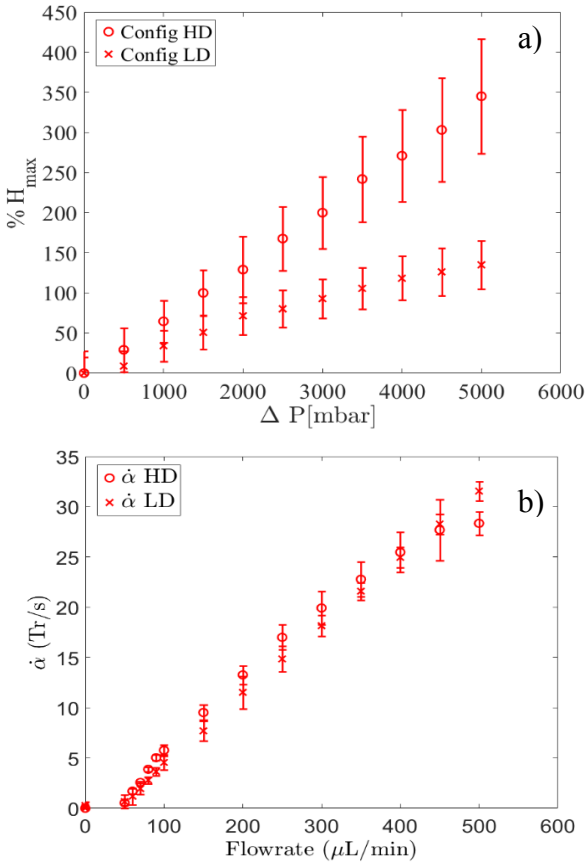

Figure 6: a) rate of deformation $\%H_{max}$ as function of the pressure difference on the fluidic circuit for both configuration (LD and HD) b) Angular speed of the wheel in both configuration.

CONCLUSION

We have developed a new flow sensor in the microfluidic range with a linear response to the flow rate and a slope response independent on the viscosity. Although the choice of PDMS to manufacture the chip could have been an influencing factor due to its deformation under pressure, the angular speed of the wheel remains the same. Further investigations are currently performed (PIV, Surface tension analysis, other materials) to describe more precisely flows surrounding the wheel to obtain a fully developed law between flow rate and rotational speed.

REFERENCES

[1] D. N. Woolfson, D. N. R. Forde, and H. Linke, "Controlled microfluidic switching in arbitrary time- sequences with low drag," *Lab Chip*, no. iii, pp. 2389–2396, 2013.

[2] J. Jang and S. Park, "Sensors and Actuators B : Chemical pH-responsive cholesteric liquid crystal double emulsion droplets prepared by microfluidics," *Sensors Actuators B. Chem.*, vol. 241, pp. 636–643, 2017.

[3] A. Baccouche *et al.*, "Massively parallel and multiparameter titration of biochemical assays with droplet microfluidics," *Nat. Protoc.*, 2017.

[4] N. Clouet-foraison, F. Gaie-levrel, L. Coquelin, G. Ebrard, P. Gillery, and V. Delatour, "Absolute Quantification of Bio-nanoparticles by Electrospray Differential Mobility Analysis : An application to Lipoprotein Particle Concentration Measurements," *Anal. Chem.*, 2017.

[5] J. T. W. Kuo, L. Yu, and E. Meng, "Micromachined thermal flow sensors-A review," *Micromachines*, vol. 3, no. 3, pp. 550–573, 2012.

[6] R. Attia, D. C. Pregibon, P. S. Doyle, J. L. Viovy, and D. Bartolo, "Soft microflow sensors," *Lab Chip*, vol. 9, no. 9, pp. 1213–1218, 2009.

[7] D. Dendukuri, S. S. Gu, D. C. Pregibon, T. A. Hatton, and P. S. Doyle, "Stop-flow lithography in a microfluidic device," *Lab Chip*, 2007.

[8] D. Dendukuri, D. C. Pregibon, J. Collins, T. A. Hatton, and P. S. Doyle, "Continuous-flow lithography for high-throughput microparticle synthesis Previous work on making particles in microfluidic devices," 2006.

[9] T. Gervais, J. El-Ali, A. Günther, and K. F. Jensen, "Flow-induced deformation of shallow microfluidic channels," *Lab Chip*, vol. 6, no. 4, pp. 500–507, 2006.

MICRO-CORIOLIS MASS FLOW SENSOR WITH RESISTIVE READOUT

T.V.P. Schut[1], R.J. Wiegerink[1] and J.C. Lötters[1,2]
[1] MESA+ Institute for Nanotechnology, University of Twente, Enschede, The Netherlands
[2] Bronkhorst High-Tech BV, Ruurlo, The Netherlands

ABSTRACT

This paper presents the first micro-Coriolis mass flow sensor with resistive readout. Instead of measuring a net displacement, a resistive readout detects the deformation of the suspended microfluidic channel. It allows for actuation at much higher amplitudes than a capacitive readout, resulting in correspondingly larger Coriolis forces in response to fluid flow. It also allows actuation in either twist or swing mode. We present measurement results for both operating modes, indicating that twist mode actuation results in higher sensitivity whereas swing mode actuation appears to be less sensitive to external disturbances.

KEYWORDS

Coriolis, Flow sensor, Flow, Mass flow, Strain gauge, Resistive, Resonator, Channel, Microfluidic

INTRODUCTION

A micro Coriolis mass flow sensor [1–3] measures true mass flow, independent of fluid properties. Figure 1 shows the operating principle of a micro Coriolis mass flow sensor, based on a vibrating channel. The ratio between the vibration amplitudes of the two modes described in the figure is a measure for the mass flow through the channel. Increasing the actuation amplitude, increases the Coriolis forces, which leads to higher accuracy due to the improved signal to noise ratio. For a capacitive readout, the allowable actuation displacement is limited by the inherent non-linearity in capacitance [4]. Furthermore, the sensitivity and non-linearity of a capacitive readout is influenced by static displacements due to temperature and residual stress in the channel material and by changes in relative permittivity of the fluid flowing through the sensor tube [4]. A resistive readout does not suffer from these issues and, although the resulting signal amplitudes are small, with this first device we demonstrate that they are still sufficient for measurement of mass flow. This resistive readout allows for operation using either twist or swing mode actuation (see Figure 1). In principle, the flow sensitivity is expected to be in the same order of magnitude for twist mode actuation and swing mode

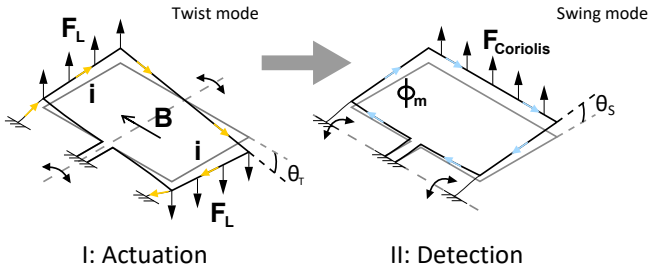

(a) Twist mode actuation induces Swing mode Coriolis forces.

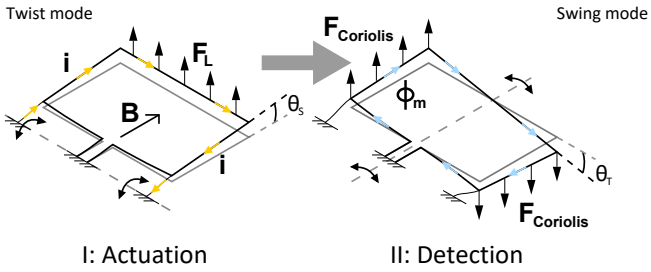

(b) Swing mode actuation induces Twist mode Coriolis forces.

Figure 1: Operation principle of a micro-Coriolis mass flow sensor. I: The channel loop is brought into resonance at actuation angle θ_T/θ_S through Lorentz force F_L, resulting from a magnetic field B and an AC current i. II: A mass flow ϕ_m through the channel induces vibration in the detection mode through Coriolis force $F_{Coriolis}$. The ratio between the two vibration mode amplitudes is a measure for the flow.

actuation. However, external vibrations on the sensor chip can cause vibrations in the swing mode. When the swing mode is used as Coriolis mode, this can cause disturbances in the output signal of the sensor, reducing accuracy and stability. Actuation in the swing mode should thus result in higher accuracy and stability. A capacitive readout is not suitable when using swing mode actuation. This is because the optimal position for picking up Coriolis motion would be in the place where the actuation motion is also most prominent. This significantly limits the actuation amplitude in the same way as described earlier. A resistive readout thus has various potential advantages and introduces the possibility of improving the accuracy and resolution of a micro Coriolis mass flow sensor.

DEVICE & FABRICATION

Integration of resistive strain gauges on top of the sensor tube is rather straightforward. The fabrication process of the sensor is based on the surface channel technology (SCT) proposed in [5]. A simplified schematic representation of the fabrication process is displayed in Figure 2. First, a layer of low stress silicon-rich silicon nitride (SiRN) (Thickness: 500 nm) is deposited on a Silicon wafer by LPCVD, see Figure 2a. On top of this, a layer of silicon di-oxide (SiO_2) is deposited (Thickness: 500 nm), serving as a hard mask. Slits of 5x2 µm are etched through both layers by plasma etching, see Figure 2b. Then the layer of SiO_2 is removed and a channel is formed by semi-isotropically etching silicon through the slits, see Figure 2c. This is done by plasma etching as well. The channel is closed by conformally depositing another layer of low stress Silicon rich Silicon-Nitride, see Figure 2d. Metal strain gauges are patterned on top the channel (Figure 2e). Following this, openings are etched through the nitride and finally the channel is released by isotropic etching of silicon by an SF_6 plasma.

Figure 3 shows a SEM picture of the sensor chip. The position of the strain gauges is indicated in the figure.

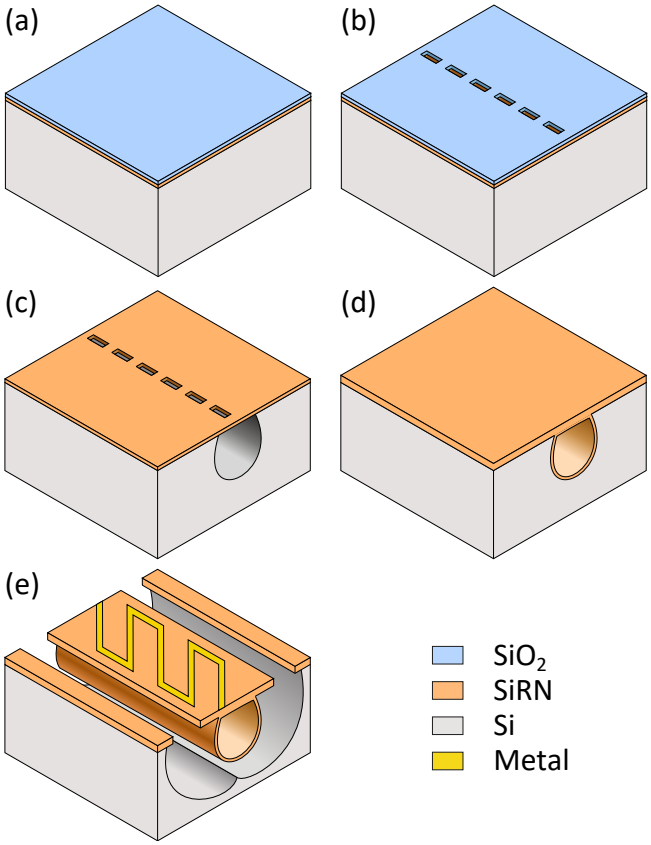

Figure 2: Fabrication process for SCT. (a): Silicon wafer with 500nm SiRN and 500nm SiO_2. (b): Patterning of slit openings. (c): Removal of SiO_2 hard mask and forming of the surface channel. (d): Closing of the channel. (e): Patterning of metal and release of the channel.

OPERATION

Figure 4 shows the operating principle of the resistive readout. In this example, the sensor is actuated in the *twist* mode. Figure 4a shows the configuration of the strain gauges when the sensor is not being actuated. The strain gauges are at a 45 degree angle with respect to the channel so that they are optimal for measuring torsion of the channel. When the sensor is actuated (Figure 4b), one strain gauge is elongated while the other is being compressed. The resistances over time of the two strain gauges are thus in opposite phase for the two strain gauges. When there is a flow through the channel, Coriolis forces induce vibration in the *swing* mode, see Figure 4c. This vibration is 90 degrees out of phase relative to the actuation. Both strain gauges are elongated at the same time and compressed at the same time due to *swing* mode vibration. The resistances over time of the strain gauges are thus in phase with each other and ±90 degrees out of phase with the resistance change due to actuation. When combining actuation and Coriolis vibrations, the resistances of the strain gauges will have a phase difference which depends on the mass flow rate

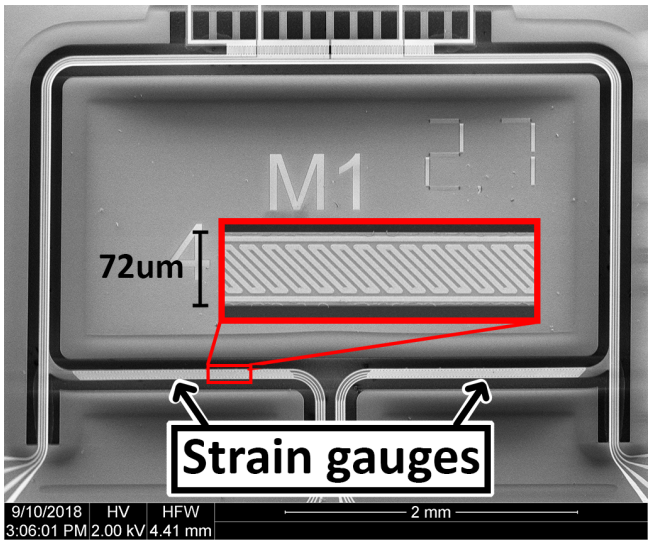

Figure 3: SEM image of the sensor chip. Strain gauges reside on two sections of channel close to the fixed in-/outlets.

through the channel.

The resistance of each of the two strain gauges is read out separately using a circuit as depicted in Figure 5. $R_{1/2}$ represents either the left or the right strain gauge on the sensor. The resistance of one strain gauge $R_{1/2}$ is converted to a voltage via a 1 MHz carrier signal and a reference resistor R_{Ref}. The carrier signal is mixed out after which a lock-in amplifier determines the magnitude and phase of the signal. Each strain gauge is read out with a circuit such as depicted in Figure 5. The phase difference between the two resulting signals is a measure for the mass flow rate.

EXPERIMENTAL

Multiple flow measurements are executed while actuating the sensor at various actuation angles $\theta_{\mathrm{S}}/\theta_{\mathrm{T}}$ in the *swing/twist* mode respectively. Figure 6 shows the fluidic measurement setup. Nitrogen gas is fed through the sensor chip at an input pressure P_{in} of 7 bar. The mass flow rate is controlled by a mass flow controller at the outlet of the sensor chip. Figure 7 shows the resulting phase difference output of the resistive readout. There is a linear relation between the output and mass flow. The sensitivity is approximately 0.5 $^{\circ}/(\mathrm{g\,h^{-1}})$ when actuating in the swing mode and approximately 0.9 $^{\circ}/(\mathrm{g\,h^{-1}})$ when actuating in the twist mode. The results show that the resistive readout is more sensitive when actuating in the twist mode. This is to be expected, since the strain gauges were designed to be most sensitive to swing mode deformation, which is in this case the Coriolis mode. However, in the swing mode, better accuracy is obtained. This could be due to lower dependency on external vibrations.

CONCLUSION & OUTLOOK

The first resistive readout integrated with a micro-Coriolis mass flow sensor has been presented. The readout shows great potential to become a better alternative to a capacitive readout since several improvements are possible: 1) Optimizing the design to increase sensitivity to a specific mode, 2) Adding on-chip reference resistors to reduce drift, 3) Adding additional strain gauges on the channel to allow for a full Wheatstone bridge readout. Based on the device in this paper, optimized devices are being designed and fabricated. Furthermore, research is done into the use of piezo-resistive materials to increase sensitivity and resolution of the readout and potentially of the micro-Coriolis mass flow sensor itself.

REFERENCES

[1] J. Haneveld et al., "Modeling, design, fabrication and characterization of a micro Coriolis mass flow sensor", Journal of micromechanics and microengineering 2010, pp. 1-10

[2] D. Sparks et al, "A portable MEMS Coriolis mass flow sensor", IEEE Sensors 2003, pp. 90-92

[3] P. Enoksson et al., "A silicon resonant sensor structure for Coriolis mass-flow measurements", Journal of MEMS 1997, pp. 119-125

[4] D. Alveringh et al., "Integrated pressure sensing using capacitive Coriolis mass flow sensors", Journal of MEMS 2017, pp. 653-661

[5] J. Groenesteijn et al., "A versatile technology platform for microfluidic handling systems, part I: fabrication and functionalization", Microfluidics and Nanofluidics 2017, Volume 21, Issue 7

CONTACT

* T.V.P. Schut, T.V.P.Schut@utwente.nl

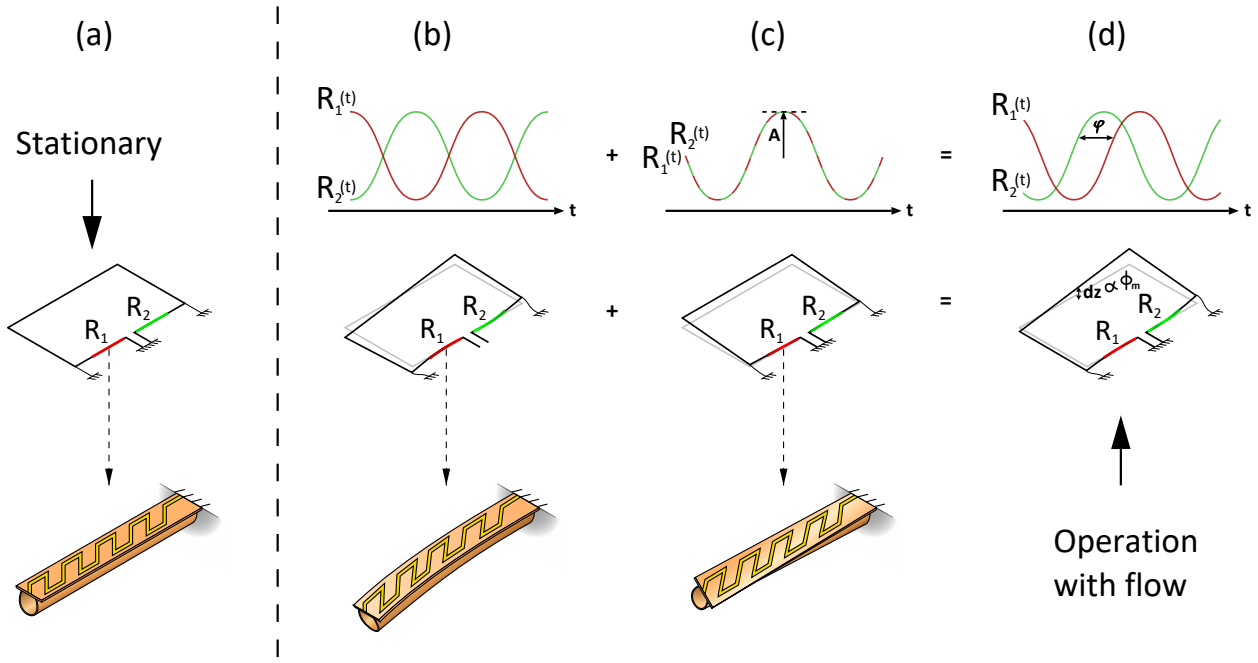

Figure 4: Principle of operation of the resistive readout. (a): Configuration of the strain gauges in rest. (b): In the twist mode, one strain gauge is elongated, the other will be compressed. This results in opposite change in resistance. (c): In the swing mode both strain gauges will be elongated due to torsion of the channel. This results in equal resistance change. (d): Combination of the two modes gives two resistance signals with a phase shift dependent on the mass flow rate.

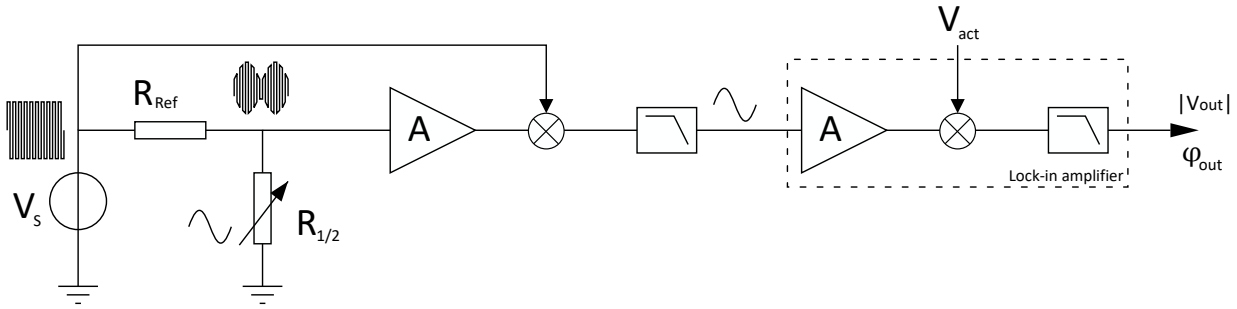

Figure 5: Schematic representation of the electronic readout circuit. The resistance of one strain gauge $R_{1/2}$ is converted to a voltage via a 1 MHz carrier signal and a reference resistor R_{Ref}. The carrier signal is mixed out after which a lock-in amplifier determines the magnitude and phase of the signal. Each strain gauge is read out with a circuit such as depicted in this figure. The phase difference between the two resulting signals is a measure for the flow.

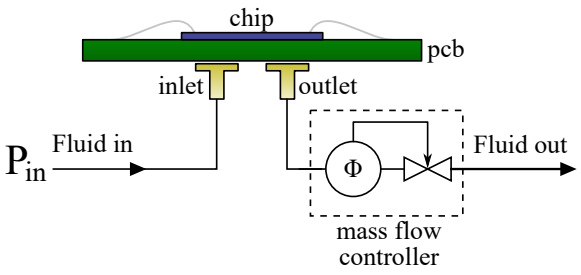

Figure 6: Fluidic measurement setup. Nitrogen gas is fed through the sensor chip at an input pressure $P_{in} = 7$ bar, while the mass flow is regulated using an external mass flow controller at the outlet.

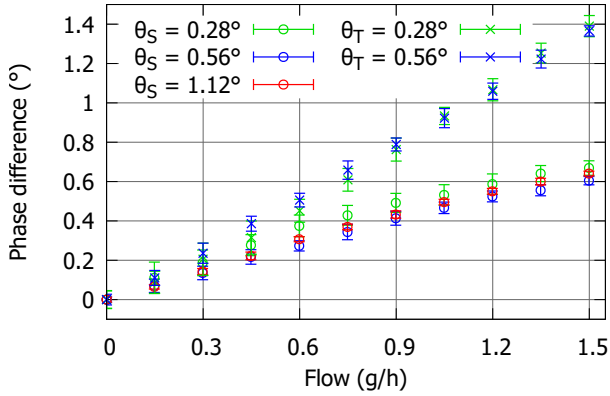

Figure 7: Output of the resistive readout in relation to the applied flow. The error bars represent the standard deviation.

DUAL BEAM OPTICAL COHERENCE TOMOGRAPHY FOR SPATIALLY-RESOLVED DEPTH-SECTION MICROFLUIDIC FLOW VELOCIMETRY

J.M. Hallam[1], E. Rigas[1], T.O.H. Charrett[1] and R.P. Tatam[1]
[1] Centre for Engineering Photonics, Cranfield University, Bedfordshire, United Kingdom, MK43 0AL

ABSTRACT

As microfluidics has matured there is an increasing requirement for imaging and velocimetry techniques. A novel dual beam Optical Coherence Tomography (OCT) instrument has been developed and its performance for spatially resolved particle flow tracking velocimetry has been studied for sloped and right-angled sections of microfluidic channel. This instrument retains the advantages of OCT compared to microscope derived imaging techniques:

- requiring only a single optical access port,
- simultaneously imaging the microfluidic channel,
- without requiring fluorescent particles,
- providing a millimetre-deep depth-section velocity profile (as opposed to horizontal-section).

The dual beams perform rapid re-sampling of particle positions improving particle tracking and allowing measurement of faster flows.

KEYWORDS

Optical Coherence Tomography, OCT, Interferometry, Microfluidics, Flow Measurement, Particle Image Velocimetry, PIV

INTRODUCTION

Context

As the microfluidic field has matured in academia and industry there is therefore an increasing need for robust and straightforward imaging tools [1] for live monitoring during industrial or scientific bio-processes [2] to observe experiments in a research environment [3] and for characterising flows during the prototyping and development of new microfluidic chip designs, and a broad selection of other needs [1]. Most microfluidic systems involve flows, for processes as diverse as mixing, separation, dropletisation, and controlled dispensing and cell delivery [2–6]. Current microfluidic applications are primarily in the biochemical and biomedical areas, including the growth and support of artificial organs, 'lab-on-a-chip' bio-analysis for point-of-care diagnostics, chemical and food processing, encapsulation for drug manufacture and delivery, drug discovery and medical research as well as environmental monitoring, and on-board cooling for 3d microprocessors [3–8].

Instrument

A novel dual beam Optical Coherence Tomography (OCT) instrument has been developed, and its use for measuring averaged flow velocity in excess of $1\,\mathrm{m/s}$ across a microfluidic channel without spatial resolution has been presented in a recent publication by the authors [9]. The dual beam OCT system retains the advantages of OCT compared to microscope-derived imaging techniques:

- requiring only a single optical access port (in this case above the microfluidic chip),
- simultaneously imaging the microfluidic channel,
- without requiring fluorescent particles,
- providing a depth-section velocity profile (as opposed to horizontal-section).

The dual beams (analogous to double exposure frames from particle image velocimetry camera systems) perform rapid re-sampling of particle positions. In the authors prior publication this allowed fast flow velocities to be measured, as particles that would have exited the imaged area by the time a single-beam system had captured a subsequent image are instead imaged by the dual beam, allow particle tracking to be performed and flow velocity vectors to be determined. Some complexity is introduced by the interaction of the flow velocity with the beam scan velocity.

A range of commercially available microfluidic chips have been studied using the dual beam OCT instrument, through the 'upper' surface of the microfluidic chip and from only that single optical access point. Compared to standard OCT systems the dual beam offers advantages including:

- higher measurable flow velocities,
- improved spatial resolution of velocity vectors,
- increased confidence in particle matching between frames.

The depth-section images provide spatially resolved mapping of flow in the vertical plane inaccessible to conventional horizontal-section microscopic techniques.

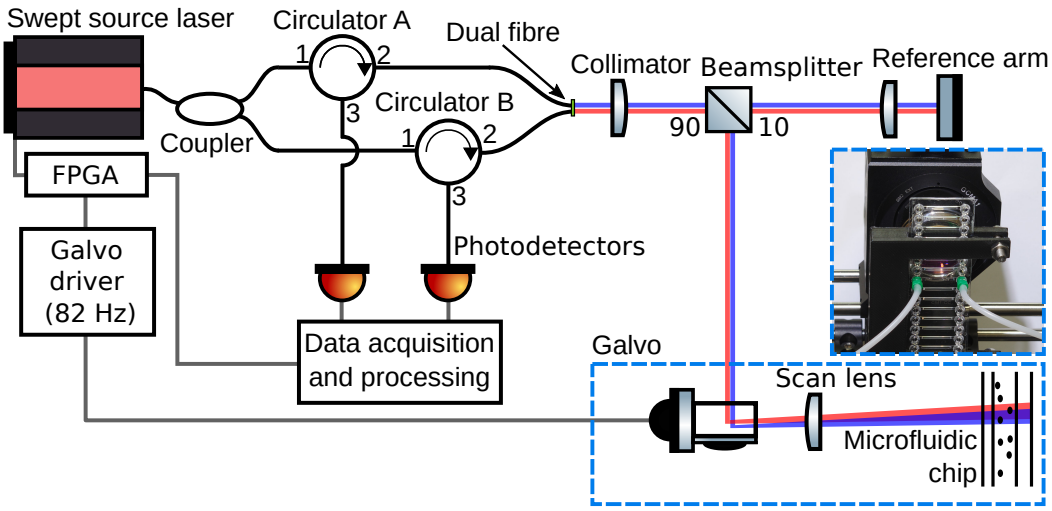

Figure 1: Schematic of dual beam OCT instrument. Red and blue indicate the light from each of the single mode fibres contained within the dual optical fibre end propagating in free space (both beams are at the same wavelength). The microfluidic chip is pictured. The beamsplitter directs 90 percent of the light to the microfluidic chip.

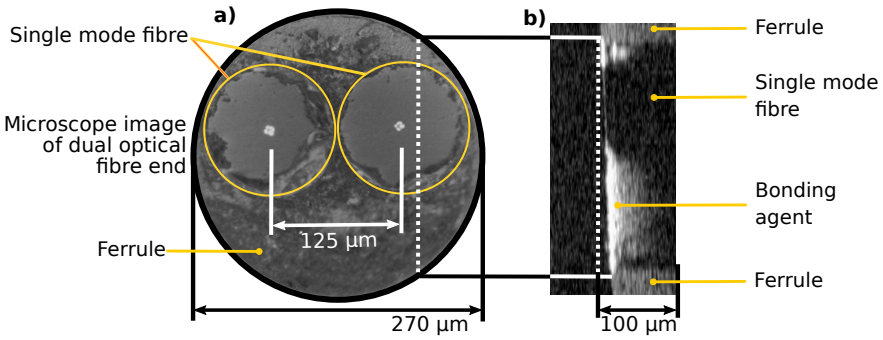

Figure 2: a) Horizontal-section microscope image of dual fibre end. Both single mode optical fibres are contained within a single ferrule. The optical fibre cores are illuminated from the far end and separated by 125 µm. b) Vertical-section OCT image of dual fibre end (at the position marked on the horizontal-section). The fibre does not reflect light and appears dark, the bonding agent and ferrule reflect light and appears bright.

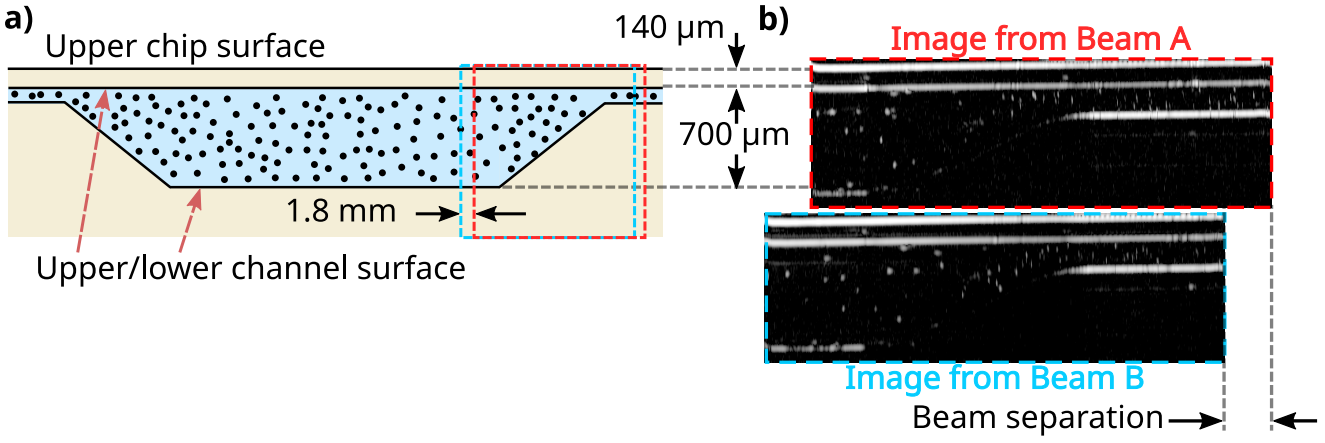

Figure 3: a) schematic of microfluidic chip with area imaged by Beam A and B of the dual beam OCT instrument marked, b) images from the dual beam OCT instrument with the appropriate beam separation.

METHOD

The dual beam OCT instrument is shown schematically in Fig. 1. The dual beams are created by separating light from a state-of-the-art solid-state swept-source laser into separate but closely adjacent optical fibres within a custom dual optical fibre end pictured in Fig. 2. This dual optical fibre end is integrated into an interferometric sensing head unit that addresses the microfluidic chip (at present through its top surface). The optics necessary for separation (and later detection) of the light are contained within a portable enclosure that also serves to isolate the instrument from changes in the environment. Optical Coherence Tomography images are reconstructed from the photodetector signals recorded by a high-rate data-acquisition card.

A colloidal suspension of $10\,\mu\mathrm{m}$ diameter latex particles was prepared at a density of $1.05\,\mathrm{g/ml}$ (matched to the particles so they would remain in suspension for a prolonged period). These particles will be imaged and tracked in order to determine the flow. The microfluidic chip is a reaction chamber chip manufactured from PMMA (microfluidic-chipshop Jena). The internal dimensions of the flow channel were $1.25\,\mathrm{mm}$ wide by $0.7\,\mathrm{mm}$ deep with a sloped input section. Flexible tubing of internal diameter $0.78\,\mathrm{mm}$ and the minimal possible length was attached to $10\,\mathrm{ml}$ plastic syringes driven by a Nexus 3000 (Chemyx) syringe pump.

A pair of OCT images from each of the dual beams is shown in Fig. 3. The separation of the images is determined by the spacing of the fibres in the dual optical fibre end. This image is produced by interferometry between the portion of reflected (or scattered) light that returns from the microfluidic chip to the dual optical fibre end forming one arm of the interferometer, and the light from the reference arm of the interferometer.

The flat upper surface of the microfluidic chip, the flat upper surface of the microfluidic channel, and the flat portions of the lower surface of the microfluidic channel can clearly be seen, as they reflect light directly back to the dual optical fibre end. The lower surface of the microfluidic channel incorporates a smooth sloped section which is not clearly seen because it reflects light away from the optical fibre end. The spherical particles in suspension within the microfluidic channel scatter light in all directions, a sufficient portion of which returns to the dual optical fibre end to allow the particles to be imaged.

Some particles appear less intensely than others, likely because they lie only partially within the plane of the dual beam scan. Particles moving quickly across the image only interact briefly with the beams performing the OCT scan, and therefore appear compressed. This can be seen occurring in the shallow section of microfluidic channel on the right (the same volume of fluid flows faster through a shallow channel than a deeper one) and to a lesser extent in the middle of the deep section of microfluidic channel on the left (flow at the center of a channel is faster than near the walls) [10]. Note however that this compression effect is too noisy for quantitative determination of particle speed and particle tracking between the beams is used to determine the flow velocity.

The area of interest is windowed to within the microfluidic channel. Particles are then identified in the image from each beam using publicly available open source software (trackpy 0.3.2 [11]). Insufficiently intense particles are rejected. This process is repeated for 300 captured pairs of images. The software takes the identified particle positions alone for the two images, and searches for a matrix of velocity vectors that connect those positions. The flow is constant over the 3.6 second duration of the measurement, so similar velocity matrices are expected to match for all pairs of images, and this condition is imposed by the software.

RESULTS

A spatially resolved flow diagram showing the velocity vectors of tracked particles over an extended measurement is shown in Fig. 4. Unsurprisingly, particles slow as they spread out from the narrow input section of the microfluidic chip (right, approximately $0.3\,\mathrm{m/s}$) to the wider section of the chip (left, approximately $0.1\,\mathrm{m/s}$). This result illustrates the flow mapping functionality of the instrument. Although particle tracking velocimetry has been used the instrument is fully compatible with particle imaging velocimetry analysis techniques that would allow higher particle densities.

ACKNOWLEDGEMENTS

Funded by the Engineering and Physical Sciences Research Council (EPSRC), UK, (EP/L014637/1, EP/H02252X/1, and EP/N002520/1). The authors acknowledge Dr M Partridge for support in creating the micro-particles mixture. We dedicate this work to our colleague Dr Helen D Ford (1963 - 2018).

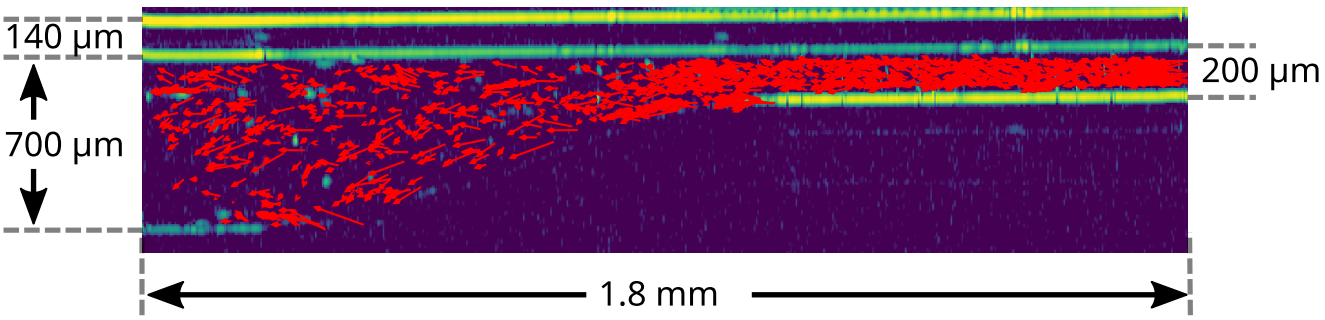

Figure 4: Enlarged OCT image from Beam A showing the microfluidic chip and particles, with superimposed spatially resolved flow velocity vectors determined by tracking particles from Beam A to Beam B shown for a two second acquisition. The flow is from right to left at a mean flow rate of $25.5\,\mathrm{ml/min}$.

REFERENCES

[1] A. van Dinther, C. Schron, F. Vergeldt, R. van der Sman, and R. Boom, "Suspension flow in microfluidic devices a review of experimental techniques focussing on concentration and velocity gradients," *Advances in Colloid and Interface Science*, vol. 173, pp. 23 – 34, 2012.

[2] M. Karle, S. K. Vashist, R. Zengerle, and F. von Stetten, "Microfluidic solutions enabling continuous processing and monitoring of biological samples: A review," *Analytica Chimica Acta*, vol. 929, pp. 1 – 22, 2016.

[3] G. T. Vladisavljevi, N. Khalid, M. A. Neves, T. Kuroiwa, M. Nakajima, K. Uemura, S. Ichikawa, and I. Kobayashi, "Industrial lab-on-a-chip: Design, applications and scale-up for drug discovery and delivery," *Advanced Drug Delivery Reviews*, vol. 65, no. 11, pp. 1626 – 1663, 2013.

[4] A. Liga, A. D. B. Vliegenthart, W. Oosthuyzen, J. W. Dear, and M. Kersaudy-Kerhoas, "Exosome isolation: a microfluidic road-map," *Lab Chip*, vol. 15, pp. 2388–2394, 2015.

[5] P. S. Clegg, J. W. Tavacoli, and P. J. Wilde, "One-step production of multiple emulsions: microfluidic, polymer-stabilized and particle-stabilized approaches," *Soft Matter*, vol. 12, pp. 998–1008, 2016.

[6] Y. S. Zhang, A. Arneri, S. Bersini, S.-R. Shin, K. Zhu, Z. Goli-Malekabadi, J. Aleman, C. Colosi, F. Busignani, V. Dell'Erba, C. Bishop, T. Shupe, D. Demarchi, M. Moretti, M. Rasponi, M. R. Dokmeci, A. Atala, and A. Khademhosseini, "Bioprinting 3d microfibrous scaffolds for engineering endothelialized myocardium and heart-on-a-chip," *Biomaterials*, vol. 110, pp. 45 – 59, 2016.

[7] G. S. Clinton-Bailey, M. M. Grand, A. D. Beaton, A. M. Nightingale, D. R. Owsianka, G. J. Slavik, D. P. Connelly, C. L. Cardwell, and M. C. Mowlem, "A lab-on-chip analyzer for in situ measurement of soluble reactive phosphate: Improved phosphate blue assay and application to fluvial monitoring," *Environmental Science & Technology*, vol. 51, no. 17, pp. 9989–9995, 2017.

[8] S. Wang, Y. Yin, C. Hu, and P. Rezai, "3d integrated circuit cooling with microfluidics," *Micromachines*, vol. 9, no. 6, 2018.

[9] E. Rigas, J. M. Hallam, T. O. H. Charrett, H. D. Ford, and R. P. Tatam, "Metre-per-second microfluidic flow velocimetry with dual beam optical coherence tomography," *Optics Express*, vol. 27, June 2019.

[10] C. Tropea, A. Yarin, and J. Foss, *Springer Handbook of Experimental Fluid Mechanics*. 01 2007.

[11] D. Allan, T. A. Caswell, N. Keim, F. Boulogne, R. W. Perry, and L. Uieda, "trackpy: Trackpy v0.3.2," Aug. 2016.

CONTACT

* R.P.Tatam, r.p.tatam@cranfield.ac.uk

DESIGN OF A SLOT PHOTONIC CRYSTAL WAVEGUIDE FOR HIGHLY SENSITIVE EVANESCENT FIELD ABSORPTION SENSING IN FLUIDS

Reyhaneh Jannesari[1], Gerald Pühringer[1], Thomas Grille[2], Bernhard Jakoby[1]

[1] Institute for Microelectronics and Microsensors, Johannes Kepler University, Linz, Austria
[2]Infineon Technologies Austria AG, Villach, Austria

ABSTRACT

The design of a highly sensitive sensor based on slot photonic crystal waveguide (slot-PCWG) is presented. These types of waveguides feature a hexagonal array of holes in a silicon slab, which are filled with SiO_2. The waveguide is formed by removing elements from the regular photonic crystal grid in a row and embedding a slot in the center position. This concept allows a vast enhancement of the evanescent field ratio leading to a strong overlap between the field of the waveguide mode and the analyte. In the present work, we show that the sensitivity at constant slab thickness and waveguide-length of the slot-PCWG modes is greatly enhanced up to a factor of 7.6 compared to corresponding PCWGs modes or Si slab WGs.

KEYWORDS

Photonic crystal, slot waveguide, evanescent field absorption sensing

INTRODUCTION

Recently on-chip optical sensing has become increasingly attractive for lab-on-a-chip applications particularly due to their small size [1] [2]. Many photonic devices have been proposed as optical sensors, such as micro-ring resonators [3], slot waveguides [4] [5] and photonic crystals [6] and those based on Bragg gratings [7]. Optical sensing by guided-wave devices has attracted considerable attention [8] where the sensitivity is related to the strength of light-matter interactions [9]. However, many light guiding mechanisms feature only moderate overlap of the guided optical field with the sample, which results in severe limitations for the maximum sensitivity achievable under specific constraints on the waveguide geometry (i.e. waveguide length, slab thickness, bends, etc.). The achieved measurement sensitivity depends on optical field distribution in the analyte, so one of the most important design tasks is the optimization to maximize its sensitivity achievable concerning the geometric constraints mentioned earlier. Due to the high ability to control guided light, photonic crystals (PhCs) are suitable candidates for improving the performance of slab-based guided-wave devices. At the same time, slot waveguides are able to confine light outside the conventional high-index guiding material. This work presents the concept and design of a new platform by finite difference time domain (FDTD) for optical sensors, which provides higher sensitivities by combining both concepts to spatially confine the peak energy of the guided mode within the desired sample (analyte).

PHOTONIC CRYSTALS

A photonic crystal can be described as an artificially created periodic array of structures composed of dielectric materials. In such structures, light can be confined to high-quality factor cavities, directed, split, or even slowed down (i.e. it can be guided at low group velocities) [3]. Complete photonic bandgaps can particularly forbid the transmission of photons with certain frequencies in all directions. The periodic array can be designed as one-dimensional (1D), two-dimensional (2D) or three-dimensional (3D) [10] structure. The ability of PhCs to control the flow of light, confine light in a small volume, and enhance light-matter interaction makes them promising candidates for sensor applications. Employing photonic crystals one can engineer the dispersion properties of guided modes and this enables designs where electromagnetic radiation strongly interacts with an analyte at a specific wavelength λ determined by the periodicity and the geometric design of the photonic crystal [11]. Another feature of PhCs is the possibility to create local states in the bandgap by locally creating defects into the periodic lattice (crystal defects) [12]. Series of defects in photonic crystals will break the existing symmetry of the photonic crystal and a narrow defect mode is created inside the photonic bandgap, which is a waveguide mode. The corresponding guided mode is confined to these defects and light can only travel along the waveguide [13].

In this study, as an example, we considered a mid-IR wavelength of λ=5.85 µm, which was reported to be suitable for the determination of deterioration in lubrication oil [14]. As silicon is transparent in the mid-IR, it is particularly attractive to utilize silicon MEMS technology. To this end (and also for similar applications), the utilization of a rather thick slab waveguide would facilitate the efficient coupling to an integrated infrared emitter [15]. Simultaneously, the mode is well confined into the Si-slab in this case but

features a low evanescent field ratio (EFR). The evanescent field ratio, which is a crucial parameter for the sensing application, is defined using the following equation [5]

$$EFR = \frac{\int_{\text{analyte}} \vec{S}.\vec{n}dydz}{\int_{\text{all}} \vec{S}.\vec{n}dydz}$$

where $\vec{S}$ is the Poynting vector and $\vec{n}$ the unit normal vector pointing in the direction of propagation (x). The surface integrals extend over the cross-sectional yz-plane of the slab waveguide.

The EFR of a slab WG is plotted as a function of the slab thickness in Figure 1. It can be seen that the EFR decreases as slab thickness increases. Therefore, conventional methods (i.e. slab WG) of evanescence-field absorption demand rather thin slabs in order to achieve the required EFRs and, subsequently, sensitivities. The requirement of a thin slab stands in sharp conflict with the benefits of a thicker slab (i.e. better source coupling and less spurious leakage of the WG mode), as mentioned earlier. This area of conflict can be resolved with PCWGs [16].

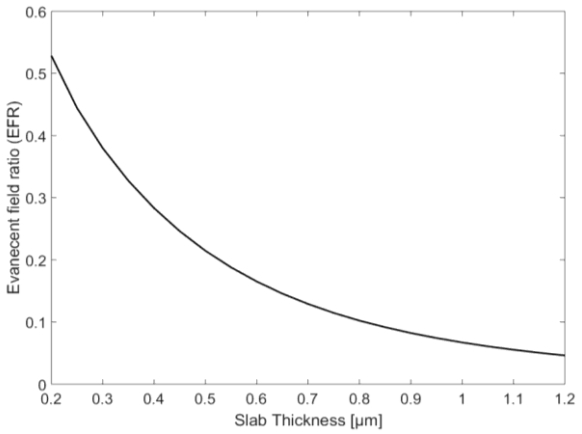

Figure 1: Evanescent field ratio (EFR) of slab waveguides (vertical profile Air-Si-Air) with different thicknesses for the Si layer at λ=5.85µm. The EFR gives the fraction of electromagnetic energy that is guided in the evanescent field.

RESULTS AND DISCUSSION

In this work, we present a design to enhance the light-matter interaction of a photonic crystal WG mode by a fluid analyte in a rather thick slab. In such a way, one can also facilitate efficient coupling to an integrated infrared emitter. The photonic crystal waveguide mode features high confinement of the electric field inside the Si-slab. The lower inset in Figure 4 shows the E-field profile of the photonic crystal waveguide mode. The proposed structure is a slot photonic crystal waveguide in which the guided mode is an eigenmode of photonic crystal and therefore fundamentally has a low loss. The optical field in this structure is enhanced and confined in the low index

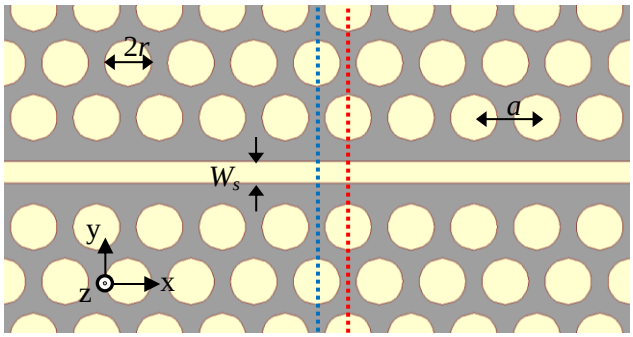

Figure 2: Two-dimensional schematic view of the slot-PhC waveguide. The blue and red dashed lines define the position of the monitors to calculate the evanescent field ratio (EFR) presented in Figure 4.

material, which is a typical feature and strength of slot WGs. Hence, the designed device has a rather high evanescent field ratio, results in the strong light-matter interaction, which contributes to high sensitivity. Only TE polarized light-wave, which has the electric field dominantly oriented in the photonic crystal plane, is considered here. The basic structure of the photonic crystal used in this paper is a two-dimensional structure, which is to be realized on a silicon slab (n = 3.57) by arranging a triangular lattice of circular air holes with period a, which are filled with SiO_2 with radius $r = 0.37a$. By removing one line of filled holes from regular PhC lattice, a waveguide is formed. A slot with width Ws is embedded in the center position of the waveguide. The slot also filled with SiO_2. Figure 2 shows a schematic view of the PhC waveguide with an additional slot within the waveguide.

The dotted blue lines Figure 3 show the dispersion bands of a 2D photonic crystal with $r = 0.37a$ which supports TE polarized modes with a bandgap that ranges from 0.211-0.305a/λ. Only modes bellow the light line (black line in Figure 3) can confine into the photonic crystal. Modes in the gray shadow area are radiating modes. As mentioned above, a photonic crystal waveguide is formed by removing one line of SiO_2 holes creating a series of defects. The photonic crystal waveguide (PCWG) creates additional bands in the bandgap of the unperturbed crystal. Also, the dispersion diagram of a PhCWG without slot (not shown) features poor energetic separation between the waveguide modes. By adding a low-index slot into the PCWG, the energies of the guided modes drift apart resulting in a reduction of loss by mode coupling as shown by red lines in Figure 3. In particular, the mode at $\omega a/2\pi c$=0.283 entails excellent mode separation by

the adjacent bandgaps and maximum light-matter interaction due to the low group velocity (small slope near the edge of Bril1ouin-Zone). The Plane Wave Expansion (PWE) method is used to calculate the photonic bandgap and propagating modes of the structure.

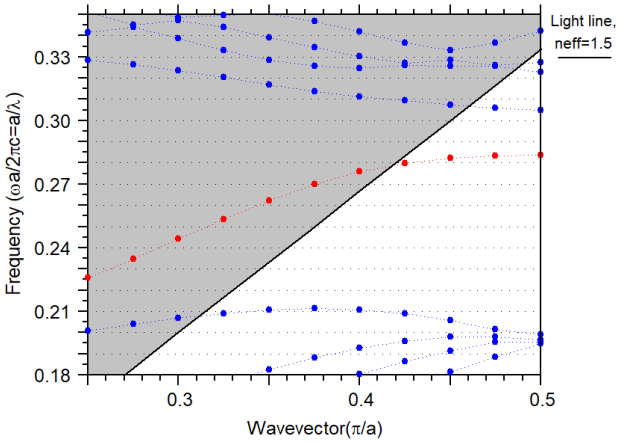

Figure 3: The red line present dispersion band diagram of the slot PhC waveguide with slot width Ws =0.9µm. The slab thickness is h=0.9µm and r=0.37a. The modes above the light line (black line), in the shadowed gray area, are leaky modes.

Changing the slot width allows tuning the energy of the WG mode as well as the evanescent field ratio. The latter vs. slot width for the slot PhC waveguide in two different cross-sections featuring high symmetry in the PhC lattice (shown in Figure 2 with dotted blue and red line) was calculated. The evanescent field ratio can be pushed to about 63% (see Figure 4), which is up to a factor of 7.6 larger than for the associated slab WG without a slot. The simulated electric field profile is given in terms of the field component E_y (z is perpendicular to the PhC surface) of the PCWG modes with the highest EFR is shown higher inset of Figure 4. The lower inset shows the profile of the transverse electric field of a quasi-TE mode in a waveguide with Ws=0 and the upper inset for Ws=0.9 µm. The FDTD method was used to calculate the field profile.

CONCLUSION

In conclusion, we presented a design for a slot photonic crystal waveguide facilitating the enhancement of interaction among analyte and light, which leads to the enhancement of effectively detected analyte absorption. An enhancement factor of 7.6 in the evanescent field ratio compared to slab waveguide with similar thickness has been achieved by tuning the slot width. The slot photonic crystal waveguide is simulated by using the PWE and the FDTD methods. We have demonstrated the potential for highly sensitive liquid detection with a slot photonic crystal waveguide. This high sensitivity could be achieved because of the large overlap of the waveguide mode with the analyte.

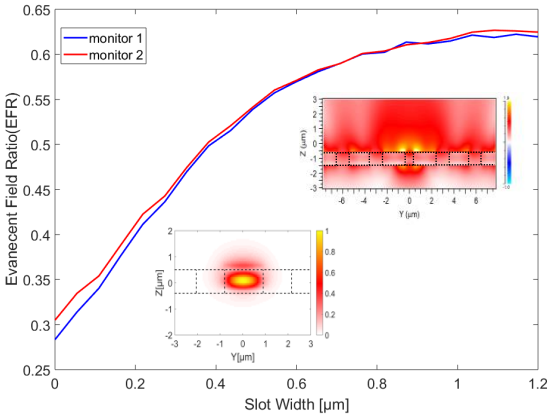

Figure 4: EFR vs. slot width for the slot PhC waveguide in two different cross-sections featuring high symmetry in the PhC lattice. The position associated with the blue and the red lines is indicated in Figure2. The insets show the profile of the transverse electric field of a quasi-TE mode in a waveguide with Ws=0 (lower inset) and Ws=0.9 µm (upper inset), respectively.

ACKNOWLEDGMENT

This work has been supported by the COMET-K2 "Center for Symbiotic Mechatronics" of the Linz Center of Mechatronics (LCM) funded by the Austrian federal government and the federal state of Upper Austria.

REFERENCES:

[1] M. G. Scullion, T. F. Krauss and A. Di Falco, "Slotted Photonic Crystal Sensors," *Sensors*, vol. 13, pp. 3675-3710, 2013.

[2] Dell'Olio, F., Passaro, V.M. N., "Optical sensing by optimized silicon slot waveguides," *OPTICS EXPRESS*, vol. 15, no. 8, p. 4977, 2007.

[3] R. Jannesari, T. Grille, U. hedenig, B. Jakoby, "High sensitivity liquid sensing by optimized slot photonic crystal ring resonator," *Proc. SPIE 10249 Integrated Photonics: Materials, Devices, and Applications*, vol. IV, p. 102490B, 2017.

[4] Witzens, J., Baehr-Jones, T., Hochberg, M., "Design of transmission line driven slot waveguide Mach-Zehnder interferometers and application to analog optical links," *OPTICS EXPRESS*, vol. 18, no. 16, p. 16902, 2010.

[5] C. Ranacher, C. Consani, R. Jannesari, T. Grille,

B. Jakoby, "Numerical Investigations of Infrared Slot Waveguides for Gas Sensing," *Proceedings*, vol. 2, no. 13, p. 799, 2018.

[6] Lee, M., Fauchet, P.M., "Two-dimensional silicon photonic crystal based biosensing platform for protein detection," Opt. Express, vol. 15, p. 4530–4535, 2007.

[7] Hopman, W. C. L., Pottier, P., Yudistira, D., van Lith, J., Lambeck, P. V., De La Rue, R. M., Driessen, A., "Quasi-One-Dimensional Photonic Crystal as a Compact Building-Block for Refractometric Optical Sensors," IEEE J. Sel. Top. Quantum Electron. , vol. 11, p. 11, 2005.

[8] Di Falco, A., O'Faolain, L., Krauss, T. F., "Photonic crystal slotted slab waveguides," Photon. Nanostructures–Fundamentals Appl., vol. 6, no. 1, pp. 38-41, 2008.

[9] Y. Zhang, Y. Zhao, D.i Wu and Q. Wang, "Theoretical research on high sensitivity gas sensor due to slow light in slotted," Sensors and Actuators B, vol. 173, pp. 505-509, 2012.

[10] M. Notomi, "Theory of light propagation in strongly modulated photonic crystals: Refractionlike behavior in the vicinity of the photonic bandgap," Physical Review B, vol. 62, 15 OCTOBER 2000.

[11] N. A. Mortensena and S.i Xiao, "Slow-light enhancement of Beer-Lambert-Bouguer absorption," Applied Physics Letters, vol. 90, p. 141108, 2007.

[12] Yablonovitch, E., Gmitter, T. J., Meade, R. D., Rappe, A. M., Brommer, K. D., Joannopoulos, J. D., "Donor and acceptor modes in photonic band structure," Physical Review Letters, vol. 67, pp. 3380-3383, 1991.

[13] Joannopoulos, J. D., Johnson, S. G., Winn, J. N., Meade, R. D., Photonic Crystals: Molding the Flow of Light, Princeton University, 2011.

[14] A. Agoston, C. Ötsch, J. Zhuravleva, B. Jakoby, "An IR-Absorption sensor system for the determination of engine oil deterioration.," proc., IEEE Sensors, vol. 1, p. 463–466, 2004.

[15] G. Pühringer, B. Jakoby, "Highly Selective CMOS-Compatible Mid-Infrared Thermal Emitter/Detector Slab Design Using Optical Tamm-States," Materials, vol. 12, p. 929, 2019.

[16] J. Kasberger, T. Fromherz, A. Saeed, B. Jakoby, " Miniaturized integrated evanescent field IR-absorption sensor: Design and experimental verification with deteriorated lubrication oil.," Vibrational Spectroscopy, vol. 56, no. 2, p. 129–135, 2011.

HIGHLY PARALLEL MICROBIOREACTOR FOR CELL LINE DEVELOPMENT BASED ON A MICROTITER PLATE WITH FUNCTIONAL MICROFLUIDIC LID

A. Itani[1], C-H. Tsai[1,3], D-H Kuan[2], S. Zimmermann[1], R.Zengerle[1,4], and P. Koltay[1,4]
[1]Laboratory for MEMS Applications, IMTEK – Department of Microsystems Engineering, University of Freiburg, Germany
[2]Bio-Optofluidic System Lab, Graduation institute of biomedical electronics and bioinformatics, National Taiwan University, Taiwan
[3]cytena GmbH, Freiburg, Germany and
[4]Hahn-Schickard Freiburg, Germany

ABSTRACT

Cell line development (CLD) is a complicated process in biotechnology that is time consuming, costly, and labor-demanding. In this context, it is required to accelerate the CLD by developing novel technologies that can optimize early-stage cell culture, and cell line monitoring. Therefore, we have developed a microbioreactor (MBR) for miniaturized and highly parallel cell culture. The systems consists of a standard micro titer plate (MTP) and a so called functional lid (FL) that enables highly parallel reciprocal mixing of cell suspensions for at least 7 days with small culture volume (150 µl). Compared to the standard dynamic shaking cultures in MTP, the FL concept generates significantly less shear rate, and results in remarkably (1.5-x) increased cell growth, from which pharmaceutical cell line development (CLD) might benefit significantly in the future.

KEYWORDS

Microbioreactor, cell line development, functional lid, microfluidic mixing, simulation

INTRODUCTION

In 1984, Dr. Georges J. F. Köhler and colleagues developed a technique for producing monoclonal antibodies (mAb) and received the Nobel Prize in Physiology or Medicine [1]. This discovery was a basic step forward in exploiting antibodies to produce diagnostics and therapeutics in mammalian cells. Cell line development (CLD) is a core process that enables a high production yield and product quality in the production of therapeutic mAbs and other recombinant drugs [2]. However, high protein expression is exhibited by only a few cells, thus to find the highest and most stable producers, massive parallel screening of thousands of clonal cell lines is required. In order to improve CLD, low volume MBR's and selection of clones must be brought to an early stage. An ideal MBR requires high parallelization, small volume, high production quality, and low shear rate during mixing. This is realized by continuous, gentle, and controlled agitation of cell suspension, while parameters essential to cell viability, like pH [3] or dissolved oxygen [4] levels, are monitored. Thus in order to significantly accelerate CLD, a MBR must be designed with high mixing efficiency and low shear rate, high degree of automation and parallelization, and high flexibility regarding future integration of sensors for monitoring essential process parameters. Continuous, gentle, and controlled mixing of cells inside a MBR benefits the process by providing: 1. Homogenously distributed cells that utilize the 3D space optimally, allowing growth to much higher cell densities, 2. Homogenously distributed oxygen and nutrition in the medium, and 3. A significantly low shear rate as compared to standard methods. A highly concentrated cell suspension results in a reduced number of seed train steps as dilation of the cell suspension during scale up can be prevented, thus accelerating CLD.

METHOD

Figure 1 shows the working principle of the functional lid based MBR (FL-MBR) that enables continuous mixing. All the 96 fluidic channels (Dimensions: inner diameter: 3 mm, outer diameter: 5mm, length: 11mm) of the FL are connected to one central manifold, and the full lid is mated with a standard 96-well plate. Positive and negative pressure are provided to the central manifold of the FL which is connected to a dual piezo pump that pumps air in/out the manifold like sketched in figure 2. Thus, all the fluidic channels experience the same pressure change simultaneously when the pressure in the manifold changes. When the FL is put on top of the 96-well plate filled with cell suspension, reciprocated mixing is generated as the FL aspirates and releases liquid from each well of the 96-well plate. The liquid level is monitored by means of a pressure sensor, the output of which is fed back to an embedded Linux system, hence allowing periodic and autonomous operation of the reciprocating mixing during long term cell culture. As compared to standard shaker based microbioreactors – predominantly used for early stage cell culture agitation – the entire system remains

at rest with the reciprocating method, allowing easy integration of optical sensors for oxygen monitoring, and results in much lower shear rate on the surfaces of the MTP. In the real situation, the measured pressure and the liquid levels differ due to capillary rise. A mathematical model presented in [5] was derived to correlate the reciprocating volume with the measured pressure. Thus, by the control of the pressure in the manifold, the liquid volume distribution between micro well and fluidic channel can be controlled.

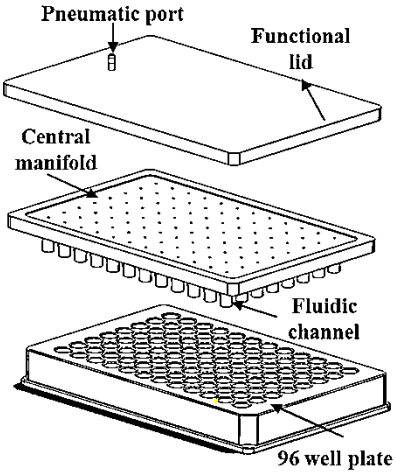

Figure 1:The system view of a functional lid (FL) with 96-fluidic channels compatible with a standard 96-well plate.

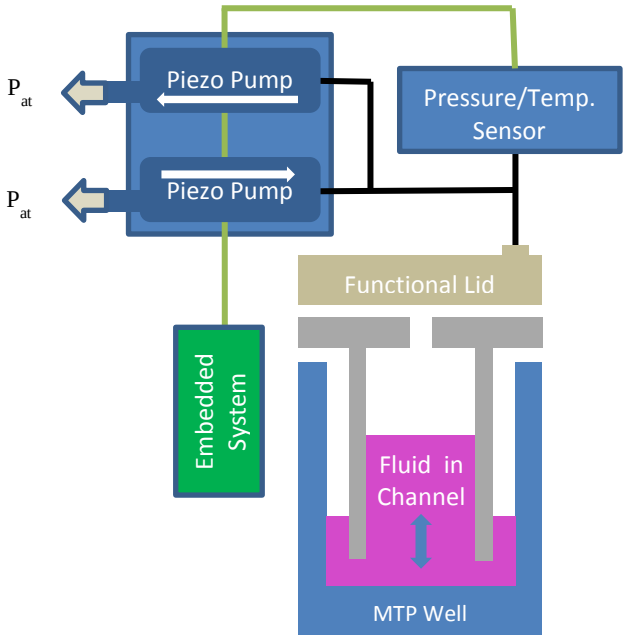

Figure 2: Schematic sketch of the working principle of the FL microbioreactor (MBR) consisting of a 96-well plate covered by the FL that is operated by a dual piezo pump and a raspberry Pi based embedded system.

In the following we present a model for determining the shear rate during the reciprocating mixing process to prove that the mixing is more gentle than with established methods. This shear rate was determined via a two-phase flow simulation using COMSOL multiphysics by modelling the reciprocating motion of an individual well.

SIMULATION

In order to determine the shear rate the cells are subjected to, the fluid flow in a single well and inside the fluidic channel was modeled by COMSOL Multiphysics software (Version 5.0.). The volume-of-fluid (VOF) method was used to simulate the two phase flow (i.e. air and water) during reciprocating mixing. The simulation was done in a 2D axisymmetric model to simplify computations as the considered well and channel have cylindrical symmetry. The physics selected for this case was “Two phase flow, level set”, which is applicable for modeling situations in which only an approximation of the shape of the gas-liquid interface is necessary, hence saving again computational effort. As depicted in figure 3, the geometry to be revolved was drafted to represent the fluid in the fluidic channel (cylinder with ϕ3 mm, height of 5.45mm), the fluid between the outer surface of the channel and the surface of the well (annular geometry with inner ϕ5mm and outer ϕ6.5mm, height of 5.45mm), the air on top of the latter two (same geometries, height 4.85mm), and the fluid between the bottom of the tube and the bottom of the well (cylindrical geometry, ϕ6.5mm, height 0.7mm). The sum of the heights therefore represents the maximum height the fluid can reach in the tube (0.7+5.45+4.85=11mm). The height differences due to capillary rise were not considered in this simulation. Water was selected as the fluid in the device, however the viscosity and density were adjusted to that of DMEM at 37°C (0.78mN-s/m, and 1020 kg/m3 respectively).

Three different laminar flow conditions were imposed on the inlet of the tube at the top cylindrical surface with flow rates of 80, 110, and 180 µl/min, corresponding to a total reciprocating volume of 46 µl with a duration of 30, 50 respectively 70s for a full periodic pumping cycle. The outlet at the annular surface was modelled as atmospheric pressure boundary conditions. The shear rates at the bottom of the well, where considered for evaluating the maximum shear rate, because there the highest values are obtained, except for the inner edge of the microfluidic channel, where the shear rate is higher than at the bottom, but appears in a negligible volume only. The results of the simulation are visualized in figure 4 and compared to the shear rates estimated for

other standard mixing methods in table 1. The results are clearly showing that the reciprocating mixing generates significantly smaller maximum shear rates.

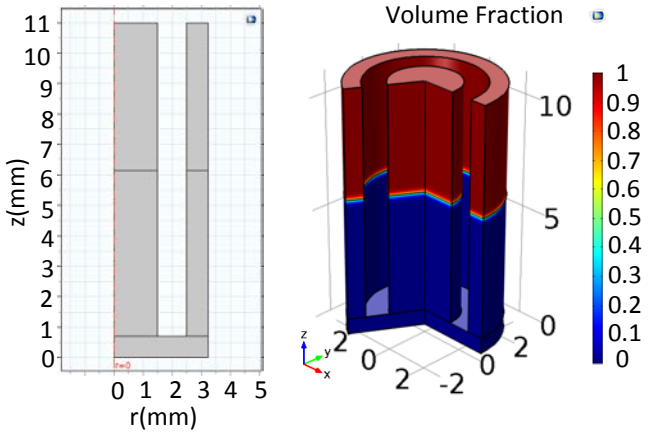

Figure 3: (a) the geometry representing the fluids before revolution around the r=0 axis (b) the geometry after revolution and phase initialization where red represents the volume fraction of air, and blue that of water.

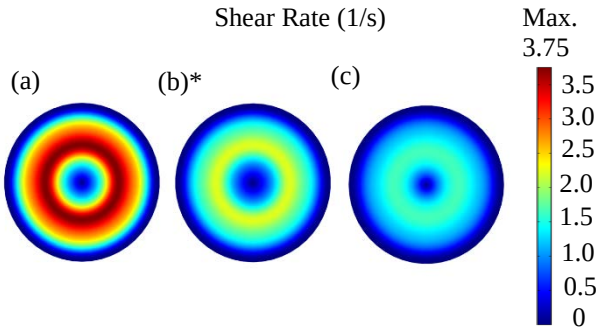

Figure 4:(a) The shear rate distribution at the bottom of the well for a reciprocation period of 30 seconds, (b) 50 seconds, and (c) 70 seconds (46µl volume). The reciprocating frequency applied in the experiments is marked by *.*

Agitation Method	Rotation Speed/ Reciprocation Period	Orbital Diameter/ Reciprocating Volume	Shear Rate (s^{-1})
Shaking	150 rpm	50 mm	46.2
Shaking	150 rpm	70 mm	170
Shaking	50-200 rpm	25-100 mm	180
Reciprocating	30s	46 µl	~3.7
Reciprocating	50s*	46 µl	~2.3
Reciprocating	70s	46 µl	~1.7

*Table 1: Different shear rates in shaking MTP, and reciprocating FL-MBR in 96-well MTP. The reciprocating frequency applied in the experiments is marked by *.*

EXPERIMENTAL RESULTS

The experimental results shown in the following were carried out to validate the concept of the FL-MBR by a cell culture experiment. A prototype system of the FL-MBR described elsewhere [6] was used where each well of the 96-well plate was mated with a functional lid containing fluidic channels with the same dimensions as in the simulations presented before. For the experiments, the wells were filled with 100 µL of cell culture medium (DMEM), and the embedded system inside the prototype actuator module (raspberry PI zero) was used to measure the pressure in the central manifold by a MEMS pressure sensor (Honeywell-HSCDRRN010MD2A3) and to control the two piezo pumps (Bartels-mp6), in order to reciprocate the liquid as described before. As described in [6], the system will switch pumping direction when the measure pressure reaches an upper and lower limit, corresponding to a higher and lower liquid level respectively, thus realizing periodic reciprocating operation.

The cells used for culture were from a Chinese Hamster Ovarian (CHO) cell line that expresses the breast cancer drug Trastuzumab, a monoclonal antibody (mAb) that targets HER2 (CHO mAb cells). Pharmacological cell culture conditions in a chemically defined medium (CD Hybridoma medium (#11279-023 von GibCo) + Cholesterol + 8 mM Glutamin + 150 U/ml Hygromycin + Pen/Strep) were used to grow the cells. CHO mAb cells were maintained in a shaking well culture, and static culture in a 96-well plate as a control group, preloaded with 150 ul cell suspension with concentration of $4x10^5$ cells/ml in each well. The three groups were cultured for 6 days in an incubator, and the cell concentration was determined from day 0 by counting trypan-blue-stained cells from selected wells. The shake flask culture was covered with a standard lid, and was placed at 80 rpm in an incubator shaker. The FL-MBR was operated continuously, while recirculating a volume of ~46 µL per reciprocating pump cycle. The same number of individual wells (N=4) was evaluated in both groups and the cells were counted in each well to determine the average cell number by Trypan blue staining of the cells and their subsequent counting in a hemocytometer. It is noteworthy that cell counting using a hemocytometer is of convenience in small scale suspension cell cultures of 150 µl due to minimal sample consumption. A minimum of 4 independent wells were assessed per functional variant and time point by this method in order to reduce the statistical error.

As shown in Figure 5, at day 1, there is no difference visible between the three groups, as all reach a cell concentration of around 8.0 x 10^5 cells/ml.

However, after two days, the static and shaker culture reaches a plateau of cell concentration (~1.5 x 10^6 cells/ml), while the cell concentration of the FL-MBR group continuously increases until day 3 reaching around 2.7 x 10^6 cells/ml. According to a student's two sample t-test, there is a significant difference in the cell concentration between the FL-MBR and the standard culture methods during days 2 through 6. From day 4 onwards, there is a decline in cell concentrations of all groups, most likely due to medium exhaustion typically caused by lack of fresh medium. Still, the experiment demonstrates that the FL-MBR can significantly increase the cell growth and total cell number in a miniaturized cell culture.

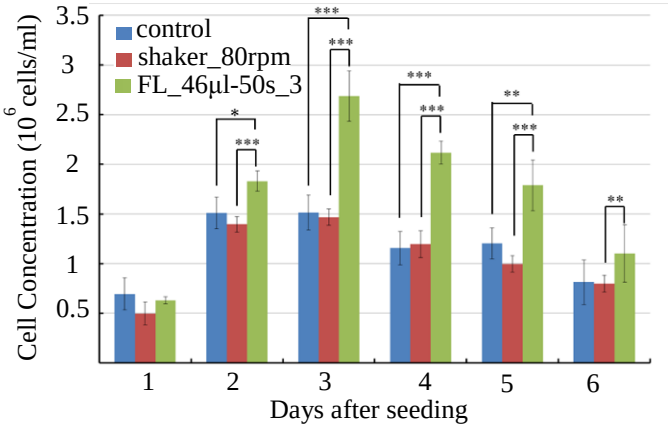

Figure 5: Cell growth of CHO mAb cells in FL-MBR compared to shaking of 96 well plate(*) indicates p<0.05, (**) p<0.01, and (***) p<0.001[5].

SUMMARY AND CONCLUSION

A novel concept of a microbioreactor (MBR) based on reciprocating mixing in a conventional micro plate enabled by a functional lid (FL) has been presented in this work. The FL-MBR is designed for highly parallel mixing cell suspensions in cell culture related applications compatible with standard laboratory methods and equipment. The FL-MBR consists of: 1. a conventional 96-well plate, 2. a FL, and 3. an embedded control system with microfluidic components. Homogeneous mixing of cell suspensions is achieved by the FL-MBR by reciprocation of liquid in all wells of a standard 96-well plate. As compared to traditional shaking methods, the FL-MBR offers a gentle, more stable and efficient method that generates a significantly smaller maximum shear rate in the range of 1.7 to 3.7 s^{-1} as has been proven by the VOF simulations in this work. As compared to a traditional static culture used in early stage CLD, the cell concentration in a 96-well has been shown by experiments to increase significantly when using the FL-MBR with an antibody producing CHO cell line. The cell concentration could be increased by a factor of 1.5 compared to the conventional method of a static cell culture achieving a final yield of 2.7 x 10^6 cells/ml.

ACKNOWLEDGEMENTS

We thankfully acknowledge financial support from the Studienstiftung des deutschen Volks, the Federal Ministry of Education and Research of Germany (Mono-cy-Clone, GA 031B0114C), and technical support from cytena GmbH.

REFERENCES

[1] G. KÖHLER and C. MILSTEIN, "Continuous cultures of fused cells secreting antibody of predefined specificity," Nature, vol. 256, p. 495, Aug. 1975.

[2] TF Lai, YS Yang, and SK Ng, "Advances in Mammalian Cell Line Development Technologies for Recombinant Protein Production", pharmaceuticals, 6, 579-603, 2013.

[3] G. John, D. Goelling, I. Klimant, H. Schneider, E. Heinzle, "PH-Sensing 96-well microtitre plates for the characterization of acid production by dairy starter cultures", Journal of Dairy Research, vol. 70, pp. 327-333, 2003.

[4] G. T. John, I. Klimant, C. Wittmann, E. Heinzle, "Integrated optical sensing of dissolved oxygen in microtiter plates: A novel tool for microbial cultivation", Biotechnol. Bioeng., vol. 81, pp. 829–836, 2003.

[5] C.-H. Tsai, "Highly parallel microbioreactors for cell line development based on well plates with functional lids" PhD Diss., University of Freiburg, 2019.

[6] C.-H. Tsai, S. Zimmermann, R. Zengerle, P. Koltay, "A highly parallel microbioreactor for cell line development based on a microtiter plate with functional microfluidic lid", MFHS 2017, Twente / The Netherlands, 04. - 06.10.2017

CONTACT

Peter Koltay, peter.koltay@imtek.uni-freiburg.de

PRINTING WITH SATELLITE DROPLETS IN LIQUID AND GASEOUS ENVIRONMENT

D. Li[1], Y. Liu[1], and Y. Zhang[1,2]
[1] China University of Petroleum, College of Mechanical and Electronic Engineering, Qingdao, China
[2] Centre of micro-photonic, Swinburne University of Technology, Melbourne, Australia

ABSTRACT

With the advancement of science and technology, there are many techniques emerging for generating and manipulating extremely fine droplets. Ultra-small droplets have a wide application field, including micro-reactor, mechanical, optical, and even biological issue. Here we propose a novel method to generate satellite droplets, whose diameter can be 30 times smaller than the orifice. Femto-liters droplets can be obtained utilizing a nozzle with 100 μm inner diameter. Benefiting from this feature, this can handle liquor reagents with viscosity ranging from 1 mPa s to over 1000 mPa s without worrying about the blockage caused by the viscosity increment. And this approach can be applied to immiscible liquid phase and gas environment. The generated droplets can be controlled by electricity or air stream.

KEYWORDS

Satellite droplets, Inkjet printing, Femto-liters, High viscosity.

INTRODUCTION

As known to all, the generation and manipulation of ultra-fine droplets are the key research points in microfluidic handling systems [1]. And due to its superior set of advantages such as direct writing, flexibility, cost effective and high resolution, etc., inkjet printing plays an important role in microfluidic handling systems, such as micro reactor [2], sensors, mechanical fabrication, and biological cell and tissue engineering [3]. However, in the conventional inkjet printing field, the satellite droplets will be generated with the mother droplets in some cases, as shown in Fig. 1, which will reduce print accuracy and bring an ill impact on the printing results. So many experts are making efforts to seek the mechanisms and different methods to avoid its appearance [4]. And if smaller droplets (for example, submicrometer droplets) are needed, nozzles of the corresponding scale should be fabricated. But the production costs will increase several times as the scale decreases. And obviously, the smaller orifices are fragile, and easy to clog. The factors stated above constrains generating smaller droplets and printing higher viscosity media using inkjet printing technology, and limits the further development of inkjet printing.

Contrary to the conventional sight, here we propose a new concept to utilize the satellite droplets as the printing objects. And a novel approach based on a controllable meniscus break-up procedure has been developed (Fig. 2a), which can generate satellite droplets steadily and continuously [5], which can be named as satellite droplets printing (SDP). The radius of satellite droplets can be 30 times smaller than the orifice, and the volume of which can be 27,000 times smaller than the mother droplets in conventional printing, as shown in Fig. 2b. So this method can handle a wide variety of liquid media regardless of their viscosity and contents. In our experiments, the glycerol satellite droplets of 1500 mPa s were successfully generated in another immiscible phase. An electric field can be applied to manipulate the droplets in the liquid phase. Moreover, this satellite generating technology was realized in air environment [6]. And a confined gas stream was applied as the transportation phase. Precisely positioned patterns with femto-liters droplets can be obtained in the liquid phase and gaseous phase.

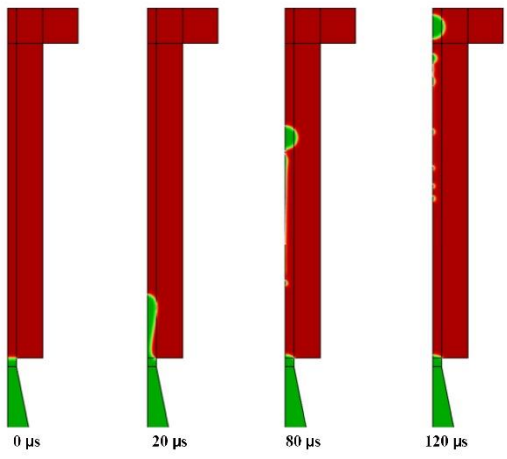

Figure 1: Axisymmetric model of conventional inkjet printing process with a series of satellite droplets.

RESULTS AND DISCUSSION

Fig. 2b shows the satellite droplets generating process, which is recorded by high speed camera (Neo

sCOMS, Andor, EU) connected to an optical microscope (ECLIPSE, TE2000U, Nikon, Japan). A computer controlled syringe drives the liquid out of the symmetrical orifice precisely until they gather together. Then it sucks back to form a meniscus, which will finally breaks up into an ultra-small satellite droplet in silicone oil due to the Rayleigh-Plateau instability. Droplets with different volumes can be obtained using the same device only by adjusting the distance between the orifices *L* and the drainage rate *Q*. The basement of the meniscus attaches to the outer of the liquid supply tube, whose radius is 750 μm. And the smallest radius of the satellite generated by the same nozzle can be 23 μm.

As this approach can generate tens times smaller droplets than the orifice size, the clogging phenomenon of the fragile glass nozzle during printing process can be overcame, because we can obtain droplets of the same size by a bigger nozzle comparing with the conventional inkjet printing methods. This outstanding property makes it especially suitable for printing high viscosity media. And in our experiments, glycerol with viscosity of 1500 mPa s was used as one printing reagent, and satellite droplets with radii smaller than 20 μm were successfully generated by a glass tube with outer wall of 1500 μm radius and inner orifice of 375 μm radius. And this technology can handle a variety of suspensions such as liquid containing another phase or two or more liquid/solid phases. Oil-in-water emulsion was processed by this method, and the capsuled micro droplets can be applied to many conditions.

After the droplets being generated, the electrical field was applied between the orifice and the substrate to realize the manipulation of droplets (Fig. 2a and 2c). A power supply was mounted onto the experimental device. The positive pole was connected to the tube, and the negative pole was connected to the ITO substrate to form the electric field. The charged droplets can be transported to the substrate with opposite charge and thus form a precisely located pattern with a positioning system. And a series of experiments revealed that it is better to arrange the two orifices' end surface at an angle of 45° to the bottom substrate, as shown in Fig. 2c. Finally the generated satellite droplets can be placed onto a micro-positioning system to form a pattern. And another droplet can be placed again at the same position to control the volume of the final droplet. What's more, another reagent can be dispensed to the former satellite droplets to realize the chemical reaction, admixture, encapsulation, and etc.

Then we extended the application of this technology to air environment, as shown in Fig. 3 and Fig. 4. Although generating ultra-fine satellite droplets in the immiscible liquid phase is easy to observe and manipulate the droplets, considering the constraints of the surrounding media. And the micro droplets will evaporate at a very fast speed. We overcame the above obstacles to realize the printing and observing of the satellite droplets in the atmosphere condition. We placed the nozzles as close as possible to the substrate surface. And the high quality high speed camera (Photron, SA-Z, Japan) combining with the microscope (Leica, DM i8, Germany) were utilized to observe the whole process.

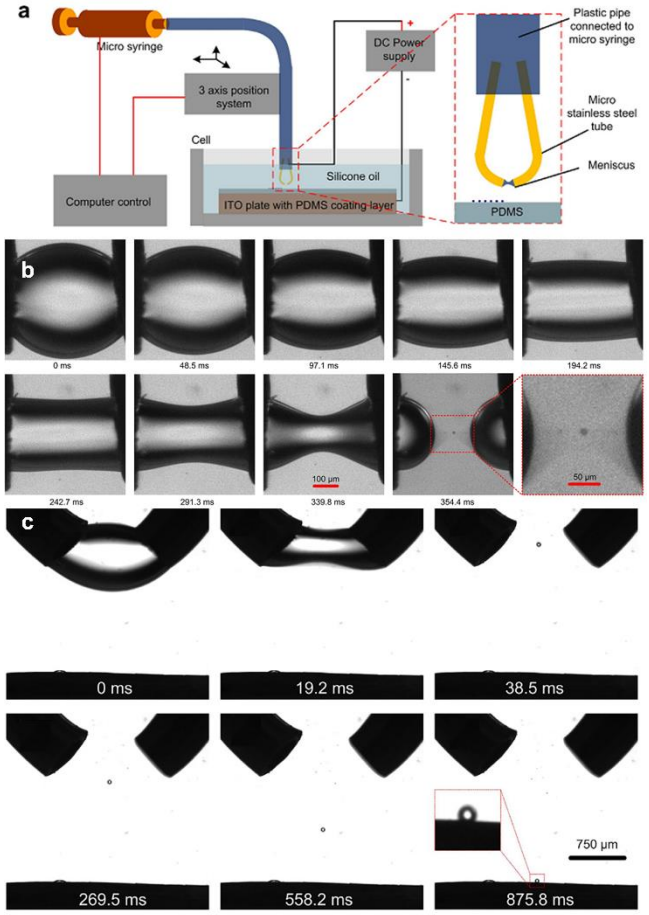

Figure 2: (a) Schematic of the experimental device in liquid environment; (b) Formation process of satellite droplets; (c) Manipulation of the charged droplets.

And efforts were made to investigate the pinch-off process of the satellite droplets. Firstly, COMSOL multiphysics 5.3a was applied to simulate mechanism of the whole process. The simulation results in Fig. 3a show that after merging, the liquid in the meniscus is redistributed and the meniscus assumes a hyperbolic shape under the influence of surface tension (70–120 μs). Afterwards the liquid will be aspirated back into the ink chamber of the nozzle. The volume reduction of the meniscus leads to thinning (112–182 μs) and ultimately to the breakup of the meniscus in its middle section at 183 μs. Before the moment of break-up, a thin liquid filament will be formed in the middle section of the meniscus due to the drainage of the liquid through the two necks connecting the filament with the

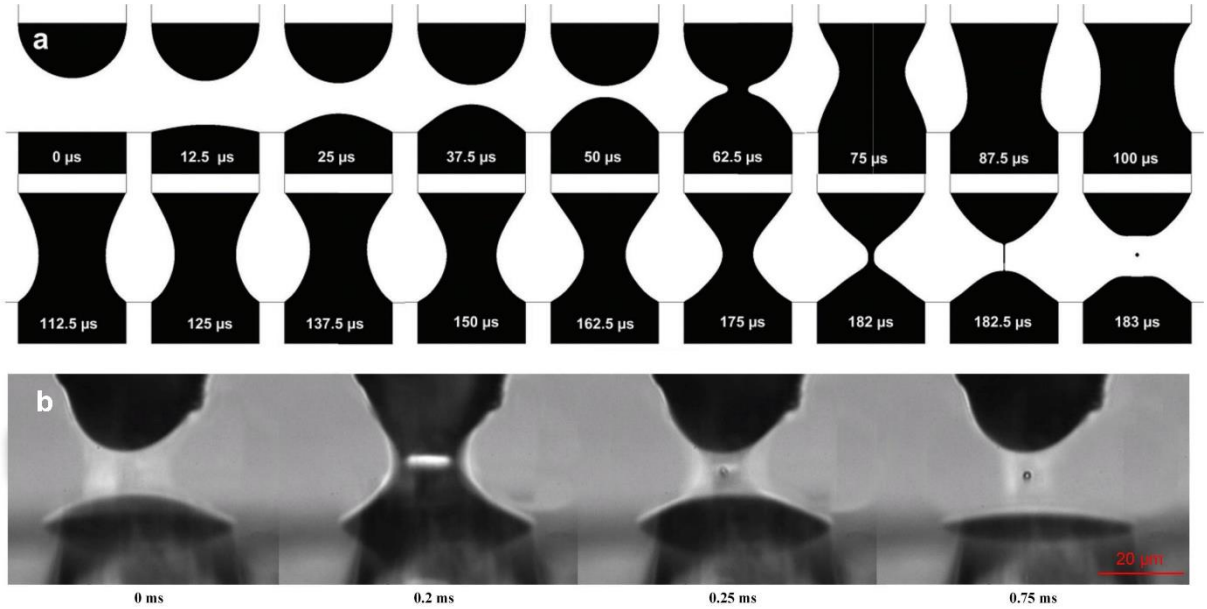

Figure 3: Formation of satellite droplets in gas environment. (a) Simulating the formation of satellite droplets using COMSOL; (b) High speed camera recorded satellite droplets formation process.

upper and lower tapered reservoirs. The drainage rate is largest in the necks and approaches zero in the middle of the filament. Therefore, the drainage leads to further shrinkage of the diameter of the necks and to its eventual break-up within only one microsecond. Under the influence of surface tension, the isolated, elongated filament assumes the spherical shape of the satellite droplet. The whole process only lasts about 200 μs or sooner. So the theoretical printing frequency can exceed 5 KHz. The high speed camera observation results were shown in Fig. 3b. But the break up process is only several micro seconds, which is so fast that even the high speed camera cannot record more details about it. Despite this, we have captured some shots of satellite droplet generation. And the results of experiments and simulations agree with each other, which all indicate the feasibility of generating satellite droplets in air atmosphere. Due to the generating process takes place at the horizontal direction and close to symmetric, there is nearly no kinetic energy for droplets to move down. And the droplets will make some slight irregular movements with the fluctuation of the surrounding air, as shown in Fig. 3b. Here we choose the eco-friendly constrained airflow to control droplets movement.

Fig. 4 illustrates the patterning system in air. The piezoceramics was applied at the orifice side as the driver, implementing drop-on-demand printing. One pretreated metal rod is mounted at the opposite side, which is coaxial with the orifice. There is one gas pipeline perpendicular to the axis of the orifice and the rod with a diameter similar to the orifice. The gas pipe was connected to a gas source with an air regulator. After the satellite droplets being generated, the confined air stream will carry them to the moving substrate, forming the predesigned patterns. Since the radius of the satellite droplet is only several micrometers, the trajectory of the droplets will coincide with the surrounding laminar air stream.

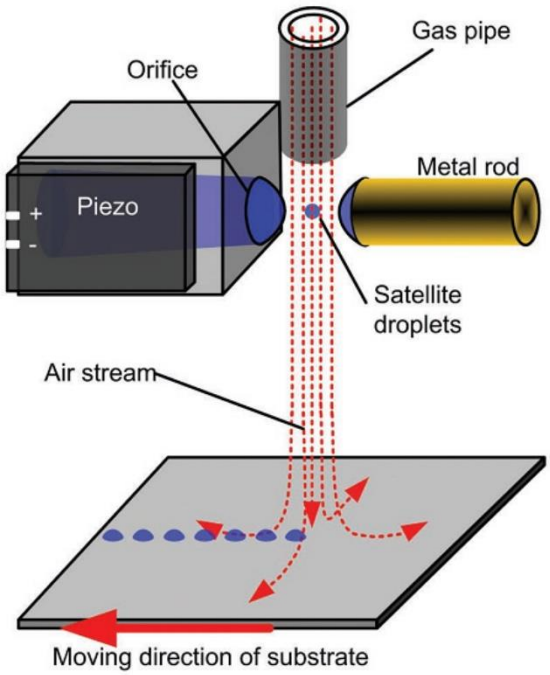

Figure 4: Schematic of the patterning system in air environment.

Besides the velocity and area of the airstream, the trajectory of the satellite droplets can be affected by many parameters, including relative position between orifice, metal rod, and gas pipe, drainage rate of the meniscus and etc. The best position of the air pipe should be just above and centered on the satellite droplet. And the results showed that the air stream should be with appropriate magnitude (several m/s). Too strong air current will hinder the formation of the liquid meniscus and too weak air current cannot transport the satellite droplets to the substrate. With the printing frequency f = 2 kHz, the diameter of the orifice R_{ori} = 18 μm, and printing distance D_H = 300 μm, we obtained the best printing performance with an air stream speed v between about 4–20 ms^{-1}.

This fancy processing method can generate femto-liters droplets with high resolution using dozens of times greater orifice, and can handle viscous inks with a superior performance. Furthermore, the pressure strike in the generating and transporting process are both quite gentle, which makes this approach full of application prospects in micro-reactor, electronic, chemical synthesis, even bio-printing field. A well patterned Chinese character was obtained using this device (Fig. 5).

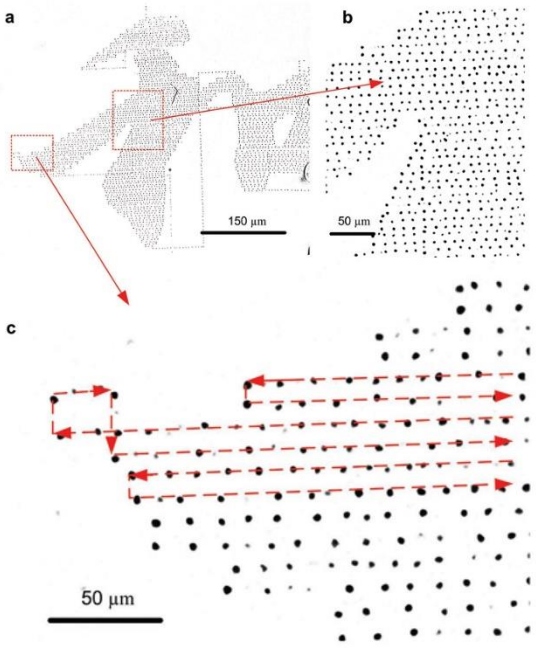

Figure 5: A Chinese character meaning for peace printed using satellite droplets in air.

CONCLUSIONS

The proposed novel method in this paper can generate ultra-small satellite droplets, which can be 30 times smaller than the size of the dispense orifice. This superior characteristic enables the bigger orifice to generate smaller droplets with a high resolution and without worrying about nozzle clogging and breakage. Experimental and simulation results showed that the meniscus break-up as well as the satellite droplet pinch-off process are very robust and repeatable. After pinch-off, the satellite droplets can be precisely conveyed to the substrate surface by electrical field or laminar air stream. And another advantage is the ability to handle media with high viscosity. Even inks with viscosity higher than 1000 mPa s can be swimmingly handled, comparing with conventional inkjet printing methods only can process media no more than 20 mPa s. Moreover, the whole process is very gentle, which can greatly reduce damage to the print media. Future efforts will enable double-orifice structures to improve the printing frequency, and highly integrated nozzle designs and orifice arrays to multiply the printing efficiency.

REFERENCES

[1] Thorsen T, Maerkl Sebastian J., Quake Stephen R., " Microfluidic Large-Scale Integration", Science, Vol. 298, pp. 580-584, 2002.

[2] J.H. Jang, S.Y. Park, "pH-responsive cholesteric liquid crystal double emulsion droplets prepared by microfluidics", Sens. Actuators B: Chem., Vol. 241, pp. 636–643, 2016.

[3] Sanjairaj Vijayavenkataraman, Jerry Y H Fuh and Wen Feng Lu, "3D Printing and 3D Bioprinting in Pediatrics", Bioengineering, 4, 63, 2017.

[4] Q. Yang, H. Li, M. Li, Y. Li, S. Chen, B. Bao, Y. Song, "Rayleigh Instability-Assisted Satellite Droplets Elimination in Inkjet Printing", ACS Applied Materials & Interfaces, Vol. 9, pp. 41521-41528, 2017.

[5] Y. Zhang, B. Zhu, G. Wittstock, D. Li, Y. Liu, "Generating ultra-small droplets based on a double-orifice technique", Sens. Actuators B: Chem., Vol. 255, pp. 2011-2017, 2017.

[6] Y. Zhang, D. Li, Y. Liu, G. Wittstock, "Printing with Satellite Droplets", Small, Vol. 14(39), pp. 1802583, 2018.

CONTACT

* Y. Liu, liuyhupc@163.com

A CONTACT-FREE MICROPUMP FOR FLUID TRANSPORT AGAINST HIGH BACKPRESSURE

A. R. Smith[1], D. Oudejans[2], J. C. Lötters[2,3] and P. Müllner[1,4]
[1] Shaw Mountain Technology LLC, Nampa, Idaho, USA
[2] Bronkhorst High-Tech BV, Ruurlo, The Netherlands
[3] University of Twente, Integrated Devices and Systems, Enschede, The Netherlands
[4] Boise State University, Boise, Idaho, USA

The market offers micropumps covering a wide range of flow rates. However, the dynamic flow rate range of such pumps is typically limited to two to three orders of magnitude and the rise pressure often is below 1 kPa, with high performing piezoelectric pumps reaching 10-20 kPa. We present a magnetic shape memory (MSM) micropump delivering water against a backpressure up to 300 kPa (3 bar). When properly regulated in closed loop control, the pump may transport fluids at flow rates from 0.01 to 1000 µl/min.

A cuboid element of monocrystalline MSM alloy forms the entire pump mechanism. This smart material is an alloy of nickel, manganese and gallium (Ni-Mn-Ga). The MSM effect, which is the coupling of the material's structural and magnetic order, is responsible for the large shape change (nominally 6%). A variation of magnetic field causes the shape change through a process known as twinning. Magnetic actuation is advantageous in that the material's shape can be precisely changed without contacting the device itself. The magnetic dipole field of a small, diametrically magnetized magnet creates a localized shrinkage in a nearby MSM element. This shrinkage follows the poles of the magnet as the magnet rotates and moves through the MSM element. The MSM micropump is realized by encapsulating the MSM element in a sealed conduit – the shrinkage then becomes a cavity and moving the cavity allows for fluid transport. The MSM micropump transports fluid peristaltically similar to how humans swallow. Thus, the MSM material is analogous to a metal muscle.

The viability of this technology has been demonstrated across multiple applications. In 2012, Ullakko *et al.* built an MSM micropump and demonstrated compatibility with PCR and human DNA profiling [1]. Barker *et al.* delivered drugs to the brain of rats with an MSM micropump in a neurophysiological study on schizophrenia [2]. Thomas *et al.* studied transport properties of artificial cell membranes (i.e. droplet interface bilayers) by controlling the size of aqueous micro-droplets in organic suspension [3].

The response time of MSM alloys in pulsed magnetic field experiments is below 5 µs [4] allowing for theoretical actuation frequencies in the kHz range. Self-induction and eddy-currents may impair the material actuation at such high frequency, and microfluid dynamics may further limit pumping at such high frequencies. However, Smith *et al.* demonstrated flow rates up to 30 µl/s (or 1,800 µl/min) at an actuation frequency of 270 Hz [5].

We built an MSM micropump with a Ni-Mn-Ga element contained in a PMMA housing, actuated by a diametrically magnetized N52 Nd-Fe-B magnet. We actuated the pump with a NEMA 8 stepper motor and controlled the motor using a Raspberry Pi computer. Figure 1 shows the micropump. The magnet actuates the pump contact-free.

As shown in Figure 2, we connected the MSM micropump to Bronkhorst's Micro Coriolis Mass Flow Meter BL100 to precisely measure the performance of the MSM micropump [6]. The BL100 is a true mass flow Coriolis meter for the flow range of 0.01-2 g/h (0.17-33 µL/min) for water. The mass flow measurement is independent of the type of liquid, has a fast response (200 ms) and has an unrivaled accuracy in this flow range (1% reading plus 0.1% full scale). Therefore, it is very suitable to characterize microfluidic pumps and flow sensors.

Figure 3 shows the measured flow rate as a function of actuation frequency at zero back pressure. The flow rate increased linearly up to the maximum frequency of 320 revolutions per minute (RPM) where it reached 2.2 g/h (132 µl/min). Figure 4 shows the flow rate as a function of back pressure with constant actuation frequency of 320 RPM. The flow rate decreased monotonically with increasing actuation frequency. A back pressure of 3 bar suppressed the flow.

In these experiments, the software limited the actuation frequency. Extrapolating the data shown in Figure 2 to 1,000 RPM (which is within the specifications of the NEMA 8 stepper motor) yields a flow rate of 400 µl/min, and with Figure 4, a potential maximum back pressure of 10 bar. The MSM alloy Ni-Mn-Ga has a blocking stress of about 5 MPa (50 bar) [7], which denotes the theoretical backpressure limit of the MSM micropump.

Word Count: 693

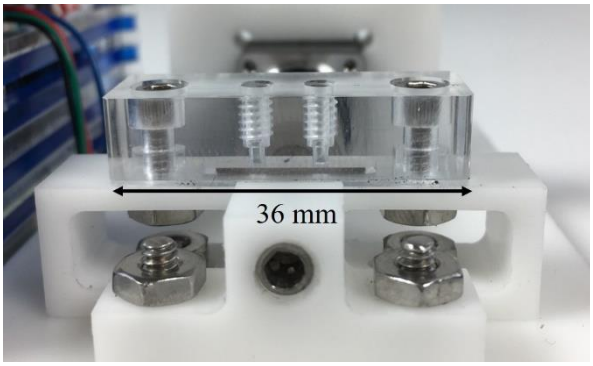

Figure 1: The MSM micropump. The inlet and outlet ports in the acrylic housing are threaded to accommodate two microfluidic 6-32 connectors with 1/16 steel ferrules. A rotating magnet actuates the pump contact-free.

Figure 2: Measurement set-up consisting of the MSM micropump (left) and Bronkhorst's Micro Coriolis Mass Flow Meter BL100 (right).

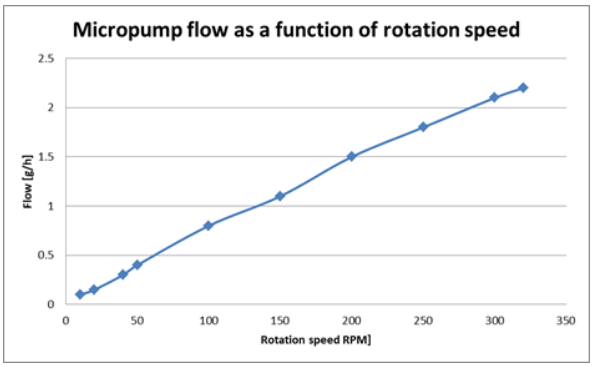

Figure 3. Flow rate as a function of rotation speed. The flow rate increases linearly with actuation frequency.

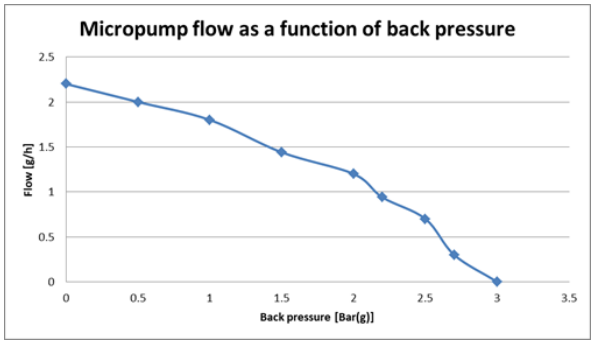

Figure 4. Flow rate as a function of back pressure at an actuation frequency of 320 RPM. The flow rate decreases monotonically and vanishes at 3 bar.

REFERENCES

[1] K. Ullakko, L. Wendell, A. Smith, P. Müllner, G. Hampikian, "A magnetic shape memory micropump: contact-free, and compatible with PCR and human DNA profiling", Smart Mater. Struct. 21, 115020, 2012.
[2] S. Barker, E. Rhoads, P. Lindquist, M. Vreugdenhil, P, Müllner, "Magnetic shape memory micropump for submicroliter intracranial drug delivery in rats", J. Med. Dev. 10, 041009, 2016.
[3] C. A. Thomas, D. Richtsmeier, A. Smith, P. Mullner, D. Fologea, "Lysenin channel reconstitution into unsupported droplet interface bilayers", Biophysical Journal 114/3 suppl. 1, 264A, 2018.
[4] A. Smith, J. Tellinen, K. Ullakko, "Rapid actuation and response of Ni-Mn-Ga to magnetic-field-induced stress", Acta Mater. 80, 373-379, 2014.
[5] A. Smith, A Saren, J. Järvinen, K. Ullakko, "Characterization of a high-resolution solid-state micropump that can be integrated into microfluidic systems", Microfl. And Nanofl. 18, 1255-1263, 2015
[6] W. Sparreboom et al., "Compact mass flow meter based on a micro Coriolis flow sensor", Micromachines 4, 22-33, 2013
[7] H. E. Karaca, I. Karaman, B. Basaran, Y. I. Chumlyakov, H. J. Maier, "Magnetic field and stress induced martensite reorientation in NiMnGa ferromagnetic shape memory alloy single crystals", Acta Mater. 54, 233-245, 2006.

PROPORTIONAL MICROVALVE USING A PIEZOELECTRIC UNIMORPH MICROACTUATOR

A. Gunda[1], G. Özkayar[1], M. Tichem[1], and M.K. Ghatkesar[1]
[1] Delft University of Technology, Delft, The Netherlands

ABSTRACT

Microvalves are important flow-control components in many standalone and integrated microfluidic circuits. Although there is a large body of work regarding microvalves, there is still a need for an easy-to-fabricate, small-footprint, low-power device that can control both liquids and gases at moderate pressures. This paper details the development of a piezoelectric microvalve compatible with both liquids and gases with a maximum driving pressure of $1\,\mathrm{bar}$. A novel combination of accessible methods like 3D-printing and laser-cutting has been used to realize this device. The device has a flow range of 0 - $90\,\mu\mathrm{L\,min^{-1}}$ at $1\,\mathrm{bar}$ inlet pressure. When fully closed, a leakage of $0.8\,\%$ open-flow was measured with a power consumption of $37.5\,\mu\mathrm{W}$.

KEYWORDS

microvalve, proportional, piezoelectric, 3D-printing, unimorph

INTRODUCTION

The need for techniques that more efficiently utilize chemical and biological reagents in chemical analysis systems led to the introduction of micro-total analysis systems (μTAS) [1]. The versatility of miniaturizing fluidics was realized and subsequently utilized in applications like drug-delivery [2], lab-on-a-chip devices [3], and even micro- and nano-spacecraft thermal cooling and propulsion systems [4].

An essential component in integrated microfluidic devices is the microvalve. In conjunction with a pressure source, it is used to control, direct, or regulate the pressure or flow rate of media within microfluidic circuits. Valves that operate in the μm- to cm-length scales are generally classified as microvalves and they are usually fabricated using microfabrication techniques like (soft-)lithography, etching, etc. Conventional microvalves consist of a microchannel that is obstructed by an active/passive element. Active microvalves, as opposed to their passive counterparts, have a controllable element within the device. These valves are usually classified by the working principle of the active element.

In this work, an active proportional microvalve was designed, fabricated and characterized. It is based on a piezoelectric actuation method that uses a commercially available piezoelectric plate as the active element. As the active element functions without any further processing, all the advantages of piezoelectric actuation were retained while the usual manufacturing disadvantages of thin-film piezo-MEMS (Micro Electromechanical Systems) devices were eliminated. The valve deflection was controlled by applying a desired voltage across the piezoelectric material. Thus, the fluid flow-rate in the microvalve was proportionally controlled. The following sections detail the design, fabrication, and characterization of the microvalve.

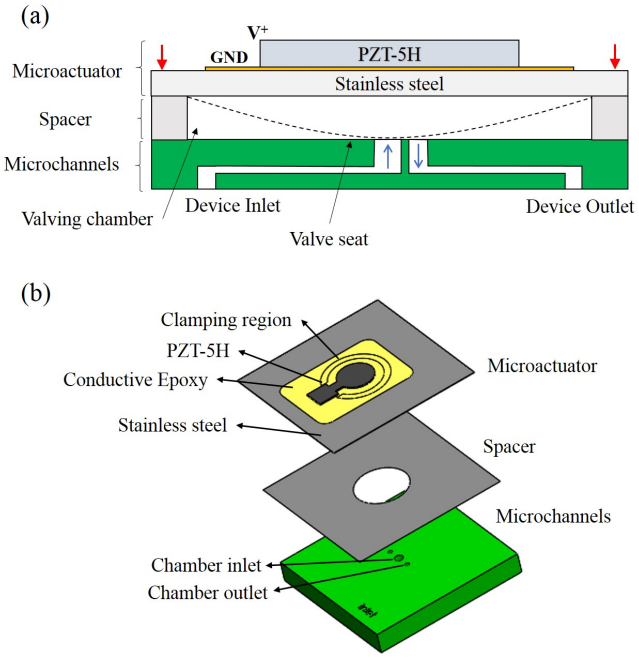

Figure 1: (a) Schematic of the microvalve: It consists of a piezoelectric unimorph microactuator, a spacer, and 3D-printed microchannels. The microactuator is placed on top of the microchannels with an intermediate spacer and the entire assembly is clamped. Red arrows indicate the direction of the clamping force. Black dashed lines indicate the membrane deformation when actuated. (b) Exploded 3D view of the microvalve.

DESIGN AND FABRICATION

A piezoelectric microvalve with a small footprint of $5\,\mathrm{mm} \times 5\,\mathrm{mm} \times 1.8\,\mathrm{mm}$ that can withstand a pressure of $1\,\mathrm{bar}$ and compatible with both liquids and gases was developed in this work. As shown in Fig. 1 (a), the piezoelectric microactuator bows down on the application of a voltage and blocks the inlet orifice. This modulates the flow-rate in the microvalve. The downward displacement of the microactuator is magnified with respect to the lateral displacement of the piezo-layer because of the clamped geometry of the structure. This type of structure, where an active layer (in this work, Lead Zirconate Titanate, PZT-5H) is bonded to a passive substrate (in this work, stainless steel) is called a unimorph.

The design shown in Fig. 1 was optimized for two objectives. The first one was to maximize the microactuator displacement for a given voltage. This was done to decrease the voltage required to close the valve. An analytical approach was adapted from the work done by Mo et al [5]. A constrained optimization study was performed to find the optimal PZT dimensions where the central displacement of the actuator is maximized.

The second aspect that was optimized was the fluid flow-rate through the microvalve; de-ionized (DI) water was used as it was the test fluid. Due to a low range of the liquid flow sensor that was available, it was desired to have a maximum flow-rate of $90\,\mu\mathrm{L\,min^{-1}}$ at the maximum pressure of $1\,\mathrm{bar}$. The fluid flow was modelled analytically using an electrical-analogue approach [6]. It was found that the thickness of the spacer was the primary control variable.

Numerical modeling using COMSOL Multiphysics v5.3 were used to validate both the analytical models mentioned above. This resulted in the final dimensions as shown in Table 1. Some dimensions were not realizable with the available facilities, so the closest possible values were used.

Table 1: Microvalve Design Parameters

Parameter	Analytical	Numerical	Fabricated
PZT diameter	4 mm	4.2 mm	4 mm
PZT thickness	76 µm	68 µm	127 µm
Epoxy thickness	-	$< 5\,\mu\mathrm{m}$	$< 15\,\mu\mathrm{m}$
Steel diameter	5 mm	5 mm	5 mm
Steel thickness	25 µm	25 µm	50 µm
Spacer thickness	3.5 µm	3.6 µm	5 µm

The top part in Fig. 1 (b) is the actuator designed in this work. It consists of a thin PZT-5H plate that is laser-cut to the desired shape and then glued with con-

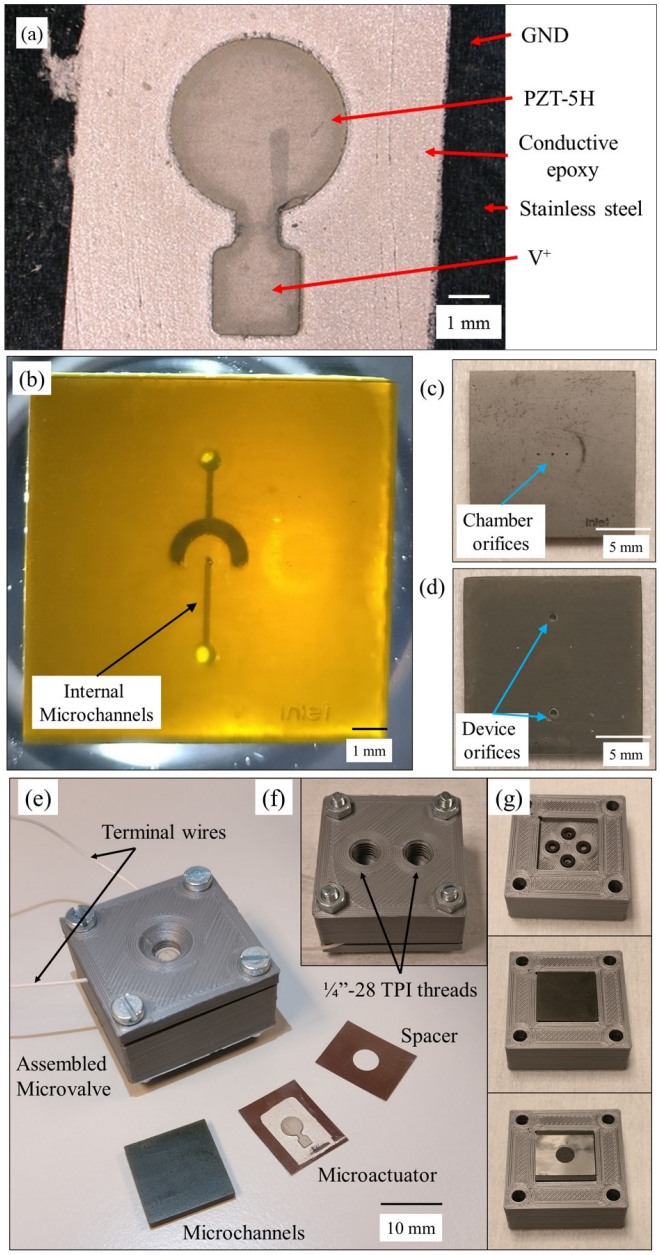

Figure 2: (a) Fabricated microactuator with a laser-cut PZT part bonded to a stainless steel membrane using conductive epoxy. Positive (V^+) and Ground (GND) terminals are indicated. Wires were attached using conductive tape (bottom terminal) and a press-fit (top terminal) (b) Microchannels with a light source underneath to illuminate the internal channels (c) Top view: Central orifice is the valve chamber inlet, neighbouring orifices are chamber outlets (d) Bottom View: Top orifice is the device inlet, bottom orifice is the device outlet, surface is sanded with 1000-grit sandpaper (e) Assembled microvalve holder with constituent parts. Terminal wires are copper with $0.5\,\mathrm{mm}$ diameter. (f) Bottom view of the holder (g) First step: O-rings placed in grooves, Second step: Microchannels placed in groove, Third step: Spacer placed over microchannels, Fourth step (not shown): Actuator is placed and then assembly is clamped.

ductive epoxy to a stainless steel (SS) plate to form a unimorph piezoelectric microactuator (UPM). The fabricated UPM is shown in Fig. 2 (a).

The microchannels (bottom part in Fig. 1 (b)) were 3D-printed using stereolithography, a technique that uses UV-light to selectively polymerize a UV-sensitive resin layer-by-layer. The fabricated microchannel part is shown in Fig. 2 (b-d). The material used is a hard polymer called HTM-140 (High-Temperature Mold) and is proprietary to the EnvisionTec SLA printer that was used. The spacer in the middle defines the initial separation between the actuator membrane and valve seat. It was made using $5\,\mu\mathrm{m}$ thick shim-steel that was laser-cut.

The entire assembly shown in Fig. 1 (b) needs to be clamped for the actuator to function and for the assembly to be leak-tight. A valve holder that can clamp the entire microvalve and enable fluidic and electrical interfacing was designed and is shown in Fig. 2 (e-g).

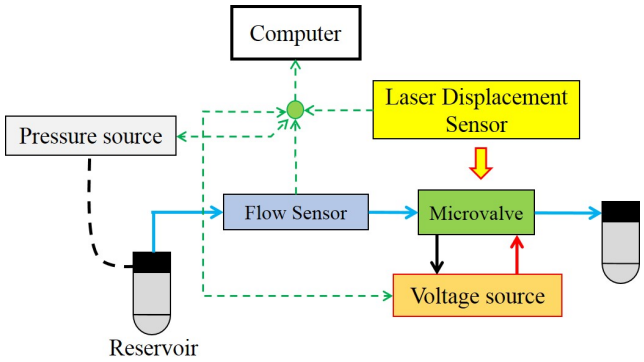

Figure 3: Layout of the test set-up for measuring flow-rate and displacement of the microvalve: Green dashed arrows are signal wires, red and black arrows are terminal wires of the microvalve, blue arrows are microfluidic tubing, and the black dashed line is tubing from the pressure source.

A test-setup was used to interface with the valve holder. A schematic is shown in Fig. 3. It was used to apply fluid pressure across the valve, measure fluid flow through the valve, apply voltage to the UPM, and measure the displacement of the UPM. The UPM was controlled by a high-voltage, current-limited, programmable DC power-supply (Delta Elektronika ES0300-0.45). The central displacement of the UPM was measured using a high-resolution laser displacement sensor (Keyence LC-2420 sensor-head with a Keyence LC-2400W laser displacement meter). The microvalve was connected to a microfluidic circuit consisting of a pressure source (Elveflow OB1 Mk3+) which could apply pressure from $-1\,\mathrm{bar}$ to $6\,\mathrm{bar}$, and a thermal flow-sensor (Elveflow MFS3) which could measure a maximum flow-rate of $90\,\mu\mathrm{L\,min^{-1}}$ (accuracy: 5% measured value).

RESULTS AND DISCUSSION

The main results from this work are related to the flow-rate behaviour of the microvalve. They are shown in Fig. 4 and Fig. 5. DI water was used for all experiments.

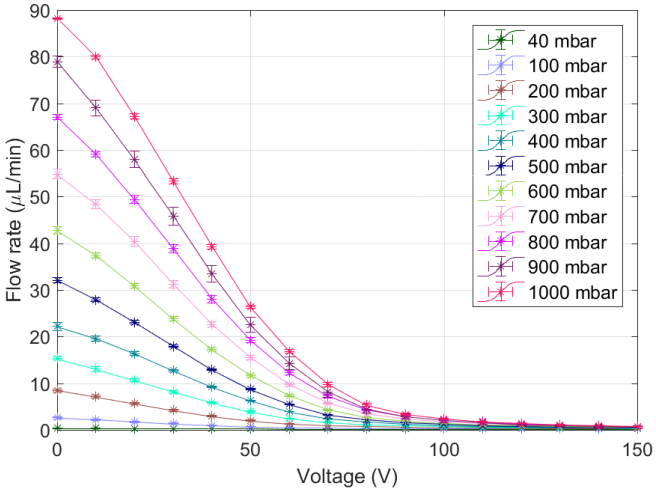

Figure 4: Proportional control of flow rate at different pressures. Error-bars indicate one standard-deviation of three measurements.

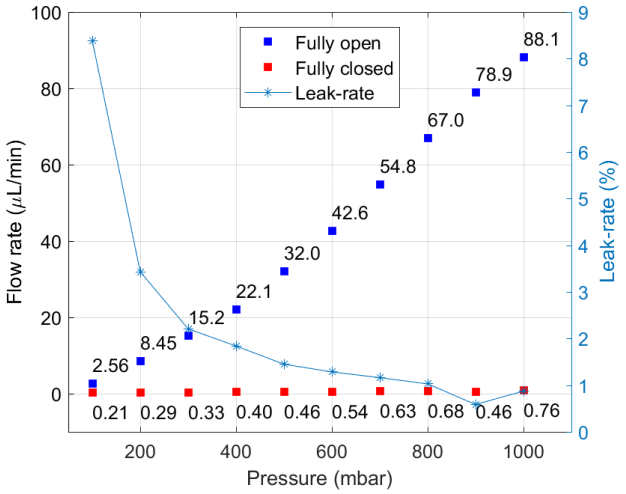

Figure 5: On-off behaviour and leak-rate of the microvalve at different pressures: The numbers are the flow rates at those data points. Leak-rate is the ratio of closed and open flow rates.

The main objective of this work was to prove proportional control of fluid flow. This is shown clearly in Fig. 4. For a set pressure, the voltage was increased from $0\,\mathrm{V}$ to $150\,\mathrm{V}$ and the flow rate was measured. A uniform upward shift in the flow rate curve is seen as the

pressure increases. The small standard deviation (error bars) shows that there is good repeatability of the valving behaviour. It can also be seen that, at all pressures, a bulk of the valving is done from 0 - 100 V. The slope changes rapidly from 90 V and the flow rate appears to asymptotically decrease to zero. The residual flow observed even at a high voltage might be due to valve seat defects that could not be blocked by the actuator membrane.

The leakage behaviour of the microvalve is shown in Fig. 5. Here, leakage rate is defined as the ratio of closed and open flow rates. The industry standard is to measure leakage using Helium gas but this facility was not available. A high leakage-rate is observed at low pressures; this is because flow rate at open condition is low, but a constant leakage is always present due to valve seat defects. As pressure increases, open flow rate increases while closed flow rate remains relatively constant, effectively decreasing the leakage-rate. Some methods to decrease leakage include decreasing the valve-seat area by using a knife-edge contact and introducing a soft material like PDMS or a parylene layer to the actuator or valve-seat.

CONCLUSION

A proportionally-controlled piezoelectric microvalve was designed, fabricated and characterized. De-ionized water at room temperature was used for characterization. Most piezoelectric devices use MEMS fabrication techniques which are not very accessible. Here, a novel combination of accessible rapid-prototyping methods were used to fabricate an active piezoelectric microfluidic device. The specifications of the final microvalve are given in Table 2.

Table 2: Obtained Microvalve specifications

Specification	**Measured value**
Flow range	0 - 90 µL min^{-1}
Flow control resolution	0.2 µL min^{-1} at 500 mbar
Leakage	0.8% open-flow at 1000 mbar
Max. differential pressure	1 bar
Static power consumption	37.5 µW
Operating voltage	0 - 150 V
Typical response time	40 ms
Dimensions (effective)	5 mm × 5 mm × 1.8 mm

Due to limitations in the available flow sensor, the full potential of the microvalve could not be explored. The projected flow-range for this microvalve is 0 - 750 µL min^{-1} (DI water). A low power consumption of 37.5 µW has been measured, which, to the best of the author's knowledge, is the lowest reported in literature for this pressure range.

REFERENCES

[1] A. Manz, N. Graber, and H. á. Widmer, "Miniaturized total chemical analysis systems: a novel concept for chemical sensing," *Sensors and actuators B: Chemical*, vol. 1, no. 1-6, pp. 244–248, 1990.

[2] S. Böhm, B. Timmer, W. Olthuis, and P. Bergveld, "A closed-loop controlled electrochemically actuated micro-dosing system," *Journal of Micromechanics and Microengineering*, vol. 10, no. 4, p. 498, 2000.

[3] P. S. Dittrich and A. Manz, "Lab-on-a-chip: microfluidics in drug discovery," *Nature reviews Drug discovery*, vol. 5, no. 3, p. 210, 2006.

[4] C. M. Marrese-Reading, J. Mueller, and W. C. West, "Microfluidic electrospray thruster," Oct. 7 2014. US Patent 8,850,792.

[5] C. Mo, R. Wright, W. S. Slaughter, and W. W. Clark, "Behaviour of a unimorph circular piezoelectric actuator," *Smart Materials and Structures*, vol. 15, no. 4, p. 1094, 2006.

[6] I. Fazal and M. C. Elwenspoek, "Design and analysis of a high pressure piezoelectric actuated microvalve," *Journal of micromechanics and microengineering*, vol. 17, no. 11, p. 2366, 2007.

CONTACT

- G. Ozkayar, g.ozkayar@tudelft.nl
- M. K. Ghatkesar, m.k.ghatkesar@tudelft.nl

CHARACTERIZATION OF A GAS DENSITY SENSOR BASED ON SURFACE CHANNEL TECHNOLOGY

J. Groenesteijn[1], N. de Jonge[1], E.J. van der Wouden[1], W. Sparreboom[1], T.S.J. Lammerink[2] and J.C. Lötters[1,2]

[1] Bronkhorst High-Tech BV, Ruurlo, The Netherlands

[2] MESA+ Institute for Nanotechnology, University of Twente, Enschede, The Netherlands

ABSTRACT

We report on the characterization of a gas density sensor for a wide pressure and temperature range. The sensor has been fabricated using the surface channel fabrication technology [1]. The density is measured using the resonance frequency of a freely suspended U-shaped channel with a diameter of 60 µm and a wall thickness of only 1 µm. The sensor has been characterized using a pressure between 1.3 and 10 bar(a) and temperatures in a range of 10 °C to 70 °C. This resulted in an accuracy better than 1% for a density range of 0.18 kg m^{-3} to 17 kg m^{-3}.

KEYWORDS

MEMS, micro gas density sensor, surface channel technology

INTRODUCTION

Gas density sensing is an important part in real-time gas composition measurement and for quality control [2]. In the past, we presented a gas density sensor based on a micro Coriolis mass flow meter [3]. However, this sensor was designed for flow sensitivity and not for density measurement. Now, we redesigned the sensor to be more sensitive to density and less to flow. To do this, we changed the rectangular free-hanging channel to a u-shape as shown in Figure 1.

The resonance frequency of the channel depends on the density of the fluid according to:

$$f_0 = \frac{1}{2\pi}\sqrt{\frac{k(P,T)}{m_{\text{channel}} + m_{\text{fluid}}(\rho)}} \qquad (1)$$

where f_0 is the resonance frequency, k the modal spring constant of the free-hanging channel which depends on pressure P and temperature T, m_{channel} the modal mass of the channel (channel wall and metal tracks) and m_{fluid} the modal mass of the fluid inside the channel which depends on the cross-sectional area of the channel, the length of the channel and the actual density (ρ) of the fluid. By also measuring the pressure and temperature, the actual density can be converted to a density at standard conditions (20 °C, 1 atm) to be able to use it for, for instance, gas composition measurement. Five different designs, with a height and width as shown in Table 1, are characterized. A sixth design (design #3a) with the same height and width of design #3 was characterized as well. However, for this design, the channel diameter of the horizontal free-hanging part was increased from 60 µm to 110 µm, resulting in a larger amount of gas at this part of the channel.A photograph of a chip with design #1 is shown in Figure 2.

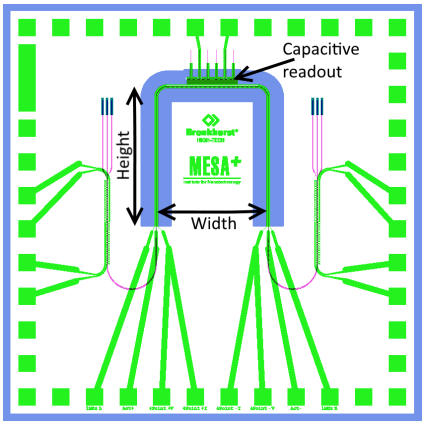

Figure 1: Schematic design of the gas density sensor with a free-hanging u-shaped channel.

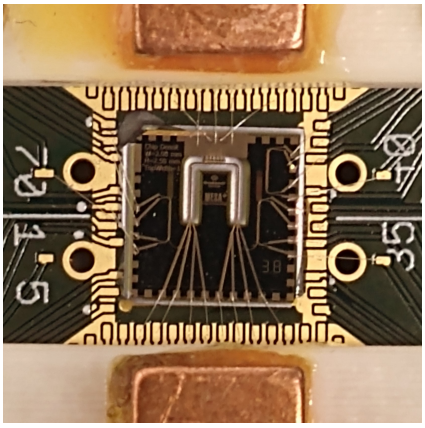

Figure 2: Photograph of the gas density sensor chip (7.5 mm x 7.5 mm) with magnets at the top- and bottom side to provide a magnetic field for the Lorentz-force actuation.

Table 1: Height and width of the different designs

Design	Height (mm)	Width (mm)
#1	2.5	2
#2	3	1.5
#3	3	2
#4	3	2.5
#5	3.5	2

ACTUATION

The sensor is actuated using an alternating current through metal tracks on top of the channel. In combination with a magnetic field B, this current will result in a alternating Lorentz force with brings the free-hanging channel in motion. Figure 3 shows the two actuation modes. The twist mode is actuated by placing magnets to the left and right side of the chip, resulting in a horizontal magnetic field. The swing mode is actuated by placing magnets above and below the chip, resulting in a vertical magnetic field. At the top of the free-hanging tube are comb-structures C_1 and C_2 which can be used to capacitively measure the displacement of the channel. These comb-structures are placed on either side of the twist-rotational axis. A phase-locked loop (PLL), implemented in a digital signal processing (DSP) module uses the signals measured from these comb-structures to generate the actuation current. When the input of the PLL is generated by subtracting C_1 and C_2 and the magnetic field is as shown in Figure 3a, the resulting actuation current will actuate the sensor in the twist mode at resonance. When the input of the PLL is generated by adding C_1 and C_2 and the magnetic field is as shown in Figure 3b, the resulting actuation current will actuate the sensor in the swing mode at resonance. In a third mode, the DSP will function as a transfer analyser by generating an actuation current in a frequency sweep and comparing that to the read-out signals of either comb-structure. An example of this is shown in Figure 4.

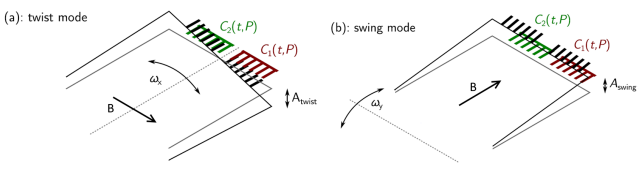

Figure 3: The two resonance modes of the gas density sensors and the magnet placement to actuate each mode. (Adapted from [4])

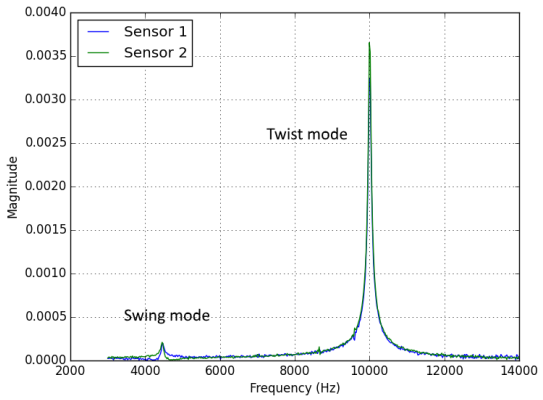

Figure 4: Measurement results of both read-out combs (sensor 1 and sensor 2) when read-out using the transfer mode of the DSP. The magnets are configured for twist mode, but still slightly actuate the swing mode due to small misalignment of the magnetic field.

PRESSURE SENSITIVITY

The channels made using surface channel technology are not completely round, but have a flat top. When a pressure is applied, the flat part will bend, which can be used as a pressure sensor [4]. When this happens in a free-hanging channel, it will result in a change in stiffness of the channel as indicated in equation 1. In practice, this means that for very light gasses (ie. helium), the stiffness of the channel will increase more rapidly with pressure than the density (and resulting mass), resulting in an increase in resonance frequency. For heavier gasses, the resonance frequency decreases with increasing pressure. This can be seen in Figure 5. At the left, the swing mode is shown for design #1. It shows that the resonance frequency increases slightly for higher pressure Helium, while it decreases much more when Argon is used. In the right figure, the same is shown for the twist mode of design #1.

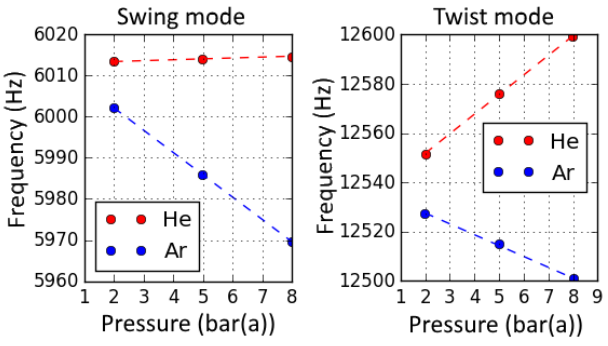

Figure 5: Frequency of the vibrating channel of design #1 as a function of pressure for Helium and Argon. Left: Swing mode. Right: Twist mode

Here, the increase in frequency for Helium is much more visible. This indicates that the twist mode is, in comparison to the swing mode, more sensitive to pressure. For accurate density measurement in either mode, this effect has to be compensated by measuring the pressure of the fluid in the sensor. This pressure can then be used to calculate an "effective resonance frequency" at a standardized pressure.

MEASUREMENTS

Measurement setup

The used measurement setup is shown schematically in Figure 6. A pressure controller is used to control the applied pressure of several different gasses with different densities to the device under test (DUT). The outlet of the DUT is closed using a valve to prevent a gasflow through the channel. Between measurements of the different gasses, the valve was opened to flush the setup. To measure the influence of temperature on the measurement, the DUT was placed inside an temperature controlled environment during some measurements. The temperature of the chip was measured using a PT100 element mounted close to the chip.

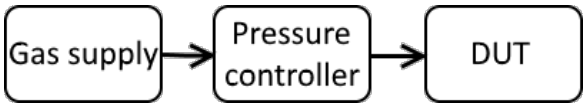

Figure 6: Schematic overview of the measurement setup

Sensitivity to density

In order to determine the sensitivity of the chips for density changes (in $\mathrm{Hz}/(\mathrm{kg}/\mathrm{m}^3)$), the corrected resonance frequency is used. The measurement results are shown in Figures 7 and 8 and the resulting sensitivities are shown in Table 2.

Table 2: Measured sensitivity in $\mathrm{Hz}/(\mathrm{kg}/\mathrm{m}^3)$ for the different chip designs

Design	Swing	Twist
#1	-4.0	-8.4
#2	-3.0	-8.3
#3	-2.8	-6.6
#3a	-4.0	-6.6
#4	-3.4	-6.0
#5	-2.2	-5.6

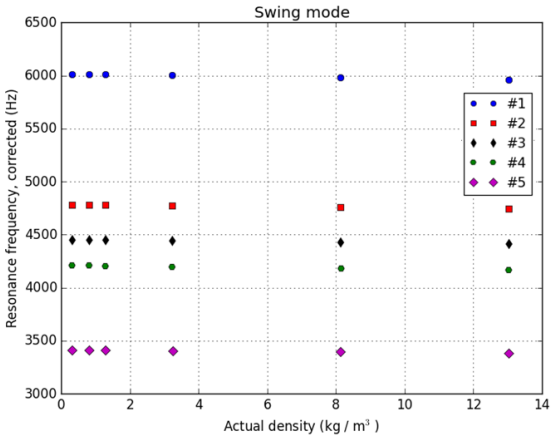

Figure 7: The resonance frequency in swing mode as a function of the actual density. The data was corrected for the pressure dependency of the stiffness.

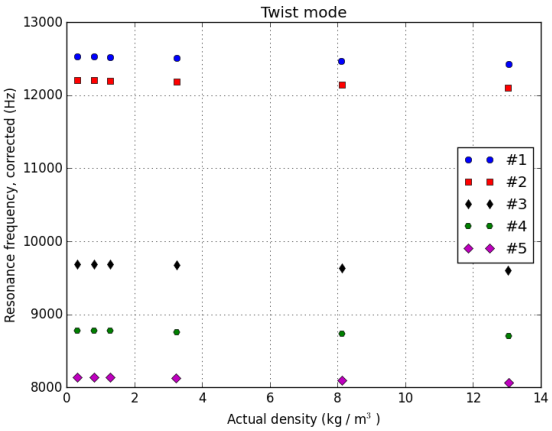

Figure 8: The resonance frequency in twist mode as a function of the actual density. The data was corrected for the pressure dependency of the stiffness.

From this can be concluded, that design #1 is most sensitive to density, so this design was used for further measurements. As expected, design #3a has a higher sensitivity than design #3 for the swing mode, while the sensitivity in twist mode is the same.

Standard density

Using the measured temperature and pressure, the standard density can be calculated using equation 2:

$$\rho_{\mathrm{std}} = \left(C_1 \frac{1}{(2\pi f_0)^2} - C_2 \right) \frac{T_{\mathrm{actual}} p_{\mathrm{std}}}{T_{\mathrm{std}} p_{\mathrm{actual}}}, \qquad (2)$$

where ρ_{std} is the standard density at standard temperature (T_{std} =20 °C) and standard pressure (p_{std} =1.013 bar(a)). f_0 the measured resonance frequency. C_1 and C_2 are parameters depending on the channel geometry (height, width, diameter, etc) which are calibrated. Figure 9 shows the standard density calculated from measurements using helium, nitrogen

and argon at an applied pressure of 1.3 bar(a) up to 10 bar(a), corresponding to an actual density between 0.21 kg m^{-3} and 16.5 kg m^{-3}.

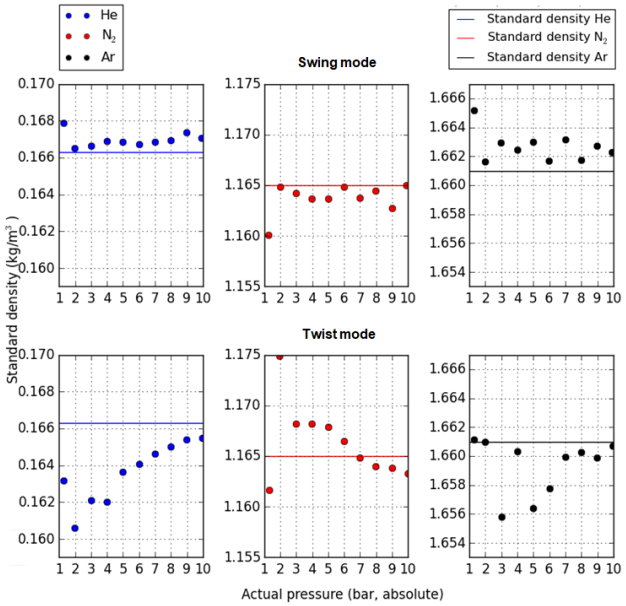

Figure 9: Measured standard density of helium, nitrogen and argon at different pressure.

These results again show the pressure sensitivity of the twist mode. While the measurements in swing mode are accurate over the whole pressure range (within 1%), the measurements in twist mode show a large error (up to 3% for Helium), depending on pressure.

By placing the sensor in a temperature controlled environment, the temperature of the sensor and fluid can be changed. Table 3 shows the results of the measurements (design #1, swing mode) at 10 and 70 °C and at 1.3 and 10 bar(a) using Argon and Helium. This corresponds to a minimal and maximal actual density of 0.1823 and 1.695 kg m^{-3} for Helium and 1.821 and 17.1 kg m^{-3} for Argon.

Table 3: Calculated standard densities at 10 and 70 °C *and 1.3 and* 10 bar(a).

Fluid	Conditions	Calculated standard density (kg m^{-3})	Error (%)
Helium	1.3 bar(a)/70 °C	0.1655	-0.49
Helium	10 bar(a)/10 °C	0.1655	-0.48
Argon	1.3 bar(a)/70 °C	1.669	+0.49
Argon	10 bar(a)/10 °C	1.669	+0.49

CONCLUSION

We have reported on a MEMS gas density sensor with an accuracy better than 1% in a temperature range of 10 to 70 °C and a pressure range of 1.3 to 10 bar(a). Future work will focus on using the integrated pressure and temperature sensors for more accurate measurement and measurements with flow.

REFERENCES

[1] J. Groenesteijn, M.J. de Boer, J.C. Lötters, R.J. Wiegerink, "A versatile technology platform for microfluidic handling systems, part I: fabrication and functionalization", Microfluid Nanofluid (2017) 21:127.

[2] E.J. van der Wouden, J. Groenesteijn, R.J. Wiegerink, J.C. Lötters. "Multi Parameter Flow Meter for On-Line Measurement of Gas Mixture Composition", Micromachines (2015), 6, 452-461.

[3] W. Sparreboom, G. Ratering, W. Kruijswijk, E.J. van der Wouden, J. Groenesteijn, J.C. Lötters, "Micro Coriolis gas denity sensor", Microfluidic Handling System conference (2017).

[4] D. Alveringh, "Integrated throughflow mechanical microfluidic sensors", PhD thesis, University of Twente Press, 2018.

[5] J. Groenesteijn, "Microfluidic platform for Coriolis based sensor and actuator systems", PhD thesis, University of Twente Press, 2016.

CONTACT

* J. Groenesteijn, j.groenesteijn@bronkhorst.com

ROBUST THERMAL MASS FLOW METER – COMPARISON BETWEEN ANEMOMETRIC PRINCIPLE AND 3-OMEGA METHOD TO MEASURE FLOW

R. E. Bernhardsgrütter[1,2], C. J. Hepp[1], K. Schmitt[2,3], M. Jägle[3], H.-F. Pernau[3] and J. Wöllenstein[2,3]

[1]Innovative Sensor Technology IST AG, Ebnat-Kappel, Switzerland

[2]Department of Microsystems Engineering, University of Freiburg, Freiburg, Germany

[3]Fraunhofer Institute for Physical Measurement Techniques IPM, Freiburg, Germany

ABSTRACT

For the first time, constant temperature anemometry (CTA) and the 3ω-method are directly compared with respect to liquid flow measurement by using a sensor based on platinum thin film technology. The results show that the 3ω-method is less sensitive to the transition between laminar and turbulent flow profile. The accuracy of the 3ω-method is a factor of 1.7 better than that of the CTA. The findings can play a vital role for future sensor systems measuring flow in the laminar-turbulent transition zone or for sensors which combine the anemometric flow measurement for flow measurement and the 3ω-method for thermal parameter detection.

INTRODUCTION

State of the Art

Thermal flow sensors are widely used because of their simplicity and possibility of miniaturization. In the field of thermal flow sensors, it is differentiated between anemometric, calorimetric and time-of-flight principle. The focus in this paper lies on the constant temperature anemometric principle [1].

A constant temperature anemometer typically consists of a temperature sensor and a heating element, called heater. The two sensitive elements are made of a material with a defined temperature coefficient of resistance (TCR) e.g. platinum or nickel. The working principle is based on the cooling effect of flow on a heated body. The heater is usually regulated by electronics such that the temperature difference between heater and temperature sensor is constant. As the flow increases, the needed power increases as well to hold the temperature difference constant. The needed power is a quantity which is directly related to the flow.

Thermal anemometers are limited to either the laminar flow region or the turbulent flow region because of different manifestations of the flow profile. Otherwise the thermal anemometer losses much of its accuracy or a complicated extension is needed for taking both flow profiles in to account and loses its simplicity.

Contribution

The 3ω-method is a good candidate to measure in both laminar and turbulent flow regions with high accuracy due to its high sensitivity and its local heating. The 3ω-method is a well-known method to measure thermal conductivity and heat capacity and it is used to investigate thin films [2], solid or fluid bulk materials [3.4], or multilayer systems [5,6]. The conventional 3ω-method uses a metallic resistor, which is in direct contact with the specimen. An AC current with angular frequency ω is driven through the resistor and heats up the resistor due to Joule heating. The heating has then an AC component at 2ω. The AC component acts as thermal wave. The propagation of the thermal wave depends on the thermal conductivity and the heat capacity. Because the electrical resistance is proportional to the temperature, the resistance is also modulated with 2ω. The voltage across the resistor has then an AC component at frequency 3ω and is dependent on the thermal properties of the specimen. The resistor acts as heater and as a sensing element.

Because the resistor is used as heater, it is sensitive to flow just as a conventional thermal flow sensor. But the so far presented 3ω-sensors are mainly operated in the 3ω-method mode [4]. The following contributions are shown:

- CTA and 3ω-method are directly compared with the same sensor system.
- The effect of the local heating of the 3ω-method with respect to flow is investigated.

SENSOR AND EXPERIMENTAL

Design and Fabrication

The sensor system is shown in figure 1. It consists of two platinum thin film elements, temperature sensor and heater, and a stainless-steel tube. The platinum thin film elements are processed on an Al_2O_3-substrate by standard MEMS processes. The temperature sensor is designed as a resistance of 1000 Ω and the heater as a resistance of 50 Ω. A thin glass layer is screen-printed on the platinum layer as a passivation layer.

Platinum is chosen because of its TCR of 3850 ppm/K. The Al_2O_3 is chosen because of its high thermal conductivity, 25 W/(m K), which reduces the Biot number and increases the sensitivity. The manufactured elements are soldered on a flat part of the stainless-steel tube. Stainless-steel is chosen because of its high resistance to corrosion and chemicals. Because the Biot number must be minimal, the solder

connection must be cavity free. Such solder connections can be achieved by vacuum soldering.

Both temperature sensor and heater are used for the CTA. For the 3ω-method, the heater is only needed in this investigation.

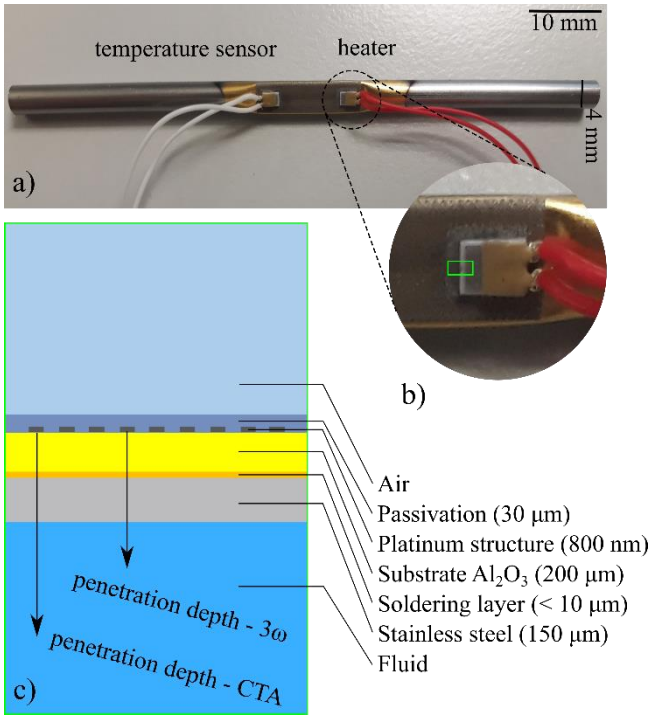

Figure 1: Sensor system design: a) Photo of sensor, temperature sensor (white wires) and heater (red wires) soldered on a stainless-steel tube with a distance of 8 mm in between, the diameter of the tube is 4 mm and has a flat section; b) Zoom of heater, the thin film element on a Al_2O_3-substrate with welded wires; c) Cross-sectional layer structure of the sensor, the thermal penetration depth of the CTA is larger than of the 3ω-method.

Experimental and Measurement Procedure

The CTA and the 3ω-method need different excitation procedures. The CTA measurement and feedback loop are done mainly by a digital circuit based on a microcontroller. The microcontroller controls the setpoint of the heater by using the measured temperature of the temperature sensor and the predefined overtemperature (8 K in this case). The electronics do the entire calculation and regulation.

The setup to do a 3ω-method measurement consists of a 16-bit data acquisition (DAQ) card (National Instruments, NI USB DAQ 6225), a voltage-current amplifier based on an operational amplifier and a computer. The DAQ and voltage-current amplifier generates the AC current. The measurements are done with a current amplitude of 30 mA and a frequency of 0.1 Hz. The voltage at the heater is again measured by the DAQ. The setup is phase sensitive and acts as a digital lock-in amplifier because both signal generation and acquisition are done by the DAQ. This kind of setup allows to resolve the signal generated by 3ω-method which is several orders of magnitude smaller than the driving signal.

Both methods, CTA and 3ω-method, are used to measure flow between 1 kg/h and 80 kg/h. The fluid is water. The reference flow meter is a Coriflow M15 from Bronkhorst.

RESULTS

CTA measurement

The investigation of the CTA is done between 1 kg/h and 80 kg/h for three different temperatures (5 °C, 25 °C, 45 °C). Figure 2 shows the resulting characteristics, the needed power as function of mass flow. First, the needed power increases for increasing mass flow as expected because more heat is transferred, and, therefore, more power is needed to hold the overtemperature of 8 K. This characteristic is often descripted with King's law,

$$P = A + B\dot{m}^C, \qquad (1)$$

where the quantity P is power, $\dot{m}$ is mass flow and A, B and C are coefficient which are typically found experimentally.

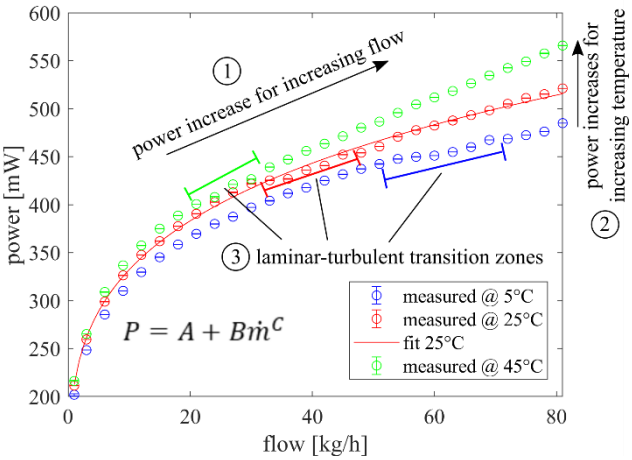

Figure 2: Mass flow-power-characteristics of the sensor using the CTA (overtemperature is 8 K). The characteristic is shown for different temperatures (5°C, 25°C, 45°C). (1) Effect of flow. (2) Effect of temperature. (3) Transition from laminar to the turbulent flow profile generates a rough region which is visible and indicated by the bars. The transition zone is shifted to lower flow range for increasing temperature, mainly due to viscosity change. The fit ($\dot{m}$ = mass flow, A, B, C = fit constants), exemplarily shown for 25°C, < 8% of the reading with respect to mass flow.

Moreover, the power increases for increasing temperature due to the change of the thermal properties of water, mainly due to the increase of the thermal conductivity of water.

Furthermore, the laminar-to-turbulent transition, also indicated in figure 2, are visible. This transition

zone can be defined by the Reynold's number Re,

$$Re = \frac{\dot{m} \cdot D}{\rho \cdot A \cdot \nu}, \qquad (2)$$

where the quantity D is the diameter of the tube, ρ is the density of water, A is the cross-section of the tube and ν is the kinematic viscosity. The laminar region is approximated if Re < 2300, the turbulent region is defined if Re > 5000.

Table 1: Density and kinematic viscosity and the critical Reynold's numbers (laminar-turbulent transition zone) of water for different temperatures.

	5°C	25°C	45°C
ρ [kg/m^3]	1000	997.1	990.2
ν [10^{-6} m^2 s]	1.52	0.89	0.60
$\dot{m}(Re = 2300)$ [kg/h]	40	23	16
$\dot{m}(Re = 5000)$ [kg/h]	80	46	31

Because the kinematic viscosity of water decreases if the temperature increases, therefore, the transition zone is shifted to lower mass flow as the measurement confirms. The transition zone is even clearer visible if the derivation of the signal is taken (figure 3). The derivation obtains a rough behavior at the transition zone which is a further indication that the dynamics of the flow profile change. Theoretical calculations of the Reynold's number (see table 1) also agree with the measurement.

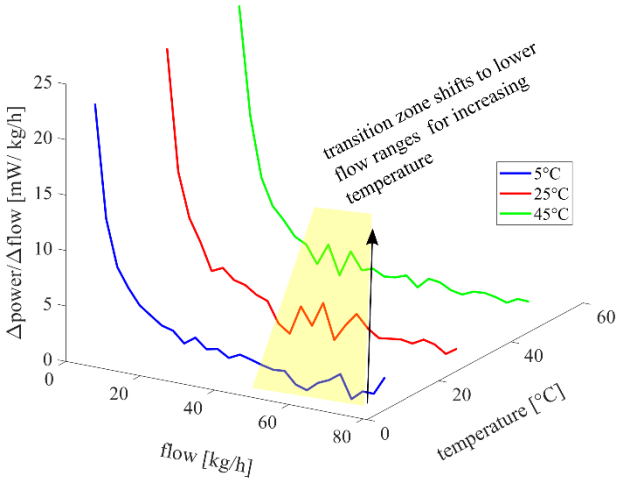

Figure 3: Approximated derivative of characteristics of figure 2. The transition zone (yellow shaded) is visible more clearly compared to figure 2, the transition zone is shifted to lower flow regions if the temperature increases, mainly because of viscosity reduction.

3ω-method method

The result of the 3ω-method is shown in figure 4. Both amplitude and phase are plotted. The amplitude is a decreasing function with respect to mass flow because flow can be generally understood as increase of thermal conductivity and specific heat capacity and therefore the signal is decreasing. The phase information is an increasing function with respect to mass flow and approaches asymptotically 0 °C. However, the information content of amplitude and phase is the same.

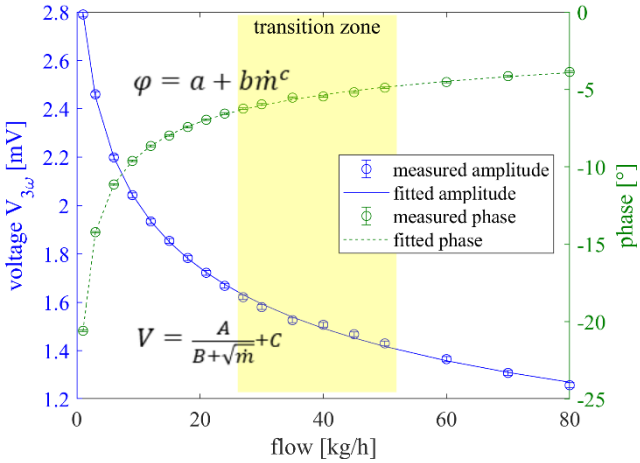

Figure 4: Flow-voltage and the related phase-flow characteristics of the 3ω-method at 25°C. A clear transition zone is not visible. The yellow shaded area is the expected transition zone. The fit matches well with the measured data, < 5 % of the reading.

The transition zone is not visible in figure 4. However, the transition zone is visible if the derivation of the two graphs are taken (see figure 5). The derivation obtains some rough behavior where the transition zone lies and agrees well with the CTA measurements and the theoretical predictions.

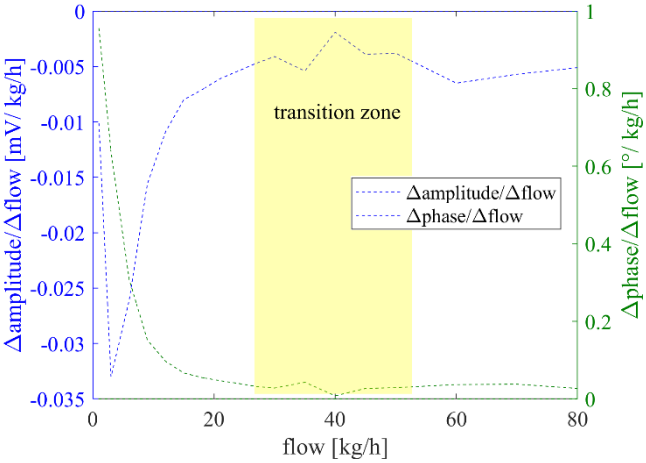

Figure 5: Approximated derivative of the characteristics of figure 4. The transition zone (yellow shaded) is visible. The pathway is rougher in the transition zone as expected.

Comparison between CTA and 3ω-method

Because both CTA measurements and 3ω-method measurements are done with the same sensor, a first

direct comparison can be done with respect to flow measurements.

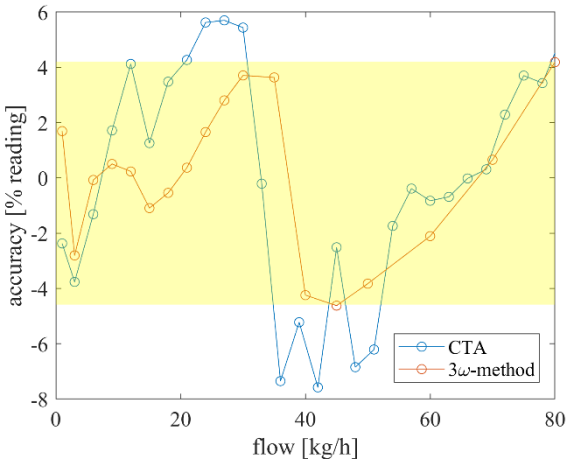

Figure 5: The accuracies of each fit are shown. Generally, the shape of both accuracy plots looks similar. However, the accuracy given by the 3ω-method is typically better than of the CTA. The accuracy of the 3ω-method is 4.6 % of the reading (yellow shaded area) at worst whereas it is 7.6 % of the reading for the CTA.

The CTA result at 25 °C is fitted by King's law (see figure 2). It is clearly visible that the fit does not match well, the different dynamic behavior of laminar and turbulent flow profile are the reason and the mismatch is most pronounced in the transition zone.

The result is qualitatively similar for the result of the 3ω-method (figure 4). The fit functions were $V = \frac{A}{B+\sqrt{\dot{m}}} + C$ for the amplitude and $\varphi = a + b\dot{m}^c$ for the phase. The biggest deviation between measured data and fit is again in the transition zone.

If the absolute accuracy of both methods is quantitatively compared, the 3ω-method performs better, as visible in figure 5. The most inaccurate point is 7.6 % of the reading for the CTA measurement whereas it is 4.6 % of the reading for the 3ω method. The 3ω-method performs by a factor of 1.7 better than the CTA. The behavior of the absolute accuracy is the same for both methods as it should be because the flow profile and the corresponding Reynold's number are the same. However, the two sensors do not sense the same area of the flow profile because the penetration depth of generated heat are different. The theory of the 3ω-method gives the following expression for the penetration depth δ,

$$\delta = \sqrt{\frac{k}{2\omega\rho c_p}} \propto \sqrt{\frac{1}{\omega}}, \qquad (3)$$

where the quantity k is the thermal conductivity, ω the frequency, ρ the density and c_p the specific heat capacity. The penetration depth becomes bigger if the frequency becomes smaller and runs to infinity if the frequency is zero. The CTA measurement senses much deeper into the fluid compared to the 3ω-method (indicated in figure 1). Therefore, the CTA measurement is more sensitive to turbulences because the flow velocity is higher in the middle of the tube.

CONCLUSION

The paper shows the first direct comparison between CTA and the 3ω-method with respect to mass flow measurements. It is shown that the 3ω-method is less sensitive to the transition zone. The accuracy is up to a factor of 1.7 better than the CTA.

There will be a tradeoff between the loss of overall sensitivity and sensitivity with respect to turbulences. Finding the optimal working point is the next step.

The findings have an important impact for future flow meters. The 3ω-method has the ability to measure thermal properties like thermal conductivity and heat capacity and also mass flow which is necessary for a fluid independent thermal mass flow meter.

REFERENCES

[1] J. H. Lienhard, "A heat transfer textbook", p.269, Phlogiston Press, Cambridge MA, 3th edition (2004)

[2] D. G. Cahill, M. Katiyar, and J. R. Abelson, "Thermal conductivity of a-SI:H thin films", Phys. Rev. B, 50, 9 (1994)

[3] I. K. Moon, Y. H. Jeong, and S. I. Kwun, "The 3ω technique for measuring dynamic specific heat and thermal conductivity of a liquid or solid", Rev. Sci. Instrum., 67, 29 (1996)

[4] C. Clausen, T. Pedersen, and A. Bentien, "The 3-Omega Method for the Measurement of Fouling Thickness, the Liquid Flow Rate, and the Surface Contact", Sensors, 17, 552 (2017)

[5] J. H. Kim, A. Feldman, and D. Novotny, "Application of the three omega conductivity measurement method to a film on a substrate of finite thickness", J. Appl. Phys., 86, 3959 (1999)

[6] B. Shen, et al., "Thermal conductivity measurement of amorphous Si/SiGe multilayer films by 3 omega method", Int. J. Therm. Sci., 66 (2013)

CONTACT

*R.E. Bernhardsgrütter, tel: +41-71-9920233;
ralf.bernhardsgruetter@ist-ag.com

A MULTIPARAMETER CAPACITIVE SENSING PLATFORM FOR THE ASSESSMENT OF THE COMPOSITION OF GAS MIXTURES

A. Boersma[1], J. Sweelssen[1] J. Núñez[1] and H. Blokland[2]
[1]TNO, HTC 25, 5656 AE Eindhoven, The Netherlands
[2]TNO, Leeghwaterstraat 44, 2628 CA Delft, The Netherlands

ABSTRACT

TNO, together with industrial and academic partners, has developed a new gas sensor that is able to measure the composition of various gas mixtures. A first prototype was realized that was small enough to be inserted in low and medium pressure gas pipes (100 mbarg – 8 barg). Adding the pressure and temperature data to the chip readings enables the determination of the concentrations of several alkanes, hydrogen, nitrogen and carbon dioxide, including small fluctuations in water vapor pressure and subsequently calculate the Calorific Value, Wobbe Index and Methane Number. Several field tests have demonstrated the feasibility of the technology.

KEYWORDS

Energy Transition, Gas Composition Sensor, Capacitive Sensor Array, Chip Technology

INTRODUCTION

The Netherlands and other regions are facing major changes during the coming decades in the production and use of natural gas for domestic and industrial applications. Both economic and political changes induce an accelerated reduction of the use of the nationally produced natural gas, and require a shift towards LNG from different sources all over the world and sustainable solutions such as biogas and hydrogen. All of these gasses have a deviating composition compared to the traditional sources. This requires a more intense monitoring of the composition along the gas grid. The currently available gas quality measuring systems (e.g. GC, Wobbe Index analyzer, etc.) cannot fulfill the need for a cost-effective inline measuring method. The number of biogas feeds into an existing gas grid will increase significantly during the coming years. This not only asks for a clear monitoring of the distribution of this gas along the grid, but also a more intense monitoring of the gas feed quality. Biogas may suffer from larger fluctuations in composition and accompanying contaminations. These should be recognized before entering a gas grid. Currently, gas chromatographs are used for these 'gate keeper' activities, but lower cost solutions may be required in order to facilitate starting biogas producers. Furthermore, hydrogen is generally considered as an important fuel gas in the transition towards renewable energy. Gas grid operators are assessing the feasibility of feeding hydrogen into the gas grid to reduce the amount of fossil fuel required for heat generation. For that reason, TNO started the development of a new type of gas sensor, based on gas sensitive coatings on an array of electronic chips.

TECHNOLOGY

Porous materials can absorb significant amounts of gasses. This absorption is influenced by the chemical and physical interactions between the gas and surface of the porous material and depend heavily on the pore sizes and surface chemistry. These interactions can be tuned by modification of the porous structure of the materials. Coatings made from these materials can be used to selectively absorb specific gasses. When these coatings are applied to a transducer, changes in material properties because of the absorption can be quantified. An array of these transducers can be used to fully determine the composition of gas mixtures. The chosen transducer described in this paper is an interdigitated (IDE) capacitive electrode [1-3].

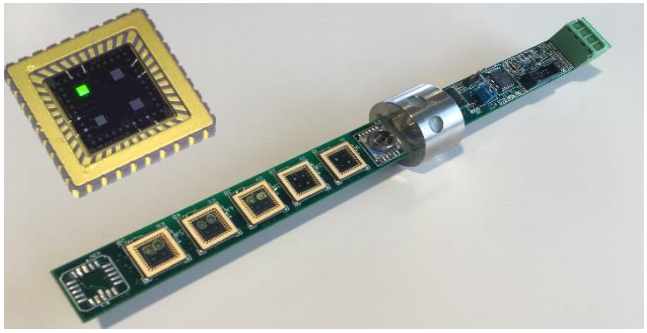

Figure 1: Sensor Array having 5 coated chips (left). Inserted is a capacitive chip having 4 electrodes (insert).

The IDE concept has the ability for miniaturization, since the electrodes can be made using CMOS compatible technologies, and the read-out electronics only require a small PCB. So, the approach disclosed in the current paper is an important step in miniaturization of a gas sensor array (figure 1).

An important step in this process is the reproducible manufacturing of the coating layers, having thicknesses between 1 and 5 μm. This is currently in progress, using a BiofFluidix BioSpot

BT600 workstation. Droplets are dispensed from the small nanodispensers (125 – 500 µm capillaries). Since every functional coating formulation has its own specific solvent, and corresponding viscosity, surface tensions, etc., all printing parameters must be addressed for each coating separately. For some formulations, a single droplet is sufficient to coat the whole IDE surface (figure 2), others require multiple droplets.

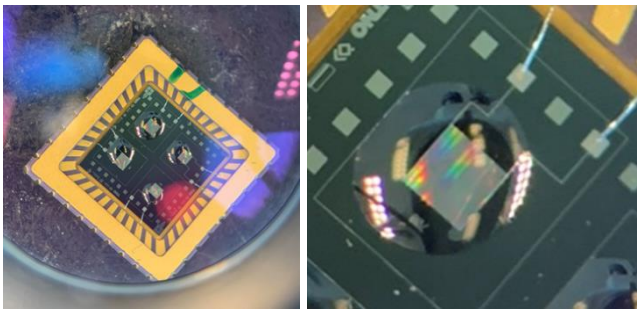

Figure 2: Printed droplets on the fours IDE's of the chip.

The printing of one polymer coating revealed that the thickness of the coating cannot be influenced by the amount of droplets (figure 3), but only by the concentration of the polymer in solution.

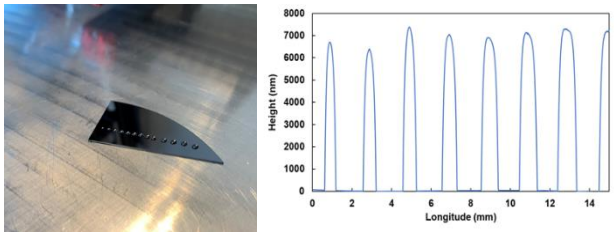

Figure 3: Height dependency on the number of droplets

After manufacturing of the sensor array, the device is calibrated by exposing to various gas mixtures. Combining the response of multiple sensor chips makes it possible to simultaneously obtain the concentrations of the individual components of the target gas mixtures. Subsequently, other gas parameters can be calculated from the composition, such as the calorific value, Wobbe index, and density. The gas sensor technology is demonstrated for three cases: the Gas Grid, LNG and Hydrogen mixtures.

There is one important prerequisite for the application of the sensor: the number and types of gasses in a gas mixture must be known, because the sensor is using the full response of all chips to calculate the full composition. Any unknown gas will decrease the reliability of the result

GAS GRID MONITORING

The validation of the sensors was done in field tests, where the sensors were installed in several real gas grids that transports natural gas and/or mixtures with biogas. One field test was operating for several weeks to monitor changes in composition due to the feed of biogas from a sugar processing plant into a local gas grid (figure 4).

Figure 4: Sugar biogas plant in Groningen, and gas sensor installed in Gas Distribution Station.

The sensors that were installed in the gas grid were calibrated on site, using the available GC data from the first week of exposure. For the duration of the field test (3-4 weeks), the composition and corresponding energy values were calculated from the raw sensor data. The calculated methane concentration and calorific value are plotted versus time (figure 5).

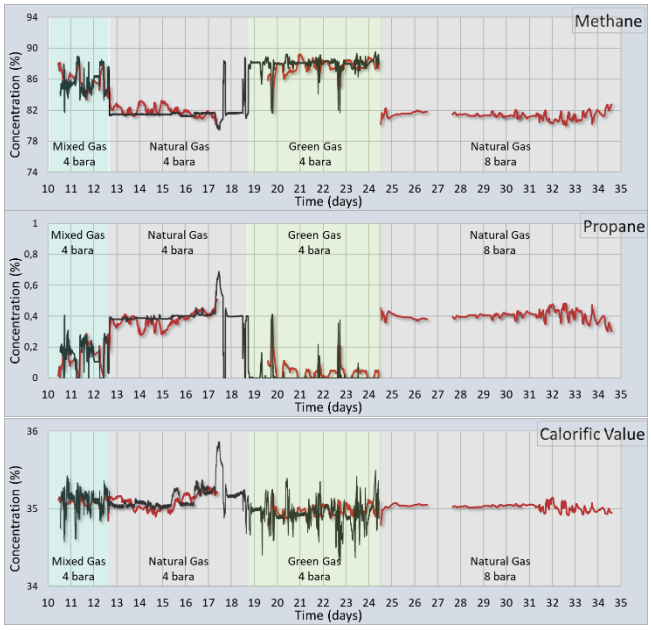

Figure 5: Comparison of Sensor and GC data for a switch between mixed, natural and Biogas. Calorific Value is calculated from the composition.

The calculated sensor data follows the GC values very nicely when changing from a mixture of biogas/natural gas to natural gas and finally to biogas. The differences in methane concentration between natural gas (~82 vol%) and biogas (~88 vol%) can be clearly validated. Furthermore, although the gas concentrations change significantly when switching from natural gas to biogas (e.g. biogas does not contain any higher hydrocarbons), the calculated Calorific Value (CV) is rather constant (~35 MJ/m^3) over time, which is confirmed both in the GC as well as the sensor data. The average deviation between calculated and real CV (obtained from the GC data) is around 0.5 %.

LNG QUALITY FOR GAS ENGINES

Another application for the gas composition sensor is the quality monitoring of LNG as an engine fuel. For this application, the quality is not only expressed as Calorific Value, but also as Methane Number (MN). This parameter indicates the knocking behavior of an LNG or dual fuel (diesel and LNG) engine. Pure methane fuel has a methane number of 100. When the concentration of higher hydrocarbons is increasing, the MN decreases and the engine will have a higher degree of knocking. The MN can be measured using a standard LNG engine, or calculated from the full composition, using a specific algorithm [4].

The challenge in the measurement of LNG is the much larger amounts of higher hydrocarbons. These gasses must be measured with a high accuracy, since they influence the MN significantly. In order to realize this, a new series of porous coatings was developed and implemented. The specific challenge was to discriminate between the higher hydrocarbons, which all have similar chemical and physical properties. A series of experiments was performed with gas mixtures containing methane, ethane, propane, n & iso-butane, n & iso-pentane. The raw sensor data of 20 points was used as calibration to calculate the composition development during a 2.5 days experiment. The results of the higher alkanes is shown in figure 6.

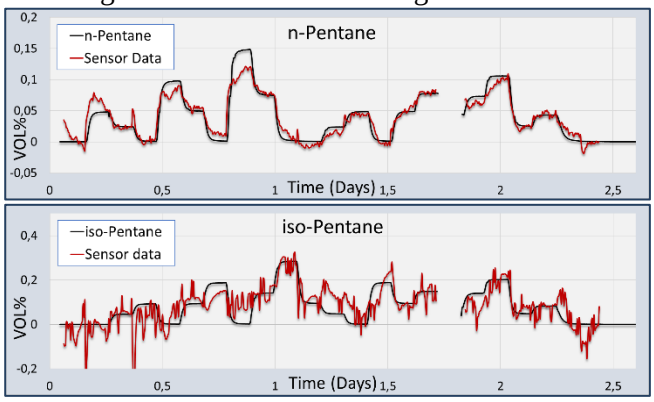

Figure 6: Traces of the GC data (black) and calculated gas concentrations (red) for n & iso-pentane in the gas mixtures.

The calculated concentrations follow the GC values well. It is clear that some gas concentrations are calculated with a higher accuracy than others. For example, the scattering in the iso-pentane results is higher than for the n-pentane. This is partly caused by the experimental procedure. During the experiments, the gas composition is changed, and the new gas mixtures must stabilize, before the sensor can start producing accurate data. Furthermore, each of the signals of the ten coated electrodes has its own response time and fluctuations. This means that during transitions, the accuracy may fluctuate.

The calculated gas concentrations can be converted to the Calorific Value and Methane Number. For this calculation, only one measurement point was taken for each gas composition, at the end of the stabilization period. The results are shown in figure 7.

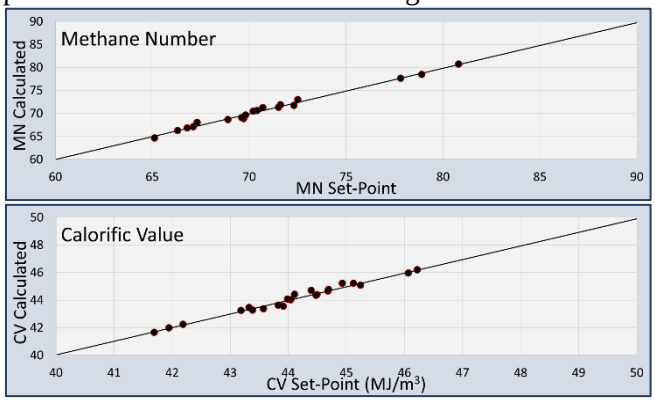

Figure 7: Calculated Methane Number and Calorific Value versus set-point values.

The accuracy of this calibration and validation experiment is shown in table 1. Twenty measurement points were taken as calibration, and five additional points as validation of the sensor. The average error calculated between set-point value and calculated concentration is listed in table 1 for both the twenty calibration points and the five validation points.

Table 1: Average error in composition, MN and CV

Parameter	Average error	Parameter	Average error
Methane	0.60 vol%	n-Pentane	0.005 vol%
Ethane	0.94 vol%	Iso-Pentane	0.024 vol%
Propane	0.33 vol%		
n-Butane	0.14 vol%	MN	0.31
Iso-Butane	0.13 vol%	CV	0.25 %

This table shows that for the given example, all the measured values are well within the requirements. The requirement for the MN was given by the engine operators. The requirements for the composition were calculated from the maximum deviation of 2.0 for the MN. The requirement for the CV was given by the gas grid operators.

HYDROGEN DETECTION

The last example for a relevant application for the gas composition sensor is the assessment of the concentration of hydrogen in the natural gas grid. It is expected that the amount of hydrogen that will be mixed with natural gas or biogas in the gas grid will increase in the future, when the production of hydrogen using renewable energy (wind or solar) will starts to take off. It will become very important to measure the amount of hydrogen mixed with the gas in order to assure a certain gas quality.

For hydrogen detection a new coating material was developed, based on porous metal oxides. Just as is the case for the other gasses, when the hydrogen is absorbed by the coating, the capacitance of the IDE changes, which can be correlated to the hydrogen concentration.

Gas exposure experiments are performed in the gas mixing system. A thermal conductivity detector (TCD) is used to validate the sensor results and increase the accuracy of the hydrogen detection. The response of the hydrogen sensing chip and the TCD is monitored when the hydrogen content in the gas is changing. Hydrogen exposure experiments were performed with nitrogen, methane and natural gas as carrier gas. An example of a test is shown in figure 6.

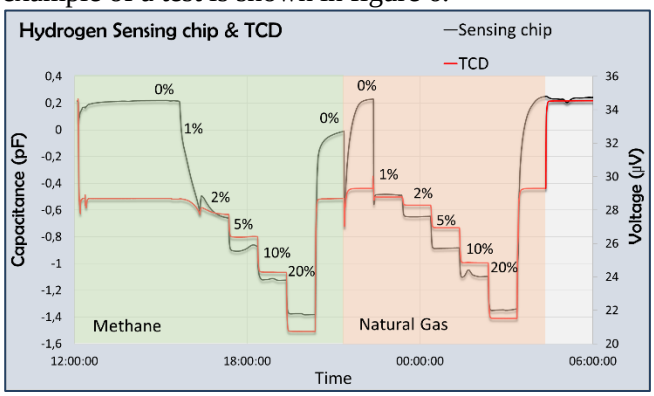

Figure 6: Response of the hydrogen sensing chip (in pF) and TCD (in mV) for hydrogen concentrations between 0 and 20 vol% in methane and natural gas at 1 bara.

The response of both the sensor chip and the TCD are plotted versus the partial pressure of hydrogen. The particle pressure is calculated from the known pressure and hydrogen concentration. Figure 7 shows the results of the two detectors. There is a clear difference between the two plots: the hydrogen sensing chip shows a dependency for the partial pressure, also at lower pressures at concentrations entering the ppm level. The TCD not only depends on the particle pressure, but also on the total pressure. In fact, it appeared that the TCD relies more on the hydrogen concentration instead of pressure. Furthermore, the sensitivity of the TCD at low hydrogen concentrations is relatively low, which means that the TCD cannot be used reliably at ppm levels of hydrogen. But, by combining both detectors, the accuracy in the calculated hydrogen concentration in a mixture can be enhanced significantly.

Since the hydrogen chip depends on the partial pressure, it can be integrated with the other chips (as described above) very well. The exact behavior of the sensor when exposed to hydrogen still must be elucidated, because a logarithmic dependency cannot be explained by a simple absorption equilibrium between gas environment and coating.

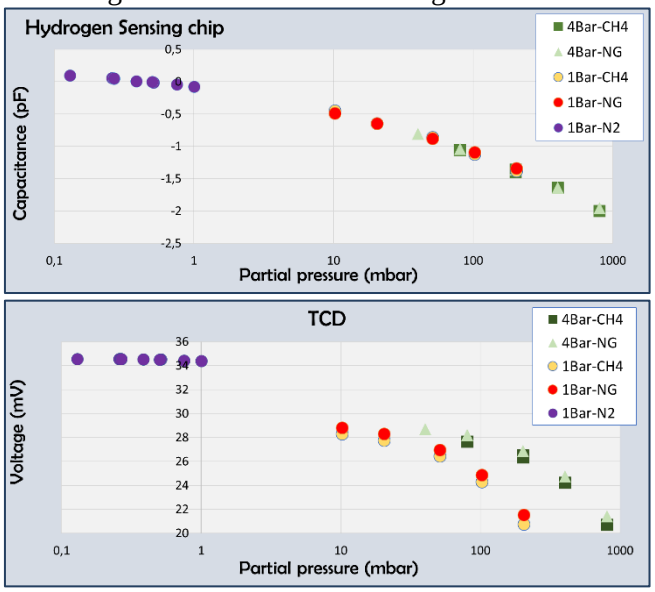

Figure 7: Response of the capacitive hydrogen chip and TCD versus partial pressure of hydrogen at different pressures.

CONCLUSIONS

This paper show the versatility of the capacitive sensor platform. By functionalizing the interdigitated electrodes using functional selective coatings, the sensor array can be made suitable for the detection of a large variety of gasses. The reproducible deposition of these coatings is important for a reliable operation.

REFERENCES

[1] D. Snelders, A. Boersma, A-J. de Jong, Gas Sensor Array and Method, WO2016003272, 2014

[2] A. Boersma, J. Sweelssen, H. Blokland, Gas composition sensor for natural gas and biogas, *Proc. Engin. 168*, 2016, pp. 197 – 200.

[3] C.H. Clausen, G.E. Skands, C.V. Bertelsen, W.E. Svendsen, Coplanar electrode layout optimized for increased sensitivity for electrical impedance spectroscopy, *Micromachines*, *6*, 2015, pp. 110-120.

[4] B. Gieseking, A.S. Brown, Novel algorithm for calculating the methane number of liquefied natural gas with defined uncertainty, Fuel, *185*, 2016, pp. 932-940.

CONTACT

*Arjen Boersma, arjen.boersma@tno.nl

MULTIPARAMETR GAS MONITORING SYSTEM COMBINING A FUNCTIONALIZED AND A NON-FUNCTIONALIZED MICROCANTILEVER

C. Huber[1], A. Mehdaoui[1], M. P. Pina[2], J.J. Morales[2]
[1] TrueDyne Sensors AG, Reinach BL, Switzerland
[2] University of Zaragoza, Nanoscience Institute of Aragon, Zaragoza, Spain

ABSTRACT

A novel multiparameter online gas monitoring system is presented combining a pressure and a temperature sensor with two resonating microcantilevers from which one is functionalized with a highly sensitive hydrophilic nanoporous material. By simultaneously observing eigen-frequencies and quality factors of the two cantilevers gas density and viscosity can be determined as well as gas humidity in the parts per million (ppm) range. With this sensor information we can deduce molar concentrations of binary or even ternary gas mixtures in a % range and the gas vapor ratio in a medium to low ppm range.

KEYWORDS

microcantilever, density, viscosity, humidity, gas monitoring, functionalized cantilevers, nanoporous solids, zeolite

INTRODUCTION

The aim of the presented sensor project is to develop a compact, robust and maintenance free gas monitoring system for industrial use in the field of inert gases e.g. welding gas or modified atmospheric packaging gas mixing application. In such applications typically binary or ternary mixtures of argon, helium, nitrogen, carbon dioxide, oxygen or hydrogen are used. Gas concentrations must be controlled with accuracies in the % range. In most cases, the humidity must also be monitored in these applications. Typical threshold values are between 200 and 40 ppm [1]. The state of the art of technology is to connect several independent sensors in series, e.g. thermal conductivity, together with specific optical absorption and dew point sensors. Such installations are bulky and require frequent recalibration. To bring the same functionality in one multiparameter sensor system, we combined two resonating microcantilevers together with a pressure and a temperature sensor on one PCB board that is exposed to the process gas.

Commercially available silicon microcantilevers initially designated for atomic force microscopy from SCL-Sensor.Tech. were used (see Figure 1). One cantilever was used to measure the density and the viscosity of the gas as reported by Badarlis et al. [2] or Huber et al. [3] and the other to measure water vapor in low concentration by adding a functionalized surface layer layer based on a hydrophilic nanoporous material, as reported for example by Urbiztondo et al [4].

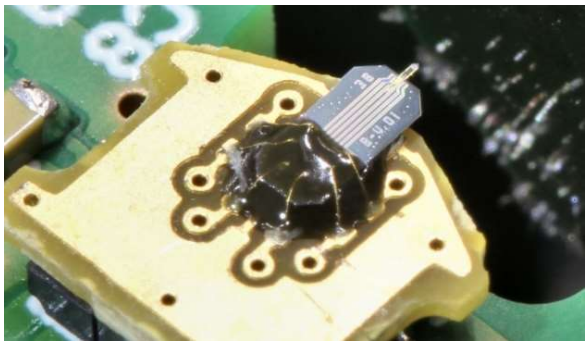

Figure 1: Sensor PCB with the a first microcantilever in front of a permanent magnet. The second cantilever is placed on the backside of the PCB. Actuation occurs by sending a small AC current over the metal coil on the cantilever tip.

FUNCTIONALIZATION

Hydrophilic Materials

The pristine cantilevers have been modified with low Si/Al ratio microporous zeolite, i.e. commercial CBV100 (~1000 nm) supplied by Zeolyst with a Si/Al ratio of 2.55 (Y-type zeolite, Na as extraframework cation) and MCM-48 mesoporous silica particles (~200 nm) synthesized in the lab [6] (see Table 1). 9 cantilevers were coated in total ether with MCM-48 or CBV100. Two different methods were developed and tested to apply the particles to the cantilever surface.

Table 1: Main properties of the NaY type microporous zeolite (CBV100) and mesoporous silica (MCM-48) used in this work

Material	BET Surface Area (m^2/g)	Pore Volume (cm^3/g)	Pore Size (Å)	Particle Size (µm)
CBV100	758	0.247	6.9	<0.7
MCM-48	1287	1.11	35	0.2

Method 1: Oxygen Plasma and Immersion

Prior to the chip incubation step in the aqueous suspension 2 % wt, the top surface of the

microcantilever was activated by O_2 plasma to promote the self-assembly of the particles onto the surface. The optimal experimental conditions for the sensing materials herein investigated have been defined from the experimentation with Si/SiO_2 and Si/Al_2O_3 chips respectively. As an example, Fig. 2 shows the top surface of the modified microcantilever with MCM-48 spherical particles. A tightly packed arrangement of MCM-48 particles over the whole SiO_2 surface (top layer of the chip) and preferentially on the Al_2O_3 coil is attained.

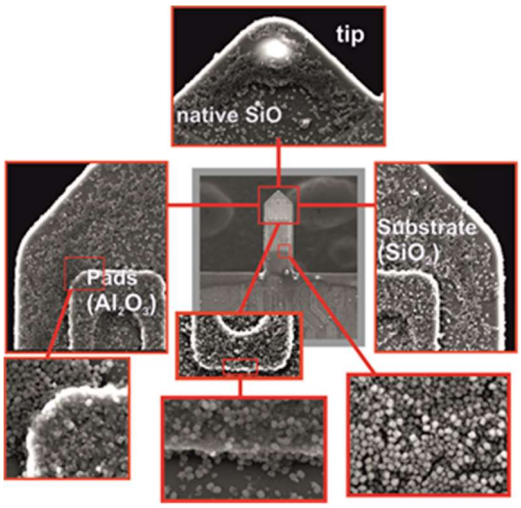

Figure 2. SEM images of the mesoporous silica coating on the top of the microcantilever obtained by self-assembly of MCM-48 nanoparticles onto plasma activated surfaces.

Method 2: Direct Spotting of Material

A Micro Array Spotter was used for the coating of cantilever probes. Such an instrument is a non–contact piezo dispensing system, which allows spotting and dispense of liquids in the pico- to nanoliter range. This methodology offers many advantages: automatic and rapid spotting process, reproducible coatings for a given dispensing solution and target, no damage to sensitive surfaces and easily scalable to high-throughput production.

The probe solutions were the following:

1. Ethanolic suspension 2% wt. of MCM-48 nanoparticles
2. Aqueous suspension 1% wt. of CBV100 crystals. A previous separation by centrifugation is carried out to reduce the particle size below 700 nm.
3. Aqueous suspension of poly-(diallyldimethylammonium chloride) (PDDA), 0.2%wt used on two cantilevers as cationic polyelectrolyte to improve the coverage of the surface with MCM-48 spherical nanoparticles by electrostatic interactions.

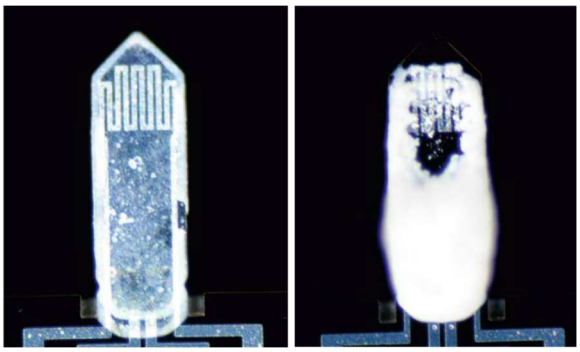

Figure 3. Optical microscope images of a MCM-48 (left) and a Zeolite (CBV100) (right) coated microcantilever obtained by spotting of a suspension of nanoparticles directly onto the cantilever surface.

EXPERIMENTAL SETUP

Resonance frequencies and quality factors of the microcantilevers were measured using a specific phase lock loop as described by Sell et al. [6]. Additionally, a heater was implemented to bring the cantilever instantly to temperatures up to 250°C while still measuring. The heating step was needed to release captured water molecules from the hydrophilic layer and reset the humidity measurement. The measurements were carried out by placing the cantilever PCB in a gas-tight measuring cell which could be purged with different gases, pressurized, cooled or tempered.

The sensor system has been calibrated and qualified with 4 different gases in a temperature range of 0 to 60°C and a pressure range of 1 to 10 bar abs. The humidity sensitivity experiments were performed using a reference dew point sensor in the measuring cell.

Density and Viscosity Measurement

The achievable density and viscosity measurement performance is shown as an example in Figure 4. The density can be measured with an accuracy (95%) of <0.03 kg/m^3 and the viscosity <0.2 µPas what corresponds to about 1% of reading for the investigated gases.

When knowing density and viscosity with such an accuracy it becomes possible to differentiate a large number of gases and thus to reliably detect these gases or, in the case of gas mixtures, to determine the individual proportions of binary or even ternary mixtures. In the case of natural gas, the Wobbe index, calorific value and inert gas fraction can also be determined from such measurements as described in [3].

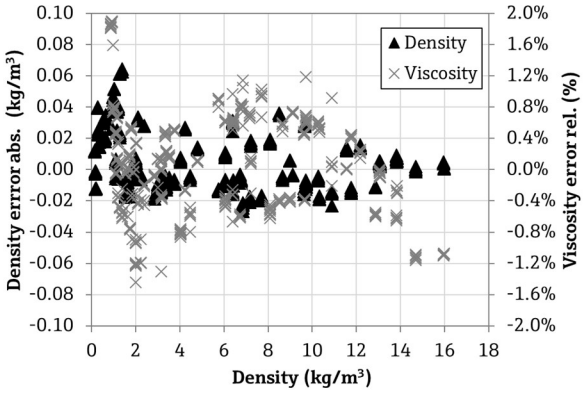

Figure 4. Typical density and viscosity measuring accuracy. Measurement of 4 gases (N_2, CO_2, Ar and He) between 4.5 and 60°C and 1 to 8 bar abs are shown.

Humidity Measurement

To qualify the functionalized cantilevers and to characterize their moisture detection properties, measurements were taken with standard gas mixtures (argon with 100 ppm water content) or mixtures of dry and ambient air. The residual humidity was determined by means of a reference sensor directly in the gas measuring cell. By adjusting the volume flow through the cell, the moisture content could be varied.

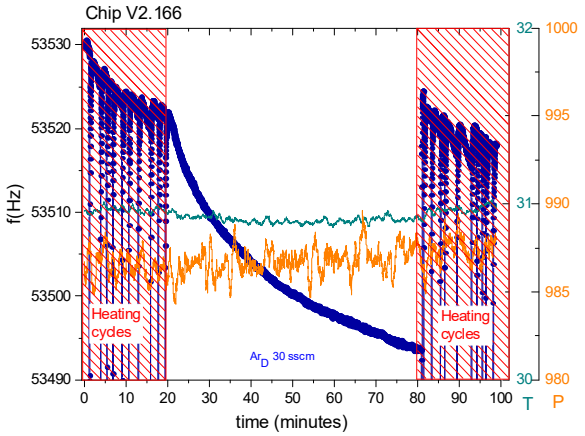

Figure 5. Frequency response of an MCM-48 coated cantilever exposed to argon with 100 ppm H_2O.

Figure 5 shows a typical measurement behavior. After a heating cycle, the frequency (f) drifts slowly downwards due to the adsorption of water molecules and the associated increase in mass (Δm) according to Eq. (1). If the cantilever is heated again to > 200°C, the hydrophilic layer is degassed again and the frequency returns to the initial value.

$$f(x) = \text{Const}' \sqrt{\frac{k}{m}} = \text{Const} \sqrt{\frac{E(T, n_{H2O})}{m_0 + \Delta m}} \qquad (1)$$

Approach 1: Adsorption-Desorption

The principle idea is now to measure the initial frequency change rate to determine the vapor ratio. To be able to do this, the rate of change must of course depend on the vapor ratio. It is also to be expected that the adsorption process is strongly dependent on the temperature. In order to detect frequency changes caused by process changes, temperature, pressure, density and viscosity are continuously monitored by the measuring system and after each heating cycle sensor potential drifts could be adjusted to the uncoated cantilever.

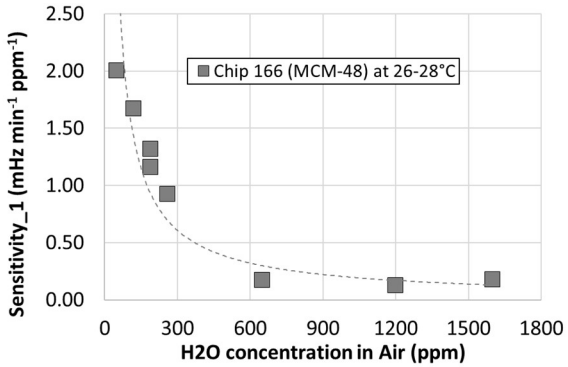

Figure 6. The sensitivity (frequency change rate per ppm H_2O and time) of an MCM-48 coated cantilever versus vapor ratio at one temperature.

That such an approach is feasible is shown in Figure 6. Here the sensitivity is plotted as frequency change rate per ppm H_2O and time against the vapor ratio. One can see that the sensitivity is high at small water vapor ratio, in accordance with a Langmuir type sorption process. Thus, in the concentration window where we aim to measure (<200 ppm) the sensitivity is high.

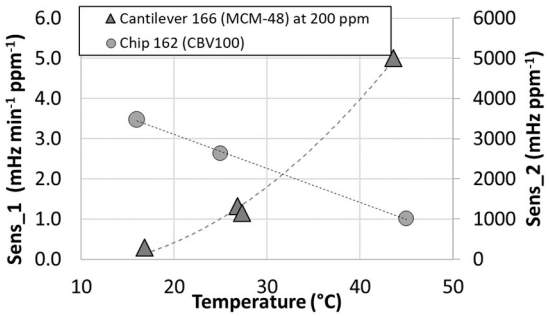

Figure 7. Temperature dependency of the sensitivities according to approach 1 (left axis, triangles) and according to approach 2 (right axis, circles).

In Figure 7 the temperature dependency of the sensitivity of approach 1 is plotted. The sensitivity increases with temperature what contradicts the expectation. We know that the adsorption of water

in zeolite is inversely proportional to the temperature. However, all our cantilevers showed the same temperature behavior. This means the frequency drift cannot be explained by a mass effect only, but it will most probably also be a stiffness effect involved. Baimpos et al. [7] describes, for example, a change in the elastic properties i.e. the stiffness (k) or Young's modulus (E) of zeolite films upon molecular adsorption. This effect was also determined to be temperature dependent. Such an effect could therefore amplify or weaken a mass effect.

Approach 2: Thermodynamic Equilibrium

For further indication that an adsorption dependent stiffening may be involved two series of measurements with cantilevers covered with very thick zeolite layers (Figure 3 - right) were carried out. These cantilevers could only be degassed very poorly by the heater. So, we used these cantilevers in a static (equilibrium) mode instead of a dynamic mode (heating - adsorbing - heating – etc.). This means that the cantilevers were simply left in thermodynamic equilibrium with the environment. Surprisingly, these cantilevers showed a very strong direct correlation of frequency with the vapor concentration of the environment (Figure 8).

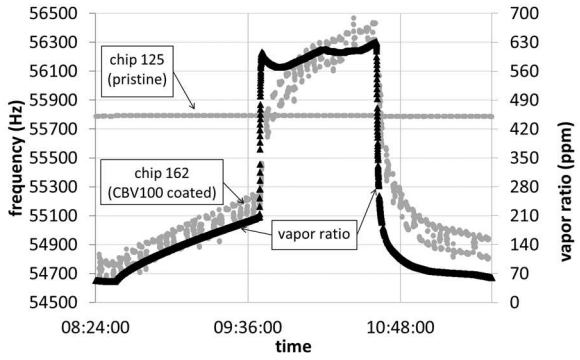

Figure 8. Frequency response of a pristine (chip 125) and a CBV100 coated cantilever (chip 162) exposed to air with changing vapor ratio at 25°C. The frequency of the chip 162 follows nicely the vapor ratio changes whereas the frequency of chip 125 stays constant.

A direct correlation according to Eq. (1) indicates a dominant stiffness effect, since the mass effect would act in the opposite direction. In contrast to approach 1, the sensitivity decreases with increasing temperature (Fig. 7 right). This could be an indication that the mass effect in approach 1 was attenuated by a superimposed temperature-dependent stiffness effect. Whether this is the case, we cannot judge yet with certainty and further experiments must be carried out.

CONCLUSIONS

A novel multiparameter gas sensor concept was presented, based on two microcantilevers and a pressure and temperature sensor, which is able to determine the density and viscosity of gases with high accuracy over a wide temperature and pressure range. Furthermore, different methods were developed and tested how a microcantilever can be provided with a functional layer in order to react sensitively to smallest water vapor concentrations. The first series of measurements have shown that a humidity measurement is basically possible, but that a lot of qualification work still needs to be invested in order to finally understand the sensor behavior and the dependencies on process parameters such as temperature and pressure.

REFERENCES

[1] ISO 14175:2008, “Welding consumables -- Gases and gas mixtures for fusion welding and allied processes”, 2008

[2] A. Badarlis, A. Pfau, A. Kalfas., “Measurement and Evaluation of the Gas Density and Viscosity of Pure Gases and Mixtures Using a Micro-Cantilever Beam”, Sensors, 15(9), pp. 24318-24342, 2015

[3] C. Huber, P. Reith, A. Badarlis, “Gas Density and Viscosity Measurement with a Micro-cantilever for Online Combustion Gas Monitoring”, 19.GMA/ITG-Fachtagung Sensoren und Messsysteme, Nürnberg Germany, 2018

[4] M. A. Urbiztondo, A. Peralta, I. Pellejero, J. Sesé, M.P. Pina, I. Dufour, J. Santamaría, “Detection of organic vapours with Si cantilevers coated with inorganic or organic layers”, Sens. Actuators B, Chem., 171–172, pp. 822–831, 2012.

[5] H. Nigar, B. García-Baños, F. L. Peñaranda-Foix, J. M. Catalá, R Mallada, J. Santamaría, “Amine-Functionalized Mesoporous Silica: A Material Capable of CO2 Adsorption and Fast Regeneration by Microwave Heating”, AIChE Journal, Vol 62, No 2 (2016).

[6] J.K. Sell, A.O. Niedermayer, B. Jakoby, “A digital PLL circuit for resonator sensors”, Sensors and Actuators A: Physical, 172, pp. 69– 74, 2011

[7] T. Baimpos, I.G. Giannakopoulos, V. Nikolakis, D. Kouzoudis, “Effect of gas adsorption on the elastic properties of faujasite films measured using magnetoelastic sensors” Chem. of Materials 20 (4), pp. 1470–1475, 2008

CONTACT

christof.huber@truedyne.com

CONSTRUCTION OF A WELL OPERABLE CRYSTALLIZATION METHOD FOR CHEMICAL ANALYSIS APPLYING A MICRODROPLET DEVICE

S. Hattori[1], D. Tanaka[2], D. H. Yoon[1], T. Sekiguchi[2], Y. Nozaki[2], T. Akitsu[3] and S. Shoji[1]
[1] Department of Electronic and Physical Systems, School of Fundamental Science and Engineering, Waseda University
[2] Research Organization for Nano & Life Innovation, Waseda University
[3]Department of Chemistry, Faculty of Science, Tokyo University of Science

ABSTRACT

In this work, we developed a simple microfluidic device from which fragile protein crystals grown in microdroplets were successfully removed without becoming damaged. This device was easily fabricated by performing rapid prototyping and deploying modular assembly systems. The device was mainly made of polydimethylsiloxane (PDMS): Because PDMS-PDMS bonds can be easily broken, little force needed to be exerted to disassemble the device, and hence the protein crystals could be easily removed from the device channel. Dried protein crystals were subjected to chemical analysis to determine their components. This paper proposes a novel technique for crystallization and handling of protein crystals, which is expected to contribute to the study and application of protein analysis.

KEYWORDS

Microfluidics, Microdroplet, Crystallization, Protein, Lysozyme

INTRODUCTION

Protein Crystallization

Metal complex-containing proteins are very important materials for pharmaceutical and structural biology studies. For example, Dasari et al. reported the mechanism of action of platinum complex-containing proteins (called cisplatin) used as an anticancer drug [1]. Structural analysis of proteins is essential for their pharmacological applications, and X-ray crystallography is a key technique for carrying out such analysis. When using this technique, protein crystallization is the most important step for obtaining good results because crystal quality critically depends on the crystallization conditions. Various methods for crystallization such as vaper diffusion, batch crystallization, dialysis buttons have been devised so far. However, gravity has been shown to be at least somewhat detrimental to crystal growth when using these conventional methods [2]. Gravity causes density difference convection, which impedes a uniform crystal growth. For this reason, crystallization in outer space is being attempted [3]. However, experiments in outer space are very expensive and take a long time to carry out. Recently, microfluidics has been used to reduce the effects of gravity on crystallization, and the use of microfluidic devices has been reported by Zheng and co-workers to yield high-quality protein crystals [4]. The effect of surface tension becomes more influential than that of density difference convection. After crystallization, researchers have typically analyzed crystals left in the fluidic channel, using X-ray diffraction (XRD) [5]. To perform a more detailed analysis, however, intact crystals need to be removed from the device, which is very difficult to do. Many types of protein crystals are extremely fragile, and thus crystals are easily broken if excessive force is applied to the crystal during the removal process. Therefore, we set out to develop a new method for applying no extra force to crystals and easily removing them from a microfluidic device.

Research Concept

Figure 1 shows the concept behind our research. First, the protein solution and precipitating agent solution were mixed and microdroplets of that mixture were formed. Then, the microdroplets were placed into a simple PDMS channel of our microfluidic device in order to suppress evaporation of the solvent and maintain their integrity. The device was then left alone for several days. This microfluidic device was designed to be easily disassembled by having a very simple structure and using the self-adhesiveness of PDMS for assembly. Therefore, when protein crystallization was completed in the device, it was disassembled without exerting any strong force, and protein crystals were removed without being damaged. The removed protein crystals were observed, and specifically had their shapes identified, using field-emission scanning electron microscopy (FE-SEM, S-4800, Hitachi High-Tech., Japan). In addition, the crystals were analyzed by energy-dispersive X-ray spectroscopy (EDX, Genesis V6.44J, EDAX) to identify their constituent elements.

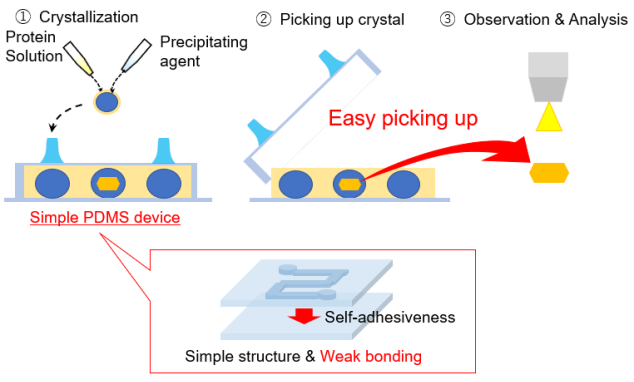

Figure 1: The concept of our research.

EXPERIMENTAL

Device Concept

Our microfluidic device was divided into two units to improve its operability and customizability. In crystallizations, an enormous number of conditions should be examined, and many samples were required in each experiment. To increase the experimental efficiency, the device had a microdroplets generation unit (hereinafter, the "capillary unit") and a microdroplets containing unit (hereinafter called "PDMS unit"). While the capillary unit was reused many times, PDMS units were replaced from time to time to prepare a lot of samples. In addition, since many different types of solutions are generally tested for crystallization, device materials should be chosen according to the solutions to be used. In this research, glass was chosen as the main material of the microdroplets generation unit for its high chemical resistance. On the other hand, PDMS was chosen as the main material of the microdroplets containing unit because of its transparency and self-adhesiveness.

Fabrication of the Capillary Unit

Figure 2 (a) shows the process used to fabricate the capillary unit. The unit was fabricated in two steps. The first step involved preparation of the components. Two different types of glass capillaries were prepared: one with outer/inner diameters of 1.2 mm/0.47 mm and which was heated and stretched mechanically to form a tapered structure, and the other with outer/inner diameters of 1.39 mm/1.95 mm. Two types of jigs used to connect the inlet and outlet capillaries were fabricated using a 3D printer (Objet Eden500V, Altech). One jig was made of two rectangular poles and the other had rectangular holes that enabled alignment of the positions of the capillaries and the positions of the jigs. Eyelets were glued to the jigs to make inlets. The second step involved the assembly of the components. Glass capillaries were inserted into the jig holes and then the jigs were mechanically assembled. UV-curable resin was applied to fill the gap between the capillaries and jigs as well as join the jigs together.

Figure 2 (b) shows an image of the capillary unit. Glass capillaries and jigs were assembled as designed. Furthermore, the glass capillaries were positioned almost coaxially.

Droplet Generation Mechanism

Figure 2 (c) shows the mechanism of droplet generation. The protein solution was made to flow into the left side of the inner capillary and the precipitating agent solution was made to flow into the outer capillary. These two solutions were mixed at the space between the inner capillaries. Oil was flowed into the outer capillary from the direction opposite that from which the protein solution and precipitating agent solution were injected. At the entrance of outlet capillary, droplets of the solution mixture were generated by flow-focusing.

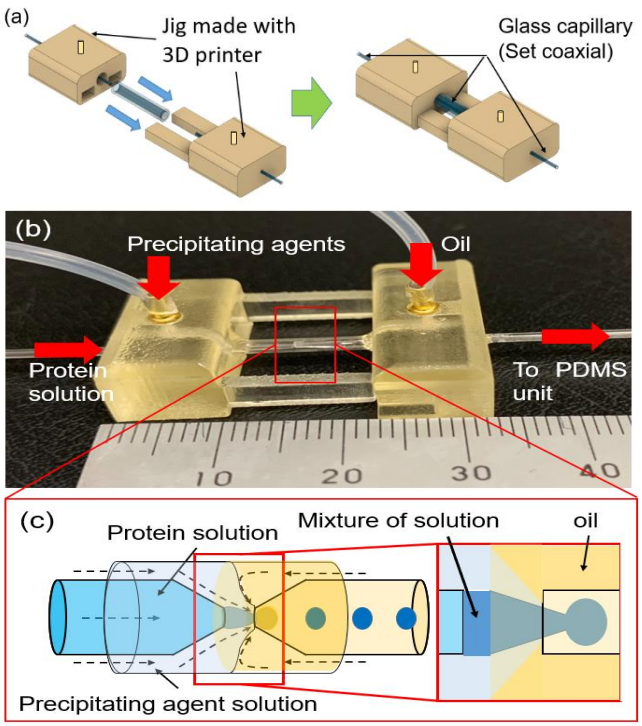

Figure 2: (a) Fabrication process of the capillary unit. (b) Photograph of the capillary unit. (c) Droplet generation mechanism.

Fabrication of the PDMS Unit

Figure 3 shows the process used to fabricate the PDMS unit. This unit was fabricated using a PDMS molding. A glass substrate with a patterned polyethylene terephthalate (PET) film was used as a mold for the PDMS channel. The channel width and length were approximately 2 mm and 40 mm, respectively, with the width designed to be greater than the average diameter of the microdroplets to prevent crystals from adhering to the walls of the channel. The channel height was the same as the PET film thickness (200 μm). These channel parameters and design could be easily changed by changing the PET film structure and thickness. After attaching the PET film, eyelets were bonded onto the film and silicone tubes were connected. When making the device, uncured PDMS was poured into the mold and heated at 120 °C to cure for tens of minutes. After heating, the cured PDMS was removed from the mold and put on a PDMS sheet. The molded PDMS and PDMS sheet were bonded with their self-adhesiveness. The device was left alone for a while until adhesion was completed. In addition, a metal weight was placed on the upper side of the PDMS channel to fix the position during the adhesion.

Figure 4 shows photographs of the PDMS unit. The channel was formed as designed. Furthermore,

there was no leakage of colored liquid introduced into the PDMS unit.

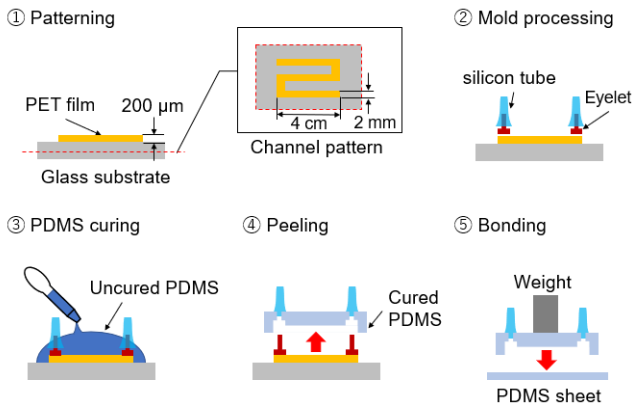

Figure 3: Fabrication process of the PDMS unit.

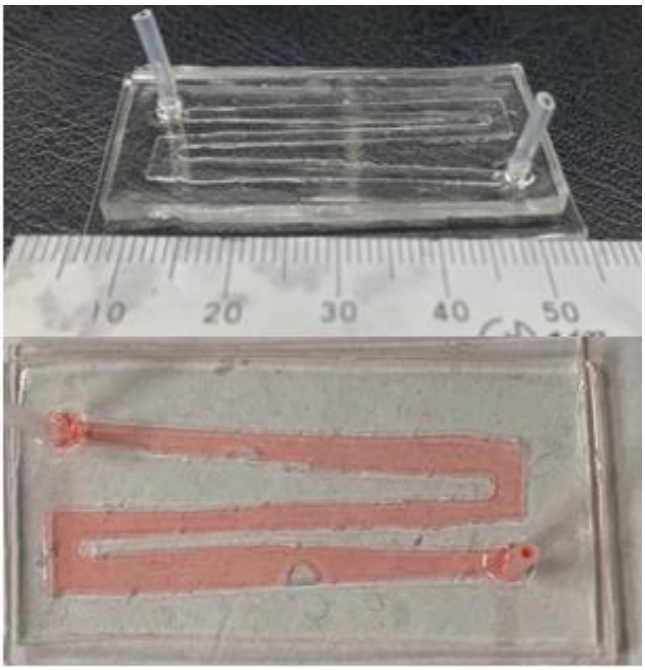

Figure 4: Photographs of the PDMS unit.

Experimental Procedure

Figure 5 shows the experimental system. Syringes were connected to the inlets of the capillary unit, and this unit was connected to the PDMS unit by a silicone tube. In the experiment, lysozyme (0.007 mol/L) was used as the protein. polyethylene glycol (PEG) 6000 (30% w/v) and NaCl (1 mol/L), which were dissolved in an aqueous citrate buffer solution, were used as precipitating agent. The lysozyme solution and the precipitating agent solution were pumped into the capillary unit from the syringe using syringe pumps. Thereafter, microdroplets of the mixture of these solutions were generated, and then carried into the PDMS unit by the flow of the solutions. Upon being filled with microdroplets, the PDMS unit was removed from the connecting tube, and then its inlet and outlet were sealed. The sealed PDMS unit was left at room temperature for 3 days. Droplets in the PDMS unit were observed with an optical microscope until the protein crystallized. Figure 6 shows the method used to pick up the crystals. As mentioned above, the PDMS unit was put together using weak adhesion forces and could therefore be manually separated into the PDMS sheet and channel. After disassembly of the device, the crystals on the PDMS sheet could be easily picked up. Specifically, a thin blade cutter was used to pick up the crystals. The blade was slid into the gap between the crystal and PDMS sheet and was then lifted. The crystal on the blade was put on a filter paper to absorb the solutions. Finally, the obtained crystals were observed by SEM and analyzed by EDX.

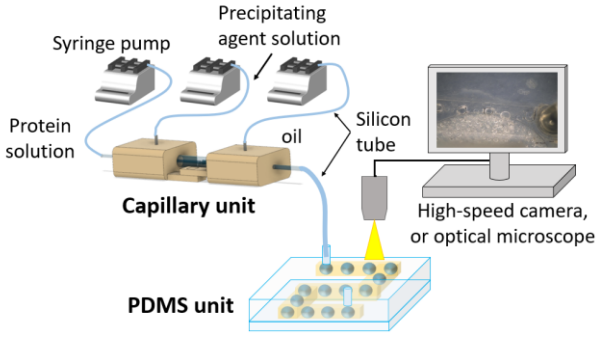

Figure 5: The experimental system.

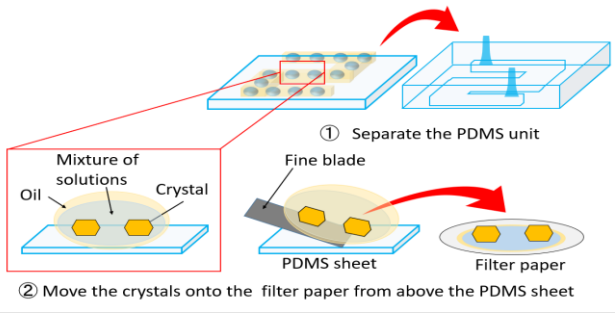

Figure 6: Method used to pick up crystals.

RESULTS AND DISSCUSSION

Observation results

Figure 7 shows a microdroplet contained in the PDMS unit. The diameter of microdroplets was approximately 400 μm. One crystal appeared in the droplet 1 day after mixing the solutions. Microscopic observation showed that the crystal in the microdroplet was large and of high quality. Figure 8 shows an SEM image of the crystal removed from the PDMS unit. The length of the long side of the crystal was measured from this image to be approximately 120 μm. Also, based on inspection of the SEM image, no crack was observed in the removed crystal. These results confirmed that our device and method are suitable for handling fragile protein crystals.

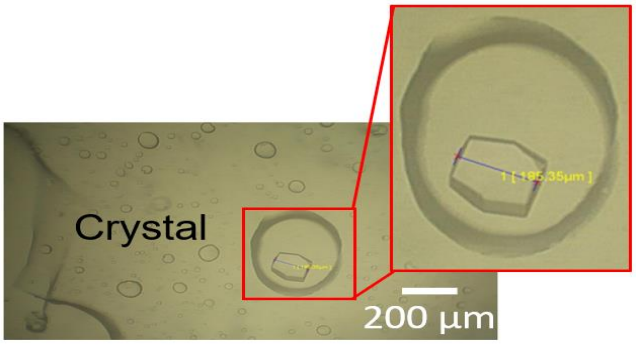

Figure 7: A crystal that appeared in the PDMS unit.

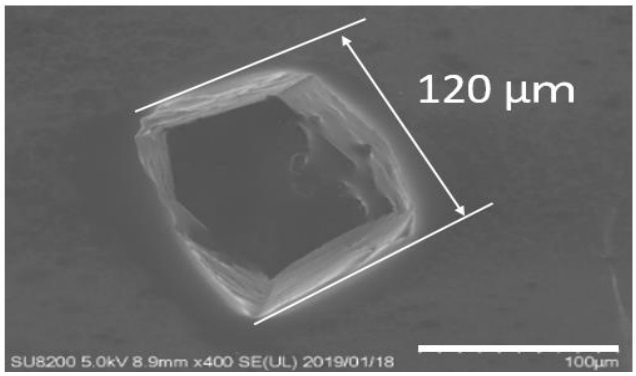

Figure 8: SEM image of the crystal.

The results of EDX analysis

Figure 9 shows the EDX analysis results. The strongest observed EDX peak was attributed to carbon and there were also small peaks due to oxide and sulfur. These peaks were derived from lysozyme. Carbon accounts for most of the constituent elements of any protein. Moreover, all proteins have peptide bonds (CO-NH) and many have disulfide bonds (S-S). There were also EDX peaks corresponding to sodium and chlorine, which were derived from sodium chloride; an aqueous solution including sodium chloride was used as a precipitating agent. In the microdroplets, the crystals were soaked in the precipitating agent solution. Solution attached to the crystal was evaporated and some sodium chloride solids apparently adhered to the crystal surface during its preparation for SEM observation and EDX analysis. Taken together, our SEM and EDX results suggested that the crystallization of lysozyme in the microdroplet was successful.

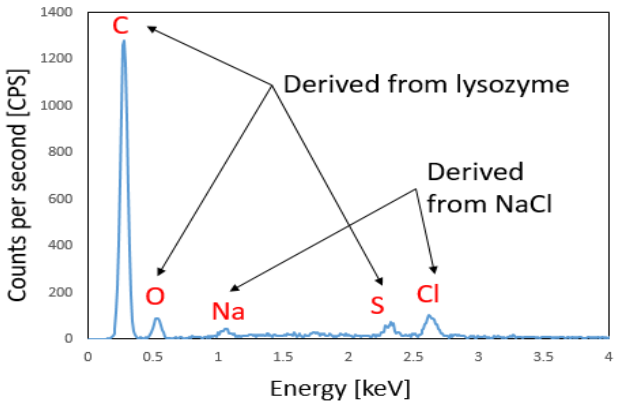

Figure 9: EDX analysis results.

Future work

In future work, we plan to take on the challenge of crystallizing and carrying out structural and chemical analyses of Zn (II) complex-containing lysozyme. This composite is expected to find applications as a tumor marker and in fuel cell electrodes. Furthermore, we plan to optimize the channel design and materials as necessary.

REFERENCES

[1] Dasari S., Tchounwou P.B., "Cisplatin in cancer therapy: Molecular mechanisms of action", Eur. J. Pharmacol., Vol. 740, pp. 364–378, 2014.

[2] Ferré-D'Amaré, A., "Crystallization of Biological Macromolecules", Cold Spring Harbor Laboratory Press, New York, 1999.

[3] Takahashi, S., Tsurumura, T., Aritake, K., Furubayashi, N., Sato, M., Yamanaka, M., Hirota, E., Sano, S., Kobayashi, T., Tanaka, T., Inaka, K., Tanaka, H., Urade, Y., "High-quality crystals of human haematopoietic prostaglandin D synthase with novel inhibitors", Acta Cryst., Vol. 66 (7), pp. 846-850, 2010.

[4] Bo Zheng, et al., "Screening of protein Crystallization Conditions on a Microfluidic Chip Using Nanoliter-Siza Droplets", J. Am. Chem. *Soc.*, Vol. 125 (37), pp. 11170-1, 2003

[5] Maeki, M., Yamaguchi, H., Tokeshi, M., Miyazaki, M., "Microfluidic Approaches for Protein Crystal Structure Analysis", Anal Sci, Vol. 32 (1), pp. 3-9, 2016

ACKNOWLEDGEMENTS

This work is partly supported by the Canon Medical Systems Corporation and the authors are also thankful for the MEXT Nanotechnology Platform Support Project of Waseda University.

CONTACT

hattori@shoji.comm.waseda.ac.jp

ON THE FEASABILITY OF FOR USING A MULTI-PARAMETER SENSOR FOR THE INLINE CHARACTERISATION OF MEDICINE MIXTURES

R.J. Dijkink[1], J.C. Lötters[2,3], B.I. van den Berg[4] and C.A.J. Damen[1]

[1] Saxion University of Applied sciences, Nano Physics, Enschede, The Netherlands

[2] University of Twente, Integrated Devices and Systems, Enschede, The Netherlands

[3] Bronkhorst High-Tech BV, Ruurlo, The Netherlands

[4] Medical Spectrum Twente, Enschede, The Netherlands

ABSTRACT

Initial investigations into the use of a MEMS based multi-parameter sensor for the characterization of medicine mixtures are presented. The current results show good results for density and mediocre results for heat capacity. Viscosity measurements have not yet produced any usable results. However there are clear flaws in the setup which could be the cause of this and which will not be present in the final integrated chip design.

KEYWORDS

Medical analysis, multi-parameter sensor, infusion, mass flow, density, heat capacity, viscosity, temperature.

INTRODUCTION

In hospitals medicine containing fluids fluids are commonly administered intravenously (IV), often combining multiple fluid lines into one single IV line. It is particularly important for prematurely born babies to keep the the number of access points to a minimum is as these neonates are very fragile and the risk of inflammation at the access site is high. IV therapy in this special patient group is associated with extreme low total flow rates and relatively high concentrations of medicines contained therein [1].

Although the combining of multiple single medicine IV lines through a manifold (multi-infusion) might seem relatively straight forward, the underlying physics can actually be quite complex. Multi-infusion can lead to undesired medication flow rates or even serious dosage errors. To understand these complex mixture flows and prevent adverse effects during therapy, a verification of the exact composition of the medicine mixture as well as the flow rate just before entering the patient is required [2].

The system requirements to measure a composed medicine flow are multiple: the measurement should be fast, accurate, real time, close to the admission site without affecting the medicines or medicine flow. Most of the current solutions for identifying components in a mixture fail at least one of these requirements (e.g. chromatography). Here we propose to utilize a MEMS based multi-parameter sensor, developed at the University of Twente, for checking the mixture on a set of specific physical parameters [3].

If the separate flows and the effects of the different medicines on the physical properties of the total flow are known, the properties of the total flow at the admission site can be predicted and compared against the actual measurements by using the multi-parameter sensor. Any deviation between measured and predicted values means the mixture is not as expected and could be reason for alarm.

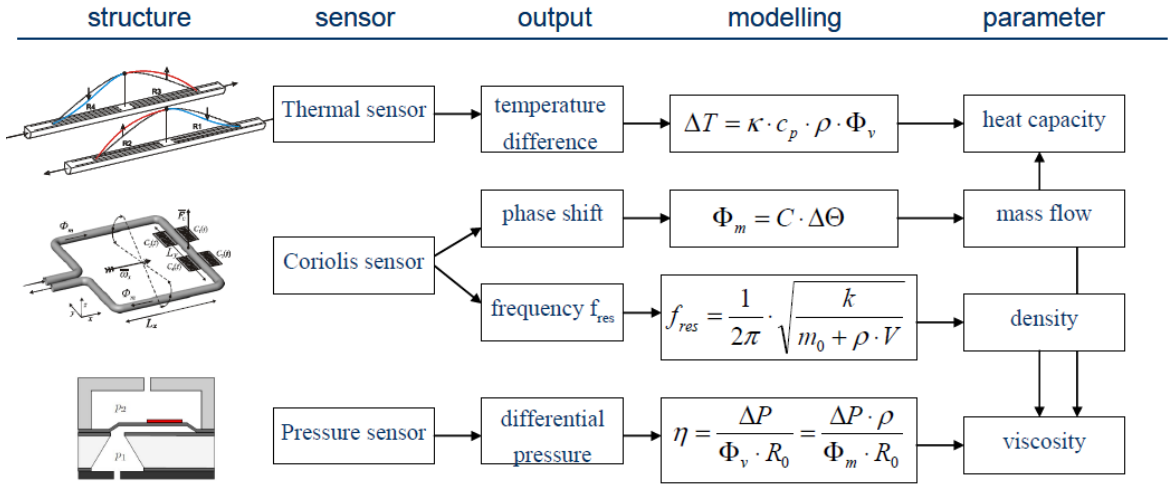

Figure 1 : Schemtic showing the different sensors and how the data combines to obtain the different physical parameters. Obtained from [3].

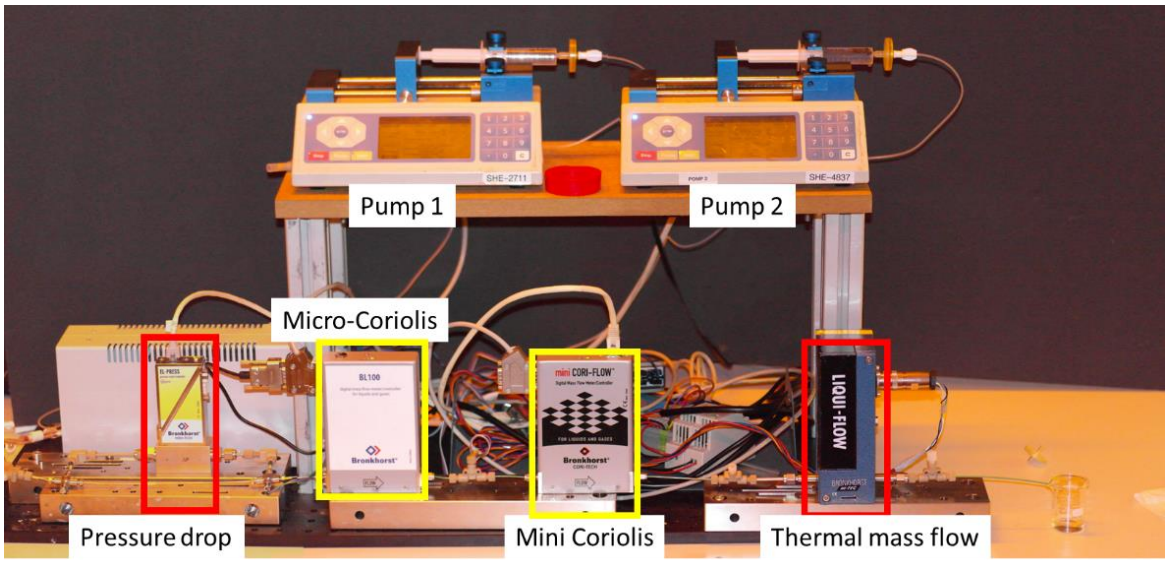

Figure 2: Overview of the multi parameter setup with two syringe pumps allowing the concentrations of binary mixtures to be changed during a measurement run. The measurement section of the setup contains a differential pressure sensor, a thermal mass flow sensor and two Coriolis sensors. The micro-Coriolis is a prototype MEMS sensor similar to the multi parameter chip being developed. All sensors were supplied by Bronkhorst HighTech BV [5].

THEORY

The chosen approach is to track medicine concentrations through their effect on the physical properties, such as density and heat capacity, of the fluid mixture. These effects are undocumented for medicines and first need to be determined for each separate medicine before mixtures can be characterized.

The density and mass-flow of a liquid can be measured directly using a Coriolis sensor, but for the other parameters of the multi-parameter sensor multiple measurement signals need to be combined (see Figure 1). The heat capacity is obtained from combining the thermal mass-flow and Coriolis mass-flow sensor and for the viscosity even three signals are used, namely differential pressure, Coriolis mass-flow and Coriolis density.

Because we are dealing with low mass fraction solutions it is expected that a linear mixing model can be used. A linear mixing model implies a linear relation between concentration and a change in physical properties as well as an adding of effects when multiple medicines are combined. Taking the density of water as the base density the total density can then be defined as follows [4]:

$$\rho_{mix} = \rho_w \left(1 + \sum_i c_{\rho i} \cdot w\%_i\right)$$

Here ρ_{mix} is the total density of the mixture, ρ_w is the density of water, $w\%_i$ are the mass fractions of the different dissolved medicines and $c_{\rho i}$ are the effects of these medicines on the density of the mixture. Similar equations exist for the heat capacity and the viscosity of the mixture.

METHODS

The current prototype of the MEMS multiparameter chip (BL100, [5]), containing only the Coriolis mass-flow and density sensor, is combined with a separate thermal mass flow sensor (LiquiFlow, [5]), and a differential pressure sensor (EL-Press, [5]), to simulate the final design of the multi-parameter sensor[1]. The medicine mixture is created by combining two separate medicine flows from two syringe-pumps [6] whose mixing ratio can be changed during the experiment (see Figure 2).

RESULTS

Initial experiments are aimed at verifying the linear behavior of the physical properties as a function of medicine concentration and to characterize the slopes of these relations. As an example Figure 3 shows the change in heat capacity as the weight

[1] The focus of this research is not the chip itself but an investigation into the feasibility of using the MEMS-chip to detect the required medicine concentrations. For further information on the workings of the chip and its ongoing development the reader is directed to other talks and posters at this conference.

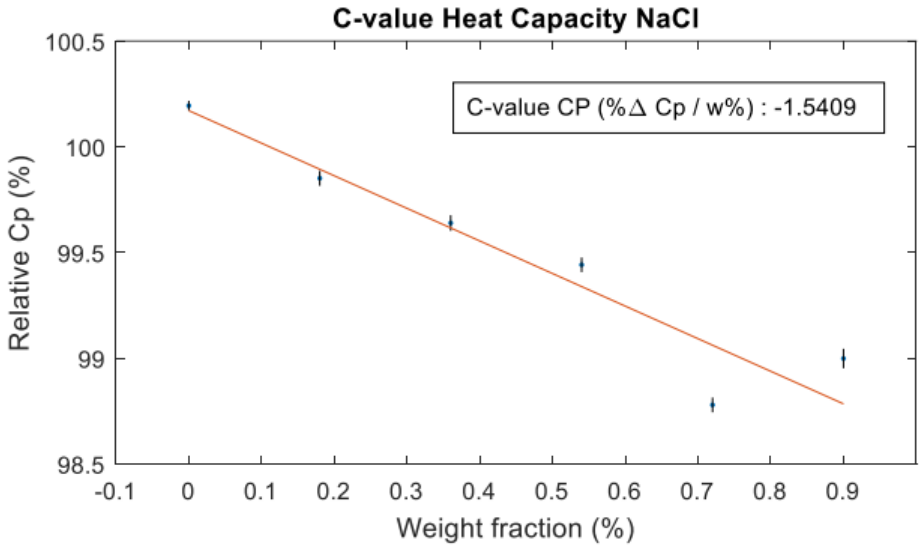

Figure 3: a measurement series showing the dependence of the relative heat capacity (with respect to pure water) as a function of the weight fraction of a medical salt solution.

fraction of NaCl in solution increases. Though the data does seem to indicate a linear effect, the scatter in the data for weight fractions higher than 0.5% is still too high. A possible reason is that heat capacity is based on the signal of two different sensors which are still situated some distance apart in our current setup. Similar measurements were performed for viscosity but the results are as of yet unsatisfactory and are thus not shown here.

In contrast, Density does show a linear relation to the mass concentration. This can be seen in Figure 4 where a 1.25% Dobutamine solution is phased out in exchange for a 4% Dopamine solution. The two pure solutions and the intermediate mixed steps show a linear trend in density indicating that the linear model holds for mixtures.

DISCUSSION

Relative heat capacity seems a useful measurement parameter as it showed a nice linear relation with weight fraction of a salt solution for fractions smaller than 0.5%. Density also has a linear relation to the mass concentration. However, similar measurements on viscosity are still unsatisfactory, probably caused by the strong temperature dependence of fluid viscosity. This effect may be reduced by integrating the pressure difference sensor into the multi-parameter sensor in order to minimize temperature gradients within the measurement section .

A second source of measurement errors is the physical distance between the three sensors from

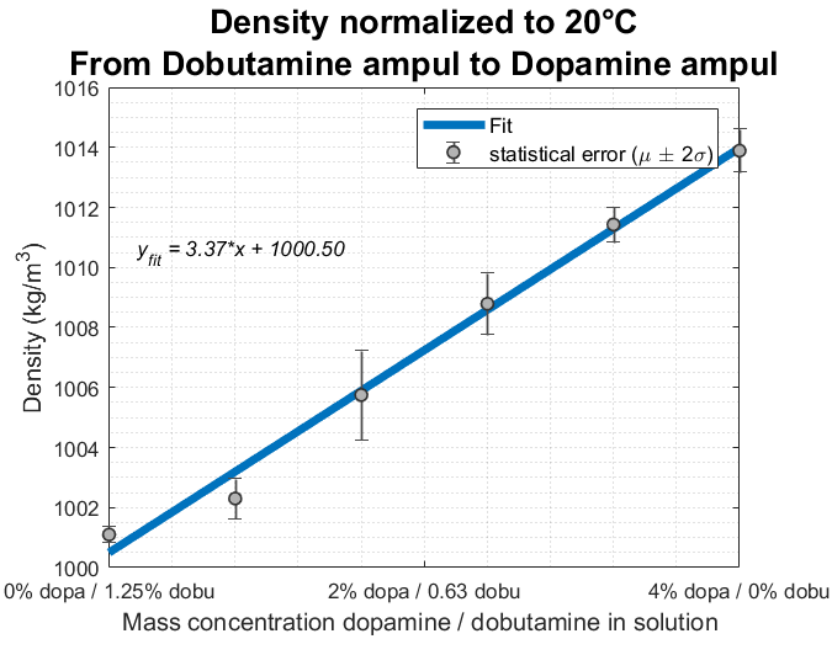

Figure 4: a measurement series showing density as a function of the concentration of Dopamine and Dobutamine. On the far left the mixture contains only Dobutamine which is linearly blended out in favor of Dopamine when moving to the right along the horizontal axis. It can be seen that in this two medicine mixture the density dependence is indeed linear. The total flow is kept constant during this measurement.

which the viscosity is calculated. Fluctuations in the composition of the flow will pass through the different sensors at different moments in time. This same effect is also present in the heat capacity measurement. Like the thermal gradient this phase shift between sensors is also expected to be significantly reduced when all sensors are combined on a single chip.

CONCLUSIONS

The linear mixing model has been shown to applicable in the medical range of medicine concentrations, both for single and binary solutions. The density and heat capacity have shown good and promising results respectively. Viscosity has been unreliable so far, probably due to temperature gradients within the setup. It is expected that on-chip integration will improve these results are gradients and delay effects will be strongly reduced.

REFERENCES

[1] A.C. van der Eijk, R.M.F.P.T. van Rens, J. Dankelman, B.J. Smit, “A literature review on flow-rate variability in neonatal IV therapy”, Pediatric Anesthesia, Vol. 23, pp. 9–21, 2013.

[2] A.M.D.E. Timmerman, B. Riphagen, J.H.G.M Klaessens, R.M. Verdaasdonk, “Confirmation of uncontrolled flow dynamics in clinical simulated multi-infusion setups using absorption spectral photometry”, Proc. of SPIE, Vol. 7556, pp. 75560U1-9

[3] J.C. Lötters, E. van der Wouden, J. Groenesteijn, W. Sparreboom, T.S.J. Lammerink and R.J. Wiegerink, “Integrated multi-parameter flow measurement system”, MEMS 2014, San Francisco, CA, USA, January 26 - 30, 2014, pp. 975-978.

[4] E. van der Wouden, J. Groenesteijn, R.J. Wiegerink, J.C. Lötters, “Multi Parameter Flow Meter for On-Line Measurement of Gas Mixture Composition”, Micromachines, Vol. 6, pp. 452-461, 2015.

[5] Bronkhorst High-Tech, Ruurlo, NL.

[6] Fusion 200, Chemyx Inc., USA.

FLOW MEASUREMENT AND CONTROL IN THE MICROFLUIDIC FLOW RANGE : LIQUID MICROFLUIDIC APPLICATIONS AND MARKET REQUIREMENTS

D.A.P. Oudejans, H.F. Luimes, J.C. Lötters
Bronkhorst High-Tech, Ruurlo, The Netherlands

ABSTRACT

This abstract summarizes a number of liquid microfluidic applications. A summary of established and emerging microfluidic applications is given and intended to give direction to microfluidic developments.

KEYWORDS

Microfluidic applications, micro liquid flow

INTRODUCTION

Liquid microfluidic flow control is a well-established technology in the industry. Besides the established applications of Liquid Chromatography, Layer Deposition, Enhanced Oil Recovery and Odorization of Natural Gas, a number of emerging applications is gaining traction. The flow rates are in the microfluidic flow range of 10 nL/min - 10 mL/min (0.6 mg/h – 600 g/h) and pressures vary from near zero to 1200 Bar. This abstract summarizes a number of established and emerging liquid microfluidic applications, in which flow measurement and control play an important role.

MICROFLUIDIC APPLICATIONS

The following liquid microfluidic applications are identified.

Established Applications
○ Liquid Chromatography
○ Layer Deposition
○ Enhanced Oil Recovery
○ Odorization of Natural Gas

Emerging Applications
○ Drug Delivery
○ Carbon NanoTubes & Graphene fabrication
○ Micro-reactor Technology
○ Organ-on-a-Chip

DESCRIPTION OF APPLICATIONS

The following pages will describe each microfluidic application one by one.

Liquid Chromatography

A well-established application in the microfluidic flow range is Liquid Chromatography (LC). This technique is used for detection of drugs, explosives and vitamins. Also environmental samples, biological samples from humans, plants and animals, cosmetics, food and beverages can be analyzed for its composition with Liquid Chromatography [1].

The so called mobile phase in Liquid Chromatography is a mixture of water and acetonitrile, methanol or other solvents that takes the sample material through a column for separation in time. Detection of the time-separated sample is for instance performed with Mass Spectrometry.

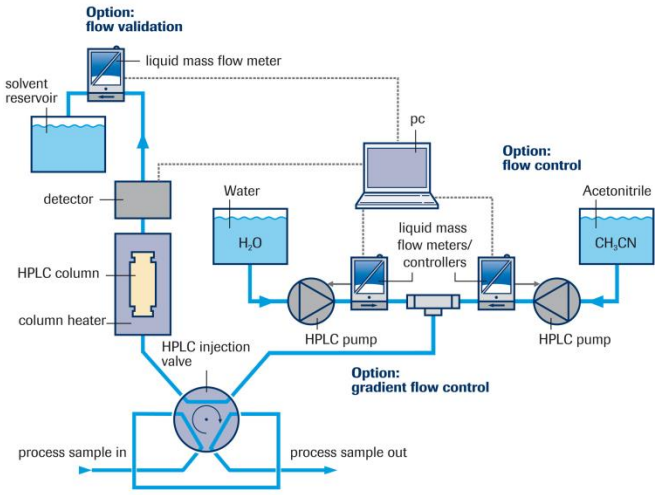

Figure 1: Schematic diagram of Liquid Chromatography equipment. High pressures and ultra-low flows are used to extract the process sample into separate components in time.

Liquid Chromatography uses pressures up to 50 Bar. High Pressure Liquid Chromatography (HPLC) is also referred to as High Performance Liquid Chromatography extends the pressure range to 1200 Bar. Flow rates are from 1 µL/min – 10 mL/min and will possibly go to lower flow rates for smaller sample volumes.

Layer Deposition

Chemical Vapor Deposition is used to deposit layers onto Solar Panels, Flat Panel Displays, Glass windows, Tools and Semiconductor substrates. Atomic Layer Deposition (ALD) and Metal Organic Chemical Vapor Deposition (MOCVD) are examples of layer deposition methods that involve low liquid flows. Liquid precursors are dosed by flow controllers, evaporated and released into a deposition

reactor. Flow rates are in the upper microfluidic range [2].

In ALD and MOCVD, precise dosing and evaporation of expensive liquids is performed. This is for layer thickness control and cost control. The liquids that are involved in ALD and MOCVD can be chemically aggressive to the instruments and tubing. The liquids are sensitive to contamination and humidity. Therefore, the instruments need to be leak-tight and chemically inert.

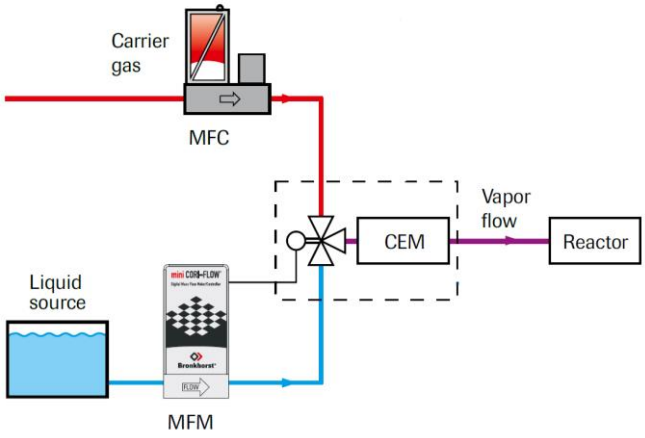

Figure 2: Schematic diagram of a vapor flow setup in which liquid is dosed in the microfluidic flow range. Vapor flow is used in Layer Deposition. A similar setup is used in Carbon NanoTubes and Graphene fabrication.

Enhanced Oil Recovery

Oil Research laboratories fine-tune their methods and chemical composition for oil extraction with microfluidic systems. Researchers use high pressure pumps, flow meters and a microfluidic representation of artificial porous rock, called a Micromodel. Known quantities of oil, water, surfactants and chemicals are injected into the Micromodel, while the output is analyzed for the quality of the extraction. Density, viscosity and electric conductivity are of interest to determine the mixture composition. Used flow rates are over the full microfluidic flow range [3].

Figure 3: Microfluidic technology is used in research of Enhanced Oil Recovery. So called Micromodels are perfused with oil, water, surfactants and chemicals.

Odorization of Natural Gas

The typical smell of Natural Gas originates from THT, which is a compound that has been added artificially to commercial Natural Gas. Its aim is to act as a 'warning agent' in case of a leakage of this highly flammable gas during transport or use. Commercial natural gas in the Netherlands has to contain at least 18 mg of THT per cubic meter gas. [4]

A master flow meter measures the Natural Gas flow and sends a signal to the mass flow controller for THT via a PLC. For Natural Gas installations in the range of 50 m^3/hour, a mass flow rate of close to 1 g/h THT is set.

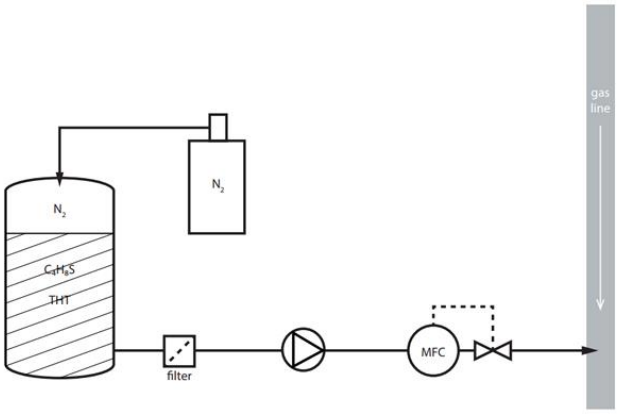

Figure 4: The liquid THT (C4H8S) is pressurized and added to a stream of Natural Gas. THT acts as a 'warning agent' with an easy distinguishable smell. Dosing is in the microfluidic flow range.

Drug Delivery

Some therapy of patients involve long duration delivery of a medicine or insulin. For instance, for insulin dosing, a basal rate of insulin is infused continuously over the day and keeps the glucose levels in range between meals and overnight. When the patient eats, he will program the insulin pump to deliver an additional insulin dose called bolus. The dosing pumps for insulin deliver basal flow rates in the order of 100 mg/h and bolus flow rates of around 5 g/h, corresponding to around 2 – 100 µL/min [5].

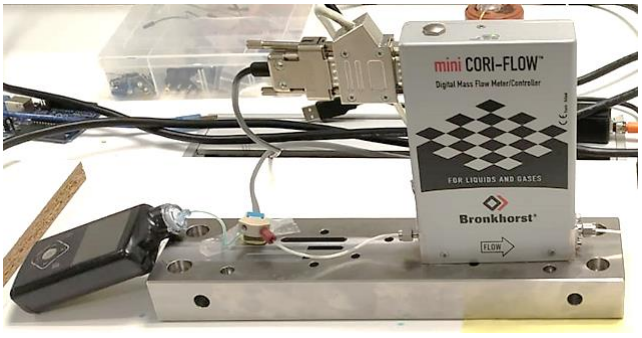

Figure 5: A medical pump in combination with a Bronkhorst CORI-FLOW microfluidic Coriolis flow meter. The large dynamic flow of each medical pump is

characterized and tested before use.

Dosing of medicine or insulin is often done with a portable pump that is carried by the patient. These pumps need to be very reliable and therefore, are characterized with microfluidic instruments.

Carbon NanoTubes and Graphene fabrication

Carbon NanoTubes and Graphene are new materials that are still under development to optimize their properties. These carbon-based materials have exceptional properties, like exceptional strength, electrical conductivity and thermal conductivity. Fabrication of these materials involve reactor furnaces. Catalyst liquid and carbon-containing liquid are evaporated to enter the reactor furnace. Liquid flows are respectively, around 50 mg/h and 5 g/h. The fiber or sheet materials is extracted from the furnace for post-processing. The setup of Figure 2 is applied and Figure 6 shows an artistic impression of the molecular structure of a Carbon NanoTube fiber [6].

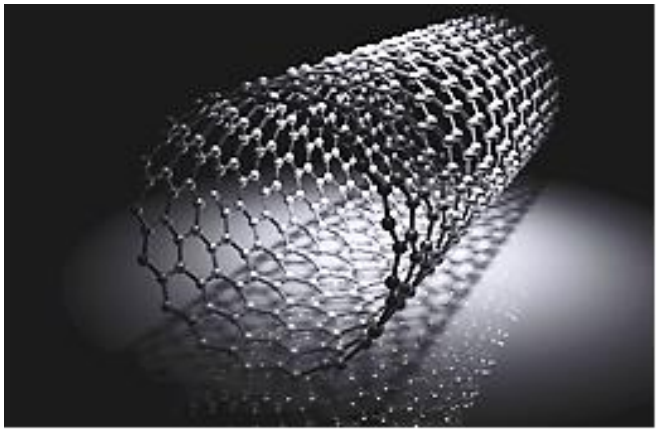

Figure 6: Artist impression of a Carbon NanoTube fiber. Carbon NanoTube fiber is a relatively new material. It has exceptional strength, electrical and thermal properties. Fabrication involves ultra-low flow catalyst dosing and microfluidic dosing of the liquid carbon source.

Micro-reactor technology

Development and scale up of a chemical reaction processes is time consuming. Fast optimization of process parameters with controlled reaction times in a micro-reactor is accomplished by accurate flow rates, pressure and temperature in an enclosed system, without interaction of the environment. Micro-reactor technology is applied in chemical analysis and chemical synthesis [7].

Nearly 90% of processes are still done in batch, despite the many challenges and drawbacks of this technology. However, due to promising advances in flow chemistry, it is becoming the processing technique of the future.

Micro-reactors are also called Lab-on-a-Chip and should be constructed from chemically resistant materials. Flow rates are in a range of 1 µL/min – 10 mL/min.

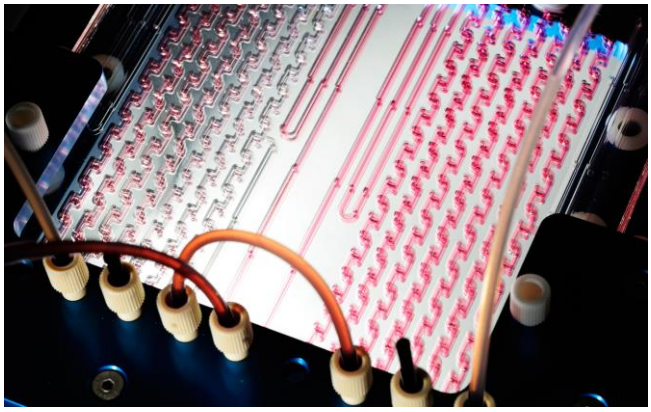

Figure 7: Micro-reactor, as used in flow chemistry. It is used for fast optimization of chemical reaction processes.

Organ-on-a-Chip

Organ-on-chip is a variant of Lab-on-a-Chip. Artificial organs of humans are grown on transparent fluidic plates for enabling drug discovery. Avoiding animal testing and faster and more accurate medicine testing are large arguments for using this technology. Another promise of this technology is to be able to develop personalized medicines.

The continuous flows of biological liquids within an Organ-on-a-Chip, in combination with stem cells from a stem cell bank or a specific patient, are used to create an artificial Organ.

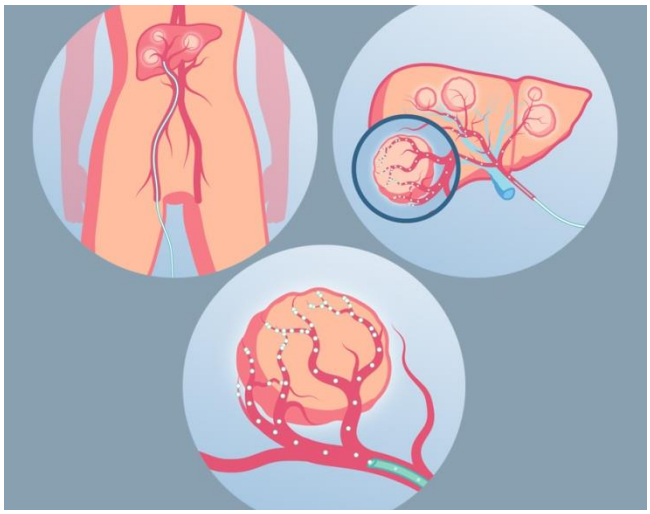

Figure 8: Human organs are now simulated by Organ-on-a-Chip models. Microfluidic liquid flows of body fluids are combined with medicines and nutrition to study their effect on a specific organ.

Examples of human organs that are being developed are Gut-on-a-chip, Lung-on-a-chip, Liver-on-a-chip, Skin-on-a-chip, Heart-on-a-chip, Intestine-on-a-chip, Kidney-on-a-chip, Thrombosis-on-a-chip, Neural or cardio-vascular networks-on-a-chip. Another example is Digestion-on-a-Chip [8]. The Gastrointestinal Tract is simulated. Saliva, gastric juice and bile are dosed in artificial mouth, stomach and intestine.

Silicone gel (PDMS), glass, Silicon and plastic (COC, PMA) are materials of choice. Controlled flow rates are between 0.1 – 100 µL/min (6 mg/h – 6 g/h). Sensors for temperature, pH, Oxygen and Carbon Dioxide concentration are desired. Heaters and valves are sometimes integrated.

MARKET REQUIREMENTS

Below information is gathered from customer communications and mentioned references.

With flow measurement and control in mentioned applications, true mass flow or true volume flow indication is much desired. Coriolis flowsensors offer liquid-independent mass flow, as opposed to thermal flowsensors, but are not yet available over the full microfluidic flow range.

Especially for desktop equipment, miniaturization and cost reduction of sensing instruments are required for next generation equipment, while accuracy, chemical compatibility, pressure resistance and liquid-independency are not compromised or even improved. This applies for HPLC and Life Science markets, like the Organ-on-a-Chip market.

Other challenges are integration of miniature sensors into micro-reactors and Organ-on-a-Chip microfluidic plates to be able to measure directly at the location of interest.

- **The microfluidic flow range is roughly defined to be 10 nL/min - 10 mL/min (0.6 mg/h – 600 g/h).**
- **Flow measurement, preferably liquid-independent.**
- **Pressure measurement**
- **Depending on the application, it is also desired to measure temperature, density, viscosity, electrical conductivity, pH, Carbon dioxide, Oxygen concentration or other parameter to determine the content of the microfluidic sample.**
- **Ripple-free flow of liquids.**
- **Gas bubble-free flow of liquids.**
- **Large dynamic range of flow and pressure measurement.**
- **Low dead volume and low volume of the microfluidic system.**
- **For chemically aggressive applications, glass, PEEK, Radel, Teflon, Tefzel, 316L, Stainless Steel, Hastelloy C-22 steel, MP35N steel, Si_3N_4, Al_2O_3 wetted materials are desired.**
- **High pressure resistance within Liquid Chromatography (1200 Bar) and Enhanced Oil Recovery (200 Bar).**
- **100 – 250 µm diameter channels and internal diameter of tubing. Large diameters up to 250 µm are used to be able to work with emulsions and cells and reduce pressure drop.**

CONCLUSIONS

Liquid microfluidics is an active multidisciplinary field in research and industry with established and emerging applications. This fact indicates the need for suitable instrumentation and methods in this field.

The collected information about microfluidic applications and market requirements is summarised to give direction to technical development in this field.

REFERENCES

[1] “The LC Handbook” by Agilent, 2016.

[2] www.bronkhorst.com
Bronkhorst “Semiconductor Market” brochure.

[3] Sekhar Gogoi, Subrata Borgohain Gogoi, “Review on microfluidic studies for EOR application”, Journal of Petroleum Exploration and Production Technology, 2019.

[4] “Working with odorants (THT)” by GasUnie, 2015.

[5] S.Girardot, F.Mousin, J.Vezinet, P.Jacquemier, S.Hardy, JP.Riveline, “Kalman filter-based novel methodology to assess insulin pump accuracy”, Diabetes Technology & Therapeutics, 2019 Jul 23.

[6] www.bronkhorst.com
Bronkhorst Blog “Controlled fabrication of Carbon Nanotubes : material of the future” by John Bulmer.

[7] Sebastiaan van den Broek, René Becker, Kaspar Koch and Pieter J. Nieuwland (Future Chemistry), “Micro-reactor technology: Real-time Flow Measurements in Organic Synthesis”, Micromachines, March 2012.

[8] Pim de Haan, Margaryta Ianovska, Klaus Mathwig, Glenn van Lieshout, Vassilis Triantis, Hans Bouwmeester, Elisabeth Verpoorte, “Digestion-on-a-Chip: a Continuous-flow Modular Microsystem Recreating Enzymatic Digestion in the Gastrointestinal Tract”, Lab on a Chip, 2019 Apr 23.

CORIOLIS MASS FLOW METERING TRACKING RAPID FUEL INJECTION PULSE TRAINS IN INTERNAL COMBUSTION ENGINES

M.P. Henry[1,2] and F. Leach[1]
[1] University of Oxford, Department of Engineering Science, Oxford, UK.
[2] South Ural State University, Chelyabinsk, Russian Federation.

ABSTRACT

A previous MFHS presentation described the tracking of rapid fuel injections (as short as 1 ms) in a diesel internal combustion engine laboratory rig using Coriolis mass flow metering and Prism Signal Processing (PSP). This presentation provides an update on this work. Petrol/gasoline engines operate at lower pressures, but may be subject to higher levels of mechanical noise. Additional PSP filtering techniques are required to remove unwanted noise sources to reveal the fuel pulses. Where fuel pulses are significantly shorter than the resonant frequency of the Coriolis flowtube, flow measurements are subject to systematic distortions that require further investigation.

KEYWORDS

Coriolis mass flow metering; Prism Signal Processing; Internal combustion engine; fuel injection; Coriolis dynamic response.

INTRODUCTION

A presentation at MFHS 2017 [1] outlined the application of Prism Signal Processing (PSP) [2, 3] to the tracking of Coriolis meter signals for fast fuel injection monitoring in internal combustion engine laboratory rigs [4]. PSP is an alternative approach to FIR filtering, replacing the conventional convolution calculation with a set of Fourier-style double integrations that can be performed recursively. The resulting technique offers the benefits of FIR calculation – numerical stability and a linear phase response – combined with the low computational burden normally associated with IIR filtering. In addition, the Fourier-style calculation means that the equivalent of filter coefficients are simply linearly-spaced sine and cosine values so that design costs are negligible. Overall, PSP offers a fast and flexible toolset for instrumentation in the era of the Internet of Things [2].

In this paper, we report our experimental findings working with fuel injection systems for petrol (gasoline) powertrains. Basic challenges include high pressure requirements (30 MPa or more), high levels of mechanical noise, and fuel injection events as short as 1 ms. While PSP enables 48 kHz real-time flow measurement updates using modest computational resources, greater challenges arise with transducer operation and the need for traceable calibration facilities.

Firstly, the design of a PSP notch filtering scheme is described which enables the successful tracking of 1ms fuel pulses, despite the high levels of mechanical noise in the experimental system. Secondly, more detailed results are presented which show that where the fluid pulse length is shorter than the resonant period of the flowtube, the observed phase difference (related to the mass flow rate) is not repeatable. It is conjectured that the instantaneous phase of the flowtube oscillation is influential on the observed phase difference in these circumstances. Finally, further steps are proposed for improving measurement quality through higher resonant frequencies for flowtubes and developing a traceable calibration facility for short injection events.

NOTCH FILTER DESIGN

Coriolis mass flow metering entails passing the fluid to be measured through a flowtube, which oscillates at the resonant frequency of a natural mode of vibration. Two sensors monitor the flowtube vibration, whereby the phase difference between the sensor signals at the resonant frequency is proportional to the mass flow rate of the fluid.

Typically, Coriolis flowtubes have a high Q factor, resulting in sharp spectral peaks at the resonant frequency and its harmonics. Other modes of vibration of the flowtube may be excited by external mechanical noise, but these effects are usually small, and a number of mechanical and signal processing techniques have been developed to minimize the effect of off-resonance noise on the flow measurement in conventional circumstances.

In the case of the fuel injection process, exceptionally high levels of noise are present in one of the sensor signals (note that both sensor signals have similar properties and here are subject to the same filter design). Figure 1 shows two spectra. The green spectra shows the unfiltered sensor data. The peak at around 150 Hz corresponds to the resonant mode of vibration of the flowtube. All the other peaks represent undesired modes of vibration belonging either to the flowtube itself (and excited by system vibration) or the external experimental system. Here 1 ms fuel pulses are being supplied at intervals of 40.15 ms.

The signal processing problem is two-fold. One the

one hand, all spectral peaks other than the desired mode of vibration must be suppressed in order to obtain the desired phase difference measurement. On the other hand, the dynamic response of the signals must be preserved sufficiently to detect the 1ms fuel injection events. This requirement rules out simply applying a narrow bandpass filter around the desired vibration mode, for example.

A cascaded set of Prism-based Dynamic Notch Filters (DNF) [2] has been used to target each of the spectral peaks marked with a circle. The resulting filtered signal is shown in blue in Figure 1, where the desired peak is preserved while all other peaks have been attenuated. Figure 2 shows the Prism-based notch filter design, which targets eight frequency peaks. The conference presentation will explain the design of this filter, and a more detailed explanation will be provided in a future journal publication.

Figures 3 and 4 show the corresponding phase difference measurement calculated from the two sensor signals, with and without the notch filtering, respectively. In Figure 3, with the unfiltered sensor data, the presence of high levels of noise masks the pattern of fuel impulses. In Figure 4, the sharp and regular flow peaks corresponding to the fuel pulse train are clearly observed. Note that the peak values in Fig 4, of around 0.35 degrees, are significantly lower than the noise amplitude in Figure 3, which is around ± 2 degrees: without filtering, it would not be possible to discern the peaks within the noise.

Although Figure 4 represents a significant improvement over Figure 3, there are still many issues to be resolved. A more detailed plot of an individual pulse would show that each 1 ms injection has been extended in duration to around 10 ms – this is believed to be due to the filtering action of both the signal processing and the flowtube. However, yet more significant difficulties arise, as discussed in the next section.

EXPERIMENTAL RESULTS

Further measurement problems may occur when, as in this case, the duration of a flow 'batch' is significantly shorter that the period of oscillation of the Coriolis flowtube. The problem is illustrated by the different behaviours shown in figures 5 and 7 (with details of each in figures 6 and 8 respectively). Both sets of results were obtained from the same Coriolis meter installed in a petrol/gasoline injection test rig (as described in [5]). The system uses a commercial Coriolis flowtube, rated for high pressure, oscillating at approximately 150Hz, and working with a prototype transmitter. The transmitter provides real-time PSP-based tracking of the amplitude of each sensor signal (among other parameters) and the phase difference between them.

In Figure 5 (with details shown in Figure 7), the pulse duration is 1.5 ms while the interval between the pulses is 40.15 ms, corresponding to exactly 6 periods of oscillation of the flowtube. The individual fuel pulses are clearly distinguishable via the phase difference measurement and show good repeatability. As Figure 7 shows, the peak height of each pulse is approximately constant, and the phase difference between pulses settles towards zero degrees, as would be expected. Around t = 15.5 s in Figure 5, a disruption in the phase difference measurement occurs: this corresponded to an audible 'misfiring' of the fuel injector during the experiment. Accordingly, this is interpreted as the system correctly detecting a true change in the flow behaviour. Note that the sensor amplitudes also adopt a specific and repeatable pattern of behavior, reflecting the response of the flowtube oscillation to the regular series of short fuel pulses.

The pattern of behavior shown Figure 6 (with details given in Figure 8) is very different to that of Figure 5, but experimentally, the only difference is that the time between pulses has been slightly increased to 40.3ms, so that it is no longer an integral number of flow tube periods. The repeatable behavior of Figure 5 is replaced with complex, essentially sinusoidal, variation for the observed amplitudes and phase difference, where pulse-to-pulse repeatability is poor. Note in particular in Figure 8 that the 'zero offset' of the phase difference measurement varies by ± 0.5 degrees, while the relative height of each flow pulse also varies over the sinusoidal trend. Analysis suggests the variations observed are a function of the flowtube phase when each fluid pulse arrives. In the case of Figure 5, as the interval between pulses is a whole number of flowtube resonant periods, repeatable behavior is observed. However, requiring such pulse intervals would place an unrealistic constraint on the operation of an engine. For the more general case, as shown in Figure 6, poor repeatability is observed due to flowtube phase shifts between fuel injections.

NEXT STEPS

Modelling and optimization of flowtube dynamics with short flow pulses may yield improved measurements techniques for this and similar applications.

However, a clear way to improve repeatability over arbitrary pulse intervals is to increase the resonant frequency of the flowtube. We have commissioned the construction of a high frequency flowtube suited for this application, and hope to report on experimental results obtained with this system in due course. We see great potential for micro-machined, high frequency, Coriolis transducers, if the pressure and vibration

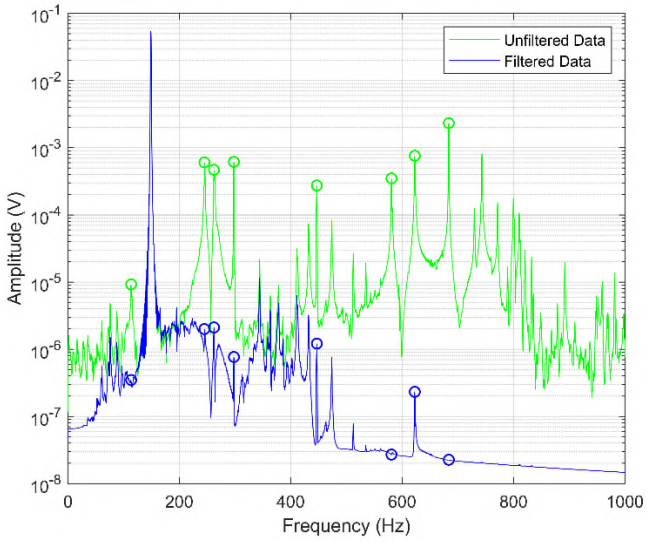

Figure 1: Coriolis sensor data frequency spectrum with and without Prism notch filtering. Notched frequencies are marked with a circle

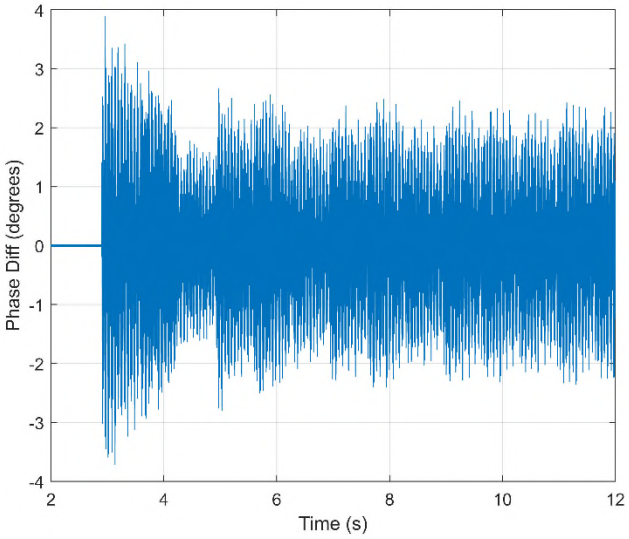

Figure 3: Phase difference measurement based on unfiltered sensor data.

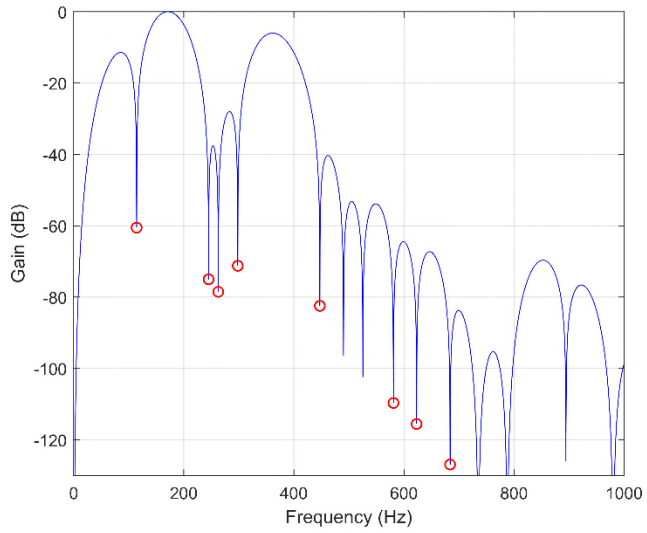

Figure 2: Design of Prism-based notch filter.

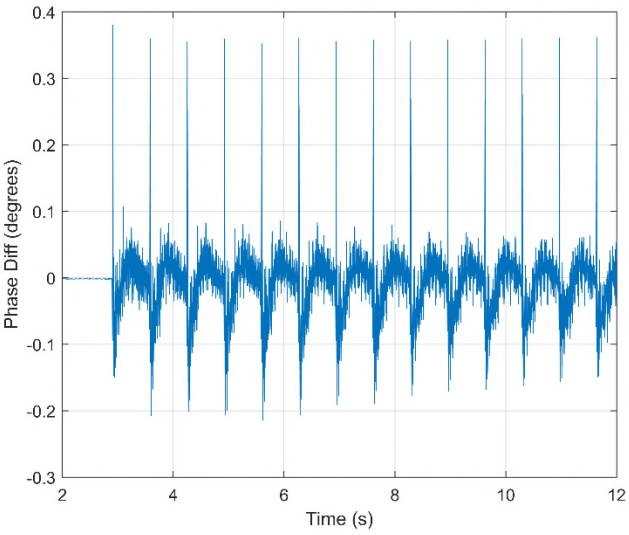

Figure 4: Phase difference measurement based on filtered sensor data.

challenges can be addressed. With, say, a resonant frequency exceeding 10 kHz, measurement updates can be provided at 100 kHz or higher using PSP. It is likely that with a higher resonant frequency, a simpler signal processing scheme could be used, as most noise sources would be far from the resonant frequency of the flowtube. However, even if a signal processing scheme of similar complexity is required, both the flowtube and signal processing dynamics would be scaled by the resonant frequency of the flowtube, so that the non-repeatability issue illustrated here would be significantly reduced or eliminated.

A further challenge to the development of Coriolis metering for fast injection applications is the provision of traceable mass flow measurement standards for instrument calibration.

The authors have completing a survey on behalf of TUV-NEL to gauge industry requirements for calibration in this domain, and will provide a brief summary of the findings at the conference.

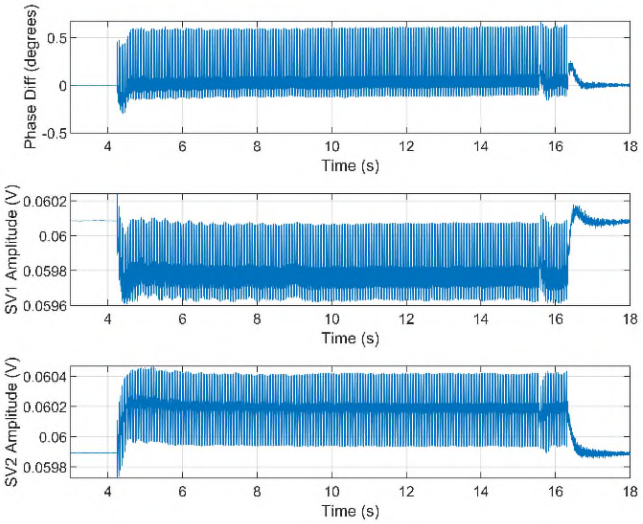

Figure 5: Phase difference and sensor amplitudes for fuel injection pulse train where the injection interval is set to 40.15 ms i.e. exactly 6 flowtube oscillation periods.

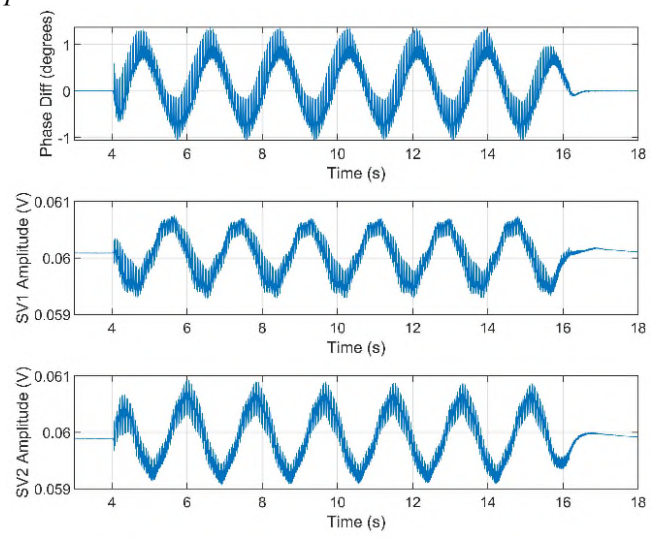

Figure 6: Results where the injection interval is 40.3 ms i.e. not a whole number of flowtube oscillation periods.

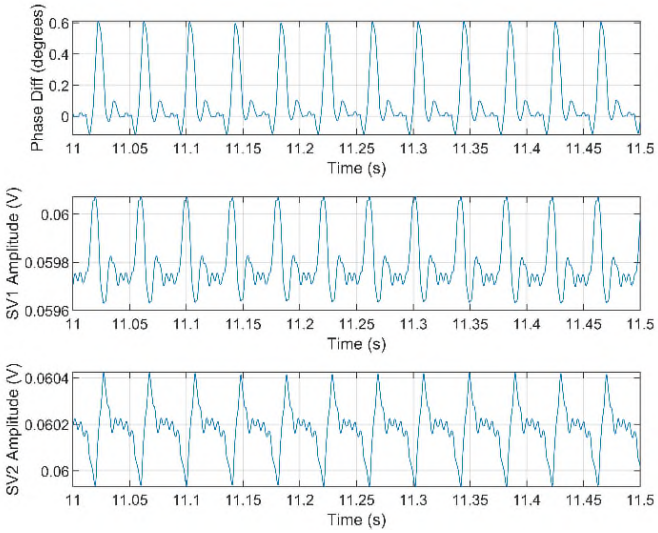

Figure 7: Detail from Figure 5, with reduced timescale.

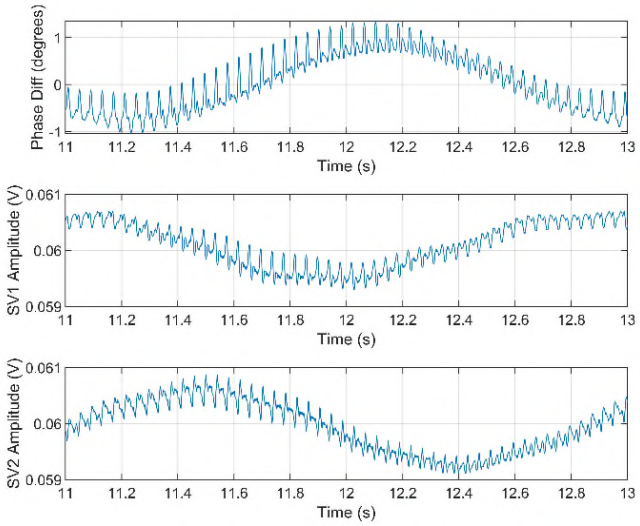

Figure 8: Detail from Figure 6, with reduced timescale.

REFERENCES

[1] Henry, MP. "Prism Signal Processing: A Recursive FIR Technique Applied to the Efficient Tracking of Resonant Sensor Systems", 3rd International Conference on Microfluidic Handling Systems, Enschede, Holland, October 2017.

[2] Henry, MP, Leach, F, Davy, M, Bushuev, O, Tombs, MS, Zhou, FB and Karout, S. "The Prism: Efficient Signal Processing for the Internet of Things", IEEE Industrial Electronics Magazine, 2017. http://dx.doi.org/10.1109/MIE.2017.2760108.

[3] Henry, MP. "The Prism: recursive FIR signal processing for instrumentation applications". IEEE Transactions on Instrumentation and Measurement, 2019. http://dx.doi.org/10.1109/TIM.2019.2916943.

[4] Leach, F, Karout, S, Zhou, FB, Tombs, MS, Davy, M and Henry, MP. "Fast Coriolis mass flow metering for monitoring diesel fuel injection", Flow Measurement and Instrumentation, 58 (2017). http://dx.doi.org/10.1016/j.flowmeasinst.2017.09.009.

[5] Leach, F. Davy, M, Henry, MP, Malladi, M, Tombs, M, Zhou, F. "Fast NGC: A New On-Line Technique for Fuel Flow Measurement," SAE International Powertrains, Fuels and Lubricants Meeting, 2019.

CONTACT

* M.P. Henry, manus.henry@eng.ox.ac.uk

LOW CAPACITANCE MEASUREMENT SYSTEM FOR INDUSTRIAL-SCALE MULTICHANNEL TESTING

A. Bonilla Fernandez, D. Alveringh, E. van Dam, S. Schepers, P. Senff and E. Kloekke
Salland Engineering (Europe) BV, Zwolle, The Netherlands

ABSTRACT

The need to measure lower capacitance is growing as more devices are now using this readout method. However, measuring such low capacitance at mass production level is not an easy task due to the complex setup it requires. In this paper, a proof-of-concept of such low capacitance meter was implemented. Our aim was to check the feasibility of incorporating it into an Automatic Test Equipment (ATE), so that we can evaluate devices in parallel. Using the ATE's standard interfaces for testing avoids building custom-made test setups for future chips that need low level capacitance measurements. This means that the Device Under Test (DUT) has to be located at a relatively long distance from the measurement system; which is not an ideal situation when measuring low-level signals. The characterization of our designed capacitance meter shows that it has a range from 0pF to 7.5pF (differential), a measurement accuracy of $\pm$5 fF and a resolution $<$1fF (theoretically 40aF). The first version of the meter can work with carrier frequencies from 80kHz up to 300kHz. Furthermore, experiments show that the DUT can still be measured up to a distance of 1.6m from the meter, with predictable gain corrections. This means that the measurement system can be implemented into a multichannel instrument for an ATE, far enough from the test point. Based on our work, we conclude that it is feasible that this technology enables optimized testing procedures for multiple MEMS devices.

KEYWORDS

Low capacitance measurement, capacitance readout, low level, meter, ATE, multi channel testing instrument.

BACKGROUND

The use of MEMS devices is continuously growing. Nowadays, one of their biggest applications is in the sensing field, where MEMS are used in pressure sensors, accelerometers, gyroscopes, inertial combos, etc [1]. For such sensors, a capacitive readout is preferred in many cases due to its advantages, which include low temperature coefficients, low power dissipation, low noise and low-cost fabrication [2]. One of the main challenges of MEMS devices' fabrication is the fact that high-volume testing normally requires custom-made test set-ups [3]. This is due to the complexity of multi-domain systems. This is further complicated if the chosen testing setup requires that the DUT is located at a relatively long distance from the measurement system; which is not an ideal situation when measuring low-level signals [4].

Low Capacitance Measurement Setups

There are many ways to build a low capacitance measurement setup. In this subsection we present a non-exhaustive list of some of the most common ones.

- Separate equipment: The typical arrangement of this kind of setup consists of a waveform generator, phase inverter, charge amplifier, filter, lock-in amplifier, oscilloscope, among others [5] [6].
  - *Advantages:* It can be used for both dynamic and static measurements.
  - *Disadvantages:* It can become a complex setup due to the number of devices involved.
- LCR Meter: This is normally an off-the-shelf device used to measure the capacitance, conductance, or inductance [7].
  - *Advantages:* Single off-the-shelf equipment.
  - *Disadvantages:* It only is capable of measuring a single channel; it is a quasi-static meter, therefore not useful for dynamic measurements; and it has a high price range.
- Specialized tester: This normally presented as a wafer probe test head module. It has various configurable mixed-signal tester resources that support the characterization of MEMS devices. An example of such a device is the STI3000 Wafer Probe Test System by Solidus Technologies, Inc. [1]
  - *Advantages:* Integrated system with accurate dynamic and static measurements.
  - *Disadvantages:* Large size, high price range and a limited number of channels.

It is possible to see that the more integrated measurement setups have very interesting advantages such as accurate dynamic and static measurements. However, there are still some improvements that could be done with regards to the size; number of measured channels, which is usually around 4; and desirably the price range. In this work, we implemented a proof-of-concept to check the feasibility of integrating a low capacitance measurement into an ATE. For this proof, special attention has been paid to the distance between both the paired DUT & measurement system and the multichannel instrument implementation. The aim of our work is to optimize the testing procedure for a wide range of MEMS devices, keeping the aforementioned advantages and improving on the areas of opportunity.

[1] STI3000 Wafer Probe Test System by Solidus Technologies, Inc. `http://www.solidustech.com/STI3000ETestHead.html`

DESIGN AND FABRICATION

The implemented capacitance meter uses charge amplification to sense the capacitance (output signal) from the DUT. A block diagram of the complete system is shown in Figure 1. Each channel has a square wave generator that creates the carrier signal (DUT input) which can have frequencies between 1kHz and 60MHz, and an amplitude of $\approx$ 2V. By having independent reference frequencies, several channels can measure different capacitances from the same MEMS device simultaneously. The output of the charge amplifier is fed into a Lock-In Amplifier to filter noise, by neglecting signals with frequencies different from the carrier signal [5]. Since a square-wave is used, optimization of the low pass filter (LPF) is needed to remove the AC components and avoid crosstalk between channels [8]. The LPF output signal is the Analog to Digital Converter (ADC) input. The capacitance value is shown and stored in a Graphical User Interface (GUI). The design was kept as simple as possible to obtain a small PCB footprint, and make easier the integration into a multichannel instrument.

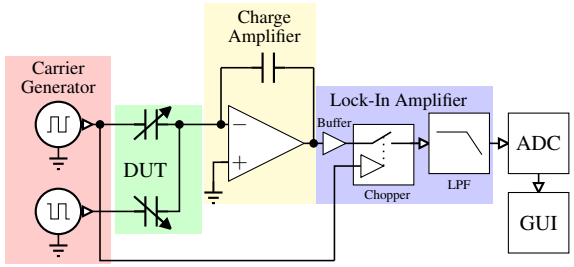

Figure 1: Block diagram for designed capacitance meter.

EXPERIMENTAL RESULTS

For the characterization of the capacitance meter, measurements where executed on fixed value capacitors located directly on a DUT PCB (0 cm from meter). Taking into account the manufacturer tolerance of 20%, all the measurements were successful. The results are shown in Figure 2.

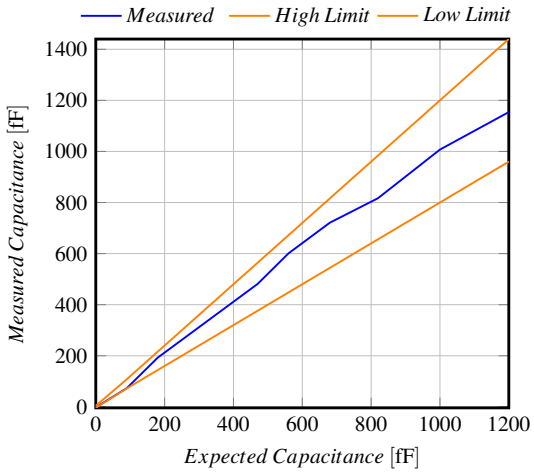

Figure 2: Measured Capacitance, High Limit and Low Limit vs Expected Capacitance. Measurements executed on 0, 90, 180, 470, 560, 680, 820, 1000 and 1200 fF capacitors with ±20% tolerance.

Knowing the accuracy of the meter, the influence of the distance between the DUT and the meter was analyzed. Figure 3 shows the decrease in amplitude, where 0% is obtained when the distance is 0cm. The gain percentage drop has a linear behavior of 0.35%/cm, and it is independent of the capacitance being measured.

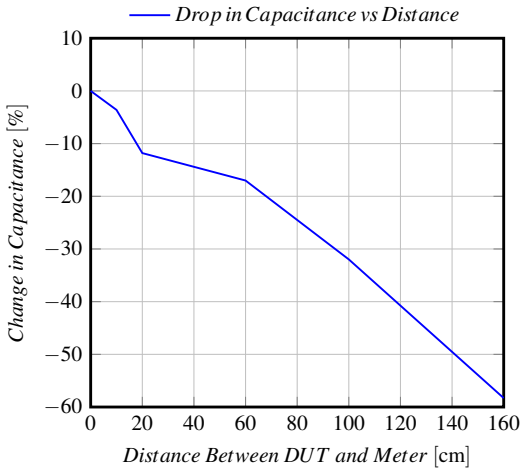

Figure 3: Change in measured capacitance vs distance between DUT and measurement system. The reason of the jump from 10 cm to 20 cm and from 20cm to 60 cm is that scrap coax cable used, while the cables used for the 60cm, 100cm and 160cm have standard commercial connectors.

During experiments with long cables the measurements showed a noise signal at 50Hz frequency, and with an amplitude of approximately +70fF. However, by using a light EMI shield, shown in Figure 4, it was possible to get rid of most of the noise present and execute good quality measurements, at up to 1.6m distance, with a noise amplitude of ±7fF for the final capacitance value. Figure 5 shows the original measured value at a long distance and the value after compensation for drop in amplitude with a fixed gain in the capacitance calculation.

One of the main requirements to measurement different capacitances at the same time is to be able to generate different carrier frequency for each DUT. Thats why the low capacitance meter was tested at different carrier frequencies. First to check the performance of the wave generator and second to characterize the bandwidth of the measurement stage. Figure 6 shows the results of an experiment with a 1.2pF capacitor. This test was repeated for several capacitances obtaining similar results. where the system has a linear behavior between 100kHz and 300kHz. The drop in measured magnitude is caused by the delay in the charge amplifier that is not able to process the input signal fast enough.

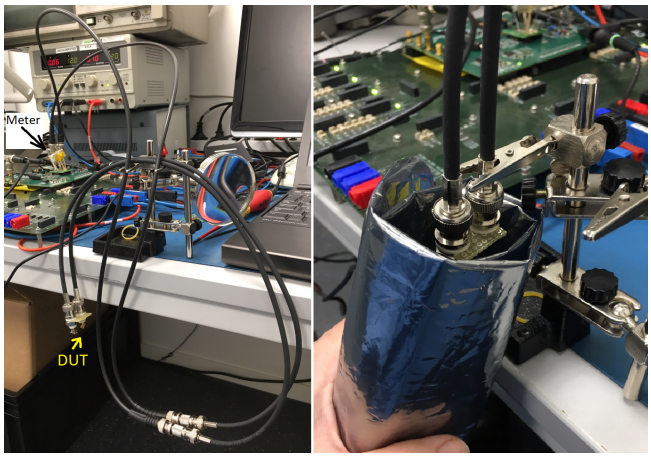

Figure 4: Left: Experiment setup using 1.6m coax cable between DUT and Capacitance Meter. Right: Shielding DUT with an ESD bag

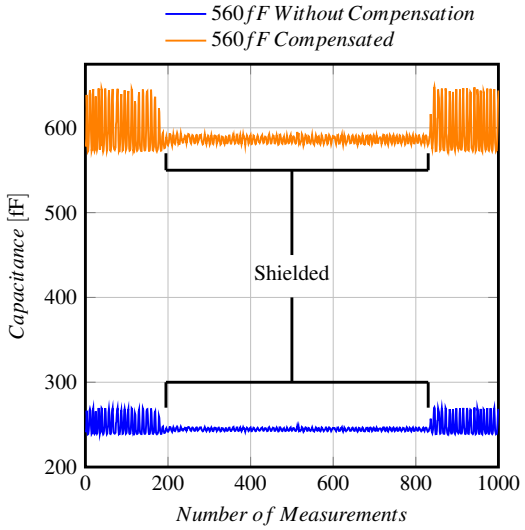

Figure 5: Capacitance measurement through 1.6m coax cable without (Blue) and with gain compensation (Orange). Also showing the effect of having and not having a shield against EMI.

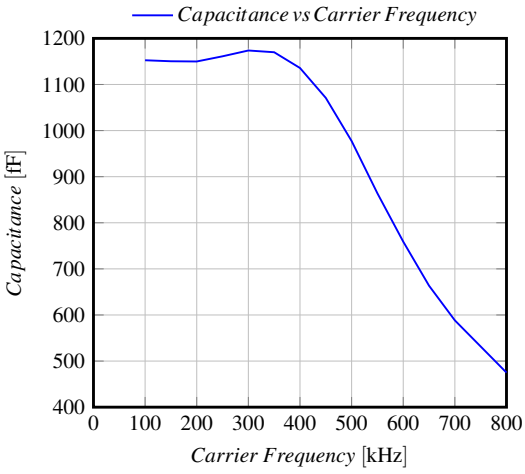

Figure 6: Change in measured capacitance vs carrier frequency for a 1.2pF capacitor.

The influence of the temperature changes in the measured capacitance was also explored; by increasing the temperature of the critical components in the amplification and filtering stage. The worst case scenario registered was a change in capacitance of 1.3% /°C of the expected value. Thus, if the meter is located in a controlled temperature environment, or inside a cabinet with constant air flow the repeatability of the measurements will not be an issue.

Finally, the meter was tested with an actual MEMS device, shown in Figure 7. This MEMS has the features of electrostatic actuation and two channels with differential capacitance readout, but its specifications were unknown. Thanks to the experiments it was possible to determine its resonance frequency. First, a square wave of 50V amplitude was used to drive the mass, Figure 8, showing mechanical vibration (ringing) at the resonance frequency. Later it was checked by driving the device with a sinusoidal wave at different frequencies (10Hz to 3kHz) and looking at the amplitude magnitude.

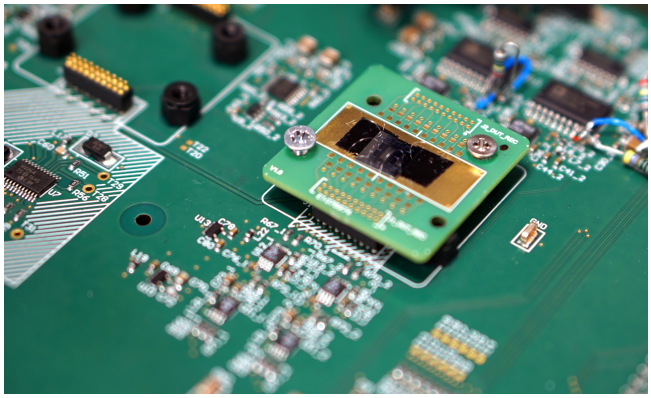

Figure 7: MEMS device on DUT PCB mounted on the low capacitance meter POC board.

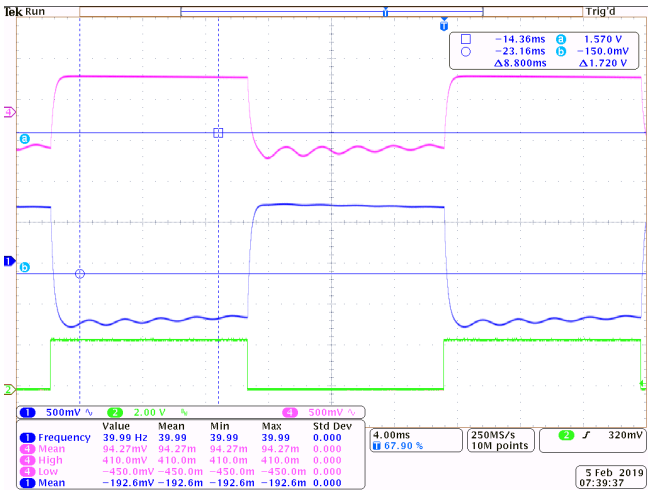

Figure 8: Blue: channel with capacitance increment in device with negative carrier. Magenta: channel with capacitance increment in device with positive carrier. Green: Actuation signal (before amplification).

CONCLUSIONS AND FUTURE WORK

A low capacitance meter based on charge amplification was presented. It was designed and fabricated to demonstrate the possibility of integrating it into a multichannel (high density) instrument to measure capacitance's in parallel and make the test procedure of devices with such readout more efficient. During experiments it was possible to measure capacitance's $<$10fF ($\approx$2fF) up to 7pF with a linear and repeatable behavior. The measurement system has a dynamic range of 1:3500 and a resolution of 40aF; and has a wide flexibility in generating different carrier frequencies to avoid cross talk between channels. The noise detected during experiments can be neglected when several measurements are averaged.
One of the constraints for a greater flexibility is the limited charge amplifier bandwidth. Because of this, we are already working on the next version where we will try to increase the accepted carrier frequency up to 2MHz, as the results from simulations shown in Figure 9 demonstrate.

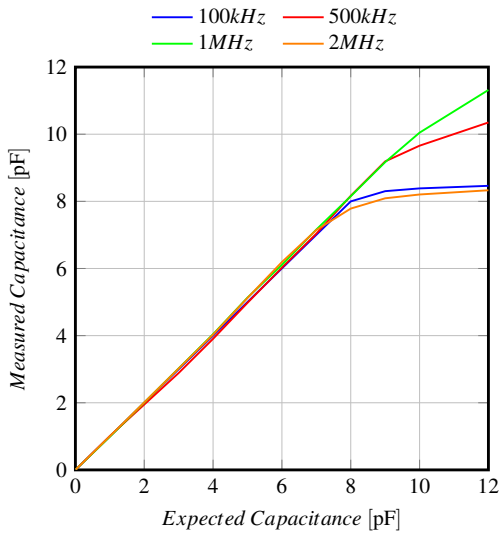

Figure 9: Simulations for measured capacitance vs expected capacitance at different frequencies to the check performance of charge amplifier with modifications to achieve higher bandwidth.

Having different carrier amplitudes is another desirable feature, at least four different will be implemented. And finally, a capture function will be added to create a sort of digital oscilloscope, and avoid the need of external equipment when executing dynamic measurements.

ACKNOWLEDGEMENTS

We thank the MESA+ Institute for Nanotechnology of the University of Twente for their support providing MEMS devices to test the dynamic behavior of our measurement system. And the Province of Overijssel for its support through the STTH subsidy.

CONTACT

*A. Bonilla Fernandez, armando.bonillafernandez@salland.com

REFERENCES

[1] E. Mounier, C. Troadec, G. Girardin, Y. de Charentenay, "MEMS Markets - Status of the MEMS Industry 2015. Market and Technology Report", Yole Développement.

[2] J. Wu, "Sensing and Control Electronics for Low-Mass Low-Capacitance MEMS Accelerometers", Ph.D dissertation, Elect. and Computer Eng., Carnegie Mellon University, 2002.

[3] H. Kerkhoff, "Testing of MEMS-based microsystems", Brain Research Reviews, Vol. 2005, pp. 223-228, 2005.

[4] Keithley Instruments Inc., "Low Level Measurements Handbook", 6th edition, Keithley Instruments Inc., 2004.

[5] D. Alveringh, "Integrated Throughflow Mechanical Microfluidic Sensors", Ph.D dissertation, MESA+ Institute for Nanotechnology, University of Twente, Enschede, April, 2018.

[6] R. A. Brookhuis, "Miniature force-torque sensors for biomechanical applications," Ph.D. dissertation, University of Twente, Netherlands, 10 2014.

[7] G. Lucovsky, V. Misra, in Encyclopedia of Materials: Science and Technology, 2001.

[8] S. Zhang, G. Li, L. Lin, J. Zhao, "Optimization of a digital lock-in algorithm with a square-wave reference for frequency-divided multi-channel sensor signal detection", Review of Scientific Instruments, Vol. 87, 085102, 2016.

CHALLENGES IN ACHIEVING OPTIMUM PERFORMANCE IN MICROFLUIDIC HANDLING SYSTEMS

M. Katerberg[1] and G.H.J.M. Ratering[1]
[1] Bronkhorst High-Tech BV, Ruurlo, The Netherlands

ABSTRACT
In this paper the effect of dissolved gas on liquid flow stability is investigated. It appears to be so that dissolved gas and gas bubbles in microfluidic systems not only cause instabilities but also deviations in the liquid flowrate. These effects can theoretically be explained by Henrys law and experimentally proven with accurate flowmeters and air pressurized water. Air bubbles originated after liquid decompression can cause deviations in the flowrate of a few percent. In order to optimize system performance the influence of dissolved gas and gas bubbles has to be taken into account or countermeasures have to be taken. A degasser can be used to minimize the effect of gas bubbles in microfluidic systems.

KEYWORDS
Low flow control, microfluidics, gas bubbles, degasser

INTRODUCTION
Optimal performance of a microfluidic process requires knowledge and know-how of the entire fluid delivery system. Only having an excellent flow meter is not sufficient. In the range of (ultra) low liquid flows, tiny disturbances in the process, ambient conditions or instabilities in the system can have a negative impact on system performance. With continuous developments and user requirements pushing the limits of low flow sensor technology, these disturbances become more and more visible and relevant to control in achieving an optimal and stable liquid flow setup. Gas bubbles causing instabilities are a common problem in microfluidic systems and the main subject of this paper.

FLOWSETUP
Because liquid flow setups can be accomplished for different applications, there is not one fix for all available. Using insights and understanding of the various influences, a system can be built with a trade-off between different requirements. A basic setup (figure 1) is commonly used to supply a process with a stable liquid flow. The inlet air pressure for the tank filled with a liquid is higher than the pressure needed to overcome the pressure drop by the controlled process flow. The air pressure at the inlet results in the dissolving of the air in the water and that causes problems.

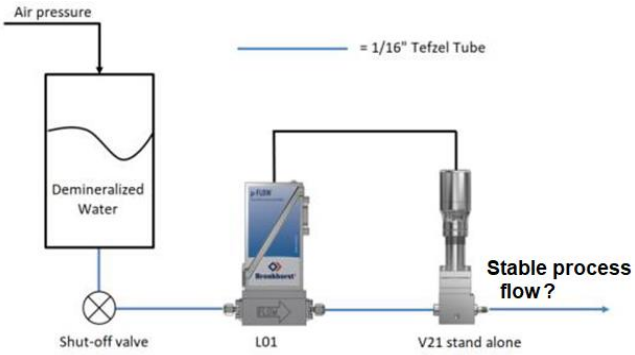

Figure 1: basic flow setup. From left to right: A pressurized storage vessel with shutoff valve, L01 thermal liquid flow meter, V21 piezo actuated control valve. All components are interconnected with 1/16"tefzel tubing.

THEORY OF GAS SOLUTION IN LIQUID
For a gas *i* that is soluble in a liquid, the mole fraction of dissolved gas in the liquid, $y_{i,\text{liquid side}}$ is related to the partial pressure of the gas $P_{i,\text{gas side}}$ by Henry's law[1]:

$$y_{i,liquid\ side} = \frac{P_{i,gas\ side}}{H} \qquad (1)$$

Where H is Henry's constant. The Henry constant increases with increasing temperature and is gas dependent. According to Henry's law the amount of dissolved gas is proportional to the pressure. So at higher pressure more gas will dissolve in the water. When the pressure is relieved the dissolved gas cannot stay in the liquid and the gas will appear as bubbles. This is for instance the case when first opening a bottle of sparkling mineral water. For microfluidic systems with a high demand for stability this effect is usually unwanted.

The mol fraction of the gas in equation 1 can be converted to volume fraction (vol%) at 1 bara using mol masses and densities. For a few gasses this results in the following as stated in table 1

Gases	Vol.%
Air	1.8
He	0.90
N_2	0.80
CO_2	79

Table 1: Solubility of a few gasses in vol.% per bar at 300K

From table 1 we can conclude that CO_2 results in the most volume expansion after decompression.

BUBBLES IN A MICROFLUIDIC SYSTEM

When controlling a flow using a setup as depicted in figure 1 at 2 bard air pressure, the volume of air gassed out of the water at the end of the process is 2x1.8%=3.6vol%. The assumption is that the water is saturated with the pressurized air at 2 bard and all of the pressure drop is over the control valve. This will results in a theoretical volume expansion due to the air bubbles of 3.6% after the valve due to the decompression. This expansion of air will result in a mass flow increase after the valve in between the emerged air bubbles of 3.6%. Because of mass flow in equals mass flow out the average massflow including the airbubles has to the same. It is to be expected that reducing the pressure or using helium as a propellant gas reduces the amount of gas bubbles

A degasser can be used to reduce the effects of dissolved gasses in liquid. A degasser consists of a gas permeable tube that is positioned in a vacuum chamber. As the liquid with dissolved gasses runs through the degasser the dissolved gasses are extracted from the liquid and this should result in a stable flow further downstream. Degassers are commercially available devices.

The following setup is used to investigate the effect of dissolved air and the effect of a degasser as depicted in Figure 2

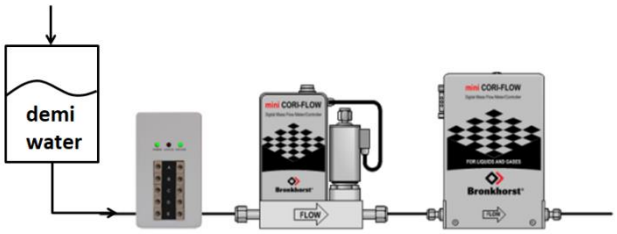

Figure 2: Experimental setup for investigating the effect of air bubbles and degasser. From left to right: pressurized storage vessel with water, degasser, M12V14 flow controller. ML120 reference flowmeter

The accuracy specifications of the used instruments as stated by the manufacturer [2] are depicted in table 2

Property	M12V14	ML120
Accuracy [%RD]	0.2%	0.2%
Zero stability [mg/h]	50	20

Table 2 accuracy specification of Bronkhorst Coriolis instruments M12 and ML120

EXPERIMENTAL

A measurement is done to monitor the process flow stability of the basic setup of figure 2. A ML120 flow sensor is placed after the M12V14 flow controller to measure the stability of its generated flow.

Initially the degasser is switched off so it leaves the dissolved air in the water. The M12 is set to control a flowrate of 1g/h. Subsequently the ML120 flowmeter measures the stability of the generated flow. After a few hours the degasser is switched on to reduce the amount of dissolved air. The results are depicted in Chart1 and discussed in the next section.

MEASUREMENT RESULTS

Chart1 is cut into two sections. The first section on the left side shows the performance with the degasser switched off. The right section shows the system performance with the degasser switched on. Since it takes quite some time for the system to become stable only the stable parts for a few hours are shown for both cases.

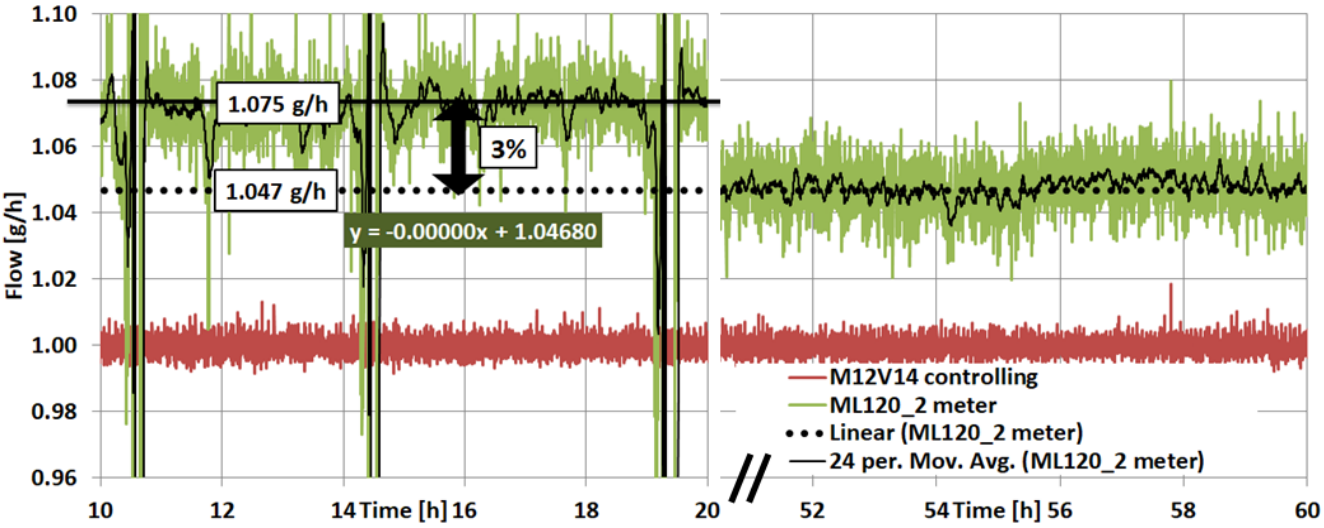

Chart 1: Results of measurement with degasser off (left side)and degasser on (right side)

In chart 1 the red line represents the measured flow of the M12 flow controller running continuously at 1 g/h for 60 hours. The green line represents the measured flow of the reference flowmeter ML120 positioned downstream after the control valve of the M12.

Clearly visible in the left section is a stable flow of the M12 as it controls while the ML120 sees a discontinuous flow caused by air bubbles.
Also a final offset of 45mg/h can be seen between the two instruments which can be caused by incorrect zeroing of the instruments or a calibration deviation. The deviation is within the combined specification limits of the flowmeters as shown in table 2

Noticeable on the right side of the chart, where the degasser is active, a lower flowrate can be seen. The flow seems less when gas bubbles are not present. It results in a drop of the massflow of approximately 3%.

The dotted line in the left and right side of the chart is the calculated average value over the entire dataset of 60 hours. This shows that in both cases the massflow is the same although it “seems” to be higher on the left side of the chart in between the air bubbles.

A zoom in on an air bubble passing the reference flowmeter reveals the following as depicted in chart 2

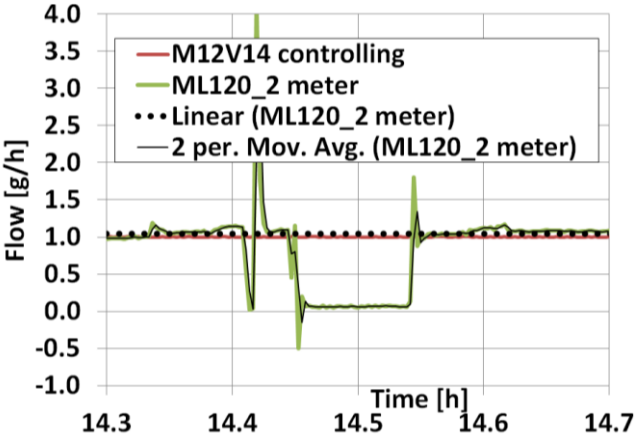

Chart 2: A zoom in on an airbubble pasing the reference meter at 14.5 hours

The airbubble takes about 0.1 hour to pass the reference flow meter while the flow seems stable in between two air bubbles. The time in between two air bubbles is approximately 3.5 hours according to the left side of chart 1. The percentage of time where an air bubble is present equals 0.1/3.5 = 3% During this time the mass flow is nearly zero as the air bubbles passes at the same speed as the liquid while the density is 0.1% of the density of water

CONCLUSION

Dissolved gasses in liquid will be released when pressure is reduced. This occurs in microfluidic systems when liquid reservoirs are gas pressurized and the flow is controlled by valves that cause pressure drop. Gas bubbles cause instability and deviations in the mass flow.

The conclusion that can be drawn from the experiment is that in the case of air bubbles being present in a system initially pressurized at 2 bara the mass flow rate is 3% higher for most of the time while in 3% of the time the mass flow rate is nearly 0. This results in the same average massflow as if the gas is still dissolved. This effect seems very little but is very well measurable with sensitive flowmeters.

Although the average mass flow is the same at stable conditions it seems to be higher in between originated gas bubbles. Since flow in our example is controlled by an accurate flowmeter it is to be expected that its delivered flow is accurate. However at the presence of dissolved gas and pressure drop the massflow in between gas bubbles can be a few percent higher after the flowcontroller. The measured amount of deviation of 3% roughly matches the calculated 3.6%. A degasser reduces the disturbance and deviations otherwise caused by air bubbles.

REFERENCES

[1] Yunus A. Cengel Michale A Boles 'Thermodynamics an engineer approach', 2011, pp 826 -833

[2] Bronkhorst, mini cori flow, visited 20190913, <https://www.bronkhorst.com/int/products/liquid-flow/mini-cori-flow>

CONTACT

m.katerberg@bronkhorst.com

ADDITIVE MANUFACTURED PURE PMMA MICROFLUIDIC CHANNELS FEATURING A SCREEN PRINTED DIAPHRAGM FLOW VELOCITY SENSOR

M. Knoll[1], M. A. Hintermüller[1], C. Offenzeller[1], B. Jakoby[1] and W. Hilber[1]
[1] Institute for Microelectronics and Microsensors, Johannes Kepler University, Linz, Austria

ABSTRACT

In this work we present a low cost and low tech method for the fabrication of microfluidic channels purely made out of PMMA featuring a diaphragm. The channel is created in three steps where first the PMMA substrate is engraved using a laser engraver, second the channel is filled with liquid gallium, and third, after the solidification of the gallium, an UV-curable PMMA topcoat seals the channel. The fabricated channel features a diaphragm with a screen printed strain gauge on top. This strain gauge is able to measure the deformation of the diaphragm thus capable of detecting flow velocities in the range from 10 to 300 µL/min.

KEYWORDS

Microfluidic diaphragm, Microfluidic channel fabrication, diaphragm flow velocity sensor

INTRODUCTION

The flow velocity is an important control parameter in microfluidic applications and therefore a variety of microfluidic flow velocity sensors are realized using different production techniques and transducing mechanisms. Measuring the flow velocity in microfluidic channels is possible using optical, thermal or mechanical working principles. Optical flow velocity measurements can be examined by, e.g. particle tracking using fluorescent marker particles in the fluid flow [1], or by measuring the Doppler shift of light scattered by moving particles in the fluid [2], [3]. If the implementation of fluorescent particles or scattering particles in the fluid is not suitable, thermal flow sensors can be used to determine the fluid flow velocity. Thermal flow sensors are, for example, time of flight measurements in which the fluid is heated with a heat pulse and the timespan between the heat pulse and the detection of the heated fluid by a sensor located downstream is measured [4]. Another thermal measurement principle is based on an anemometer, where a resistor is placed in the fluid flow and heated to a specific temperature, the heating power of the resistor correlates with the flow velocity of the fluid [5]. Mechanical sensors use the fluid drag force to cause mechanical deformations which are measured by a strain gauge, e.g. cantilevers which are located in the fluid flow and therefore show a deformation which is characteristic for the flow velocity [6], [7]. This work presents a sensor which uses also a mechanical transducing mechanism, but no objects are placed in the fluid flow which may cause unwanted disturbances. Instead, the deformation of a diaphragm is measured which is proportional to the fluid flow velocity due to the pressure change in the chamber. The Bernoullis equation describes the correlation of fluid flow velocity and the pressure, where a higher flow velocity leads to a lower pressure inside the fluid. Typically diaphragms are fabricated in a MEMS process [8], this paper is dealing with a different approach, the microfluidic channels are fabricated out of a PMMA plate using a laser engraver and gallium as a sacrificial material for the sealing layer [9]. For the fabrication of the strain gauge a variety of processes are available, e.g. classical deposition technologies as physical vapor deposition [10]. These processes require expensive equipment and are rather slow compared to printing techniques as inkjet printing or screen printing. A variety of sensor types have already been realized using screen printing technique, e.g. screen printed gas sensors [11], temperature sensors [12], and capacitive touch sensors [13]. Screen printing is well-established in sensor fabrication due to its low cost outlay, repeatability and high print output. Thus the fabricated flow velocity sensor is equipped with a screen printed strain gauge directly placed on the diaphragm.

SENSOR LAYOUT

For microfluidic applications, leakages of the channel are a serious problem and typically present if the microfluidic channel is made out of a top and a bottom layer which have to be bonded using an adhesive material or solvents [14], [15].

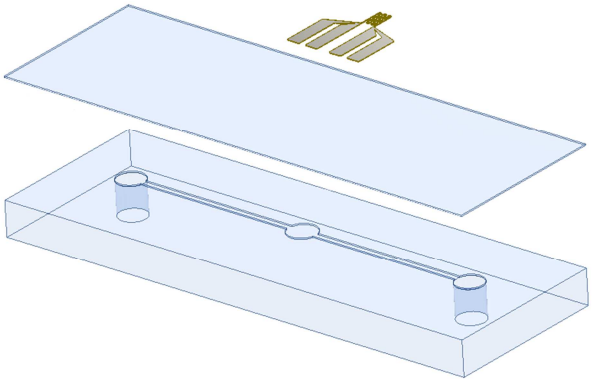

Figure 1: Schematic representation of the device consisting of a PMMA slide with a laser engraved microfluidic channel, 250 µm PMMA top layer and a screen printed silver strain gauge

In this work the microfluidic channel consists also of a top and a bottom layer but is purely made out of PMMA to circumvent adhesion problems between the channel layers. The schematic sensor architecture is depicted in Fig. 1. The channel is laser engraved into a PMMA slide which forms the bottom layer of the device, the channel features a width of one millimeter and a circular chamber with a diameter of 4.4 mm. The top layer of the microfluidic channel is a 250 µm PMMA layer which seals the channel. Atop the circular chamber a diaphragm is formed by the 250 µm PMMA layer which exhibits a flow velocity dependent deformation (different flow velocities of a fluid lead to changes of the dynamic pressure in the channel). These deformations are detected by a strain gauge with a finger width of 0.2 mm and a length of 2.9 mm.

FABRICATION

The device is fabricated in four steps which are schematically depicted in Fig. 2. In the first step a PMMA slide is laser engraved which forms the channel, the chamber for the diaphragm and the inlet and outlet of the channel. Fig. 2 a and b depict the PMMA bottom plate before and after the laser engraving step. The cross-section of the laser engraved channel, which features 200 µm in depth and one mm in width, is shown in Fig. 3. For the second step a microscope glass slide is clamped onto the PMMA slide in order to seal the channel. Liquid gallium is squeezed into the channel which is then placed in the fridge where the gallium solidifies (Fig. 2c). After the solidification step the microscope slide is removed from the PMMA slide. As the channels are filled with the gallium, the PMMA slide features a planar surface which is in the third step coated with an UV curable PMMA solution in a doctor blade process. The curing and crosslinking is performed under UV light for ten minutes (Fig. 2d).

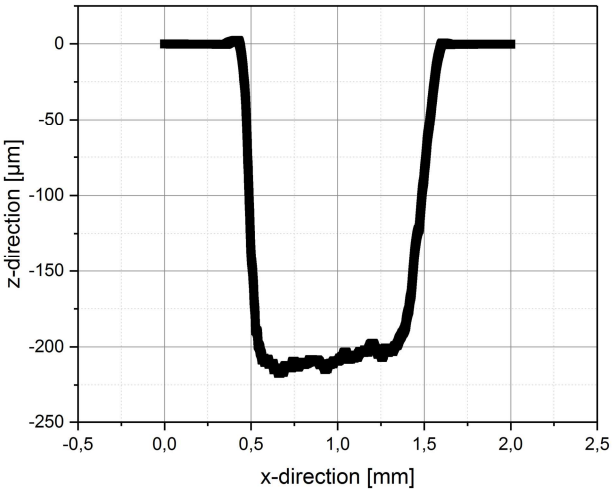

Figure 3: Cross-section of the laser engraved channel, featuring a channel depth of approximately 200 µm and a width of one mm

In the last fabrication step the strain gauge is printed onto the top side of the diaphragm in a screen printing process. The used ink for the strain gauge is a silver ink (sun-chemical C2121022D1) which has to be cured at 75°C for 15 min (Fig. 2e). Finally the channels have to be cleaned from the gallium. For this purpose the channel is flushed with 1% NaOH solution (Fig.2f). An image of the fabricated microfluidic channel and the sensor is depicted in Fig. 4. The inset shows the PMMA diaphragm with the screen printed strain gauge (meander like structure) which is connected by four broad lines acting as connections for the four wire resistance measurement.

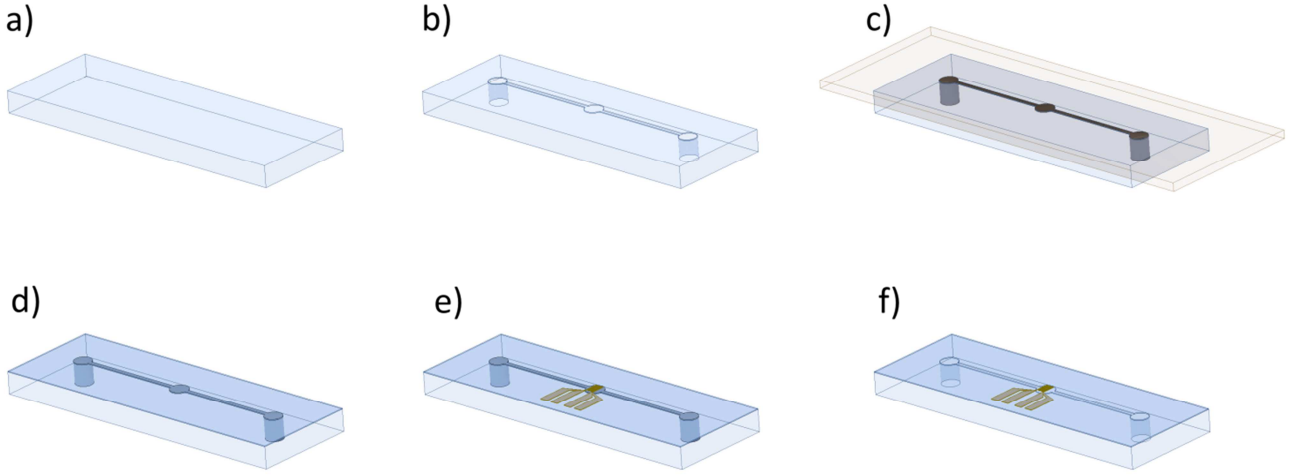

Figure 2: Schematic representation of the production steps: a) PMMA slide serving as the channel substrate, b) PMMA slide with laser engraved channel, c) channel covered with glass slide and filled with liquid gallium, d) UV curable PMMA layer applied with doctor blade after the solidification of gallium e) screen printing of the micro strain gauge, f) removing of the gallium in the channel

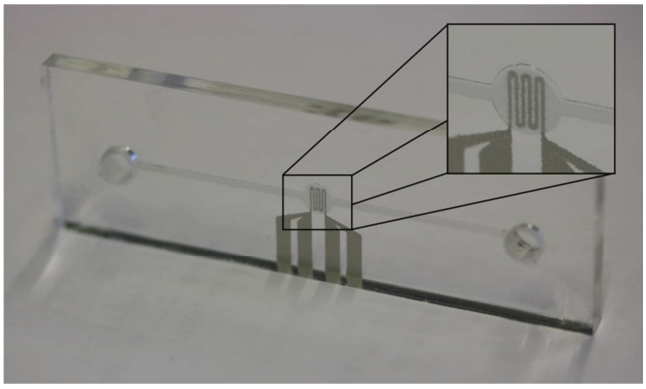

Figure 4. Microfluidic flow velocity sensor using a screen printed strain gauge on top of the PMMA diaphragm as sensing element

MEASUREMENT AND RESULTS

The test fluid used for the measurement is deionized water, the water flow is generated by a syringe pump. Fig. 5 depicts the relative resistance change over time for a fluid flow profile of 0-40-0 µL/min.

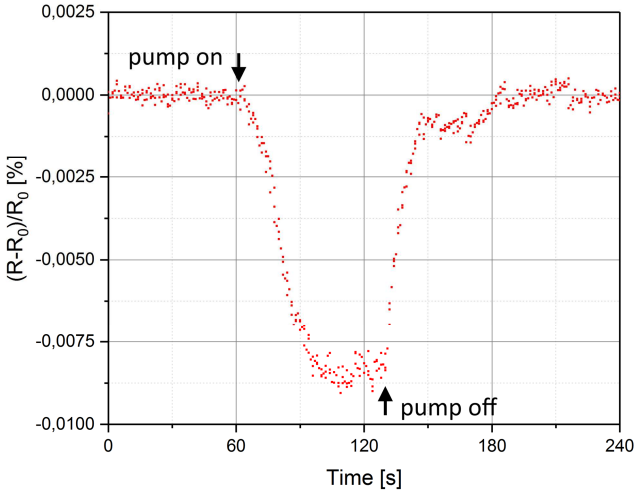

Figure 5. Resistance change of the strain gauge for a flow velocity of 40 µl/min

After the activation of the pump, the deformation of the diaphragm immediately leads to a resistance drop of the strain gauge. The recorded sensor signal shows a creeping behavior which may be caused by creeping of the elastic diaphragm to its new equilibrium state when the pressure in the diaphragm chamber is changed. The sensor signal, recorded for flow velocities form 10 µL/min up to 300 µL/min, is depicted in Fig. 6. The correlation between sensor signal and flow velocity is slightly nonlinear and flow velocities above 300 µL/min cannot be distinguished anymore as the diaphragm is physically limited in deformation. Also flow velocities below 10 µL/min cannot be detected due to the stiffness of the diaphragm. If the measurement range should be changed, the design of the diaphragm and the thickness has to be adapted for the desired flow velocities.

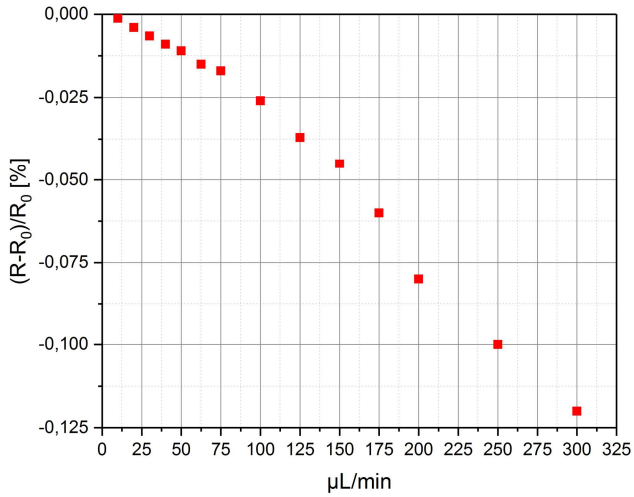

Figure 6. Relative resistance change of the sensor for different flow velocities of 10 up to 300 µL/min

Fig.7 depicts three consecutive cycles in which the water stream with a velocity of 100 µL/min was switched on and off in a 60 s interval. As it can be seen, the sensor response remained stable during cycling.

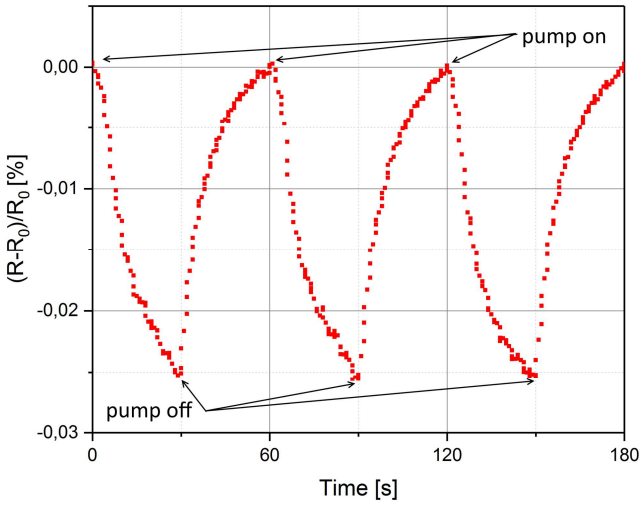

Figure 7. Three consecutive recorded cycles of 30 s fluid flow (100 µL/min) followed by 30 s pump off.

To estimate the temperature influence on the resistance of the strain gauge, the temperature response was determined; in the region of 25°C up to 75°C the resistance increases linearly by 13.6% representing an increase in resistance of 0.272% for a temperature change of 1°C. Compared to the resistance change due to the deformation of the diaphragm in the characterized range a change of 1°C would lead to a signal which is one order of magnitude larger. Thus the measurement setup has to be operated in temperature-stable environment or the

temperature drift has to be corrected.

CONCLUSION

In this work we demonstrated a fabrication method for microfluidic channels purely made out of PMMA. The fabricated microfluidic channel features a PMMA diaphragm which is imprinted with a strain gauge. The sensor fabrication is examined using a low cost screen printing process where the channel is filled with solidified gallium so that the PMMA diaphragm is not deformed during the printing process. After curing and cleaning of the channel the fluid flow induced deformations of the diaphragm were detectable for flow velocities from 10 µL/min up to 300 µL/min. During the measurement the temperature has to be held constant as the temperature drift of 1°C leads to a higher resistance change then the resistance change due to a fluid flow of 300 µL/min.

ACKNOWLEDGEMENTS

This work has been supported by the COMET-K2 "Center for Symbiotic Mechatronics" of the Linz Center of Mechatronics (LCM) funded by the Austrian federal government and the federal state of Upper Austria.

REFERENCES

[1] J. G. Santiago, S. T. Wereley, C. D. Meinhart, D. J. Beebe, and R. J. Adrian, "A particle image velocimetry system for microfluidics," *Exp. Fluids*, vol. 25, pp. 316–319, 1998.

[2] X. J. Wang, T. E. Milner, and J. S. Nelson, "Characterization of fluid flow velocity by optical Doppler tomography," *Opt. Lett.*, vol. 20, no. 11, pp. 1337–1339, 1995.

[3] Z. Chen, T. E. Milner, D. Dave, and J. S. Nelson, "Optical Doppler tomographic imaging of fluid flow velocity in highly scattering media," *Opt. Lett.*, vol. 22, no. 1, pp. 64–66, 1997.

[4] C. Offenzeller *et al.*, "Fully Screen Printed Thermocouple and Microheater Applied for Time-of-Flight Sensing in Microchannels," *IEEE Sens. J.*, vol. 18, no. 21, pp. 8685–8692, 2018.

[5] M. Ashauer, H. Glosch, F. Hedrich, N. Hey, H. Sandmaier, and W. Lang, "Thermal flow sensor for liquids and gases based on combinations of two principles," *Sensors Actuators A. Phys.*, vol. 73, pp. 7–13, 1999.

[6] N. T. Nguyen, "Micromachined flow sensors — a review," *Flow Meas. Instrum.*, vol. 8, no. 1, pp. 7–16, 1997.

[7] Y. Wang, C. Lee, and C. Chiang, "A MEMS-based Air Flow Sensor with a Free-standing Microcantilever Structure," *Sensors*, vol. 7, pp. 2389–2401, 2007.

[8] R. E. Oosterbroek, T. S. J. Lammerink, J. W. Berenschot, G. J. M. Krijnen, M. C. Elwenspoek, and A. Van Den Berg, "A micromachined pressure/flow-sensor," *Sensors Actuators A. Phys.*, vol. 77, pp. 167–177, 1999.

[9] M. A. Hintermüller and B. Jakoby, "Lab-scale prototyping of polymer based microfluidic devices using gallium as phase-changing sacrificial material," *Microelectron. Eng.*, vol. 211, pp. 50–54, 2019.

[10] K. Reichelt and X. Jiang, "The preparation of thin films by physical vapour deposition methods," *Thin Solid Films*, vol. 191, pp. 91–126, 1990.

[11] G. Martinelli, M. C. Carotta, M. Ferroni, Y. Sadaoka, and E. Traversa, "Screen-printed perovskite-type thick films as gas sensors for environmental monitoring," *Sensors Actuators B*, vol. 55, pp. 99–110, 1999.

[12] S. Duby, B. J. Ramsey, and D. J. Harrison, "Printed thick-film thermocouple sensors," *Electron. Lett.*, vol. 41, no. 6, pp. 6–7, 2005.

[13] S. Yao and Y. Zhu, "Wearable multifunctional sensors using printed stretchable conductors made of silver nanowires," *Nanoscale*, vol. 6, pp. 2345–2352, 2014.

[14] L. Riegger, O. Strohmeier, B. Faltin, R. Zengerle, and P. Koltay, "Adhesive bonding of microfluidic chips : influence of process parameters," *J. MICROMECH. MICROENG.*, vol. 20, p. 87003, 2010.

[15] M. Svoboda, Z. Slouka, W. Schrott, C. Petr, M. Pribyl, and D. Šnita, "Fabrication of plastic microchips with gold microelectrodes using techniques of sacrificed substrate and thermally activated solvent bonding," *Microelectron. Eng.*, vol. 87, pp. 1590–1593, 2010.

CONTACT

M. Knoll, marcel.knoll@jku.at

FABRICATION OF FREE-HANGING TUBES FOR A HIGH FLOW MICRO CORIOLIS MASS FLOW METER

J. Groenesteijn[1], M.J. de Boer[2], J. van Putten[1], W. Sparreboom[1], J.C. Lötters[1,2] and R.J. Wiegerink[2]
[1] Bronkhorst High-Tech BV, Ruurlo, The Netherlands
[2] MESA+ Institute for Nanotechnology, University of Twente, Enschede, The Netherlands

ABSTRACT

We have developed a micromachining fabrication process to fabricate large, free-hanging microchannels, integrated with electrodes for actuation and read-out of a micro Coriolis mass flow sensor. The process improves on the previously presented Surface Channel Technology (SCT, [1]) and includes some features of the previously presented Buried Channel Technology (BCT, [2]) to overcome their limitations. The resulting microchannels have a circular or hexagonal cross-section with a diameter up to 180 µm and a channel-wall thickness up to 10 µm without the use of waferbonding. The channels can be released from the bulk to allow the vibrational movement needed for a Coriolis mass flow meter (MFM). Integrated metal electrodes can be used for actuation and read-out of the sensor.

KEYWORDS

MEMS, micro Coriolis mass flow meter, free-hanging channels

INTRODUCTION

In the past, we presented a micro Coriolis MFM [3] for measurement of fluid flows up to $2\,\mathrm{g\,h^{-1}}$. These sensors are made in the Surface Channel Technology [1], which allows for free-hanging, semi-circular channels in a wide range of sizes and shapes [4]. However, many applications, like liquid chromatography or Lab-on-a-Chip use higher flowrates while requiring the low volumes of microfluidic flowmeters [5]. To be able to increase the flow-range and/or decrease the pressure drop of the micro Coriolis MFM the channel-diameter needs to be increased, while maintaining its advantages (fast, accurate, low volume, small form factor). However, inherent to the SCT process, the channels have a flat top and a maximum channel-wall thickness. Both of these limit the maximum size of the free-hanging channel and increase the sensitivity to pressure when the channel size increases.

The fabrication process presented in this paper implements two main changes to the SCT. By isotropically etching the channel from the bottom of a trench instead of at the surface of the wafer, the flat top inherent to SCT can be avoided as long as the radius of the channel is less than the depth of the trench. Furthermore, by using a stack of multiple materials as channel wall, the wall-thickness can be increased beyond what the intrinsic stress of the silicon-rich silicon nitride (SiRN) used in SCT allows.

FABRICATION OUTLINE

Here, a short overview of the fabrication process is shown. Details on the most important steps are given in the next section. The fabrication starts with wet thermal oxidation of a 525 µm thick, highly doped silicon wafer. This thermal SiO_2 (t-SiO_2) is used as a hard-mask during the inlet etch from the backside of the wafer. (Figure 1a) After the inlet-etch, this layer is stripped and a new SiO_2 layer is deposited using low pressure chemical vapour deposition (LPCVD) of tetraethyl orthosilicate (TEOS, $Si(OC_2H_5)_4$). This is patterned with rectangular holes of 10 µm wide and 50 µm long which form the outline of the channels. The layer is then used as a hard-mask to etch the trenches of 110 µm deep through which the channels will be etched. (Figure 1b) This layer is also deposited inside the inlets and protect them during the channel etch. Next, a thermal oxidation step is done which forms a protective t-SiO_2 layer on the silicon in the trench. This layer will protect the trench side-walls during the channel etch. Using plasma enhanced chemical vapour deposition (PECVD), a thick SiO_2 layer is deposited on the front side of the wafer. (Figure 1c) A directional plasma etch is used to remove the t-SiO_2 at the bottom of the trenches. The channels are then etched in the bulk of the wafer, through the trenches, by an isotropic gas-phase XeF_2 etch. (Figure 1d) The etch process is isotropic, so it results in a channel centering around the bottom of the etch-trenches.

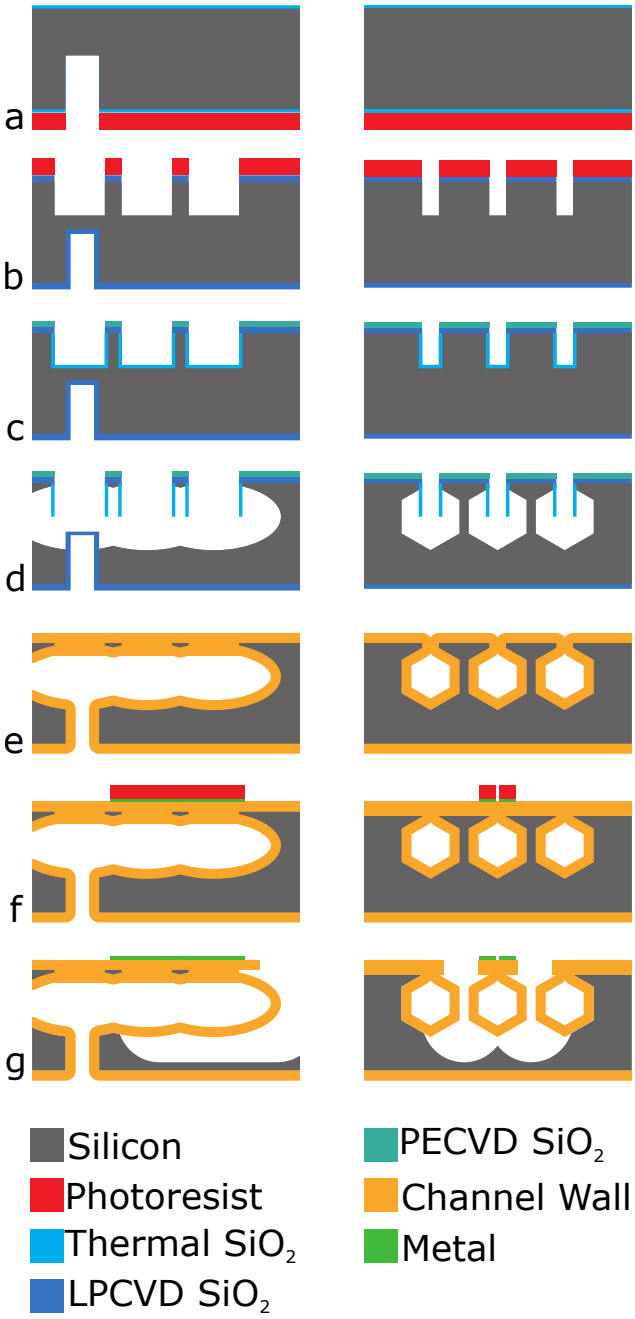

Figure 1: Schematic overview of the fabrication process. Left: cross-section along the length of the channel. Right: cross-section perpendicular to the channel.

All SiO_2 is removed using a wet HF etch and the channel wall is deposited. The first layer is a t-SiO_2 layer, followed by LPCVD of silicon-rich silicon nitride (SiRN), polycrystalline silicon (polySi) and a final SiRN layer. (Figure 1e) The thickness of the total stack can be up to 10 µm (depending on the etch-trench-width) and is conformally deposited, meaning it is deposited inside the channels and on the front- and backside of the wafer. It closes the trenches through which the channel is etched, resulting in an enclosed, leak-free channel. The only wetted material inside the channels is silicon-rich silicon nitride. After the channel is closed, a gold layer with chromium adhesion layer is deposited and patterned to form the electrodes for actuation and read-out of the Coriolis sensor. (Figure 1f) Finally, the layer-stack on top of the wafer is etched using a directional plasma etch to reach the bulk silicon next to the channel. Using a semi-isotropic SF_6 plasma etch and an isotropic gas-phase XeF_2 etch, the silicon around the channels is removed to allow for free movement of the channels. (Figure 1g)

FABICATION RESULTS

Channel cross-section

Images of the channel cross-section can be seen in Figure 2. On the left, a channel with a diameter of 96 µm is shown while the image on the right has a diameter of 159 µm. The change in shape (circular to hexagonal) is an effect of the XeF_2 etch kineticts [6].

At the start of the etch, the area of silicon available for etching is very small and plenty of etchant can reach the silicon, while the reaction products can easily be removed. This results in a completely isotropic etch. However, when the channel diameter increases, the area of silicon available for etching also increases while the trenches through which the etchant and reaction products have to diffuse does not change. As a result, the XeF_2 concentration inside channels will decrease, changing the etch kinetics, eventually resulting in a hexagonal cross-section. For the used trenches and etching system, this occurs when the diameter is approximately 120 µm.

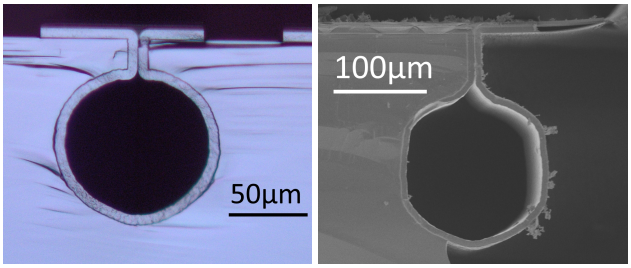

Figure 2: Images of the crosssection of two different channel diameters.

Channel wall

Previously, the channel wall was made using a single silicon-rich silicon nitride layer. Due to intrinsic stress in the layer available to us, it can only be 2 µm

thick. This means that, when the channel diameter increases, the strenght and stiffness of the channel wall does not increase with it. As a result, the mechanical behaviour of the free-hanging channel will increasingly depend on external influences like applied pressure and temperature. To make free-hanging channels with a thicker channel wall, we use a layer stack where every layer has a function.

- The SiO_2 protects the channelwall during the XeF_2 release etch. SiO_2 has a much better selectivity compared to SiRN which allows us to relesae the complete channel.
- The SiRN at the inside of the channelwall results in a chemically inert fluid path. Due to intrinsic stress, the maximum thickness of these SiRN layers is approximately 2 µm and can thus not be used for the whole channel wall. It is also deposited at the outside of the channelwall to make sure the stress in the channelwall is mostly balanced.
- The polySi can be deposited up to 10 µm. This layer can be used to reach a specific wall thickness.

Figure 3 shows the top of an etch-trench which has been closed with the layerstack. From bottom till top, it shows the t-SiO_2 and SiRN layers (indistinguishable from in this image) of 1 µm thick, the 5 µm poly-silicon layer, the second SiRN layer of 1 µm and finally a photoresist layer on top. In this case, the trench was only 10 µm wide, and it was completely closed during deposition of the polySi layer. As a result, the final SiRN layer is only on top of the wafer and not at the inside of the channel wall.

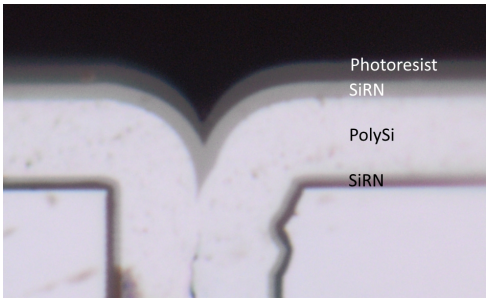

Figure 3: Image of the different layers in the channel wall.

Channel release

Releasing the channels from the bulk is done in three steps. First, the channel wall layer stack, which is also deposited on top of the wafer is patterned with release windows next to the channels using a directional plasma etch. To prevent the exposed polySi from etching during the bulk etch, a new photoresist layer is applied with smaller release windows. This photoresist requires excellent planarization properties to be able to fully cover the 10 µm step and also allow for accurate enough patterning for the comb-fingers used for capacitive read-out. Next, 200 µm deep trenches are etched through the release windows using a directional plasma etch. To remove the silicon underneath the channel, an isotropic XeF_2 etch is done through these trenches. To keep the silicon loading during this etch low (and thus the etch rate relatively fast), parallel channels were made around the free-hanging channel to act as etch-stop. This is shown in Figure 4. Figure 5 shows the free-hanging channel in detail.

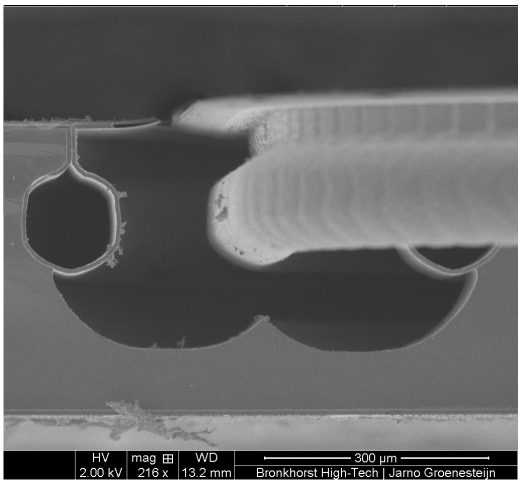

Figure 4: SEM image showing a free-hanging channel with partly released channels next to it, which act as etch-stop during the release etch.

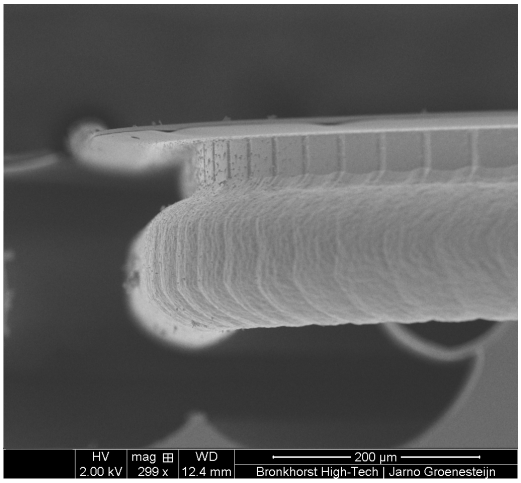

Figure 5: SEM image of a free-hanging channel. The pillars above the channel shows a periodic pattern which coincides with the 50 µm *long etch-trenches with* 10 µm *spacing between. The channel wall shows a periodic pattern with the same pitch.*

Actuation and read-out

Figure 6 shows the metal electrodes on a free-hanging channel. The microscope image on the right side shows some metal electrodes on the free-hanging channel at the top for actuation. Below that, the closed channel-etch-trenches are still visible. In the middle of the image, comb-fingers for capacitive read-out are shown. One side of the comb-structure is attached to the free-hanging channel, the other side to the bulk of the chip. Since the comb-fingers significantly reduce the etch-rate of the release-etch, extra release-holes are etched above and below the comb-fingers.

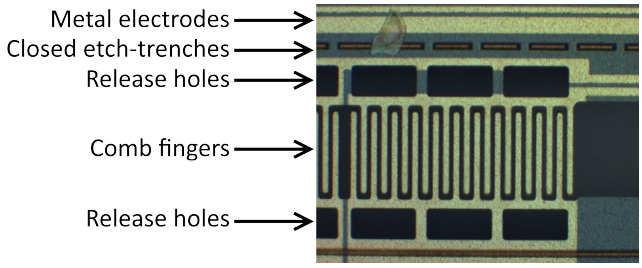

Figure 6: Microscope image of the metal electrodes on top of a free-hanging channel.

CONCLUSION

We have developed a fabrication process for the fabrication of large free-hanging microchannels. The channels can have a diameter up to 180 µm with a channel-wall thickness up to 10 µm. Integrated metal electrods can be used for actuation and read-out of a microfluidic sensor. Future work will focus on using this technology to fabricate a high flow micro Coriolis mass flow sensor.

ACKNOWLEDGEMENT

The authors would like to thank Kechun Ma and the MESA+ nanolab staff for the valuable discussions and collaboration during this project.

REFERENCES

[1] J. Groenesteijn, M.J. de Boer, J.C. Lötters, R.J. Wiegerink, "A versatile technology platform for microfluidic handling systems, part I: fabrication and functionalization", Microfluid Nanofluid (2017) 21:127.

[2] M.J. de Boer, R.W. Tjerkstra, H.V. Jansen, G.J. Burger, J.G.E. Gardeniers, M. Elwenspoek, A. van den Berg, "Micromachining of buried micro channels in silicon", J Microelectromech Syst (2000) 9(1):94-103.

[3] W. Sparreboom, J. van de Geest, M. Katerberg, F. Postma, J. Haneveld, J. Groenesteijn, T.S.J. Lammerink, R.J. Wiegerink, J.C. Lötters, "Compact mass flow meter based on a micro coriolis flow sensor", Micromachines (2013) 4(1):22-33.

[4] J. Groenesteijn, M.J. de Boer, J.C. Lötters, R.J. Wiegerink, "A versatile technology platform for microfluidic handling systems, part II: channel design and technology", Microfluid Nanofluid (2017) 21:126.

[5] D.A.P. Oudejans, "Liquid microfluidic applications and market needs in flow measurement and control in the microfluidic flow range", Proceedings of the 3rd Conference on MicroFluidic Handling Systems, MFHS 2019

[6] D. Xu, B, Xiong, G. Wue, Y. Wang, X. Sun, Y. Wang, "Isotropic Silicon Etching With XeF_2 Gas for Wafer-Level Micromachining Applications", J Microelectromech Syst (2012) 21(6):1436:1444

[7] D. Alvering, R.G.P. Sanders, J. Groenesteijn, T.S.J. Lammerink, R.J. Wiegerink, J.C. Lötters, "Universal modular fluidic and electronic interfacing platform for microfluidic devices", Proceedings of the 3rd Conference on MicroFluidic Handling Systems, MFHS 2017

CONTACT

* J. Groenesteijn, j.groenesteijn@bronkhorst.com

EMBEDDING OF SCREEN PRINTED SENSORS AND ACTUATORS INTO BULK POLYMER FOR SENSING IN MICROFLUIDIC DEVICES

C. Offenzeller[1], M. A. Hintermüller[1], M. Knoll[1], B. Jakoby[1] and W. Hilber[1]*

[1] Institute for Microelectronics and Microsensors, Johannes Kepler University, 4040 Linz, Austria

ABSTRACT

This work presents a method for integrating screen printed transducers into microfluidic chips fabricated from polymers. Screen printed structures are thin enough not to disturb the flow while being cost efficient in fabrication. In contrast to previously presented methods [1] for the integration of screen printed sensors, this fabrication technique prevents leakages originating in the gluing of several different materials, e.g. glass, paper and polymers. As an example, a thermal flow velocity sensor embedded into a microchannel made from poly(methyl methacrylate) (PMMA) is presented.

KEYWORDS

Screen printed, thermal flow velocity sensor, microfluidic channel, sensor fabrication

INTRODUCTION

In lab-on-a-chip applications, quantities like the flow velocity, its profile or the temperature inside a microfluidic channel are key parameters for controlling nearly any process. Still the monitoring of these quantities is difficult if one does not want to disturb the flow. Optical measurement techniques are one solution to this problem. However, these measurements often involve the mixing in of particles, e.g., for tracking by optical measurement systems [2]. Apart from additional particles the optical measurement methods almost all require sophisticated imaging equipment and post-processing of the generated data. Other methods to monitor, e.g., the flow velocity in a microfluidic channel measure mechanical quantities like the drag force [3], [4] on an object, differential pressure [5], [6] or thermal effects [7], [8]. All these methods, however, require electrical connections, several parts and therefore also often interfaces between different materials. These interfaces are, in combination with microfluidic channels, prone to leakages due to difficulties in sealing at interfaces between different material.

One possible solution to this problem is presented here: Screen printed sensors and actuators are thin enough not to disturb the flow in most channel geometries. These structures can be printed on polymeric parts which are then glued together using solvents resulting in a sensitive structure completely embedded in bulk polymer without leakages.

This technique is demonstrated at the fabrication of a thermal flow velocity sensor integrating an actuator (heater) and two sensors (thermocouples).

WORKING PRINCIPLE OF THE EXAMPLARY SENSOR

The sensor geometry consists of one circular heater and two thermocouples the junctions of which are located at the same distance from the center of the heater (see Fig. 1). Atop this printed structure a microfluidic channel is placed. Fluid is filled in through the inlet on one side, from where a channel leads to a circular chamber atop the heater. From this chamber two channel arms lead to two outlets, while in each channel arm there is one thermocouple measuring the fluid temperature. After the channel is filled with fluid, one outlet is sealed while the other is left open so that the fluid can flow through. If the heater now emits a heat pulse, the fluid in the chamber is heated. Since both channel arms are made from the same material and filled with the same fluid, the heat conduction from heater to the two thermocouples is identical. However, in the arm with the flowing fluid there is a second heat transport mechanism present,

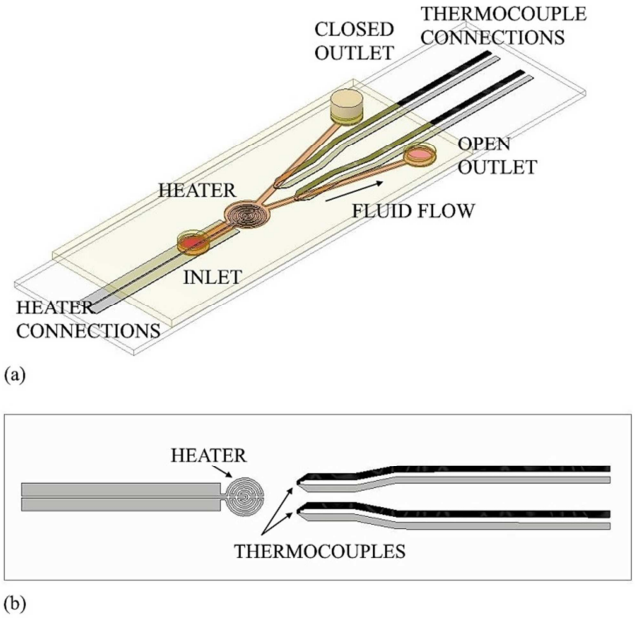

Figure 1: Schematic of the sensor layout consisting of one circular heater and two thermocouples. Atop the heater a chamber is located where the fluid is heated. One channel is sealed at the end while through the other the heated fluid flows. (a) Three dimensional view of the substrate, the sensor geometry and the channel filled with red fluid. (b) Top view of the sensor geometry.

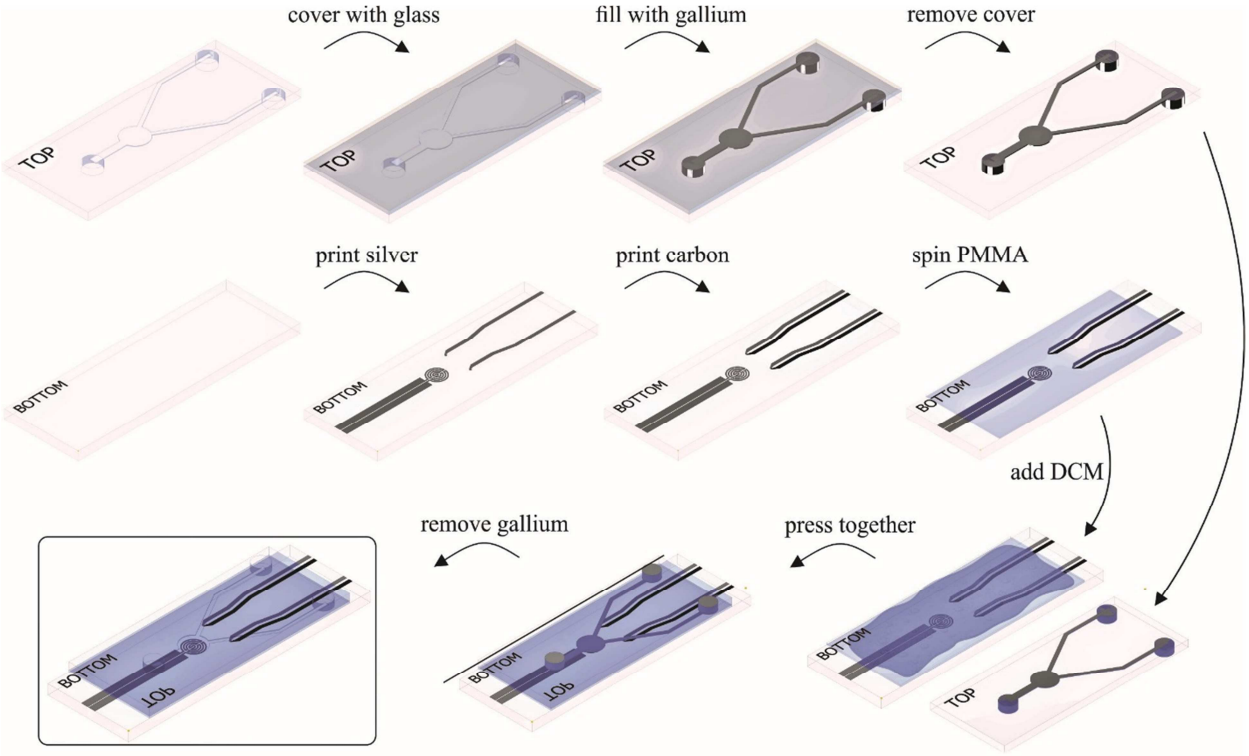

Figure 2: Fabrication procedure. Top row: Top plate with the engraved channel was covered with glass. Liquid gallium was filled into the channel and cooled until solid before the cover was removed. Middle row: The thermocouple and the heater were printed onto the bottom plate and covered with a PMMA layer. Bottom row: DCM was applied to the bottom layer and the top layer was pressed to it before the gallium was removed.

i.e. heat convection.
Therefore, when measuring the difference in temperature between the two thermocouples it can be directly related to the flow velocity.

FABRICATION

The sensor structure described above was embedded into a channel made from poly(methyl methacrylate) (PMMA).

To do so, first the PMMA pieces were fabricated: The base plate and the top plate were cut from 6 mm PMMA sheets by laser engraver (Trotec Speedy 300 flexx) to a size of 70x30 mm. Then, the channel was engraved into the top plate. The channel arms were 1 mm wide and 200 µm deep, the radius of the chamber was 3.5 mm.

Next, the sensor structure was printed onto the base plate. First the silver features (heater and one half of each thermocouple) were screen printed using a 120 threads/cm mesh from a polymer ink with silver particles (KA 801 by Dupont). The linewidth of the connections was 1 mm, the heater linewidth 100 µm. The ink was dried at 100°C for 20 minutes before the other halves of the thermocouples were printed. These were printed using a 100 threads/cm mesh from carbon particle filled polymer ink (EDAG PR 406B by Henkel). The carbon black halves of the thermocouples overlapped with the silver halves at the point where the temperature was to be measured.

Then a thin PMMA layer was applied to the printed structure. This was achieved by dissolving PMMA in anisole and applying this solution via spin coating. Then the layer was dried at 100°C. The resulting layer thickness was approximately 10 µm.

As a last step, the top and the bottom plate were glued together. This was done by applying dichloromethane (DCM) to the surface of the top plate, which slightly dissolved the uppermost layer.

Then the two halves were pressed together. However, one problem arose when using this technique: The small channels were often clogged with polymer which had been squeezed into the channel while gluing.
This problem was solved by adding a sacrificial layer of liquid metal [9]: The top plate with the channel was clamped to a glass slide. Then, gallium was heated to approximately 60°C and filled into the channel. A small chunk of solid gallium was added at the channel inlet as a seeding particle in order to prevent supercooling when the channel was then placed in a chamber at -18°C. When the gallium had solidified, the glass slide was removed leaving the channel filled with solid gallium.

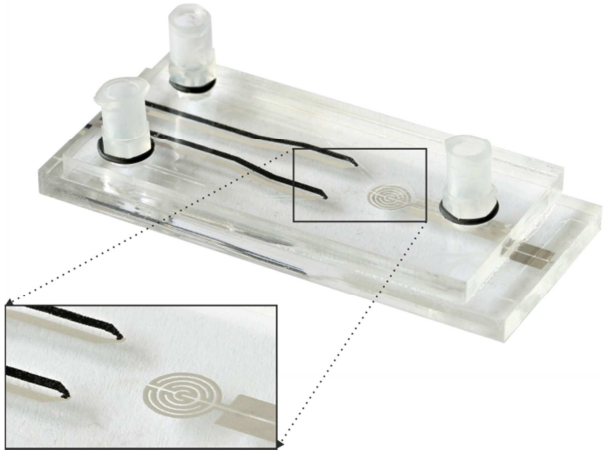

Figure 3: The fabricated device: One circular heater and two thermocouples are located underneath the channel. The polymer based sensor structure and the channel are completely embedded into bulk PMMA.

Next, the top plate with the gallium filled channel was placed with the channel side up in a single-handed quick release bar clamp. Dichloromethane was applied to the upper surface and the bottom plate with the PMMA coated sensor structure was pressed onto it in a way that the heater and the thermocouple junctions are located inside the engraved channels. After 20 minutes the clamp was opened and the top and bottom plate were bonded together.

Finally, the gallium had to be removed. To do so, the gallium-filled channel was placed in warm water and a 2% sodium hydroxide solution was pumped into the channel to push the gallium out. The fabricated channel with embedded sensing structure can be seen in Fig. 2.

To connect the heater and the thermocouples to the voltage source and the measurement setup, electrical connections were bonded to the uncovered parts of the printed structures. For connecting the heater, thin copper wires were bonded to the heater ends by silver filled epoxy resin (Epo-Tek H20E-8 by Epoxy Technology). For the thermocouples, the connections had to be made from materials with the same Seebeck coefficient as the thermocouple material. For the silver halves the connections were made similarly to the heater connections, since the Seebeck coefficients of copper and silver are equal. To connect the carbon black halves, thin strips of Kapton foil were coated with the same carbon black screen printing ink as used for printing the thermocouples and bonded to the structure also using this ink. These connections were then connected to standard cables, the connection being held at constant temperature by a water-cooled aluminum block.

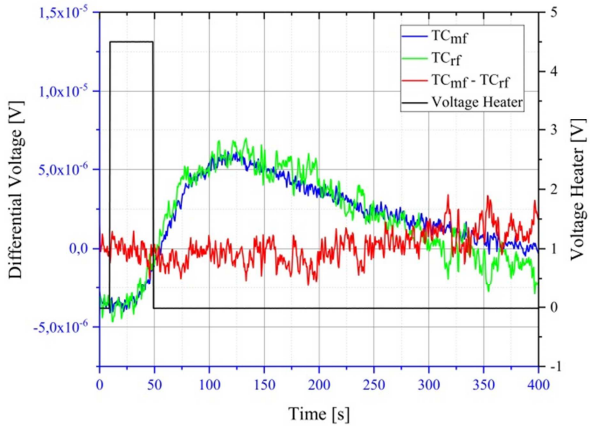

Figure 4: The voltage applied to the heater (black) and the output voltage of the thermocouples (blue and green) as well as their difference (red) for a flow of 0 µl/min. The output voltages are rather similar (as expected) and therefore the differential voltage remains almost zero.

RESULTS

The fabricated sensor in the channel was tested with oil (Titan 0W30 by Fuchs) as a testing fluid.

First, the inlet of the channel was connected to a syringe pump (ExiGo 1.0 by Cellix) and the inlet channel, the chamber and both outlet channels were filled with the fluid. Then one outlet was sealed so that no flow could take place in this channel arm.
As a first test, a power of 380 mW was applied to the heater for 40 seconds while the fluid in both channels was at rest. The thermocouple outputs were recorded during the heating and the cooling period (see Fig. 4). It can be seen that the temperature increased at both

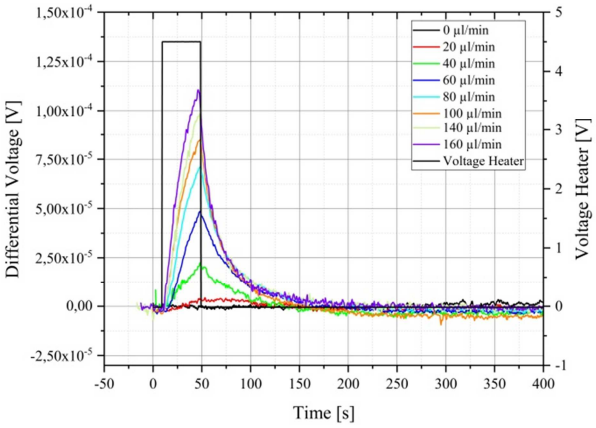

Figure 5: The voltage applied to the heater and the differential output voltage of the thermocouples for different flow velocities. The slope as well as the maximum temperature increase with increasing flow velocity.

thermocouples when the heater was turned on and continued to rise for some time after the heater was turned off due to the transport delay of the heat from heater to thermocouple. Also, the two thermocouples record the same temperatures (since the output voltages are the same) and therefore the difference remains almost zero for the whole period of heating and cooling.

Next, flow was introduced in one of the channels at different flow velocities. Again, the same power was applied to the heater and the difference in output voltage between the thermocouples was recorded. The results are shown in Fig. 5. It can be seen that with increasing flow velocity the difference in output voltage between the thermocouples increases. This is the case since with increasing flow velocity also the heat convection in the flow filled channel increases while the heat transfer in the channel with the resting fluid remains almost constant. Also, the heating and cooling process is accelerated by the flowing fluid.

CONCLUSION

The embedding technique presented here allows the integration of sensing and actuating elements into microfluidic channels made from bulk polymeric material using screen printing technique.

By gluing together polymeric parts using a solvent, leakages originating in the combination of different materials are prevented. A sacrificial layer of liquid metal prevents the clogging of the channel during the sealing process.

Since the screen printed layers are relatively thin, the flow in the microfluidic channels is not disturbed and the sensors and actuators can be completely embedded into the bulk polymer of the channel.

REFERENCES

[1] C. Offenzeller, M. Knoll, T. Voglhuber-Brunnmaier, M. A. Hintermuller, B. Jakoby, and W. Hilber, "Fully Screen Printed Thermocouple and Microheater Applied for Time-of-Flight Sensing in Microchannels," *IEEE Sens. J.*, vol. 18, no. 21, pp. 8685–8692, 2018.

[2] C. D. Meinhart, S. T. Wereley, and J. G. Santiago, "PIV measurements of a microchannel flow," *Exp. Fluids*, vol. 27, no. 5, pp. 414–419, Oct. 1999.

[3] V. Gass, B. H. der Schoot, and N. F. De Rooij, "Nanofluid handling by micro-flow-sensor based on drag force measurements," *Micro Electro Mech. Syst. 1993, MEMS'93, Proc. An Investig. Micro Struct. Sensors, Actuators, Mach. Syst. IEEE.*, pp. 167–172, 1993.

[4] Y. Su, A. G. R. Evans, A. Brunnschweiler, and G. Ensell, "Characterization of a highly sensitive ultra-thin piezoresistive silicon cantilever probe and its application in gas flow velocity sensing," *J. Micromechanics Microengineering*, vol. 12, no. 6, pp. 780–785, Nov. 2002.

[5] R. E. Oosterbroek, T. S. J. Lammerink, J. W. Berenschot, G. J. M. Krijnen, M. C. Elwenspoek, and A. van den Berg, "A micromachined pressure/flow-sensor," *Sensors Actuators A Phys.*, vol. 77, no. 3, pp. 167–177, 1999.

[6] A. Kuoni, R. l Holzherr, M. Boillat, and N. F. de Rooij, "Polyimide membrane with ZnO piezoelectric thin film pressure transducers as a differential pressure liquid flow sensor," *J. Micromechanics Microengineering*, vol. 13, no. 4, pp. S103–S107, Jul. 2003.

[7] T. Neda, K. Nakamura, and T. Takumi, "A Polysilicon Flow Sensor For Gas Flowmeters," *Proc. Int. Solid-State Sensors Actuators Conf. - TRANSDUCERS '95*, vol. 1, pp. 548–551, 1995.

[8] N. Sabaté, J. Santander, L. Fonseca, I. Gràcia, and C. Cané, "Multi-range silicon micromachined flow sensor," *Sensors Actuators A. Phys.*, pp. 282–288, 2004.

[9] M. A. Hintermüller and B. Jakoby, "Lab-scale prototyping of polymer based microfluidic devices using gallium as phase-changing sacrificial material," *Microelectron. Eng.*, vol. 211, pp. 50–54, 2019.

CONTACT

* C. Offenzeller, christina.offenzeller@jku.at

PIEZOELECTRIC THIN FILM ON SILICON RF-MEMS LAMB WAVE RESONATORS FOR FLUID PARAMETERS SENSING.

Y.L. Janssens[1] J.W. Berenschot[1] M.J de Boer[2] C.J. Hogendoorn[3] and *N.R. Tas*[1]
[1] MCS Faculty of Science and Technology, University of Twente, Enschede, The Netherlands
[2] MESA+ Institute, Nanolab, University of Twente, Enschede, The Netherlands
[3] Krohne New Technologies, Dordrecht, The Netherlands

This poster discusses the design, theory and fabrication of a Surface Acoustic Waves (SAW) device for fluid parameter sensing. To this purpose Lamb wave resonators actuated by means of interdigitated electrodes (IDT) on top of a Lead Zirconate Titanate, $Pb(Zr_xTi_{i-x})O_3$, (PZT) thin film close to the morphological boundary, x=0.53, will be used. For maximum sensing sensitivity a high Figure of Merit (FoM=k^2Q) is desired, this requires low acoustic loss inside the substrate, high electro-mechanical coupling k towards the piezoelectric thin film and high Q-factor at resonance. Edge reflections are used in order to form a standing wave increasing the Q-factor [1]. The change in phase velocity of the standing wave can directly be related to the density and viscosity of the fluid interacting with the wave [2, 3].

Lamb waves can propagate with an infinite number of unique phase velocities for both the anti-symmetric (A_n) and symmetric wave (S_n) modes as long as the Rayleigh-Lamb equation [4] is satisfied. The solution of the first two modes for a multilayered membrane are shown in Figure 1. The A_0 mode is of special interest for sensing applications as it allows for propagation below the compressional wave speed in liquids, resulting in minimum radiation loss. The phase velocity of the A_0 waves in a membrane loaded with a fluid having density ρ_0 and a compressional wave speed c_0 is:

$$f = \frac{c_p}{\lambda} = \frac{1}{\lambda}\left(\frac{B}{M_{\text{mem}} + \rho_0\delta_p + (\rho_0\mu_0/2\omega)^{1/2}}\right)^{1/2} \quad (1)$$

where λ is the wave length, c_p the phase velocity, M_{mem} the mass of the membrane, μ_0 the viscosity of the liquid and ω the angular frequency. The second term in the denominator accounts for the mass loading due to the density and the last term accounts for the mass loading due to the viscosity. The skin depth of the pressure wave as a result of the propagating wave and the effective bending stiffness equals:

$$\delta_p = \frac{\lambda}{2\pi\sqrt{1-(c_p/c_0)^2}} \quad (2)$$

$$B = \frac{\lambda}{2\pi n}T + \frac{Ed^3}{12(1-\sigma^2)} \quad (3)$$

where E is the effective Young's modulus, d the total membrane thickness, T the in plane tension, n is an integer multiple for n-th wave mode and σ the effective Poisson ratio. The additional mass loading due to the viscosity results in an additional shift in resonant frequency as shown in Figure 2. This indicates that a single measurement doesn't suffice to account for both loading effects. Decoupling can be achieved using higher order modes.

The Lamb wave resonators are fabricated by means of a five mask Silicon on Insulator (SOI) process. The thickness of the device, box and handle layer are 3/0.5/380 μm respectively (Figure 3). In the first step a 300 nm thermal silicon-oxide layer is grown. This layer acts as an electrical insulator and provides a suitable substrate during the high temperature PZT deposition process. Afterwards a 10/100 nm Ti/Pt layer is sputtered and a $LaNiO_3$/PZT layer, poly-crystalline (Figure 5), of 250 nm is grown by means of pulsed laser deposition. On top a 100 nm Pt layer is sputtered. The first mask is used to pattern the top metal followed by etching the $LaNiO_3$/PZT and bottom metal with the second mask. A connection towards the bottom electrode is made by locally etching the PZT, third mask. Around the device a contour release trench of 3 μm is etched, fourth mask. With the fifth mask the total device is released by means of a backside etch performed in two steps. First a pre-shape is made using deep reactive ion etching with a target depth of 355 μm, secondly an isotropic XeF_2 etch is performed. The advantage of this two step approach is the possibility for the release of large surface areas resulting in a flexible technology platform for the fabrication of Lamb wave resonators, a top view of a fabricated device is shown in Figure 4.

Word Count: 598

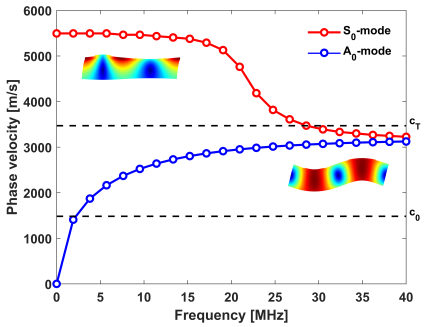

Figure 1: Numerical solution of the Rayleigh-Lamb equations for a multilayered membrane consisting of Si/SiO_2/Pt/PZT/Pt, with a thickness of 3/0.3/0.1/0.25/0.1 µm respectively, for the A_0 and S_0 wave modes. c_0 indicates the compressional wave speed in water and c_T the transverse wave velocity.

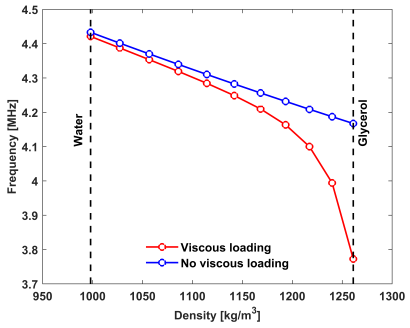

Figure 2: Numerical solution of a water-glycerol mixture at different mixing ratios for the A_0 wave mode showing the effect of additional mass loading due to viscosity for a multilayered membrane consisting of Si/SiO_2/Pt/PZT/Pt with a thickness of 3/0.3/0.1/0.25/0.1 µm respectively and a wave length equal to $\lambda = 80$ µm.

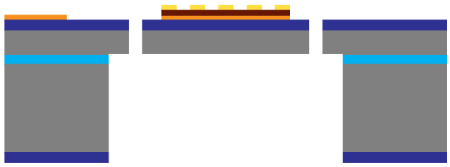

Figure 3: Cross section of the Lamb wave resonator design based on edge reflections for the propagating wave. The highlighted regions are: Silicon oxide, Pt IDT electrodes, Ti/Pt bottom electrode, Silicon , Lead Zirconate Titanate (PZT), BOX layer .

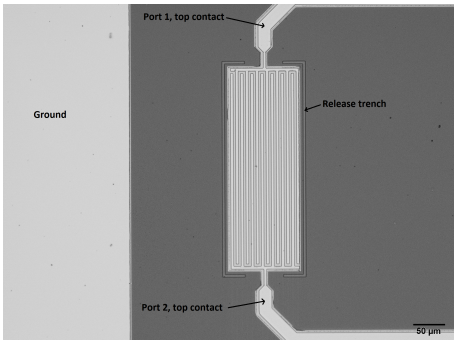

Figure 4: Top view of the designed two port PZT on silicon Lamb wave resonator, size of the resonator equals 324 × 116 µm^2.

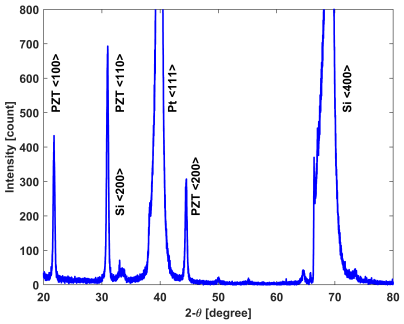

Figure 5: XRD measurement of the pulsed layer deposited poly-crystalline PZT layer. The total measured layer consists of Si/SiO_2/Ti/Pt/LNO/PZT.

REFERENCES

[1] V. Plessky and J. Koskela. Couplingn-of-modes analysis of saw devices. *International Journal of High Speed Electronics and Systems*, 10:867–947, 2000.

[2] R.M. White and S.W. Wenzel. Fluid loading of a lamb-wave sensor. *American Institute of Physics*, 53(20):1653–1655, 1988.

[3] S.W. Wenzel B.A. Martin and R.M. White. Viscosity and density sensing with ultrasonic plate waves. *Sensors and Actuators*, pages 704–708, 1990.

[4] H. Lamb. On waves in an elastic plate. *Proceedings of the Royal Society of London. Series A, Containing Papers of a Mathematical and Physical Character*, 93(648):114–128, 1917.

FABRICATION METHOD OF MICROFLUIDIC CHANNELS WITH CIRCULAR CROSS SECTION FOR MICRO-CORIOLIS MASS FLOW SENSOR

Q. Yu[1], H. Veltkamp[1], M.J. de Boer[1], R.J. Wiegerink[1] and J.C. Lötters[1,2]
[1] MESA+ Institute for Nanotechnology, University of Twente, Enschede, The Netherlands
[2] Bronkhorst High-Tech BV, Ruurlo, The Netherlands

ABSTRACT

This paper presents a new fabrication method to realize a channel underneath the surface of a single silicon substrate for micro Coriolis flow sensing application, as well as other multiparameter systems, such as thermal flow sensors. It allows to fabricate channels with a nearly perfect circular cross section without bonding of two wafers. With this technology, problems such as leakage, deformation of channels due to pressure and temperature that affect the performance of micro Coriolis flow sensor can be reduced significantly. Moreover, it leaves only very little topography on the surface of substrate, hence integration of actuation and readout systems by metal deposition can still be followed easily afterwards.

KEYWORDS

Circular cross section, Buried channel technology, Wet etch, HNA, Flow sensors, Microfluidics

INTRODUCTION

The concept of this new method for fabricating microfluidic channels for micro Coriolis flow sensing application is based on the combination of Buried Channel Technology (BCT) [1, 2] and silicon isotropic wet etching, which is known as HNA etching [3]. With this combination, it allows to fabricate a channel buried in Si substrate. With a starting point of etching at the bottom of a trench instead of at the substrate surface, a channel with a circular cross section can be realized by isotropic etching of Si. Compared to the Surface Channel Technology (SCT), which was used as a standard technology for the fabrication of Coriolis mass flow meter and other microfluidic devices [4, 5, 6], this new method has the potential to achieve much larger micro structures.

Buried Channel Technology

Buried Channel Technology, or so called BCT, derived from the well-known SCREAM process, was invented in 1999 at MESA+ Institute to fabricate micro structures for fluidic applications in silicon substrate [1, 2, 7]. It allows to fabricate channels buried in the silicon substrate. The main steps of this process are trench etching, coating, bottom coating removal and etching of channel. Figure 1 shows the cross section of channel fabricated by BCT. By adjusting the width and depth of trenches, different sizes of channels can be realized in one substrate with only one step of lithography, which gives the possibility to integrate multi microfluidic devices with one lithographic mask.

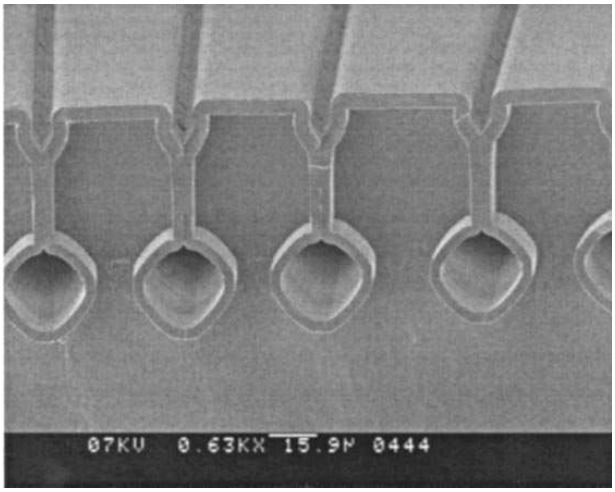

Figure 1: SEM image of cross sections of channels fabricated by BCT [1].

Si Isotropic Wet Etching

Silicon isotropic wet etching, also known as HNA etching, is a chemical etching of silicon by a mixture of hydrofluoric acid (H), nitric acid (N) and acetic acid (A), while some researchers like to use water instead of acetic acid. It is proceeded by a sequential oxidation-followed-by-dissolution process [3, 8]. The complete reaction can be described as:

$$Si + 2\,HNO_3 + 6\,HF \longrightarrow H_2SiF_6 + 2\,HNO_2 + 2\,H_2O$$

The factor that limits the etch rate is highly dependent on the composition of mixture. When the concentration of nitric acid is low and hydrofluoric acid is high, the etch rate of process is limited by the oxidation step. When in opposite situation, the limit is then the dissolution of SiO_2. B. Schwartz *et al* investigated and explained in detail the etching mechanism behind this process in [3]. Figure 2 shows

a semi-circular cross section of etched silicon substrate through a 10µm-wide line.

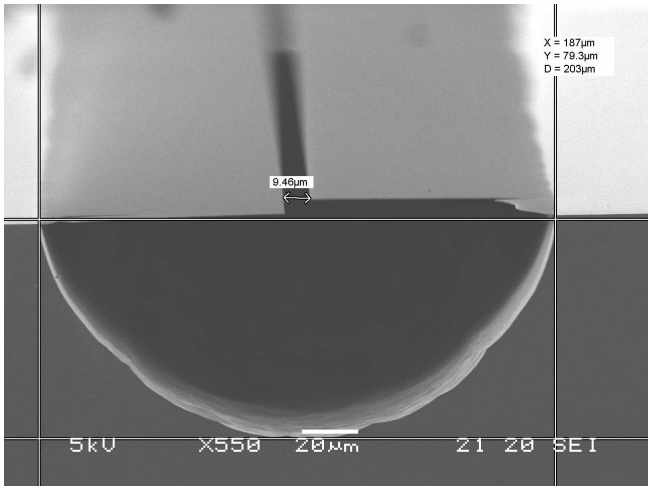

*Figure 2: SEM image of cross sections of channels etched in HNA solution (69%HNO_3:50%HF:H_2O=2:1:2) for 60*min *with SiRN mask.*

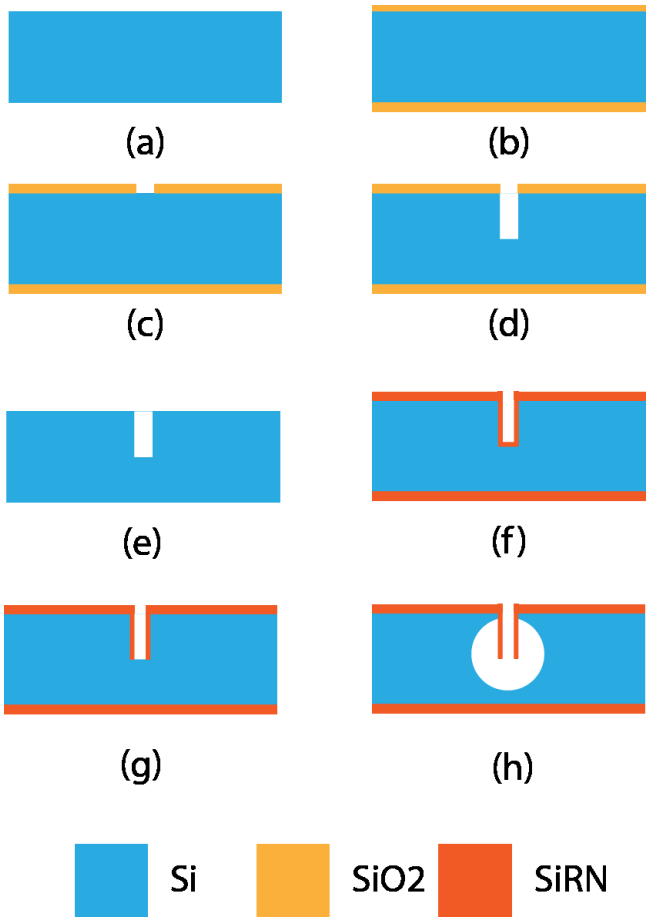

*Figure 3: Cross section view of fabrication steps for creating buried channels. (a): Bare silicon wafer. (b): Silicon wafer with 500*nm *SiO_2. (c): Patterning of line openings. (d): Trench etching. (e): Stripping of SiO_2. (f): SiRN coating. (g): Trench bottom coating removal. (h): Channel etching.*

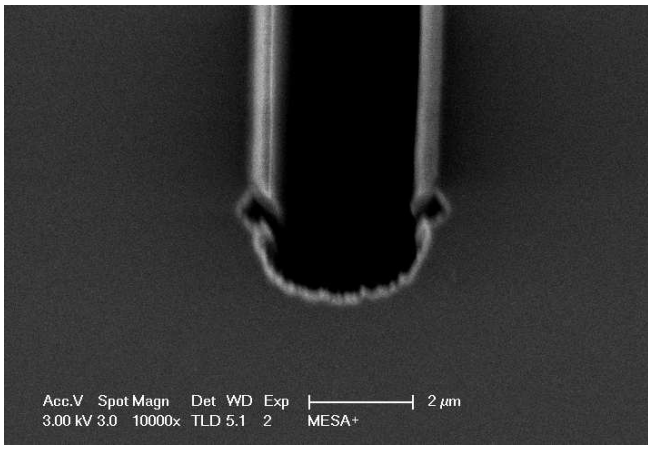

*Figure 4: SEM image of bottom coating removed trench (3*µm *wide) from early test to optimize the recipe of process.*

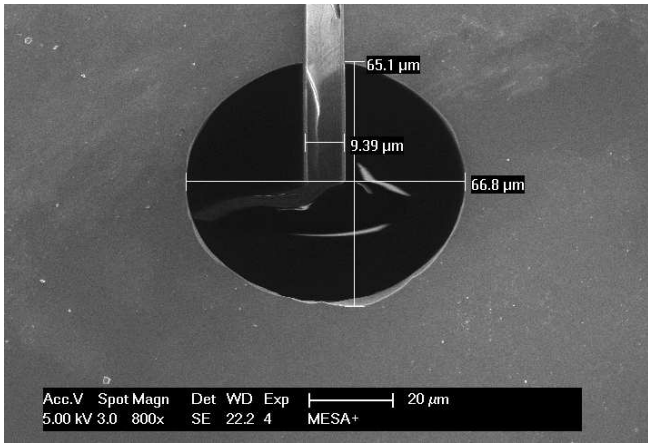

*Figure 5: SEM image of cross section of a channel after 65*min *etching in HNA (69%HNO_3:50%HF:H_2O=2:1:2).*

FABRICATION

An overview of fabrication process can be seen in Figure 3. The steps are all done with standard recipe in the cleanroom of MESA+. First, silicon substrate is cleaned and oxidized to obtain a layer of 1µm SiO_2 (Figure 3b), serving as hard mask for Si etching in later steps. Lines with width of 10µm are etched through this layer (Figure 3c) and then followed by BOSCH process to produce trenches (Figure 3d). After that, SiO_2 layer is stripped by HF (Figure 3e) and coating of trenches is done by LPCVD 1µm low stress silicon rich nitride (SiRN) (Figure 3f). To remove the coating at the bottom of trenches, a PECVD SiO_2 layer is used as mask to protect SiRN on substrate surface. Due to the fact that trenches are of high aspect ratio and PECVD is a non-conformal deposition, bottom of the trench is not covered by this SiO_2 layer. Thus by running a plasma etching of SiRN, coating at bottom of trenches can be removed while substrate surface and sidewall of trenches

stay. Figure 4 shows the bottom of trench after removing the coating layer. After successfully removing the bottom coating of trenches, the substrate is then etched in HNA solution (69%HNO_3:50%HF:H_2O=2:1:2) for 65mins. The cross section is shown in Figure 5.

DISCUSSION

Compare the result shown in Figure 5 to Figure 2, the etch rate of silicon decreases significantly, this is due to the fact that diffusion of etching product and etchant through the deep trench is more difficult than through line openings on the substrate surface. A magnetic stirrer or ultrasonic bath can be the solution to achieve a higher etch rate. Together with a sufficient supply of etchant, the maximum diameter of etched channels will be limited only by the depth of trench and thickness of SiRN mask. From the earlier test, SiRN is a good material serves as mask for HNA solution, with an etch rate of approximately 2$\sim$3nm per minute. A thicker layer of SiRN can stand longer during etching, however, as a trade-off it also becomes more difficult to remove the layer at the bottom of trenches. Thus an alternate material can be considered to serve as mask for HNA solution for the future.

CONCLUSION & OUTLOOK

A brief introduction of how to fabricate channels buried in a silicon substrate with a nearly perfect circular cross section is presented. The result is preliminary but shows a potential for producing extra-large channels of diameters up to few hundreds $\mu\mathrm{m}$ with this technology. Compared to channels fabricated by standard SCT, the main advantages of this new method are: 1) Reduction of temperature and pressure dependency for micro Corilis flow sensing application due to the nearly circular cross section, 2) A wider flow range can be covered with different sizes of channels. Furthermore, the cost of fabrication can be reduced as well since channels are etched by wet chemicals instead of plasma. Next step of the work will be focused on optimizing fabrication steps to realize an extra-large channel, then followed by sealing and releasing to achieve a free suspended tube for micro Coriolis flow sensing application.

REFERENCES

[1] Meint J. de Boer, R. Willem Tjerkstra, J.W. (Erwin) Berenschot, Henri V. Jansen, G.J. Burger, J.G.E (Han) Gardeniers, Miko Elwenspoek and Albert van den Berg "Micromachining of Buried Micro Channels in Silicon", Journal of Microelectromechanical Systems Volume: 9, Issue: 1, March, 2000, pp. 94-103.

[2] Rint Willem Tjerkstra, "ISOTROPIC ETCHING OF SILICON IN FLUORIDE CONTAINING SOLUTIONS AS A TOOL FOR MICROMACHINING" University of Twente, Enschede, 1999.

[3] B. Schwartz and H. Robbins, "Chemical Etching of Silicon IV . Etching Technology", J. Electrochem. Soc. 1976 volume 123, issue 12, 1903-1909.

[4] Jarno Groenesteijn, Meint J. de Boer1, Joost C. Lötters, Remco J. Wiegerink, "A versatile technology platform for microfluidic handling systems, part I: fabrication and functionalization", Microfluid Nanofluid (2017) 21:127.

[5] Jarno Groenesteijn, Meint J. de Boer1, Joost C. Lötters, Remco J. Wiegerink, "A versatile technology platform for microfluidic handling systems, part II: fabrication and functionalization", Microfluid Nanofluid (2017) 21:126.

[6] Jarno Groenesteijn, "Microfluidic platform for Coriolis-based sensor and actuator systems" University of Twente, Enschede, 2016.

[7] R.W. Tjerkstra, M. De Boer, E. Berenschot, J.G.E. Gardeniers, A. van den Berg and M. Elwenspoek, "ETCHING TECHNOLOGY FOR MICROCHANNELS", Proceedings IEEE The Tenth Annual International Workshop on Micro Electro Mechanical Systems. An Investigation of Micro Structures, Sensors, Actuators, Machines and Robots (Jan 1997), Nagoya, Japan

[8] Wing Cheong Hui, "How to prevent a runaway chemical reaction in the isotropic etching of silicon with HF/HNO3/CH3COOH or HNA solution", Proc. SPIE 5276, Device and Process Technologies for MEMS, Microelectronics, and Photonics III, (2 April 2004).

CONTACT

* Q. Yu, q.yu-3@utwente.nl

RELAXOR FERROELECTRIC THIN FILM FOR PIEZOMEMS

Shu Ni[1]

[1]University of Twente, Inorganic Material Science Group, Enschede, The Netherlands

For electro-acoustic devices, the figure of merit (f) of the piezoelectric layer affects the acoustic power output and the signal-to-noise ratio of the device tremendously. The f parameter is the product of electromechanical coupling K^2 and mechanical quality Q factors. The K^2 indicates the conversion efficiency between the electrical and mechanical energy, which is associated with the piezoelectric responses of the material; the Q represents the ratio between the energy loss and stored mechanical energy, which indicates the heat generation characteristics of the layer[1]. Most high coupling piezoelectric materials, for example lead zirconate titanate ($PbZr_{1-x}Ti_xO_3$ or PZT, $K^2 \approx 28\%$) usually shows low value of Q, due to its hysteric feature, which comes from its domain wall motion; High Q piezoelectric material, such as AlN ($Q \approx 2700$), usually shows low K^2($\approx 6\%$)[2]. Relaxor-ferroelectric materials, can achieve excellent K^2 and Q simultaneously, due to its the existence of polar-nano-regions (PNRs) at unit cells. PMN-PT ((1-x)Pb ($Mg_{1/3}Nb_{2/3}$)-x$PbTiO_3$) is a widely used relaxor ferroelectric materials, which show a superior K^2 ($K^2 \approx 90\%$) and a good Q ($Q \approx 850$). However, it is really challenging to fabricate PMN-PT with pure perovskite phase. S. L. Swartz and T. R. Shrout developed the columbite process in 1982 for the synthesis of bulk PMN-PT ceramics[3]. This process can bypass the pyrochlore phase formation by facilitating the reaction between MgO and NbO prior to the addition of and reaction with PbO. Nonetheless, this method is not useful for thin film growth. Avoiding prycholre in the PMN-PT thin film is still extremely hard, which limits the integration of PMN-PT thin film to MEMS devices.

By using La doped BaSnO3 (LBSO) as the bottom electrode, we have successfully deposited of PMN-PT thin film with pure perovskite phase up to 1 um thick, as shown in the XRD data Figure 1. The application of La doped BaSnO3 reduces greatly the lattice mismatch and changes the strain state from compressive strain to tensile strain. As shown in Figure 2, the Full Width Half Maximum (FWHM) of the PMN-PT (002) peak, which indicates the crystal quality of PMN-PT, is around 0.39, which is almost an order higher than the commercial bulk single crystal[4]. The surface morphology was characterized by the Atomic Force Microscopy (AFM), the resulting profile is shown in figure 2. The root mean square (RMS) roughness is around 0.9826 nm, which shows the roughness of the surface is around 0.01% of the thickness of the film.

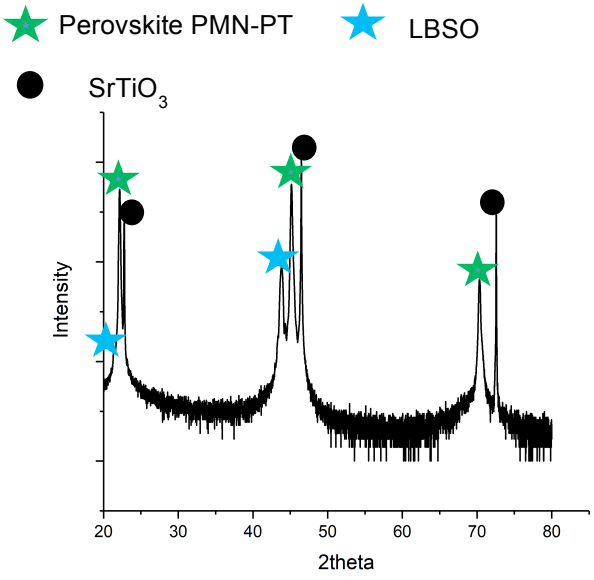

Figure 1, symmetrical scan spectrum of PMN-PT\LBSO\PMN-PT.

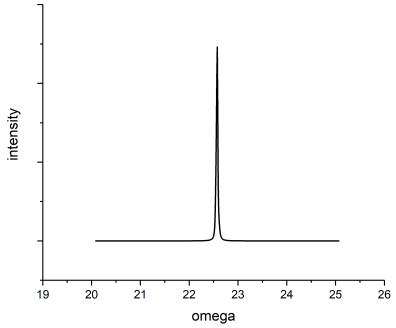

Figure 2 Rocking curve of PMN-PT of 1 um thick

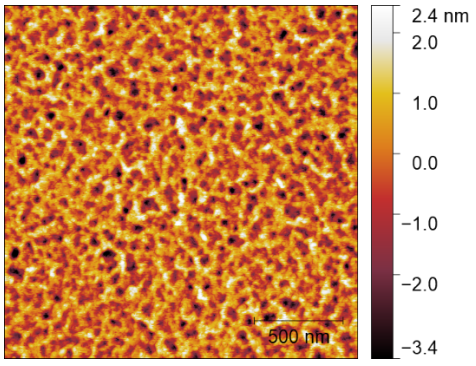

Figure 3. surface morphology of PMN-PT thin film of 1 um thick.

Word Count: 399

REFERENCES

[1] Liu, Gang, et al. "Losses in ferroelectric materials." Materials Science and Engineering: R: Reports 89 (2015): 1-48.
[2] Fu, Yong Qing, et al. "Advances in piezoelectric thin films for acoustic biosensors, acoustofluidics and lab-on-chip applications." Progress in Materials Science 89 (2017): 31-91.
[3] Swartz, S. L., and Thomas R. Shrout. "Fabrication of perovskite lead magnesium niobate." Materials Research Bulletin 17.10 (1982): 1245-1250.
[4] Baek, S. H., et al. "Giant piezoelectricity on Si for hyperactive MEMS." Science 334.6058 (2011): 958-961.

TOWARDS INTEGRATED CIRCULAR FLOW TUBES WITH LARGE DIAMETER

M. Yariesbouei[1],M.A.Rodriguez Olguin [2] , R.J. Wiegerink[1], and J.C. Lötters[1,3]
[1] University of Twente, Integrated Devices and Systems, Enschede, The Netherlands
[2] Mesoscale Chemical System, Mesa+ Institute for Nanotechnology, University of Twente, Enschede, The Netherlands
[3] Bronkhorst High-Tech BV, Ruurlo, The Netherlands

ABSTRACT

In this paper we propose two novel methods for the fabrication of microfluidic channels with circular cross-section and a relatively large diameter in the range of 300 to 1000 µm. The aim is to use such channels in a micro Coriolis mass flow sensor as an alternative to the well-known Surface Channel Technology (SCT). One method is based on sol-gel technology, where PDMS mold is coated with silicon oxide to form the channel wall. The other method involves electroplating of a copper or nickel channel wall around a wire of ABS.

KEYWORDS

Large diameter circular microchannels, micro Coriolis mass flow sensor, sol gel, electroplating

INTRODUCTION

Surface channel technology (SCT) [1] allowed fabrication of the most sensitive micro Coriolis mass flow sensor to date. However, the technology has limitations in that the channels are not really circular and that the channel diameter cannot be easily scaled to diameters larger than about 80 µm. These limitations result in drawbacks for micro Coriolis mass flow sensors such as (1) non linearity of the flow measurement, (2) pressure sensitivity of the flow and density measurement and (3) a relatively large pressure drop at high flows [2]. In order to reduce the pressure sensitivity and increase the flow range, the tube cross-section should be more circular and the diameters should be increased up to, ideally, 1000 µm. In this paper we propose two alternative fabrication methods that could result in such tubes.

One alternative method that could result in almost perfectly circular channels with various diameter and wall thickness is the sol-gel method. Figure 1 shows a process outline of how this method can be used to realize channels with a wall of silicon dioxide. A PDMS mold is made and coated with a silicon oxide layer that will form the channel wall after selectively removing the PDMS.

Another alternative method that we are investigating is electroplating [3]. Electroplating method can be performed on wires of Acrylonitrile-Butadiene-Styrene, ABS [4], which can afterwards be dissolved by acetone. Figure 2 shows the process scheme of this method.

SOL-GEL METHOD

Figure 1 shows an overview of the sol-gel that we investigated. The process starts by making a PDMS mold by using the Embedded Scaffold Removing Opening Technology, ESCARGOT [5]. An ABS wire which is commonly used in 3D printing is immersed into liquid PDMS. Next, the PDMS is cured at 60 °C for 1 hour and the ABS wire is dissolved in a PDMS-inert solvent. Figure 1(a) shows the cross-section of the PDMS channel that is used as a mold.

The PDMS mold is flushed with Piranha for 35 to 70 s, see Figure 1(b), in order to create hydroxyl groups at the PDMS surface. Next, the mold is rinsed with DI water and dried by nitrogen flow. The mold now contains hydroxyl groups at the inner surface, see Figure 1(c). If the mold is not completely covered by hydroxyl groups the subsequent sol-gel coating will not be uniform.

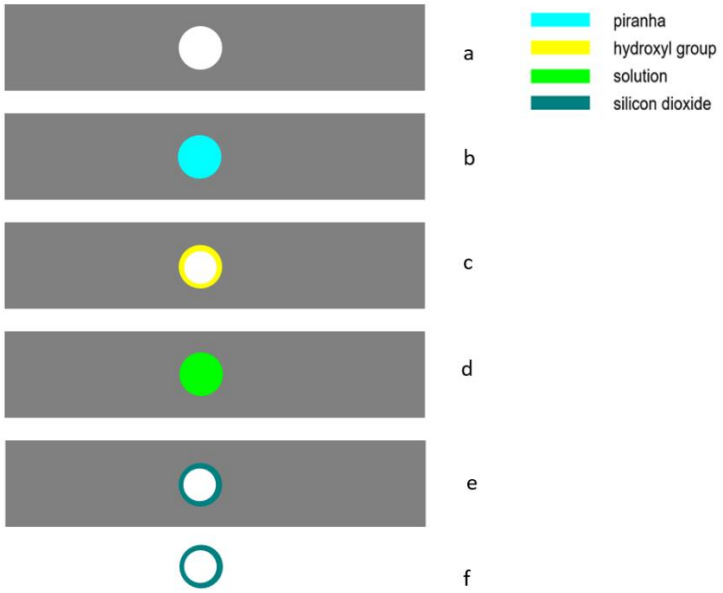

Figure 1: Schematic representation of sol-gel method (a) Circular PDMS channel (b) Oxidizing surface by flushing piranha (c) Cleaning oxidized polymer in DI water and drying with nitrogen gas (d) Flush with sol-gel solution (e) Flush with air (f) Etch PDMS in piranha.

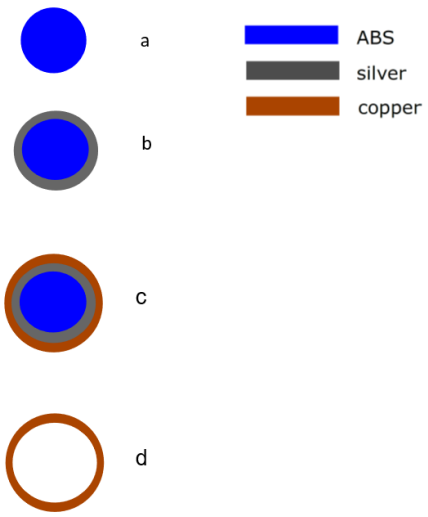

Figure 2: Schematic representation of electroplating method (a) ABS wire (b) Apply coating of silver conductive paint (c) Copper plating (d) Etch ABS wire.

The sol-gel mixture is created by mixing TEOS, MTES, ethanol and water in a 1:1:1:1 volumetric ratio. The pH of the water in this mixture is adjusted to 4 by adding HCl [6]. To speed up preconversion, the mixture is placed in an oven at 60 °C for 12 hours.

Next, the sol-gel mixture is slowly flushed through the channel using a syringe pump at a flow rate of 0.5 to 1 ml/h, see Figure 1(d). To initiate the gelation reaction, the channel must be placed on a hot plate at 55-60 ºC. This temperature is limited by 2 factors: ethanol evaporation that leads to a non-uniform channel and the glass transition temperature of PDMS. When the desired coating thickness is reached, air flow is used to flush out the remaining solution, see Figure 1(e). The last step is dissolving the mold for releasing the coating by a solution which does not affect the coating, Figure 1(f).

Figure 3 shows a SEM image of the resulting coating inside a circular channel with a diameter of 600 µm. Figure 4 illustrates the importance of the pre-treatment with Piranha. In this case only part of the channel surface contained hydroxyl groups and a very non-uniform silicon dioxide coating is obtained.

Our first results show that the thickness of the coating can be controlled by the time and temperature of the coating process, and the flow rate of the syringe pump. The time of the coating is limited by two factors. First, flushing the channel by sol gel mixture for a long time caused diffusion of the chemicals into the PDMS. Figure 5 shows the cross section of a channel after 3 hours of flushing the sol gel mixture inside the channel. It clearly shows that the structure of the PDMS around the channels has changed and this will limit the wall thickness that can be realized. Second, flushing the mixture for a short time results in a very thin wall and cracks in the coating. Figure 6 shows the cracks in a thin wall.

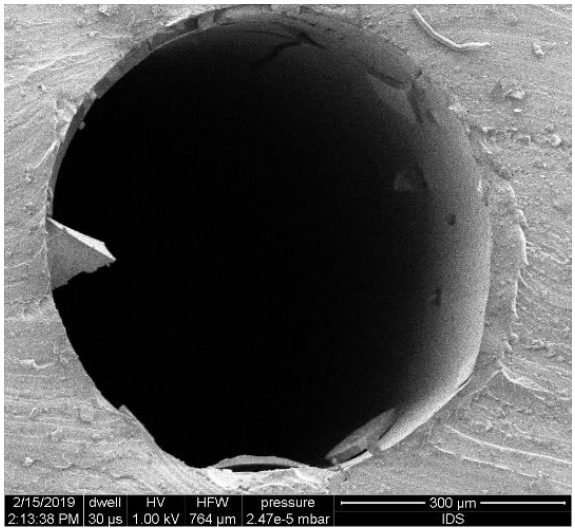

Figure 3: Scanning electron microscopy image of silicon dioxide coating in a circular PDMS channel with a diameter of 600 µm.

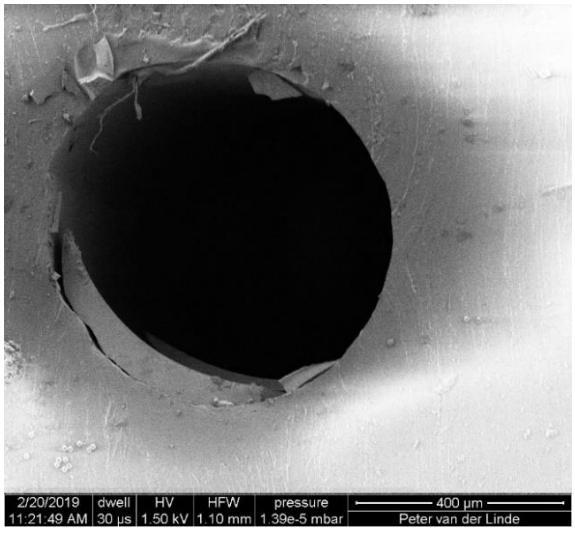

Figure 4: Scanning electron microscopy image of the non-uniform silicon dioxide coating in a circular PDMS channel which was not completely oxidized.

In order to realize a free-standing tube we tried to selectively dissolve the PDMS around the coating in Piranha. However, this appeared to be a problem because PDMS does not dissolve in Piranha easily and also part of the coating dissolved.

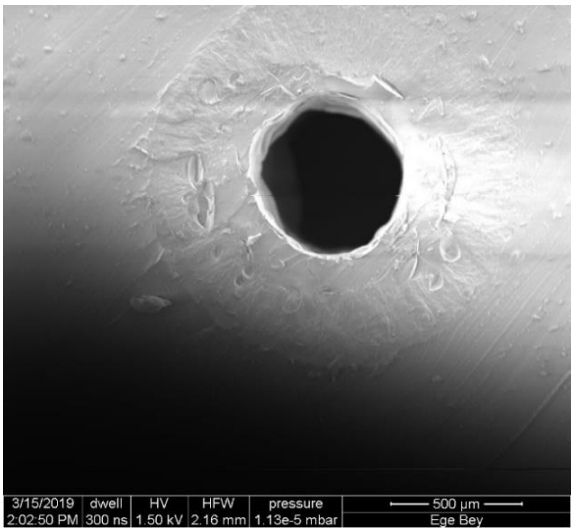

Figure 5: Scanning electron microscopy image of the circular PDMS channel after 3 hours of flushing the sol gel mixture inside the channel.

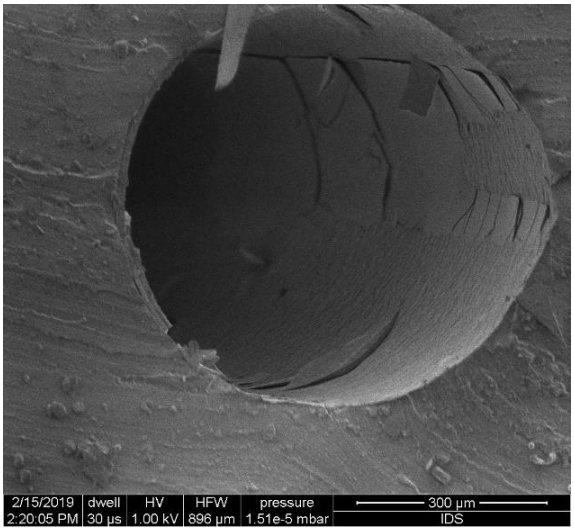

Figure 6: Scanning electron microscopy image of a thin silicon dioxide coating showing cracks in the circular PDMS channel.

ELECTROPLATING METHOD

The other technique to realize circular channels with large diameters that we investigated was electroplating on an ABS wire. A copper electroplating cell was used consisting of a copper anode, an ABS wire as cathode, an aqueous copper solution and a DC power supply. To produce an electrically conductive cathode the FDM-ABS wire, see Figure 2(a), is coated by silver conductive paint and dried in room temperature, Figure 2(b) [7]. A volume of 1 liter aqueous copper solution contains 0.1 kg copper salt, 0.11 liter 96% sulphuric acid, 0.15 ml 50%HCL, 10 ml HL11 starter and 0.25 ml HL13 grain refiner. DI water is added to reach the given volume [8]. The electroplating was done at room temperature with a current density of 3 A/dm^2, see Figure 2(c) [9]. After electroplating, the substrate is rinsed with ethanol to prevent oxidation of the electroplated copper. Next, the wire is immersed in a beaker of acetone for 12 hours to completely etch the ABS wire inside, Figure 2(d). Instead of ABS, PVA polymer could also be used which can be dissolved in hot water. Figure 7 shows a photograph of the resulting freestanding channel.

(a)

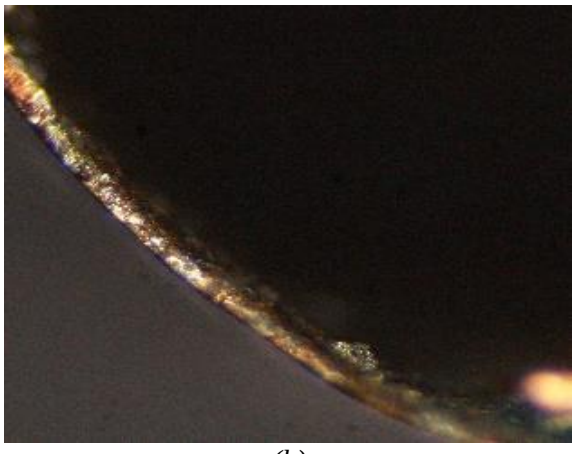

(b)

Figure 7: (a) Two channels realized by copper electroplating on a ABS wire, and (b) close up of the wall of the channel

CONCLUSION

Two alternative methods for the fabrication of large diameter circular channels were investigated: 1) by coating the inside of a PDMS mold using a sol-gel process, and 2) by electroplating an ABS wire.

Realization of free standing tubes with the sol-gel method appears to be a problem because PDMS does not dissolve easily. Further research is needed to find

a suitable method to selectively remove the PDMS from the silicon oxide coating.

The first results of the electroplating method are promising. Free standing copper tubes were successfully fabricated. Further research will focus on improvement of the electroplating method and the fabrication of channels that are attached to a substrate.

REFERENCES

[1] J. Haneveld, et al., "Modeling, design, fabrication and characterization of a micro Coriolis mass flow sensor", *J. Micromech. Microeng*., 20 (2010) 125001.

[2] D. Alveringh, et al., "Integrated pressure sensing using capacitive Coriolis mass flow sensors," *J. MEMS*, 26, 3, 2017.

[3] M. Schlesinger, and Milan Paunovic, *Modern electroplating*, 5th edition, Wiley, 2010.

[4] S. Olivera, et al., "Plating on acrylonitrile–butadiene–styrene (ABS) plastic: a review", Springer, 2016.

[5] V. Saggiomo and A.H. Velders, "Simple 3D printed scaffold-removal method for the fabrication of intricate microfluidic devices," *Adv. Sci*., 2015.

[6] A.R. Abate, et al., "Glass coating for PDMS microfluidic channels by sol–gel methods," *Lab on a Chip*, 2008.

[7] M.D. Monzon, et al., "Advantages of fused deposition modeling for making electrically conductive plastic," *Int Conf. Manuf. Autom*., (2010).

[8]A.J. Ooathoek-de Vries, et al., "Continuous flow H and C NMR spectroscopy in microfluidic stripline NMR chips," *Analytical Chemistry*, 2017.

[9] Z. Wang, et al., "Adhesion improvement of electroless copper to a polyimide film substrate by combining surface micro roughening and imide ring cleavage," *J. of Adhesion Science and Technology*, 2012.

CONTACT

* M. Yariesbouei, M.Yariesbouei@utwente.nl

MICROWAVE-BASED TEMPERATURE MONITORING OF NANOLITER WATER SAMPLES USING A WATER-ONLY TEMPERATURE CALIBRATION TECHNIQUE

G. Maenhout[1], T. Markovic[2,1], J. Bao[1], G. Stefanidis[3], I. Ocket[2,1] and B. Nauwelaers[1]
[1] Dept. Electrical Engineering, KU Leuven, Kasteelpark Arenberg 10, 3001 Leuven, Belgium
[2] Imec, Kapeldreef 75, 3001 Heverlee, Belgium
[3] Dept. Chemical Engineering, KU Leuven, Celestijnenlaan 200F, 3001 Leuven, Belgium

ABSTRACT

In this work, we present a novel electrical, non-intrusive and label-free temperature measurement technique for nanoliter water volumes. A planar interdigital capacitor (IDC) volumetrically interrogates the loaded water sample under test. A vector network analyzer (VNA) measures the reflection coefficient of the IDC, which senses temperature-dependent changes in capacitance due to the temperature-dependent permittivity of water. The system is calibrated by bringing it, while loaded with a water sample, to three, known temperatures and by measuring the corresponding reflection coefficient. An operating frequency was chosen at 2 GHz in order to achieve the most accurate results. The presented measurement and calibration technique has been validated in the temperature range from 20°C to 50°C.

KEYWORDS

Temperature sensor, microwave sensor, microfluidics, dielectric measurement, temperature calibration.

INTRODUCTION

Microfluidic devices bring new opportunities in a vast number of applications, in which the control of temperature is often required [1]. Due to the inherit size of the employed nanoliter droplets, several challenges exist with regards to temperature measurements. These challenges vary from thermal loading of to Joule-induced hot spots in the sample while ideally a minimal perturbation of the sample under test is desired [2].

While microwave heating is already applied in digital as well as continuous microfluidic platforms [3, 4], microwave-based temperature monitoring is a less established technique. Due to the initial interest in heating, the dielectric permittivity was studied in detail as a function of frequency as well as temperature. As established in [5], the dielectric permittivity is strongly temperature-dependent, which can be exploited for temperature sensing.

In the next section, the theory and core principles behind the presented technique will be explained as well as the design and manufacturing of the sensor and the measurement setup. Next, the obtained results will be displayed and discussed, followed by opportunities for future work with this novel measurement technique.

MATERIALS AND METHODS

Theory and Principles

In the work of [5], the temperature dependency of the permittivity of water is established over a broad frequency range. This creates the possibility for dielectric temperature sensing. In this field, the dominant parameter for the frequency selection is the real part of the complex permittivity (ϵ') because it directly influences the capacitive change of the sensor. To obtain the most sensitive temperature measurements, the difference $\Delta\epsilon'$ per °C should be maximal at the operating frequency. It can be observed that up to 2 GHz, ϵ' changes significantly under influence of temperature as shown in Fig. 1. At higher frequencies, the difference $\Delta\epsilon'$ diminishes and the ϵ' curves start to overlap at different temperatures, which creates less accurate results and even ambiguities in the measurement read-out system resulting in a faulty temperature. However, using higher fre-

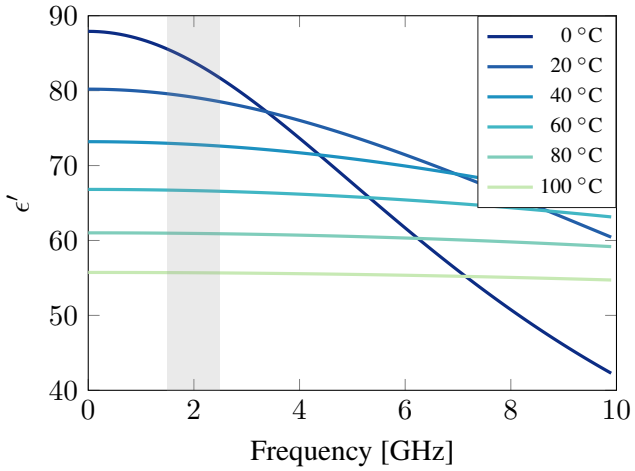

Figure 1: The real part of the permittivity (ϵ') of pure water for frequencies ranging from DC to 10 GHz and for multiple temperatures (based on [5]).

quencies shrinks the size of the microwave components. Therefore, this work focuses on the 1.5-2.5 GHz frequency range.

A standard calibration of the VNA shifts the reference plane to the SMA-connector off the chip but in order to extract the permittivity of the sample, the reference plane needs to be shifted from the connector to the permittivity-dependent capacitance. This step requires three standards, each with a different permittivity value. Since we know that the permittivity of DIW is temperature-dependent, we propose in this work to measure the reflection coefficient of the IDC when it is loaded with water at three different temperatures. The proposed water-only temperature calibration technique does not require loading different liquids with specific mixture ratios nor does it need accurate permittivity models of multiple calibration liquids. With respect to these calibration measurements, the permittivity of the sample is extracted with the following formula, used for an open-ended coaxial probe [6] as well as for an interdigital capacitor [7]:

$$\frac{(\epsilon_M - \epsilon_A) \times (\epsilon_B - \epsilon_C)}{(\epsilon_M - \epsilon_B) \times (\epsilon_C - \epsilon_A)} = \frac{(\Gamma_M - \Gamma_A) \times (\Gamma_B - \Gamma_C)}{(\Gamma_M - \Gamma_B) \times (\Gamma_C - \Gamma_A)}. \quad (1)$$

Since we can calculate the permittivity of the sample under test with (1), we can compare this extracted permittivity $\epsilon_{\text{extr.}}$ with values found in literature $\epsilon_{\text{lit.}}(f,T)$ [5] to obtain the sample temperature. The predicted temperature T is the one that minimizes the Euclidean distance $g(T)$ between $\epsilon_{\text{extr.}}$ and $\epsilon_{\text{lit.}}(f,T)$ over the entire measured frequency range:

$$g(T) = \sum_{\text{f=1.5 GHz}}^{\text{2.5 GHz}} \Big(\big(\text{Re}\left[\epsilon_{\text{extr.}} - \epsilon_{\text{lit.}}(f,T)\right] \big)^2 + \big(\text{Im}\left[\epsilon_{\text{extr.}} - \epsilon_{\text{lit.}}(f,T)\right] \big)^2 \Big)^{1/2}. \quad (2)$$

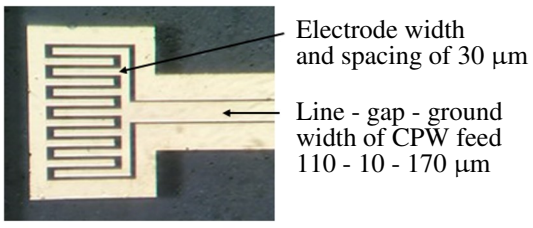

Figure 2: Photograph of the manufactured gold-on-quartz interdigital capacitor and its feeding line in coplanar waveguide with corresponding dimensions.

Measurement Setup

An interdigital capacitor (IDC) topology in coplanar waveguide (CPW) technology was chosen as sensor because of its uniplanar structure, its inexpensive fabrication process and its smooth integration with nowadays-existing microfluidic platforms. Additionally, the designed, planar IDC achieves a volumetric field distribution that allows temperature sensing of the bulk liquid and the IDC is a one-port structure that simplifies the setup and reduces the number of required connections to the measurement equipment. The electrode width and spacing are chosen at 30 µm. This results in a sensing depth of 60 µm [8], which is adequate since it corresponds with the height of channels used in microfluidic platforms.

The sensor is fabricated with a gold-on-quartz process and is shown in Fig. 2. A photoresist is spin-coated on the wafer and patterned using a UV-lithography step. Next, a 50 nm chromium layer is deposited on the wafer. This chromium layer is used to promote a better adhesion between gold and quartz. A 400 nm gold layer is deposited afterwards. At last, the resist is removed resulting in the gold IDC pattern on the quartz wafer. Afterwards, a polydimethylsiloxane (PDMS) ring is bonded to the quartz substrate to guarantee a stationary position of the sample throughout multiple measurements.

The quartz chip with the IDC is placed on an aluminum block with an embedded, regulated resistive heater, it is heated to multiple temperatures and the temperature of the sample is monitored with a type K thermocouple with a relative accuracy of ± 1°C. The thermocouple is placed in the PDMS ring as shown in Fig. 3. A system calibration with a standard open-short-load calibration kit placed the reference plane at

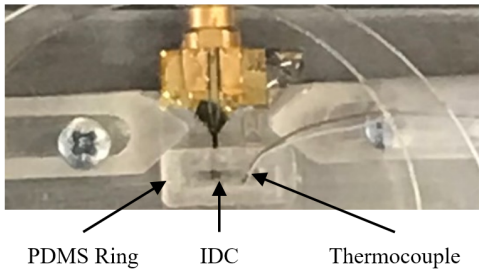

Figure 3: Photograph of the measurement setup where the PDMS ring, bonded to the quartz substrate, creates a reliable reservoir for the sample under test, in which the thermocouple is placed as well.

the SMA-connecter and the reference plane was shifted to the permittivity-dependent IDC using (1) with a DIW sample at three different temperatures (20.2°C, 24.2°C and 49.4°C).

All measurements were conducted with a Keysight PNA (E8361A). The PNA frequency range was set from 1.5 GHz to 2.5 GHz with a frequency step of 0.25 MHz. The intermediate frequency bandwidth was set to 100 Hz and a low output power level of -10 dBm was applied to avoid effects of dielectric heating, as previously demonstrated in [9].

RESULTS AND DISCUSSION

After the calibration of the VNA, the water sample under test was heated to five different temperatures, between 28.5°C and 45.5°C, and the reflection coefficient was measured at each temperature. Next, the permittivity was extracted using (1), given the three calibration measurements at three different temperatures. The extracted permittivity as well as the corresponding literature values are shown for the lowest (28.5 °C) and highest (45.5 °C) temperature values in Fig. 4 and Fig. 5, respectively.

Based on the extracted permittivity values, the predicted temperatures were calculated according to (2). The measured and the predicted temperatures are shown in Table 1. For the five measured temperatures, we observed a -0.06 ± 0.54°C temperature deviation between the measurements and the predictions. The error is maximal when the temperature of the sample deviates the most from the calibration temperatures, i.e. a temperature of 36.9°C compared to the three calibration temperatures of 20.2°C, 24.2°C and 49.4°C. This indicates that optimizing the calibration temperature distribution can improve the accuracy of the predicted temperatures.

Table 1: The predicted temperature values using the presented technique with respect to the sample temperature measured with the type K thermocouple in the PDMS ring.

Meas. T	[°C]	28.5	32.5	36.9	41.4	45.5
Pred. T	[°C]	28.5	33.0	37.6	40.8	45.2
Δ T	[°C]	0.0	0.5	0.7	-0.6	-0.3

FUTURE WORK

In this work, the sample under test was water, one of the most common liquids in biological liquids, buffers and solutions. Thus, as expected, water-based solutions also demonstrate a similar temperature-dependent dielectric behavior, e.g. sodium chloride solutions at different concentrations [10]. Additionally, the permittivity of other liquids, e.g. 2-propanol, is also temperature-dependent as demonstrated by [11] in the temperature

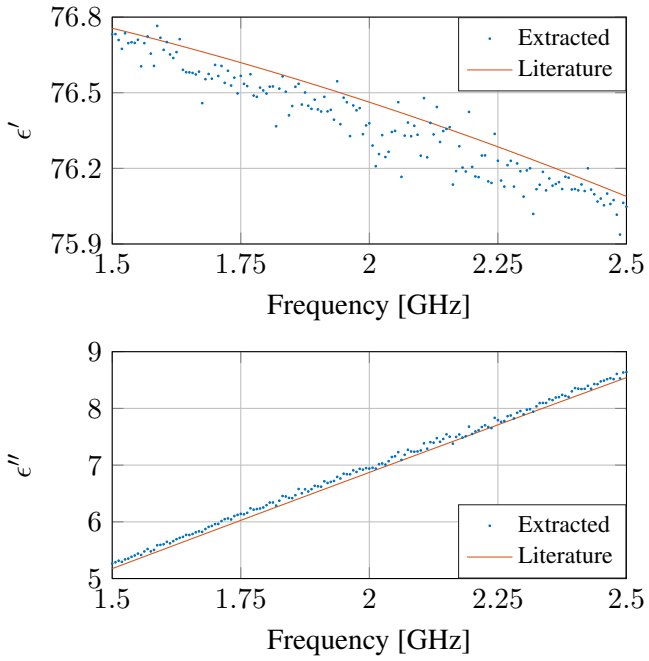

Figure 4: The extracted complex permittivity ($\epsilon = \epsilon' - j\epsilon''$) for the measurement at 28.5°C compared to the literature values at 28.5°C.

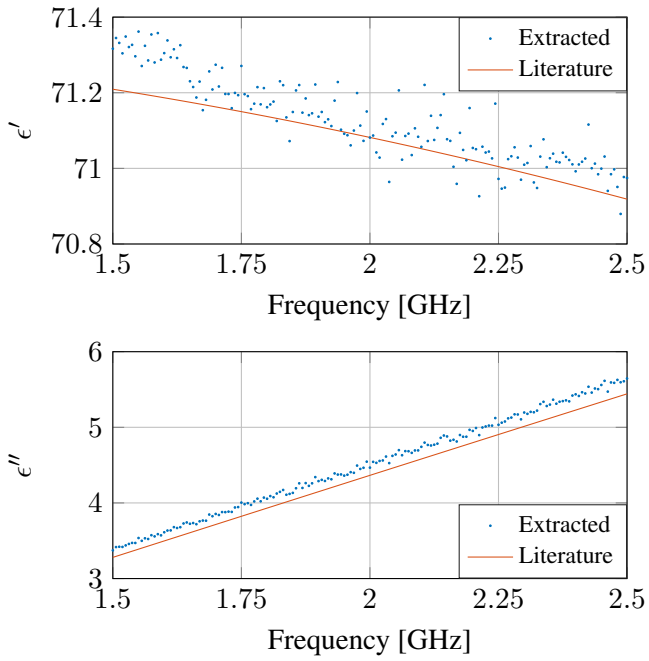

Figure 5: The extracted complex permittivity ($\epsilon = \epsilon' - j\epsilon''$) for the measurement at 45.5°C compared to the literature values at 45.5°C.

range from 20°C to 30°C. Therefore, the operating principle behind this technique is also valid for temperature sensing of different liquids provided that the calibration step changes accordingly.

Furthermore, we would improve the accuracy of the system. Since the changes in capacitance of the sensor are limited and since a resonant system improves the sensitivity in a narrow-band, it is a logical next step to add an extra matching structure to achieve a resonant system. Besides the improved accuracy, it makes it possible to immediately extract the temperature from the resonant frequency based on monitoring of only the amplitude of the reflection coefficient. This eliminates the need for a full-scale VNA and creates opportunities for small, inexpensive measurement systems. At last, since we expect a linear relation between the temperature and the resonant frequency, the number of calibration standards can be reduced from three to two.

CONCLUSION

This work presents a novel electromagnetic technique that uses the temperature-dependent permittivity of water for temperature monitoring. The system is completely calibrated with a novel water-only calibration technique, where a single water sample is heated to three known temperatures. This calibration allows the permittivity extraction of all other samples. Based on the extracted permittivity and the literature values, the temperature of the water sample can be predicted using the Euclidean distance criterion. Results demonstrate a -0.06 ± 0.54°C temperature deviation between measurements and predictions.

REFERENCES

[1] V. Miralles et al., "A review of heating and temperature control in microfluidic systems: Techniques and applications," *Diagnostics*, vol. 3, no. 1, p. 3367, 2013.

[2] P. Haro-González et al., "High-sensitivity fluorescence lifetime thermal sensing based on cdte quantum dots," *Small*, vol. 8, no. 17, pp. 2652–2658, 2012.

[3] T. Markovic et al., "A 20 GHz microwave heater for digital microfluidic," *Int. J. Microw. Wirel. Technol.*, vol. 9, no. 8, p. 15911596, 2017.

[4] T. Markovic et al., "An interdigital capacitor for microwave heating at 25 GHz and wideband dielectric sensing of nl volumes in continuous microfluidics," *Sensors*, vol. 19, p. 715, Oct 2019.

[5] W. Ellison, "Permittivity of pure water, at standard atmospheric pressure, over the frequency range 0-25 THz and the temperature range 0-100°C," *J. Phys. Chem. Ref. Data*, vol. 36, no. 1, 2007.

[6] Y. Wei et al., "Radiation-corrected open-ended coax line technique for dielectric measurements of liquids up to 20 GHz," *IEEE T. Microw. Theory*, vol. 39, pp. 526–531, March 1991.

[7] G. Maenhout et al., "Reliable, fast and reusable interfacing of high-frequency signals to disposable lab-on-a-chip devices," in *IEEE MTT-S IMBioC*, vol. 1, pp. 1–4, May 2019.

[8] A. Mamishev et al., "Interdigital sensors and transducers," *Proc. IEEE*, vol. 92, pp. 808–845, May 2004.

[9] J. Bao et al., "Investigation of thermal effect caused by different input power of biosensor using a novel microwave and optical sensing system for biological liquids," in *IEEE MTT-S IMBioC*, pp. 1–4, May 2017.

[10] A. Peyman et al., "Complex permittivity of sodium chloride solutions at microwave frequencies," *Bioelectromagnetics*, vol. 28, no. 4, pp. 264–274, 2007.

[11] T. Sato et al., "Dielectric relaxation spectroscopy of 2-propanolwater mixtures," *J. Chem. Phys.*, vol. 118, no. 10, pp. 4606–4613, 2003.

CONTACT

- gertjan.maenhout , juncheng.bao , bart.nauwelaers @esat.kuleuven.be
- tomislav.markovic , ilja.ocket @imec.be
- georgios.stefanidis@kuleuven.be

HIGHLY-DOPED BULK SILICON MICROHEATERS AND ELECTRODES EMBEDDED BETWEEN FREE-HANGING MICROFLUIDIC CHANNELS BY SURFACE CHANNEL TECHNOLOGY

Y. Zhao[1], *H.-W. Veltkamp*[1], *T. V. P. Schut*[1], *J. Groenesteijn*[2], *M. J. de Boer*[1], *R. J. Wiegerink*[1], and *J. C. Lötters* [1,2]

[1] MESA+ Institute for Nanotechnology, University of Twente, Enschede, The Netherlands
[2] Bronkhorst High-Tech BV, Ruurlo, The Netherlands

ABSTRACT

Surface Channel Technology is widely used as the fabrication process to make free-hanging microchannels in various microfluidic devices. In this extended abstract, we report an innovative fabrication method to embed highly-doped silicon electrodes between the adjacent free-hanging microfluidic channels using the SCT process. Essentially, two parameters are used to tune the final cross-sectional geometry and size of the bulk silicon electrodes. One is the distance between two adjacent rows of slits and the other is the width of flat membrane above the microchannels. The advantageous physical features make bulk silicon electrodes suitable for many sensing and actuation applications. When the bulk silicon electrodes are used as microheaters, they allow higher power dissipation. This is because of their larger cross-sectional areas compared to the commonly used thin film metal microheaters. Moreover, as sensing electrodes, bulk silicon electrodes are located between the sidewalls of two adjacent microchannels. This makes them applicable as the sidewall resistive or capacitive readout in e.g. flow sensors.

KEYWORDS

Surface Channel Technology (SCT), free-hanging microfluidic channels, embedded sidewall bulk silicon electrodes, highly-doped bulk silicon microheaters.

INTRODUCTION

The original SCT process

Free-hanging microfluidic channels with the hydraulic diameter between approximately $20\,\mu\mathrm{m}$ to $100\,\mu\mathrm{m}$ can be fabricated by Surface Channel Technology (SCT) [1]. These microchannels have very thin channel walls of a few $\mu\mathrm{m}$ thick and are made of dielectric materials such as silicon nitride. The dielectric channels can be completely released free from the bulk silicon wafer and become free-hanging. These free-hanging microchannels are useful for different micro-electro-mechanical systems (MEMS) devices, such as fluid parameter sensors [2], control valves [3], micro-Coriolis flow sensors [4], pressure sensors [5], thermal flow sensors [6], and micro-gas-burners [7], The SCT fabrication method have become the technology platform for various microfluidic applications. Therefore, SCT is suitable as the microfluidic platforms for fabricating multi-parameter sensors [2].

The demands to develop sidewall electrodes

The original SCT process shows that as long as the channels are completely released, the microchannels become free-hanging and allow mechanical movement for sensing or actuating purposes [1]. All the electrical functionalities are realized by the thin film metal wires placed on the top surface of the microfluidic channels. For example, thin film microheaters and temperature sensors, resistive strain gauges and capacitive readout. In most cases, it is only possible for sensing and actuation from the topside of the channels. The demand of electrical functionalities in the micro-devices cannot be always fulfilled by the top surface thin film metal interconnects fabricated from the original SCT process.

In practical applications, there are great demands of sidewall sensing and actuation, which can be realized by embedding the electrodes on the sidewalls of the microfluidic channels. For example, the in-line relative permittivity sensors was realized with the SCT process by isolating two silicon electrodes at the sidewalls of the microfludic channel [8]. Accurate capacitance readout was demonstrated suggesting the viability of silicon electrodes for capacitive readout. However, a SOI wafer is needed to electrically insulate the device layer silicon electrodes from the bulk handle layer.

The concept of sidewall silicon electrodes have another potential application as the robust and reliable sidewall microheaters. For the micro-gas-burners [7], $200\,\mathrm{nm}$ thick platinum resistors were patterned on the top surface of the micro-channel and function as topside microheaters and temperature sensors. However, thin film platinum resistors degraded morphologically and

electrically at high temperatures above 600 °C [7, 9]. More powerful heaters are necessary to reach 600 °C for the initiation of methane/air autoignition reaction for the micro Wobbe Index meter. It was previously reported that sidewall silicon microheaters can be embedded between the channel walls fabricated by Trench-assisted Surface Channel Technology and function as sidewall microheaters [10].

These reported approaches to integrate silicon electrodes have been proposed before using SOI wafers [4, 8] and/or refilled trenches [10], but these options require SOI wafers and add more complexity to the fabrication process.

Here we propose to integrate heavily-doped bulk silicon electrodes between the adjacent free-hanging channels, as illustrated in Figure 1(H2). The proposed fabrication scheme is completely based on the core concept of SCT in a silicon wafer, with special designs in the slits pattern and the release window location, in-plane silicon electrodes can be embedded between free-hanging surface channels. In the following sessions, firstly, the new SCT fabrication scheme will be explained. Next, the fabrication results will be presented. Lastly, the application of bulk silicon as microheaters will be discussed.

FABRICATION SCHEME

The new SCT fabrication scheme requires a highly-doped silicon wafer to make the sidewall bulk silicon electrodes electrically conductive. The schematic new SCT process is illustrated in Figure1 from A2 to H2. In comparison, the original SCT process using a silicon wafer is illustrated in Figure1 from A1 to G1.

In details, the new SCT process starts with (A2) a highly-doped silicon wafer; (B2) transfer the slit array patterns into the SiO_2 hard mask, where *d* is the spacing between two rows of slits; (C2) semi-isotropically etch the silicon wafer through the slit openings and form the semi-circular channel cavity with a flat top membrane. With properly designed *d*, there is silicon remained between two adjacent channels; (D2) conformal deposition of low-stress LPCVD silicon-rich Si_xN_y (SiRN) to seal the slit openings and form the thin dielectric channel walls; (E2) etch away the dielectric top layers until the highly-doped silicon; (F2) deposit thin film metal layers and pattern the metal wires to form electrical interconnects. This step enables electrical interconnections from external power supply to the embedded silicon electrode;

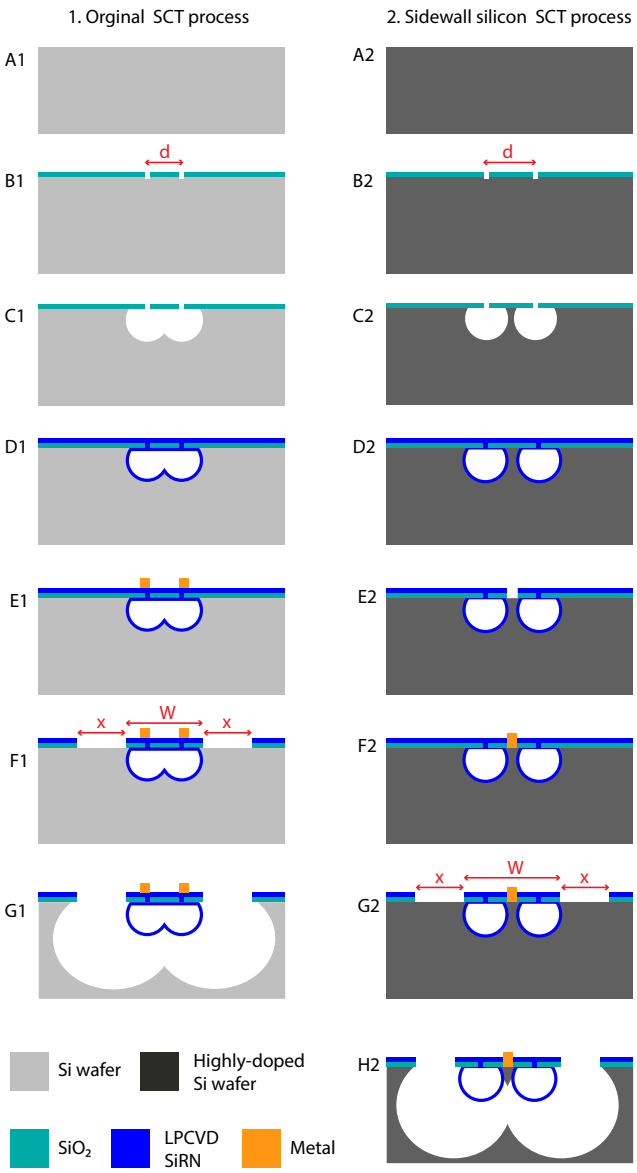

Figure 1: From A1 to G1 shows the schematic fabrication steps of the original SCT process in a silicon wafer to make free-hanging microchannels with topside electrical functionalities. From A2 to H2 shows the schematic fabrication steps of the new SCT process in a highly-doped silicon wafer to fabricate sidewall silicon electrode between two free-hanging adjacent microchannels. The original (1) and new (2) SCT fabrication process share the same sequences: (B1 and B2) etch slit arrays in the hard mask; (C1 and C2) semi-isotropically etch the channel cavity through the slit openings; (D1 and D2) deposit LPCVD SiRN to seal the slits and form channel walls; (E1 and E2, F2) deposit and pattern the metal thin films for electrical functionality. The new process requires the extra step (E2) to etch open the hard mask and uncover the highly-doped silicon between the two adjacent microchannels for metal connection; (F1 and G2) etch the front release window with width x and the flat membrane above the channel with width W in the hard mask; (G1 and H2) release etch the channel through the front release windows.

Next, design the top flat membrane above the channels with the width W, and (G2) etch frontside release window with the width x in the dielectrics top layers; (H2) release etch the channel through the frontside release mask. Use the same release etch recipe (i.e. etching method and etching time) from the original SCT process [1], by properly design the parameters x and W, there will be silicon remained between two adjacent channels after the release etch.

By controlling the release etch, the electrically conductive silicon become isolated from the bulk substrate, which is crucial for electrodes and microheaters.

RESULTS AND DISCUSSIONS

There are two parameters playing vital roles in determining the amount of the remained silicon. One is the distance between two rows of slits d, and the other is the width of the flat membrane above the channels W. In order to test the parameters to obtain the bulk silicon electrode between adjacent microchannels, structures were fabricated according to the new SCT process scheme described in the Figure 1(A2-H2). Each process recipe was kept the same as used in the original SCT process.

Firstly, different values of d between two rows of slits can result in either two separate channels or a single connected channel with larger width. In the new SCT process, larger d results in two separated channels (Figure 1(D2)). Whereas in the original SCT process, two closely placed rows of slits hence a smaller d results in one merged channel with a ridge at the bottom of the wider channel (Figure 1(D1)). Scanning electron microscope (SEM) photographs of the test structures show that, for two rows of slits with row distance $d = 60\,\mu\mathrm{m}$, two separate channels are formed (Figure 2(A-F)). For $d = 55\,\mu\mathrm{m}$, a single wider channel with bulk silicon electrode embedded inside the channel (Figure 2(G)).

Secondly, for a fixed release window width $x = 200\,\mu\mathrm{m}$, the width of the flat membrane above the channels W defines the hard mask for the channel release etch. The SEM photographs of the fully released channels with certain amount of silicon remained between the channels are shown in Figure 2. If the release windows are close to the channels hence a small W, channels are completely released and the silicon in between is completely removed (Figure 2(B)). For $W = 100$, 140 and 250 μm, an increasing amount of silicon remains between the channels, as shown in Figure 2(C), 2(D), and 2(E) respectively. For even larger W the channels are no longer completely released.

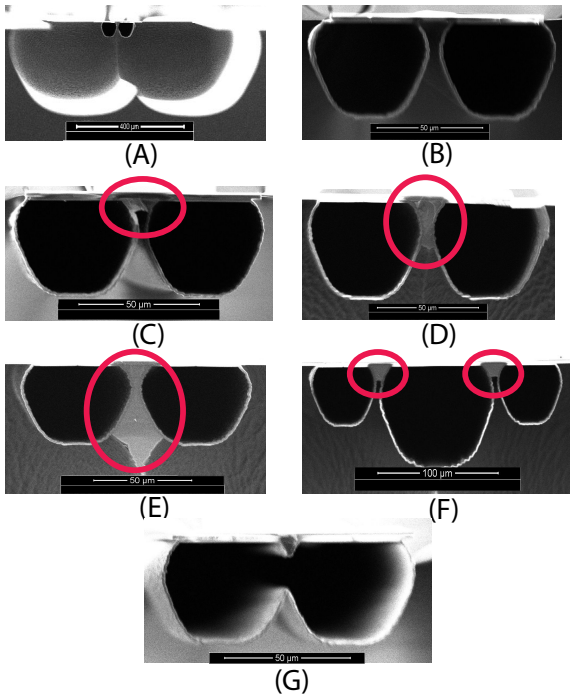

Figure 2: SEM photographs of (A) a fully released two separated channel structure, and close-ups of two channels (B) with no remaining silicon, (C) with a small ($\sim$35 $\mu\mathrm{m}^2$) silicon electrode, (D) with a medium ($\sim$230 $\mu\mathrm{m}^2$) silicon electrode, (E) with a large ($\sim$720 $\mu\mathrm{m}^2$) silicon electrode; (F) a three-channel structure with two silicon electrodes, and (G) silicon electrode embedded inside the wider channel when $d = 55\,\mu\mathrm{m}$.

The resistance of the silicon electrode depends on the doping level and cross-sectional area. We used boron-doped silicon wafers with resistivity ranging from 0.01 to 0.02 $\Omega \cdot \mathrm{cm}$. The results in Figure 2 show that the cross-sectional area can be designed from approximately 35 $\mu\mathrm{m}^2$ (Figure 2(C)) to 720 $\mu\mathrm{m}^2$ (Figure 2(E)). Table 1 lists the calculated properties of the resulting silicon electrodes in comparison to a typical 10 μm wide, 200 nm thick platinum electrode on top of the channel. Especially when used as heaters the silicon electrodes provide a clear advantage. Supplying the same current density through the electrodes a factor of 10^4 to 10^5 more power can be dissipated due to the combination of higher resistance and larger cross-section. Figure 2(F) shows that it is also possible to embed two electrodes between three adjacent channels. This could for example be used to realize a relative permittivity sensor.

1 mm long microheaters	Resistivity [Ω cm]	Area [μm^2]	Resistance [Ω]	Power per unit length [$W m^{-1}$] (supply 1 mA)	Power per unit length [$W m^{-1}$] (supply 5×10^8 A m^{-2})
200 nm thick platinum	1×10^{-5}	2	50	5×10^{-2}	5×10^{-2}
Small silicon electrode	1×10^{-2}	35	2857	2.86	8.75×10^2
Medium silicon electrode	1×10^{-2}	230	435	4.35×10^{-1}	5.75×10^3
Large silicon electrode	1×10^{-2}	720	139	1.39×10^{-1}	1.8×10^4

Table 1: Comparison between platinum and silicon electrodes for Joule heating. For current density of 5×10^8 A m^{-2}, silicon electrodes with large cross-sectional area and resistance can dissipate more power per unit length.

CONCLUSIONS

Surface Channel Technology can be upgrade to become a more diverse microfluidic technology platform, simply by introducing the bulk silicon electrodes between the adjacent channel sidewalls. Different size and geometry of bulk silicon electrodes can be customized and optimized by tuning parameters d and W. It offers advantages for various microfluidic applications, such as much higher power dissipation when used as microheaters, higher sensitivity when used as strain gauges due to the piezoresistivity of silicon, and the possibility of sidewall capacitive sensing.

ACKNOWLEDGMENT

This work is part of the research program "Integrated Wobbe Index Meter" under project number 13952 which is co-financed by the Netherlands Organization for Scientific Research (NWO).

REFERENCES

[1] Dijkstra, M., de Boer, M. J., Berenschot, J. W., Lammerink, T. S., Wiegerink, R. J., Elwenspoek, M. (2007). A versatile surface channel concept for microfluidic applications. Journal of micromechanics and microengineering, 17(10), 1971.

[2] Schut, T. V. P., Alveringh, D., Sparreboom, W., Groenesteijn, J., Wiegerink, R. J., Lötters, J. C. (2018, January). Fully integrated mass flow, pressure, density and viscosity sensor for both liquids and gases. In 2018 IEEE Micro Electro Mechanical Systems (MEMS) (pp. 218-221). IEEE.

[3] Groen, M. S., Groenesteijn, J., Meutstege, E., Brookhuis, R. A., Brouwer, D. M., Lötters, J. C., Wiegerink, R. J. (2015). Proportional control valves integrated in silicon nitride surface channel technology. Journal of microelectromechanical systems, 24(6), 1759-1767.

[4] Groenesteijn, J., de Boer, M. J., Lötters, J. C., Wiegerink, R. J. (2017). A versatile technology platform for microfluidic handling systems, part I: fabrication and functionalization. Microfluidics and nanofluidics, 21(7), 127.

[5] Alveringh, D., Schut, T. V. P., Wiegerink, R. J., Sparreboom, W., Lotters, J. C. (2017, June). Resistive pressure sensors integrated with a coriolis mass flow sensor. In 2017 19th International Conference on Solid-State Sensors, Actuators and Microsystems (TRANSDUCERS) (pp. 1167-1170). IEEE.

[6] Dijkstra, M., de Boer, M. J., Berenschot, J. W., Lammerink, T. S., Wiegerink, R. J., Elwenspoek, M. (2008). Miniaturized thermal flow sensor with planar-integrated sensor structures on semicircular surface channels. Sensors and Actuators A: Physical, 143(1), 1-6.

[7] Lötters, J. C., Lammerink, T. S., Pap, M. G., Sanders, R. G., de Boer, M. J., Mouris, A. J., Wiegerink, R. J. (2013, January). Integrated micro Wobbe index meter towards on-chip energy content measurement. In 2013 IEEE 26th International Conference on Micro Electro Mechanical Systems (MEMS) (pp. 965-968). IEEE.

[8] Alveringh, D., Wiegerink, R. J., Lotters, J. C. (2018, January). Inline relative permittivity sensing using silicon electrodes realized in surface channel technology. In 2018 IEEE Micro Electro Mechanical Systems (MEMS) (pp. 840-843). IEEE.

[9] Tiggelaar, R. M., Sanders, R. G., Groenland, A. W., Gardeniers, J. G. (2009). Stability of thin platinum films implemented in high-temperature microdevices. Sensors and Actuators A: Physical, 152(1), 39-47.

[10] Veltkamp, H. W., Zhao, Y., de Boer, M. J., Sanders, R. G., Wiegerink, R. J., Lötters, J. C. (2019, January). High power Si sidewall heaters for fluidic application fabricated by trench-assisted surface channel technology. In 32nd IEEE International Conference on Micro Electro Mechanical Systems 2019 (pp. 648-651). IEEE.

[11] Haneveld, J., Lammerink, T. S., de Boer, M. J., Sanders, R. G., Mehendale, A., Lötters, J. C., Wiegerink, R. J. (2010). Modeling, design, fabrication and characterization of a micro Coriolis mass flow sensor. Journal of micromechanics and microengineering, 20(12), 125001.

CONTACT

* Yiyuan Zhao, y.zhao-5@utwente.nl

LABEL-FREE DETECTION OF MINISCULE OBJECTS VIA DARK-FIELD MICROSCOPY FOR SINGLE-CELL PRINTING

R. Dammann [1], B. Gerdes [1,2], J. Riba [2], L. Lautscham [2], S. Zimmermann [1,2], P. Koltay [1], R. Zengerle [1]
[1] Laboratory for MEMS Applications, IMTEK, University of Freiburg, Germany
[2] cytena GmbH, Freiburg, Germany

ABSTRACT

We present a detection method for miniscule particles that can potentially be used in a single-cell printer during printing. In this work, the dark-field setup is established and measurements are performed with Chinese Hamster Ovarian (CHO)-cells ($d_{\text{cell}} = 10-15\,\mu\text{m}$) and beads sized $d_{\text{bead}} = 0.5\,\mu\text{m}$ and $d_{\text{bead}} = 1\,\mu\text{m}$. Moreover, detection of *E. coli* bacteria is carried out. By automated evaluation algorithms, the small-sized beads can be detected which is difficult *via* bright-field microscopy. The setup is therefore potentially applicable for the detection of small bacteria in the microfluidic dispensing cartridge of a single-cell printer.

KEYWORDS

Single-cell printer, Dark-field illumination, Dark-field microscopy, Bacteria detection,

INTRODUCTION

Single-cell analysis has become of increasing interest boosting the demand for technologies that enable single-cell sorting and isolation [1]. The isolation of small cells is a complex process, which typically exhibits low efficiencies. In this work, an advanced single-cell printing technology (*cytena GmbH*, Germany) is used to isolate cells and beads [2]. The printer is based on a piezoelectric actuator that creates microdroplets from a cell suspension in a drop-on-demand manner. An optical setup is used to detect whether the printed droplet contains exactly one cell, which then can be deposited on a defined position of a substrate. Droplets, containing no cells or multiple cells are separated out by a vacuum shutter. A picture of a dispenser cartridge is depicted in Figure 4 and a close-up of the chip is shown in Figure 2.
Recently, single-cell dispensing of bacteria enabled by label-free cell detection was demonstrated with this system [3]. However, optical detection of very small bacteria below 1 µm in diameter remains challenging, since the microfluidic channels of the dispensing chips are significantly larger in size than the bacteria. Further, for integration into a single-cell printer, long-working distance objectives are required, ultimately limiting the maximum resolution.
In this work, miniscule beads are monitored in the dispenser chip *via* a dark-field illumination setup. Even small objects act as a center of diffraction and are visible although their size is below the resolution limit of the optics. The shape of objects cannot be resolved, however, detection is possible.

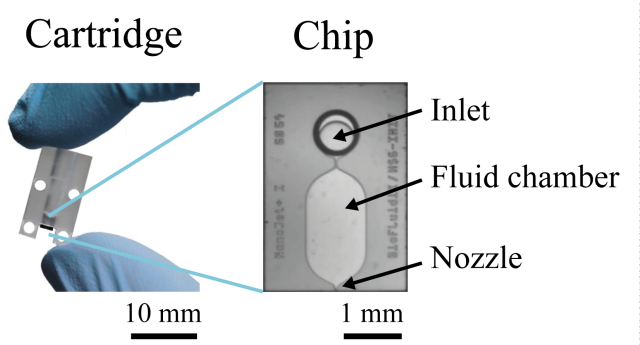

Figure 1: Single-cell printer cartridge with details of the microfluidic dispenser chip.

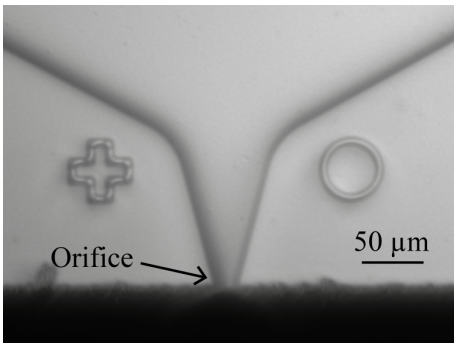

Figure 2: Exemplary bright-field image of the dispenser chip.

Materials and Methods

The setup comprises an IDS µ-eye camera (type 3240 Rev. 2) with a 210 mm tubus and a 20x microscope objective from Mitutoyo (M Plan APO SL) to record the pictures. As light source, a simple green (532 nm) laser diode is used (TRU COMPONENTS LM05GND). It features an output power of 5 mW. Figure 3 depicts a schematic view of the setup.
The incident light is largely scattered by the cartridge containing the cell suspension at an angle which is not

captured by the camera. Only a small portion of the light is reflected by the particles in such a way that they can be detected by the camera. The angle of the laser in respect to the dispenser can be adjusted. The illumination setup results in an almost dark picture of the dispenser chip. As bead or cell suspensions are present in the chip, the particles start to scatter light and they appear as bright centers of reflection on the darker background. For this work, the dark background image is subtracted from all pictures containing particles. As a result, the contrast is increased and artifacts can be avoided. An automated detection algorithm is used to detect the small particles.

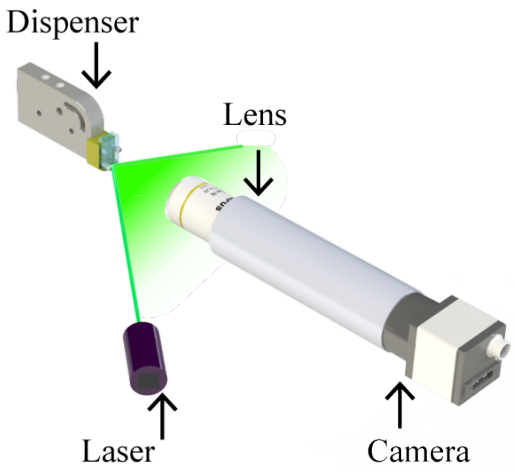

Figure 3: Schematic view of the setup comprising of a green laser that incidents on the dispenser chip. The scattered light is captured by a Mitutoyo 20x microscope objective and the image is recorded by a camera.

To reduce the amount of scattered light from the cartridge itself, the standard cartridges of the SCP are modified to eliminate shadowing of the dispenser chip in the dark-field setup as depicted in Figure 4. The chips are fabricated from silicon. A fluid chamber is structured by deep reactive ion etching (DRIE) into the silicon wafer. A pyrex wafer is covered with a thin silicon dioxide layer by low pressure chemical vapour deposition (LPCVD) and structured by hydrofluoric acid. The silicon and pyrex are subsequently attached to each other by anodic bonding. The fluid chamber has a depth of 20 µm and the chip nozzle has a width of 20 µm (cf. Figure 2).

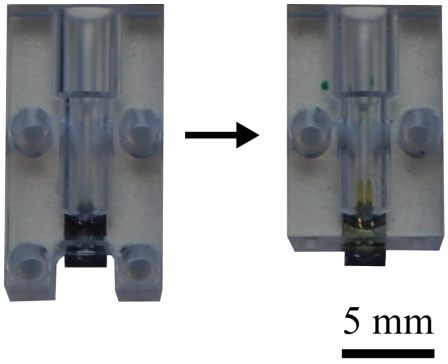

Figure 4: Original (left) and modified (right) cartridge for minimizing shadowing losses.

The cartridge is filled with a particle suspension and the nozzle is captured in a definite time interval with the optical setup. In this work silica beads featuring different diameters of $d_{\text{bead}} = 0.5$ µm and $d_{\text{bead}} = 1$ µm are used. Moreover, mammalian cells (CHO K-1) are evaluated.. The beads are used to simulate miniscule objects such as very small bacteria. Finally, *E. coli* bacteria are detected in the chip.
For a first evaluation of the setup, the printing process that usually causes the major movement of the liquid - and thus the movement of particles - was not used. In this work, the movement of the particles is mainly caused by sedimentation inside the liquid and is estimated to be in the range of a few micrometers per second. The resulting images are evaluated with an algorithm in order to detect the particles that moved in between the images. The images are normalized whereas one represents the maximum value of intensity. The maximum intensity of the particle is then compared to their local background intensity. Due to the dark-field setup, this background intensity is typically close to zero. The difference between the values is considered the contrast of the image.

Experimental results

For each evaluation, a dark background image is subtracted from the recorded picture, showing mostly the light that is scattered at the cells or beads. Evaluation of the setup is carried out by detecting CHO cells, beads and *E. coli* bacteria. The laser diode is operated at $P = 5$ mW and is used for illumination. The angle of the illumination beam in respect to the optical axis of the lens can be adjusted from 45° to 65°. Figure 5 depicts the dark-field image of the dispenser chip, filled with a suspension of CHO cells in phosphate-buffered

saline (PBS). After subtraction of the background, the cells are clearly visible and can easily be distinguished from static particles. The CHO cells can be detected at a high contrast of 82 ± 6 %.

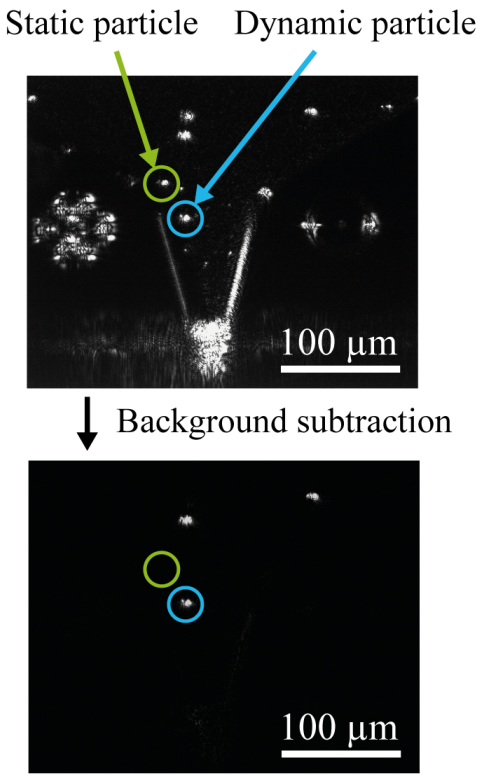

Figure 5: Detection of CHO cells via the dark-field setup. After background subtraction, cells are clearly visible in the chip.

The intensity of the background illumination of 12 ± 3 % is higher than usual for dark-field illumination. This is most likely due to the etch process of the fluid chamber resulting in a rough surface. A silicon dioxide bead suspension (d_{bead} = 1 µm) is used for further evaluation of the setup. The contrast amounts to 65 ± 10 % for an illumination angle of 45° to 55° and decreases for higher illumination angles, mainly because the intensity of the light that is scattered at the beads surface decreases. Nevertheless, at a contrast of 65 %, the detection of these small beads is possible. A detailed evaluation is depicted in Figure 6. The software-processed image (Figure 6 A) depicts the dark-field image where detected beads are shown. Figure 6 B shows a close-up of three detected 1 µm beads and an intesity distribution across one bead, showing that the bead can clearly be distinguished from the background. Table 1 summarizes the maximum intensities of the light, scattered by the beads, the background intensity and the resulting contrast of the beads against the background.

In further experiment the size of the beads was varied from 1 µm to 0.5 µm.

Table 1: Maximum intensity of the scattered light of the beads, background intesity and concluded contrast for silica beads of 1 µm and 0.5 µm.

Beadsize	1 µm	0.5 µm
Bead max. int.	71.4 ± 18.8 %	48.2 ± 12.4 %
Background	12.5 ± 3.0 %	13.0 ± 2.4 %
Contrast	58.9 ± 18.1 %	35.2 ± 12.9 %

Beads can be detected to a minimum diameter of 0.5 µm. Smaller Beads cannot be differentiated from the noise of the background, due to the diminishing intensity at which light is scattered from very small objects.

For evaluation of bacteria detection, *E. coli* bacteria are used in LB-medium. These are difficult to detect due to their small size of a few microns and their rod-shape. The inhomogeneous structure and movement of the bacteria lead to inconsistent scattering of light depending on the orientation of the bacteria in the chip. As the orientation is constantly changing, it is challenging to detect each cell. Therefore, a comparative experiment was conducted in which the medium is analyzed without any bacteria. The algorithm detects no bacteria in the cartridge that is filled only with LB-medium and detects them in the bacteria suspension with a mean contrast of 62 ± 14 %.

CONCLUSION

Dark-field illumination is used for the first time as a means to detect small objecs such as beads and cells in the cartridge of a single cell printer. The setup enables the detection of CHO cells and beads featuring minimum diameters of 0.5 µm. It is moreover capable of detecting E. coli bacteria. However, it is yet to be evaluated if all bacteria cells are detected *via* this setup as they are very small and feature a rod-like structure that can be difficult to detect depending on their orientation. For detection, an algorithm is used that subtracts the background, as some light is also scattered from the chip itself due to the rough surface of the fluid chamber. The diminishing intensity of the particles with illumination angles above 55 ° leads to a decreasing contrast for higher illumination angles. The experiments show that the oblique lighting obscures one side of the chip. By

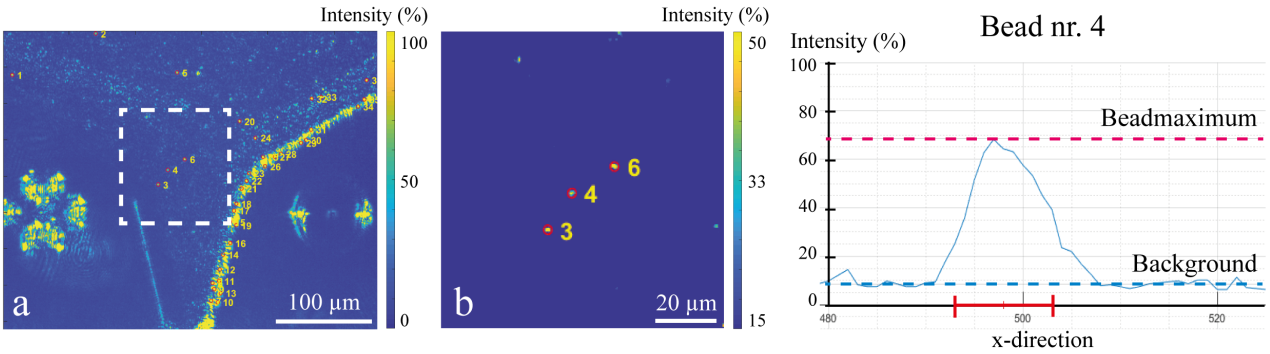

Figure 6: Software-processed result image of the dark-field setup. The fluid contains beads featuring $d_{bead} = 1$ µm (a). A magnified view of the beads (b) shows the automated bead detection. The intensity analysis across one bead (4) shows the high contrast even for miniscule beads.

using an additional light source or a more complex annular dark-field illumination, the chip can most likely be illuminated symmetrically. An improvement of the edge illumination could lead to a more reliable detection of objects at the edges of the chip nozzle. In the context of this work, no analysis has been carried out to prove that all particles are actually detected. The reliability of the particle detection could be evaluated by printing in microtiter plates and subsequent analysis by microscopy.

Acknowledgments

Funding by the Bundesministerium für Bildung und Forschung (FKZ 01QE1741C) is gratefully acknowledged.

REFERENCES

[1] Editorial, “Methods of the year 2013”, Nat. Methods, 1 , 2014, p. 1, 10.1038/nmeth.2801.

[2] A. Gross, J. Schöndue, S. Niekrawitz, W. Streule, L. Riegger, R. Zengerle, P. Koltay, “Single-Cell Printer: Automated, On Demand, and Label Free”, Journal of Laboratory Automation, 18(6), pp. 504518, 2013, 10.1177/2211068213497204.

[3] J. Riba, T. Gleichmann, S. Zimmermann, R. Zengerle, P. Koltay, “Label-free isolation and deposition of single bacterial cells from heterogeneous samples for clonal culturing”, Scientific reports, Vol. 6, pp. 1-9, 2016, 10.1038/srep32837.

CONTACT

peter.koltay@imtek.uni-freiburg.de

MEASUREMENT OF VISCOSITY FOR MEDICINE MIXTURE

S. Mejri[1], M. Yariesbouei[1], R.J Wiegerink[1], J. Groenesteijn[2], J. Lötters[1,2]
[1] University of Twente, Integrated Devices and Systems, Enschede, The Netherlands
[2] Bronkhorst High-Tech BV, Ruurlo, The Netherlands

ABSTRACT

In this paper we discuss a multi-parameter microfluidic chip, in the intent of measuring the viscosity of medicinal binary mixtures. The measurement is based on the Hagen-Poiseuille equation, where the viscosity is function of mass flow and pressure drop. For different liquids and liquid mixtures, the viscosity measured is close to that in literature.

KEYWORDS

Multi-parameter, medicine mixture, viscosity, microfluidics, flow measurements

INTRODUCTION

During simultaneous drug delivery to neonates, the administration of medicine via infusion systems must be precise and effective. Because under-dosing can result in lack of efficacy and overdosing can cause adverse effects and even be fatal. The infusion of medicine, in low dosage has to be performed with high accuracy. For instance, the mixture of Dopamine and Dobutamine can increase blood pressure and heart rate while treating advanced myocardial failure. They are usually infused together and should be monitored closely [1].

To that end, we developed a multi-parameter microfluidic chip [2, 3] containing two resistive pressure sensors fully integrated with a Coriolis mass flow sensor and a temperature sensor, as shown in Fig. 1.

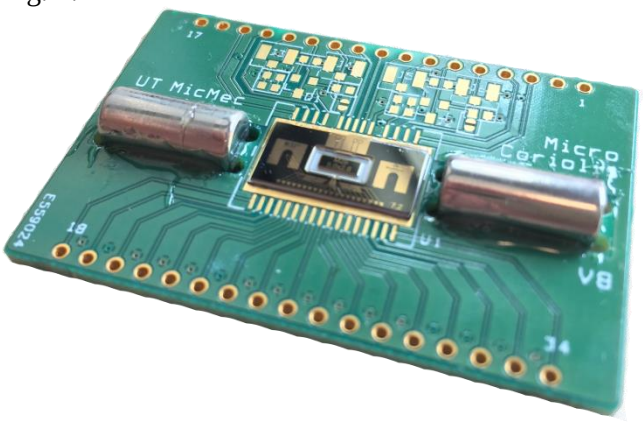

Figure 1. Photograph of the multiparameter chip glued on a PCBwith magnets on the sides to actuate the micro-coriolis sensor

The main objective is to real-time determine inline the composition of the mixture by analyzing its physical parameters. If these properties for the individual liquids are sufficiently different, it is possible to determine the mixing ratio for mixtures. Furthermore, by comparing these properties with the expected values based on the set point of the pumps, drug administration can be carried out with higher confidence, yielding a better clinical result.

In this paper we focus on the measurement of viscosity for a binary mixture of Dopamine and Dobutamine while changing the volume ratio.

BASIC STRUCTURE AND OPERATING PRINCIPLE

The pressure drop of the laminar flow within the microfluidic chip is governed by the Hagen-Poiseuille equation:

$$\Delta P = \frac{8\mu L Q}{\pi R^4} \qquad (1)$$

With ΔP is the differential pressure, μ is the dynamic viscosity, L the length of the channel, Q the volumetric flow rate and R the radius of the channel.

It is a direct relation between the mass flow and the differential pressure and from it, the dynamic viscosity is derived. Figure 2 explains the principle of measurement.

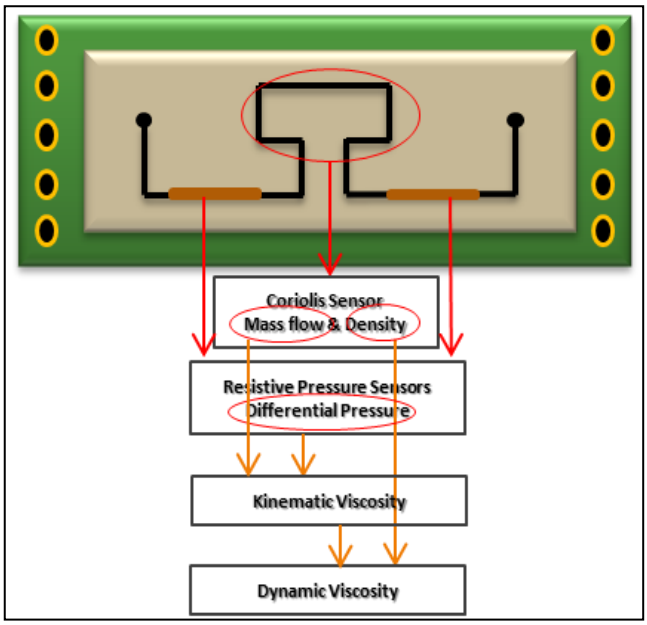

Figure 2. Principle of measurement of the dynamic viscosity

The Coriolis mass flow sensor is actuated by the fluid flowing through, which creates a vibration. The vibration can be sensed with two comb capacitors. The density therefor is measured using the resonance

frequency. As for the pressure sensors (studied and examined more in [4]), they both consist of gold strain gauges on top of the channels before and after the Coriolis sensor, creating a Wheatstone bridge. The expansion and compression of the gauges is a measure for the pressure inside the channel.

FABRICATION AND ELECTRONICS

The fabrication process of the chip is discussed and explained further in a previous paper [5]. Figure 3 is a Scanning Electron Microscope image of the sensors.

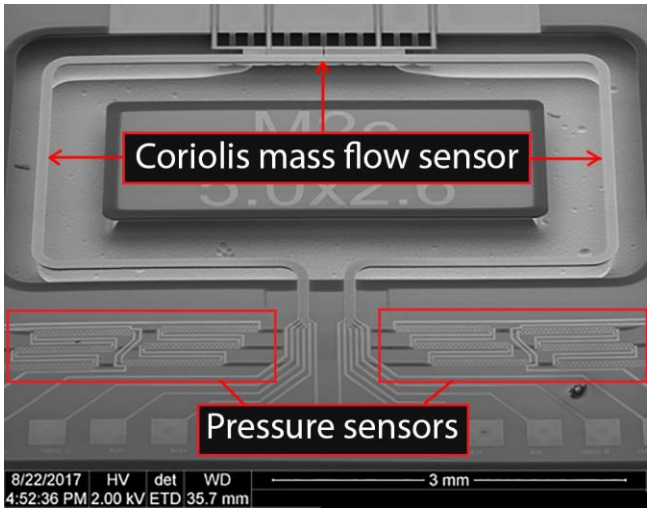

Figure 3. SEM image of the sensors

EXPERIMENTAL

We started the experiments with single liquids (H2O, IPA, Dobutamine and Dopamine) each at a time, with various flow rates, fed to the multi-parameter chip with a syringe pump at room temperature and the mass flow is set between 0 and 2ml/h (see Fig. 4).

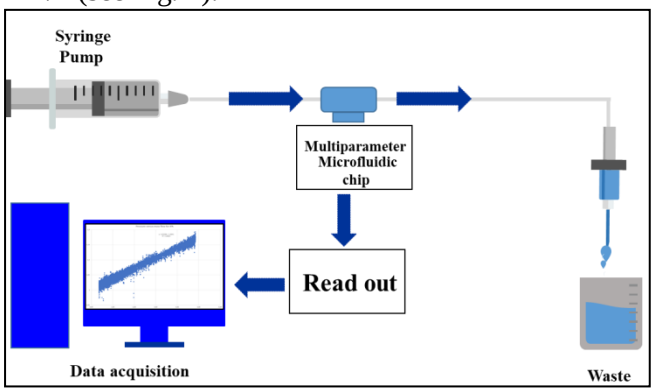

Figure 4. Schematic of the experimental setup

The raw data we extracted, as a first step, from the measurements is shown in Figure. 5. As presented we can see that the signal is quite noisy due to the low sensitivity of the integrated pressure sensors.

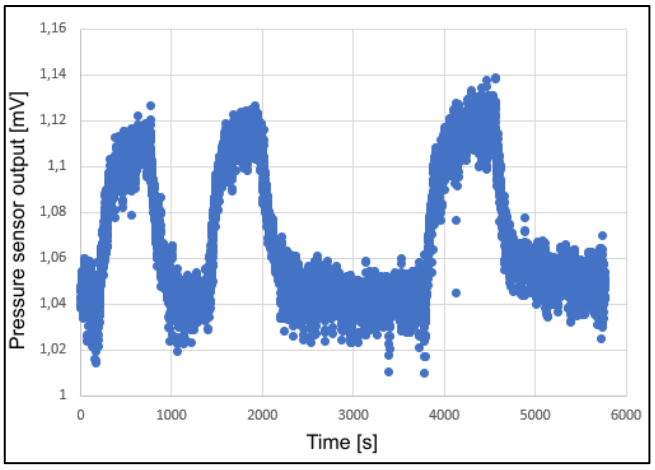

Figure 5. Typical pressure difference signal with water as a function of time.

We, then moved to a mixture of Dopamine and Dobutamine while varying the volume percentage (100/0, 75/25, 50/50, 25/75 and 0/100%).

So, for each of the liquids, the pressure drop was measured as a function of mass flow. The slope of these curves is proportional to the ratio of dynamic viscosity and density of the liquid. The density is also measured by the integrated Coriolis mass flow sensor, allowing obtaining a measure for the viscosity.

RESULTS AND DISCUSSION

From the data in Figure 5, we drew the pressure difference as a function of the mass flow, which is in turn a function of the phase shift of the Coriolis mass flow sensor. As shown in Fig. 6 and Fig. 7, where we present the slopes of the curves for water and IPA, which are respectively: 0.0124 and 0.0338, and they indicate that the measured viscosities of these liquids are different.

Furthermore, despite of the noise, a clear linear relation between the pressure drop and mass flow can be observed. Of course this is based on the previous Hagen-Poiseuille equation for a laminar flow, where the relation between pressure and mass flow is linear and is a measure as explained before of the viscosity.

Therefore, our system is able to differentiate between liquids. The same measurements and curves were applied to Dopamine and Dobutamine and the calculated slopes were 0.0139 and 0.0142, respectively. Thus, the slopes are clearly defined by the viscosity.

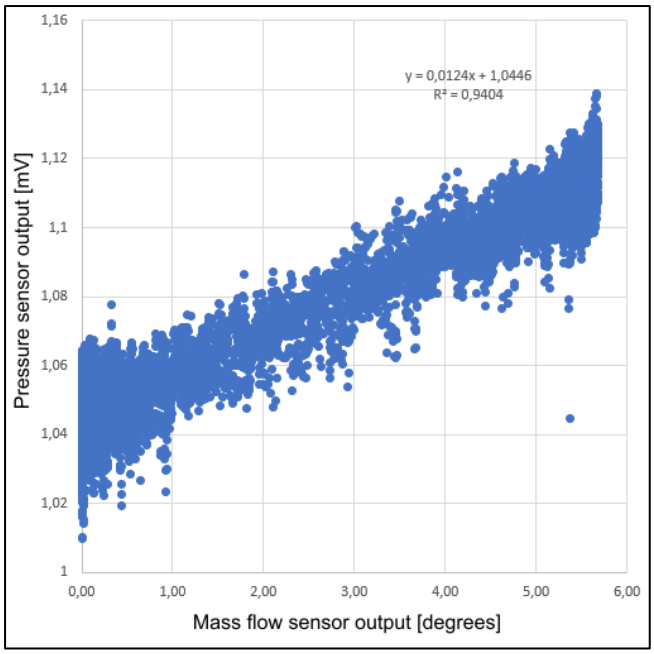

Figure 6. The measured pressure drop from figure 5 plotted as a function of the phase shift from the micro Coriolis mass flow sensor

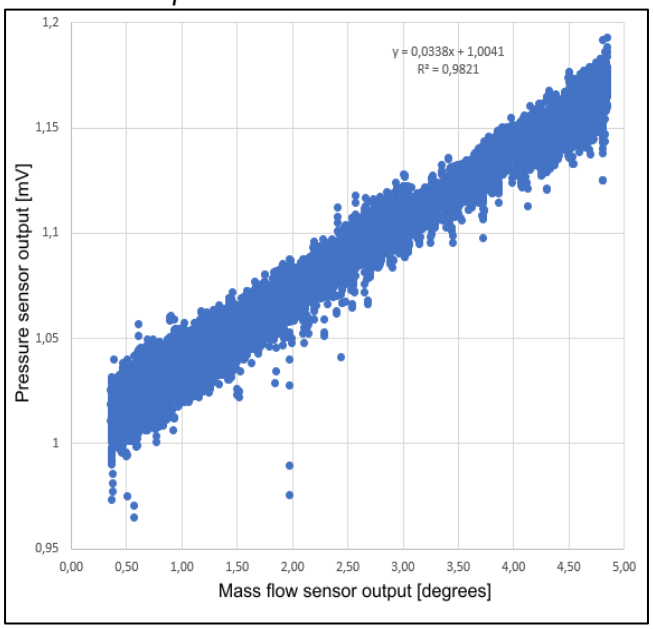

Figure 7. Measured pressure drop as a function of the phase shift from the micro Coriolis mass flow sensor for IPA.

The measured densities and viscosities of the medicine mixture are illustrated in Fig. 8 and Fig. 9. The densities of the mixture in Fig. 8 are in great accordance with the real values (only 0.2% error).

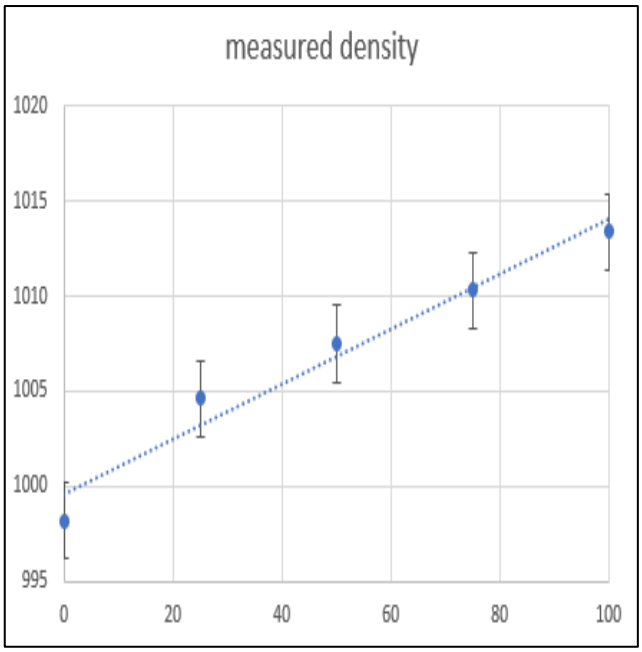

Figure 8. Measured density of the Dobutamine / Dopamine mixture based on the measured resonance frequency (error bars correspond to 0.2% error)

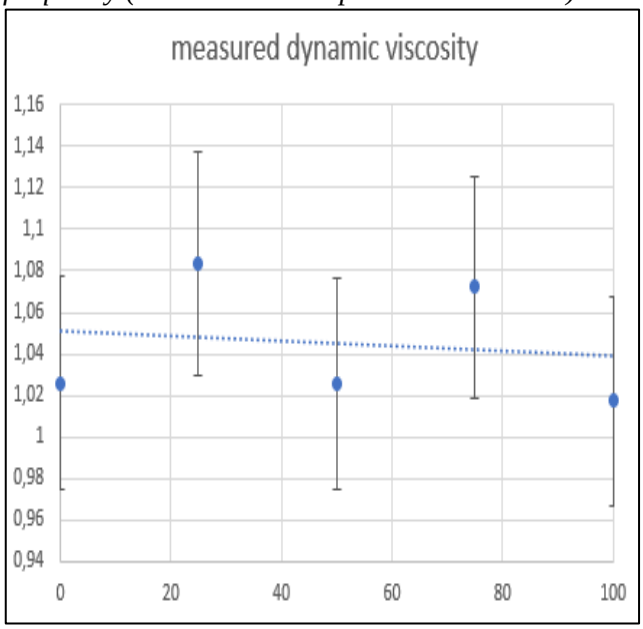

Figure 9. Measured dynamic viscosity of the Dobutamine/Dopamine mixture based on the phase of the Coriolis signals and the pressure drop measured by the resistive pressure sensors (error bars correspond to a 5% error).

However, for the viscosities, the error is larger (5%). This can be explained by two important facts. First of all, the viscosity is temperature dependent. In this case we should take into consideration the temperature variation at each measurement. Since Joule heating can occur due to the Lorentz actuation, I believe, in future measurements, an external temperature sensor (Pt 100) must be integrated within

the setup close enough to the channels to obtain real-time values of the temperature. And secondly, the nature of the liquids mixed together makes their viscosities very close in values. To remedy to this, further improvements must be brought to our microfluidic chip in terms of increased sensitivity of the pressure sensors. More sophisticated electronics along with new more developed chip will be ready soon for new measurements.

CONCLUSIONS

A multi-parameter microfluidic chip containing a capacitive Coriolis mass flow sensor integrated with two resistive pressure sensors was used to measure the viscosity of a binary medicinal mixture of Dopamine and Dobutamine. The measured densities agreed with the real values. However, for the viscosity more work and improvement need to be done to increase the sensitivity of the pressure sensors. Future work would include a ternary medicine mixture.

ACKNOWLEDGEMENTS

This work is part of the research program CHARMM which is jointly funded by the PiHC (Pioneers in Health Care), University of Twente, Saxion and MST.

REFERENCES

[1] C. Richard, J. L. Ricome, A. Rimailho, G. Bottineau, AND P. Auzepy, "Combined hemodynamic effects of dopamine and dobutamine in cardiogenic shock", Circulation 67, No. 3, pp. 620-626, 1983.
[2] D. Alveringh, T.V.P. Schut, R.J. Wiegerink, W. Sparreboom, J.C. Lötters, "Resistive pressure sensors integrated with a Coriolis mass flow sensor", Transducers 2017, 1167-1170.
[3] J. Groenesteijn, D. Alveringh, T.V.P. Schut, R.J. Wiegerink, W. Sparreboom, J.C. Lötters, "Micro Coriolis mass flow sensor with integrated resistive pressure sensors", MFHS conference 2017, 16-19.
[4] D. Alveringh et al., "Resistive pressure sensors integrated with a coriolis mass flow sensor," in Transducers, 19th Int. Conf. IEEE, 2017, pp. 1167–1170.
[5] J. Groenesteijn et al., "A versatile technology platform for microfluidic handling systems, part i: fabrication and functionalization," Microfluidics and Nanofluidics, vol. 21, no. 7, p. 127, 2017.

CONTACT

* Sabrine Mejri s.mejri@utwente.nl

TOWARDS A FULLY INTEGRATED AND DISPOSABLE DNA AMPLIFICATION CHIP

*F. Akegawa Monteiro[1], H.-W. Veltkamp[1 *], R.G.P. Sanders[1], R.J. Wiegerink[1], and J.C. Lötters[1,2]*
[1] MESA+ Institute for Nanotechnology, University of Twente, Enschede, The Netherlands
[2] Bronkhorst High-Tech BV, Ruurlo, The Netherlands

ABSTRACT

Fast point-of-use detection of early-stage zoonoses is beneficial for animal husbandry as it can save livestock and prevent farmers from going bankrupt after an outbreak. This paper describes the first steps towards a fully integrated and disposable DNA amplification chip. Based on the analysis of the milling process, metal adhesion study, COMSOL Multiphysics heat transfer simulations and chip characterization a feasible fabrication process is set up and the first batch of chips has been fabricated.

KEYWORDS

Zoonoses detection, on-chip DNA amplification, integrated heaters, disposable chips

INTRODUCTION

Zoonoses is a widespread problem in animal husbandry[1]. This group encompasses diseases which can be transferred between animals (usually vertebrates) and humans. They are transmitted through zoonotic agents (e.g. bacteria, virus, fungi, and parasites)[2]. An infamous example would be *Coxiella burnetii* (Q-fever)[2]. These diseases are of potential risk for livestock of farms. An outbreak among the livestock is disastrous to the owner of that farm, and for people living in the proximity of that farm[3]. Often, more animals of the livestock are infected and the whole livestock is exterminated out of precaution, which could lead to bankruptcy of the farmer. Therefore, early-stage detection is often the key to save livestock and farms. As these diseases are also encountered in developing countries, where farms are often remotely located, it is desired that such detection equipment is portable and as cheap as possible. A lab-on-a-chip platform can be used for this early-stage detection.

In the early stage of these diseases, the agent, and therefore its DNA, are not widespread in the infected animal, making the detection rather difficult. A detection system has to amplify the DNA of the disease until a certain threshold is reached and detection is possible. When this amplification reaction is sequence specific, for example by using polymerase chain reaction (PCR) or helicase-dependent amplification (HDA), and when a fluorescent DNA dye is used, a simple yes-or-no answer for a specific disease can be obtained. In the past, several chip-based DNA amplification devices with fluorescence detection were reported. However, in these devices heat supply for the DNA amplification reaction often comes from an external heat source[4] or is processed in a different substrate and later incorporated onto the chip[5]. A challenge that seems to remain is to incorporate heaters on a disposable, often polymeric, substrate. Incorporation of heaters will simplify the required equipment and therefore, lower its costs.

The work presented here aims at the development of a disposable, polymeric DNA amplification lab-on-chip system with integrated resistive heaters and fluorescence detection. The choice of substrate material, deposition method, and metal are studied. Although, it is mentioned above that PCR and HDA are sequence specific, the model reaction chosen is multiple displacement amplification (MDA). This reaction is more straightforward, as it amplifies any present double stranded DNA, and is therefore better suitable as a proof-of-principle amplification reaction to show the functioning of the integrated heaters.

CHIP DESIGN

A chamber-based amplification chip is designed based on the work of Bruijns *et al.*[5]. Using SolidWorks 2018 CAD/CAE software, the 3D image of the chip is drawn and with the AutoDesk HSMWorks CAD/CAM plug-in, this image is transferred into computer numerical control (CNC) milling code. The total chip size is $3\,\mathrm{cm}$ by $3\,\mathrm{cm}$ and has a chamber of $10\,\mathrm{mm}$ by $3\,\mathrm{mm}$. Two trapezoid structures are placed in the tapered channels between the inlet/outlet and the chamber. The function of these trapezoids is twofold. Firstly, they minimize the dead volume between the inlet/outlet and the reaction chamber, locating as much as possible of the reaction mixture inside the chamber. Secondly, they provide support for the chamber closure. A rectangular channel is located next to the reaction chamber and is also covered by the heaters. A thermocouple is inserted in this channel for

real-time monitoring of the temperature inside the chip. In figure 1 the SolidWorks design of the chamber-based chip is shown.

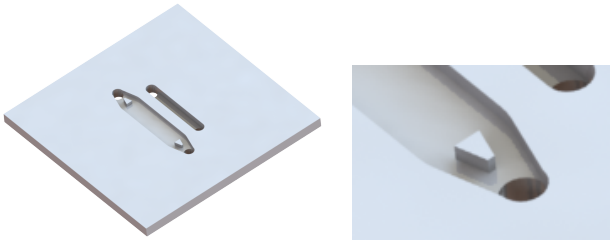

Figure 1: SolidWorks drawing of the DNA amplification chamber. This drawing is used to set up the code for the CNC mill. The small rectangular channel next to the chamber is for thermocouple-assisted real-time temperature monitoring. Total size of the chip is 3 cm by 3 cm. The close-up shows the in-channel trapezoid structure.

The heater structure will be placed at the bottom side of the chip using shadow masks. To determine the optimal heater width and heater spacing, a parametric study using COMSOL Multiphysics 5.3a finite element method simulations with the *Heat Transfer in Solids* (ht) package is done. The model is designed such that it consists of two parallel rectangles of COC (in the real device, the upper plate is a PCR adhesive foil) with water in between. The heaters are assumed to be lines. This reduces the required quality of the mesh tremendous, as the heaters in the real device will be around $100\,\mathrm{nm}$.

In figure 2, the results of two different heater widths and heater spacings are shown. The heater width for both geometries is $0.3\,\mathrm{mm}$, while the heater spacing in the left and right image are $0.3\,\mathrm{mm}$ and $2.0\,\mathrm{mm}$, respectively. In figure 3a and 3b, tables with the temperature deviation between the highest and lowest temperature at the top of the chamber ($\Delta T_{\text{top of channel}} = T_{top,max} - T_{top,min}$) and the deviation between the set heater temperature of $30\,^{\circ}\mathrm{C}$ and the lowest temperature at the top of the chamber ($\Delta T_{\text{deviation from set T}} = T_{heater} - T_{top,min}$) are shown for different heater widths and heater spacings. Based on these results, a meandering heater pattern of a $0.3\,\mathrm{mm}$ wide heater with $0.3\,\mathrm{mm}$ spacing in between the lines is designed. The pattern is divided over two shadow masks to prevent curvature of the long stainless steel beams in between the meandering structure.

FABRICATION

Cyclic olefin copolymer (COC)[6] is chosen as polymeric substrate due to its bio-compatibility, optical transparency, physical resistance, electrical insulation, and price. Injection molded COC plates of $10\,\mathrm{cm}$ by $10\,\mathrm{cm}$ and $1.5\,\mathrm{mm}$ thickness of the grade TOPAS 6017 are obtained via Kunststoff-Zentrum Leipzig. This grade is chosen because of its relatively high glass transition temperature ($\mathrm{T_g} = 170\,^{\circ}\mathrm{C}$), which minimizes melting during the milling process. The microfluidic structure explained in section is CNC-milled using a Mikron WF 21C milling machine. The milling causes a considerable loss of optical transparency due to the created roughness. This could obstruct the fluorescence detection. Therefore, a chemical post-treatment with cyclohexane vapor is done, such treatment dissolves the upper layer of COC and causes reflowing of the material due to its surface tension, restoring the optical transparency and reducing the surface roughness[7].

Metal is deposited on the substrate using laser-cut Mo shadow masks to outline the shape of the resistive heaters. Mo has a smaller coefficient of thermal expansion and is therefore chosen instead of stainless steel. Metals of interest are Au or Pt, which are commonly used metals to function as resistive heaters[8]. The deposition methods studied are DC magnetron sputtering and e-beam physical vapor deposition (evaporation). Both methods are capable of large-scale production, which will lower the production costs on an industrial scale. The metal and deposition method will be chosen based on the metal adhesion performances on the COC substrate, which is studied using the Scotch tape test[9], and the resistance versus temperature behavior in the range $20\,^{\circ}\mathrm{C}$ – $100\,^{\circ}\mathrm{C}$, which is measured in a customized Heraeus T5025 oven with electrical readout.

The chambers with the resistive heaters on the backside are closed using Microseal 'B' PCR plate sealing film from Bio-Rad, which is cut in the proper size and manually attached on top of the substrate. The reaction mixture containing DNA and the amplification mixture is pipetted inside the chip using the inlet aperture, and the inlet and outlet are closed using the same PCR film. A power is applied on the resistive heaters until they acquire the desired temperature for the amplification. The initial power is based on the resistance measurements, but will be adjusted according to the feedback loop of the thermocouple. Detection of the amplification is done by using an Horiba Scientific FluoroMax+ spectrofluorometer, but will in the near future be done by *in-situ* fluorescence measurements using an optical fiber together with the FluoroMax+.

RESULTS

The process towards a fully integrated and

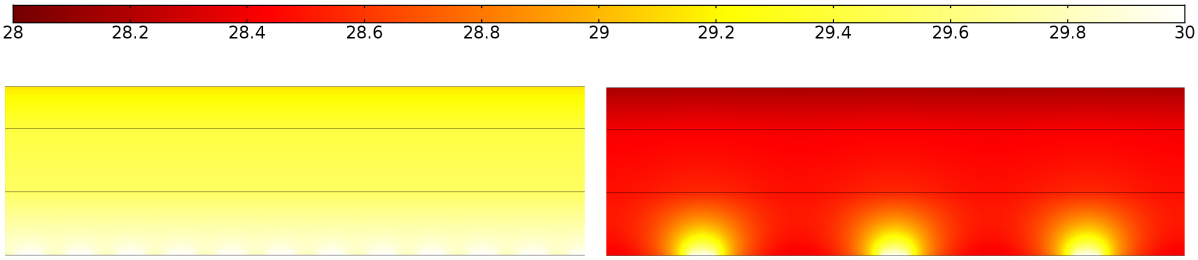

(a) 0.3 mm width and 0.3 mm spacing.

(b) 0.3 mm width and 2.0 mm spacing.

Figure 2: COMSOL heat transfer simulations of a 0.75 mm deep chamber with different heater widths and heater spacings. The scale bar applies to figure 2a and 2b.

	0.3	0.4	0.5	0.6	0.7	0.8	0.9	1.0	1.1	1.2	1.3	1.4	1.5	1.6	1.7	1.8	1.9	2.0
0.3	0.000	0.001	0.001	0.001	0.001	0.002	0.001	0.001	0.001	0.001	0.001	0.001	0.001	0.003	0.001	0.003	0.004	0.002
0.4	0.001	0.001	0.002	0.001	0.002	0.001	0.002	0.001	0.001	0.001	0.001	0.002	0.002	0.001	0.003	0.004	0.003	0.002
0.5	0.001	0.002	0.001	0.003	0.001	0.002	0.001	0.001	0.001	0.002	0.002	0.002	0.003	0.006	0.003	0.003	0.003	0.006
0.6	0.003	0.001	0.003	0.002	0.002	0.002	0.004	0.001	0.002	0.002	0.004	0.002	0.004	0.006	0.004	0.004	0.007	0.005
0.7	0.002	0.004	0.002	0.003	0.002	0.002	0.006	0.002	0.003	0.003	0.003	0.006	0.007	0.006	0.005	0.009	0.007	0.009
0.8	0.005	0.002	0.003	0.002	0.002	0.002	0.002	0.005	0.005	0.003	0.006	0.007	0.007	0.007	0.011	0.008	0.012	0.011
0.9	0.003	0.004	0.003	0.007	0.008	0.003	0.005	0.006	0.004	0.008	0.009	0.008	0.008	0.012	0.010	0.014	0.013	0.013
1.0	0.006	0.004	0.003	0.004	0.004	0.006	0.006	0.006	0.009	0.010	0.010	0.010	0.015	0.012	0.017	0.017	0.017	0.017
1.1	0.005	0.003	0.004	0.004	0.007	0.008	0.006	0.010	0.012	0.011	0.011	0.018	0.014	0.019	0.019	0.019	0.020	0.030
1.2	0.005	0.005	0.005	0.008	0.008	0.007	0.011	0.013	0.013	0.013	0.020	0.016	0.022	0.021	0.022	0.024	0.034	0.030
1.3	0.006	0.006	0.009	0.010	0.008	0.014	0.015	0.015	0.015	0.022	0.018	0.024	0.025	0.026	0.027	0.038	0.034	0.033
1.4	0.008	0.012	0.012	0.009	0.015	0.018	0.016	0.017	0.025	0.020	0.027	0.027	0.029	0.030	0.043	0.038	0.037	0.040
1.5	0.014	0.013	0.011	0.017	0.020	0.018	0.018	0.028	0.022	0.030	0.030	0.032	0.049	0.048	0.042	0.042	0.044	0.053
1.6	0.017	0.012	0.020	0.023	0.020	0.019	0.031	0.024	0.034	0.034	0.035	0.037	0.053	0.047	0.046	0.048	0.058	0.060
1.7	0.014	0.023	0.027	0.022	0.021	0.034	0.026	0.036	0.037	0.039	0.040	0.058	0.051	0.049	0.053	0.064	0.065	0.067
1.8	0.027	0.033	0.024	0.023	0.038	0.028	0.04	0.040	0.041	0.043	0.062	0.056	0.054	0.057	0.069	0.072	0.074	0.077
1.9	0.039	0.027	0.025	0.041	0.030	0.043	0.043	0.044	0.047	0.068	0.061	0.059	0.062	0.076	0.077	0.080	0.083	0.086
2.0	0.031	0.026	0.046	0.032	0.047	0.047	0.048	0.049	0.074	0.065	0.062	0.066	0.082	0.083	0.086	0.090	0.093	0.096

(a) $\Delta T_{top\ of\ channel} = T_{top,max} - T_{top,min}$.

	0.3	0.4	0.5	0.6	0.7	0.8	0.9	1.0	1.1	1.2	1.3	1.4	1.5	1.6	1.7	1.8	1.9	2.0
0.3	0.585	0.574	0.566	0.560	0.555	0.552	0.548	0.546	0.544	0.542	0.540	0.539	0.538	0.538	0.535	0.536	0.537	0.534
0.4	0.626	0.608	0.597	0.587	0.581	0.574	0.570	0.565	0.562	0.559	0.556	0.555	0.553	0.550	0.550	0.550	0.547	0.545
0.5	0.671	0.649	0.631	0.620	0.609	0.601	0.594	0.588	0.583	0.579	0.576	0.573	0.570	0.568	0.568	0.563	0.561	0.562
0.6	0.722	0.691	0.672	0.654	0.642	0.631	0.624	0.614	0.608	0.603	0.599	0.593	0.591	0.589	0.584	0.581	0.581	0.576
0.7	0.774	0.740	0.712	0.693	0.676	0.663	0.656	0.643	0.636	0.629	0.622	0.619	0.615	0.609	0.604	0.604	0.598	0.597
0.8	0.832	0.787	0.757	0.733	0.714	0.698	0.685	0.676	0.666	0.656	0.651	0.645	0.638	0.632	0.631	0.623	0.622	0.617
0.9	0.888	0.840	0.804	0.780	0.759	0.736	0.722	0.709	0.696	0.689	0.681	0.671	0.664	0.661	0.652	0.650	0.644	0.639
1.0	0.950	0.893	0.852	0.821	0.796	0.777	0.759	0.743	0.732	0.721	0.710	0.700	0.696	0.685	0.682	0.675	0.669	0.663
1.1	1.010	0.947	0.902	0.867	0.841	0.818	0.796	0.782	0.768	0.753	0.741	0.736	0.722	0.717	0.709	0.701	0.694	0.697
1.2	1.072	1.004	0.954	0.918	0.886	0.858	0.839	0.821	0.803	0.787	0.780	0.763	0.757	0.746	0.737	0.729	0.731	0.719
1.3	1.136	1.062	1.010	0.967	0.930	0.906	0.882	0.859	0.839	0.829	0.809	0.801	0.788	0.777	0.767	0.768	0.754	0.744
1.4	1.201	1.125	1.065	1.015	0.982	0.952	0.922	0.898	0.885	0.860	0.850	0.834	0.821	0.809	0.809	0.793	0.781	0.774
1.5	1.271	1.184	1.117	1.072	1.033	0.995	0.964	0.947	0.917	0.904	0.885	0.869	0.870	0.854	0.835	0.822	0.812	0.810
1.6	1.338	1.241	1.179	1.127	1.078	1.039	1.018	0.981	0.965	0.942	0.922	0.905	0.903	0.881	0.865	0.854	0.851	0.841
1.7	1.399	1.310	1.240	1.175	1.126	1.097	1.053	1.032	1.005	0.981	0.960	0.957	0.931	0.912	0.899	0.896	0.883	0.872
1.8	1.476	1.378	1.290	1.226	1.189	1.134	1.108	1.074	1.045	1.020	1.015	0.986	0.964	0.948	0.943	0.929	0.916	0.905
1.9	1.552	1.430	1.344	1.294	1.227	1.193	1.152	1.117	1.087	1.080	1.046	1.020	1.001	0.995	0.978	0.963	0.950	0.938
2.0	1.607	1.487	1.419	1.334	1.290	1.240	1.197	1.160	1.151	1.111	1.080	1.059	1.051	1.031	1.014	0.999	0.985	0.972

(b) $\Delta T_{deviation\ from\ set\ T} = T_{heater} - T_{top,min}$.

Figure 3: Temperature differences for different heater widths (0.3 mm to 2.0 mm, in the columns) and heater spacings (0.3 mm to 2.0 mm, in the rows), obtained using a parametric sweep in the COMSOL Multiphysics heat transfer simulations.

disposable DNA amplification chip can be divided into several smaller steps, each with their own results. These steps are discussed in the following subsections.

Optical transparency

With the reported surface treatment[7] we were capable of increasing the optical transmittance fivefold. Cyclohexane vapor treatment duration is depending on the grade of COC and the initial surface roughness, which on its turn is depending on the milling machine, dept, speed, etc. The transmittance measurements are done using a Woollam M-2000UI ellipsometer. The surface roughness, measured using a Bruker Icon Dimension atomic force microscope and Gwyddion 2.52 software, decreased from $310.10\,\mathrm{nm}$ to $0.97\,\mathrm{nm}$ (compared to $3.50\,\mathrm{nm}$ for pristine COC).

Metal adhesion

In order to get the most reliable heaters, four possible options are investigated. The adhesion of Au and Pt deposited by either PVD or e-beam sputtering is investigated using the Scotch tape test[9]. Test patterns consisting of rectangular strips of $2\,\mathrm{mm}$ by $14\,\mathrm{mm}$ are fabricated by depositing $100\,\mathrm{nm}$ of metal using a shadow mask made out of Kapton foil. Based on the results in table 1, the choice of heater material is sputtered Au.

Table 1: Results of the Scotch tape metal adhesion tests before and after heat cycling. Here, $+$ means passing the tape test, $-$ means failing the tape test, and $+/-$ means that not all test structures failed the tape test.

Material	Method	Tape test		Initial
		Before	After	resistance [Ω]
Au	PVD	$+$	$-$	5.0
Au	Sputtering	$+$	$+$	8.2
Pt	PVD	$+$	$+$	400
Pt	Sputtering	$+$	$+/-$	6.8

Chip functioning

Characterization of the actual heater is done using a FLIR One Pro iOS thermal camera. Thermal images of the heater structure are made while different input powers are used to heat up the heaters. The images are processed using ImageJ post-processing software. Results of these measurements are shown in figure 4.

The reliability of the heaters is tested by inserting a 162 series RS Technics thermocouple K into the reference channel. A constant input potential of $4\,\mathrm{V}$ is applied and the temperature is measured for $24\,\mathrm{h}$. This exceeds the required operation time at least twelve-fold, meaning that it is a good indication for the reliability of the heater. The results are shown in figure 5.

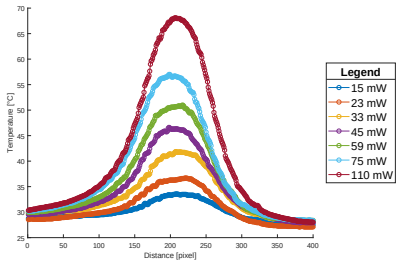

Figure 4: Temperature profiles over the heater structure for different input powers. Measurements are done using a FLIR One Pro iOS thermal camera.

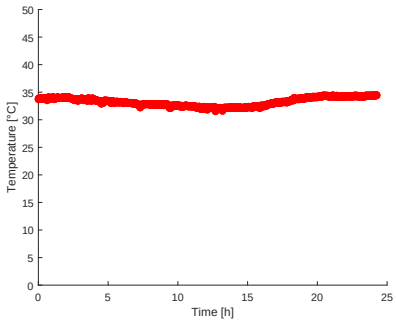

Figure 5: Duration test of the heater. A constant potential of 4 V is applied and the temperature is measured for 24 h.

DNA amplification

In figure 6, graphs of the fluorescence signal during MDA reactions at 25 °C and 30 °C, together with their non template control (NTC) are shown. These reactions are carried out in a conventional PCR machine and the results show that the chosen proof-of-principle DNA amplification reaction is temperature dependent to some extend, but that there is a wide range of temperatures at which the amplification can be performed. This makes the functioning of the integrated resistive heaters less critical.

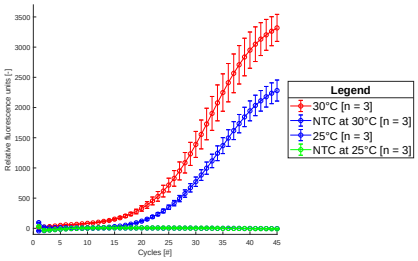

Figure 6: Fluorescence signal of MDA reactions performed at 25°C and 30°C, together with their (overlapping) NTCs.

CONCLUSION

With the obtained results of the steps towards a fully integrated and disposable DNA amplification chip, the conclusion can be made the realization of such a system will be achieved within a month after the Microfluidic Handling Systems Conference. The CNC milling and subsequent cyclohexane vapor treatment for regaining the optical transparency, and the use of adhesive PCR plate sealing film give well-defined reaction chambers. The sputtering of Au gives heater structures with good adhesion properties on COC and a long-term stability exceeding the required operation time by many hours (stability over 24 h is ±1.5 °C). All fabrication methods are chosen in such way that the production of the devices could easily be scaled-up to large-scale manufacturing plants.

ACKNOWLEDGMENTS

The authors would like to thank dr. Brigitte Bruijns from Micronit Microtechnologies for her help during the brainstorm sessions. Jörg Strack from TOPAS Advanced Polymers and dr. Thomas Wagenknecht from KUZ Leipzig are thanked for their information on COC. Pieter Post, Rob Dierink and Sip Jan Boorsma of TCO (technical center for education and research of the University of Twente) are thanked for their work in the milling and laser cutting processes, dr. Christian Bruinink for his assistance in the transparency measurements, Daniel Monteiro Cunha, M.Sc. for his assistance in the AFM measurements, and Nikki Stroot for her assistance with the initial amplification reactions.

REFERENCES

[1] B. Shin *et al. Front. Vet. Sci.*, 5(1):166/1–9, 2018. doi: 10.3389/fvets.2018.00166.

[2] L. Cantas *et al. Front. Public Health*, 2(144):1–8, 2014. doi: 10.3389/fpubh.2014.00144.

[3] W. van der Hoek *et al. Adv. Exp. Med. Biol.*, 984:329–364, 2012. doi: 10.1007/978-94-007-4315-1_17.

[4] W. Wu *et al. Anal. Bioanal. Chem.*, 400(7):2053–2060, 2011. doi: 10.1007/s00216-011-4947-x.

[5] B. B. Bruijns *et al. Sensor. Actuat. B-Chem.*, 293(1):16–22, 2019. doi: 10.1016/j.snb.2019.04.144.

[6] Topas Advanced Polymers. URL `https://topas.com/sites/default/files/files/TOPAS_Brochure_E_2014_06(1).pdf`. [Last accessed: Jun. 18, 2019].

[7] I. R. G. Ogilvie *et al. J. Micromech. Microeng.*, 20(6):065016/1–8, 2010. doi: 10.1088/0960-1317/20/6/065016.

[8] V. Miralles *et al. Diagnostics*, 3(1):33–67, 2013. doi: 10.3390/diagnostics3010033.

[9] I. F. Silvera *et al. Rev. Sci. Instrum.*, 57(7):1381–1383, 1986. doi: 10.1063/1.1138605.

CONTACT

Henk-Willem Veltkamp, h.veltkamp@utwente.nl

DISPENSING OF ATTOLITRE DROPLETS WITH INKJET TECHNIQUE

Y. Zhang[1,2], D. Li[2], and Y. Liu[2]
[1] Centre of micro-photonic, Swinburne University of Technology, Melbourne, Australia
[2] China University of Petroleum, College of Mechanical and Electronic Engineering, Qingdao, China

ABSTRACT

Generating smaller droplets in micro and submicro meters scale continuously and steadily has been a core research issue in recent years. In the conventional inkjet printing, the size of the generated droplets is close to the nozzle. And if you want to reduce the volume of the droplet, reducing the diameter of the nozzle is the only option, which can lead to a series of problems such as a sharp increase in production costs, difficulty in maintenance, and easy clogging. Here a fancy method was proposed to generate droplets over ten times smaller than the dispensing orifice. So there is no need to make smaller nozzles of comparable size to reduce the droplets size. Moreover, this method is endowed with the ability to handle high viscosity media without clogging.

KEYWORDS

Attoliter droplets, Inkjet printing, Dispensing, Droplets manipulation

INTRODUCTION

Dispensing and manipulation of small droplets is of significant importance in bioassays [1], chemical analysis [2] and patterning of functional inks [3]. So far, dispensing of small droplets has been achieved by continuous inkjet printing, drop-on-demand inkjet printing, thermal bubble driven printing, and electrohydrodynamic printing, etc. The basic principle of these methods mentioned above is squeezing the liquid out of a small orifice similar in size to the droplets. So a major drawback of these methods is if we want to obtain smaller droplets, we have to fabricate nozzles of the corresponding size, which is easier to clog and break. Meanwhile, the difficulty of fabricating smaller nozzles is a main obstacle limiting the development of the generating ultra-small droplets. So how to generate more fine droplets is a major difficulty at present.

Here we report that instead of squeezing the liquid out, small droplets can also be dispensed advantageously from large orifices by draining the liquid out of a drop suspended from a nozzle [1,2] , as shown in Fig. 1. In this way the diameter of the dispensed droplets can be several ten times smaller than size of the orifice, enabling the dispensing of politer to microliter volumes even from a millimeter-sized orifice that is rather immune against clogging when dispensing highly viscous liquids or suspensions. Furthermore, the use of orifices with diameters of several micrometres shows the capacity of dispensing sub-micrometer sized droplets. And the droplet volume can be adjusted from attolitre to microliter by proper working parameters. This method can handle suspensions and liquids with viscosities as high as thousands mPa s markedly increasing the range of applicable liquids for controlled dispensing, considering that the conventional methods only can handle media with viscosity no more than 20 mPa s. Furthermore, the movement of the dispensed droplets is controllable by the direction and the strength of an electric field potentially allowing the use of the droplet for extracting analytes from small sample volume or placing a droplet onto a pre-patterned surface.

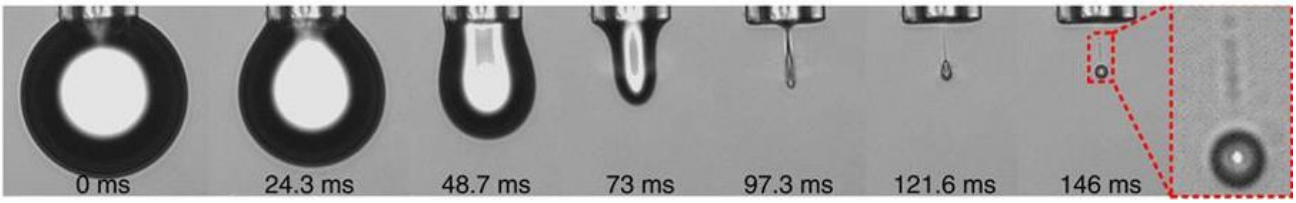

Figure 1: Droplet formation by draining the liquid out of a drop suspended from a nozzle, the outer diameter of the nozzle is 50 μm.

RESULTS AND DISCUSSIONS

In this paper we investigate the phenomenon mentioned above with a sessile surfactant-stabilized water droplet suspended from surface-treated nozzles. The whole system consists of an ink chamber, an orifice, and an inlet for ink supply. The ink chamber is coupled with a piezo ceramic actuator to drive the ink out if an electrical signal is applied to it. With the help of piezo electric inkjet nozzle, the liquid can be ejected out of the orifice (Fig. 2a) or oscillate at the orifice (Fig.2b and Fig. 2c), depending on the voltage applied on the micro piezo of the nozzle. If we drain

the liquid with different drainage rates Q, the droplet size V_d can be controlled and pinch-off regimes can be very different. As shown in Fig. 2c, the extruded liquid will be sucked back to the chamber if the voltage applied on the piezo is much smaller than the ejection voltage. And drop oscillation phenomenon will be observed in this case. Nothing will be generated if this oscillation happens in air. However, if this oscillation phenomenon happens in another liquid with a certain viscosity, which is immiscible with the ink, one small droplets will be pinched off by each oscillation under some ideal situations (Fig. 1a and Fig. 3).

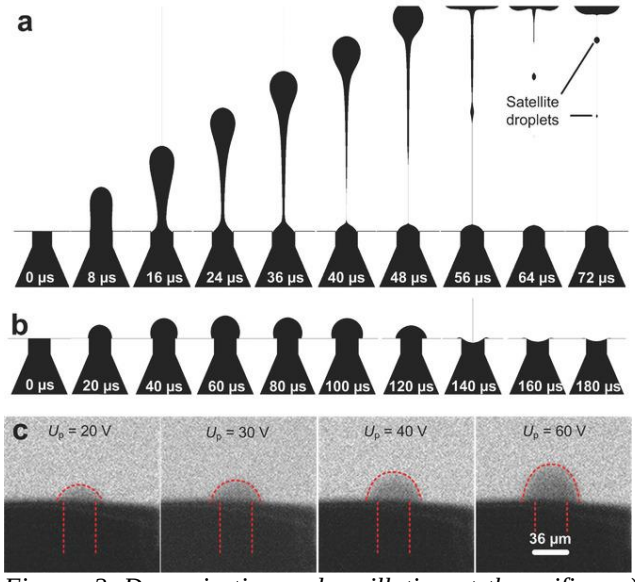

Figure. 2. Drop ejection and oscillation at the orifice. a) Simulation results of the typical drop ejection process; b) simulation results of the drop oscillation at the orifice; c) time-lapse photography images captured during the oscillation caused by different driven voltage applied on the micro piezo.

The droplets pinch-off mechanism was investigated by combining high speed imaging with CFD simulations. Fig. 1 shows that the whole pinch-off process in another immiscible liquid medium can be divided into two stages: firstly, the sphere-shaped sessile drop evolves into a cylindrical column with the height being much larger than its radius due to the drainage of the inner chamber and interfacial tensions with the outer liquid; secondly, the liquid column breaks up due to Rayleigh–Plateau instability after the stop of the drainage and pinches off one main daughter droplet with R_d much smaller than the radius of the mother droplet R_m. There is an extension factor ε, defined as the ratio of the length of the liquid column to the circumference. And when $\varepsilon > 1$, the filament will break-up and form a daughter droplet when the suck back rate is small. In addition, several ultra-fine satellite droplets may be formed under some certain circumstance, as shown in the right side of Fig. 1. But the total volume of all the very fine droplets accompanying the main droplet can be neglected, which only occupies less than 1% of the whole volume.

A series of experiments show that the size of the droplets increases with the increasing voltage applied to the piezo actuator, pressure at the inlet of the chamber and the external electric field between the nozzle and the substrate. It decreases with increasing dispensing frequency. The “burst dispensing mode” of the nozzle allow us to apply a given number of pulses and to pinch off the same number of droplets. As shown in Fig. 3a, different numbers of droplets will be pinched off by applying the corresponding number of electric pulses to the piezoelectric actuator, which is defined as drop-on-demand. Droplets also can be pinched off continuously by applying a continuous sequence of electric pulses as shown in the last two panels in Fig. 3a. This is the “continuous dispensing mode” of the nozzle.

The gravity of the droplets can be neglected due to the extremely small size of the daughter droplet and the small density difference between ink and carrier liquid. Without outside disturbance, the daughter droplets will keep still in the carrier liquid. So we can make a further investigation of the mechanism of the daughter droplets’ formation. As recorded by the high speed camera in Fig. 3a, the pinch-off position of the daughter droplets is at a fixed location until the next ink drop extrusion process pushes the previously pinched-off droplet away from the orifice. Then the subsequent drainage will generate a new daughter droplet and haul back the previously generated daughter droplets. Actually, the daughter droplets, especially the droplets near the orifice, will move back and forth due to the oscillation of the mother drop and finally be pushed away by the later generated daughter droplets. What’s more, the mother drop oscillation has little influence on the daughter droplets which are far away from the orifice. Therefore, the movement of those droplets is mainly due to the push of the later daughter droplets. In the continuously dispensing mode, a queue of daughter droplets will be formed and gradually being pushed away from the nozzle (Fig. 3a). And as investigated in other literatures, the droplet in the queue will coalescent if they meet each other, and the process only takes 1 micro second, which is difficult to record the phenomenon by high speed camera. However, the captured time-lapse photography images in the last two panels of Fig. 3a clearly justify the above statement about the pinch off and droplets movement. With the random coalescence, the droplets will become larger.

To gain insight into the mechanism behind the daughter droplet formation, we simulated the mother drop oscillation process in liquid environment by computational fluid dynamics (CFD). And as shown in Fig. 3b, the numerical results coincide well with the experiment observation as indicated by the same pinched off position (Fig. 3b, panel for 230 μs and its zoom-in). CFD results showed that the breakup of the neck is caused by the Rayleigh–Plateau instability. In analogy to our previous work [4,5], which investigated the daughter droplet generation from larger orifices, the simulation results in this paper indicate that the pinch-off follows similar mechanisms, although there is a large difference in space and time scales.

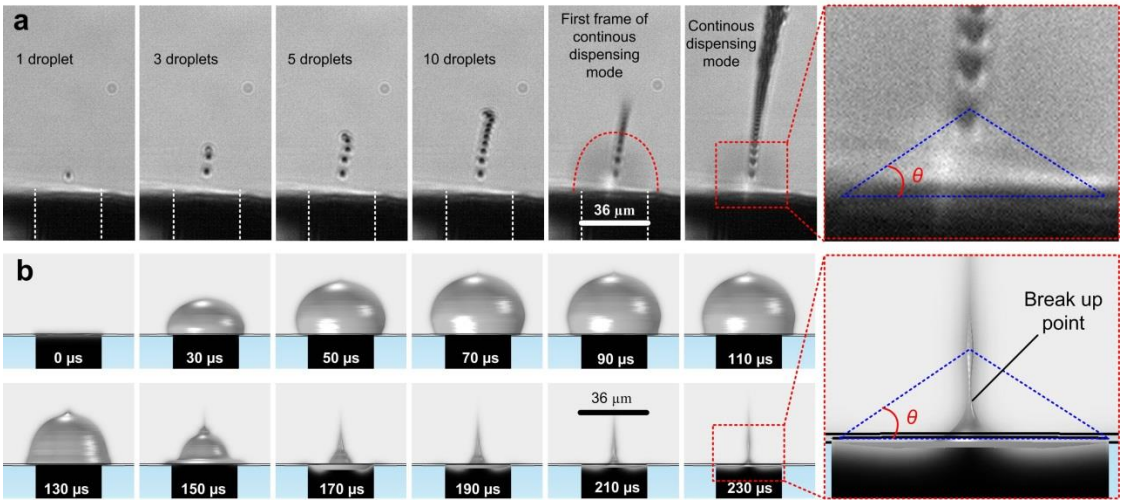

Figure. 3: Droplets pinched off in a carrier liquid. a) Droplets pinched off in burst mode (the first for panel) and continuous dispensing mode (the last two panels); b) simulation of a single drop volume oscillation period including the pinch off event in a carrier liquid.

After the generation, in order to realize the manipulation of droplets and avoid the aggregation of them, the electric field was introduced into this droplet generation system. By applying suitable voltage between the nozzle and the substrate, the pinched off droplets can be guided to the substrate, as shown in Fig. 4. Inkjet printing in liquid environment can be performed, but with much high printing resolution. In electric field, the droplets will be charged and move according to the direction of the field (Fig. 4a-h), forming an ordered queue. The results showed that the droplet moving velocity, v_d, increases with increasing U_s. In addition, the droplet size and moving velocity also increases with increasing U_s due to the electric force acting on the liquid column during the pinch-off process. The "burst dispensing mode" of the dispenser allow us to print femtoliter droplets arrays which are of significant interest for a variety of scientific applications. And variety droplets with different volumes can be obtained by adjusting the relative parameters.

Patterns with high resolution can also be printed. In Fig. 4i-k, the average diameter of the droplets on the substrate is about 2 and 13 μm, respectively. For comparison, Fig. 4l shows drops printed in air using the same nozzle employed for the printing in the carrier liquid. The volume of the drops printed in air (100 pL in Fig. 4l) is about 20 000 times larger than those printed in liquid (5 fL in Fig. 4j).

Different from the traditional inkjet printing in air which can eject ink drops with a frequency as high as several tens kHz, the printing frequency is limited in liquid environments by the moving velocity of the droplets. In air, the ejection process can give the ink drops enough momentums to attain a velocity v_d of several m/s, whereas in liquid, the droplets can only move at a relatively low velocity due to the viscous and inertia of the carrier liquid, for the sake of the obstruction of surrounding liquid medium. Although v_d can be slightly increased by using carrier liquids of lower viscosity and applying higher electric fields, v_d remain far below the corresponding values in air. Although low v_d in the carrier liquid represents a disadvantage limiting the printing efficiency, for high resolution printing, low f and v_d should be adopted to assure the precision of the pattern. And removing the carrier liquid without destroying or affecting the printed pattern on the substrate is very challenging. Therefore, this printing-in-liquid technique is not suitable for printing objects that will finally be used in air. For printing-in-liquid, we anticipate application in the areas where small droplets are used in an immiscible carrier liquid anyway such as micro- and nanofluidics, formation of defined nanometer sized interfaces for immiscible

electrolyte solutions and artificial constrained.

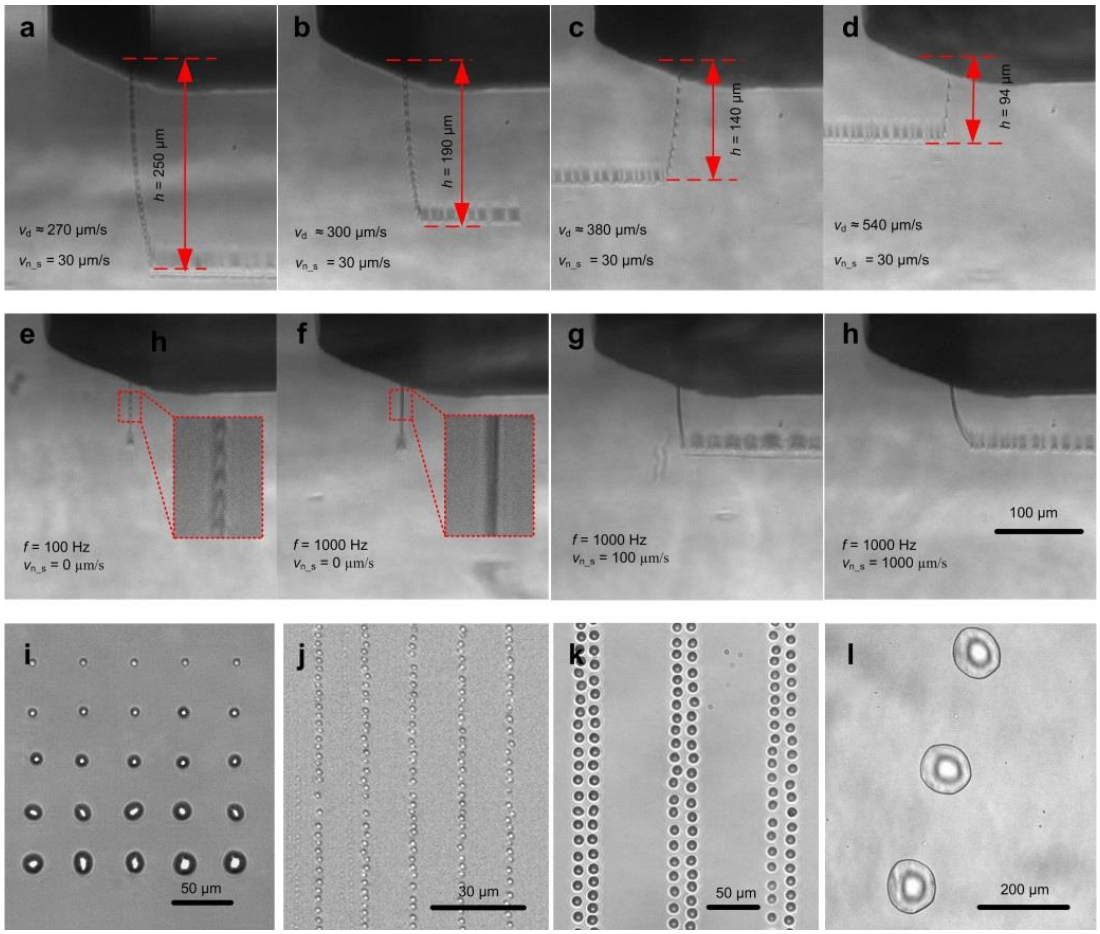

Figure 4: Printing in carrier liquid. a-d). Printing with different distance from the substrate; e-h). Printing with different frequency and nozzle moving velocity; i-k). Patterns printed in carrier liquid; l). droplets printed in air with the same nozzle for comparison.

CONCLUSIONS

In this work, a novel and unique working mode of the traditional piezoelectric inkjet nozzle is demonstrated. Femtoliter and attoliter droplets arrays and patterns can be easily printed just by immersing the inkjet nozzle into a carrier liquid which is immiscible with the ink, and the size of the generated droplets can be tens times smaller than the orifice. Millimetre-sized orifices facilitate dispensing nano/picolitre droplets of highly viscous liquids, emulsions or suspensions that are difficult to process by established ink-jet technologies due to the clogging of smaller nozzles. The method also exhibits remarkable capacity for manipulation of the droplets after the dispensing process using an electric field between the nozzle and the substrate. We expect our method to pave ways for new developments in drop-on-demand devices, for example, for dosing of reactive and temperature sensitive solutions, emulsions and suspensions, for the release of droplets to be used as small reactors or for placing miniature samples onto plasmonically and/or electrochemically active micro- and nanostructure for their chemical analysis within microfluidic biotechnological devices.

REFERENCES

[1] Meckenstock, R. U. et al., “Water droplets in oil are microhabitats for microbial life”, Science, Vol. 345, pp. 673-676, 2014.

[2] Y. Zhao, Z. Xu, H. Niu, X. Wang, T. Lin, “Magnetic liquid marbles: toward ‘lab in a droplet’”, Adv. Funct. Mater. Vol. 25, pp. 437-444, 2015.

[3] G. Azzellino, A. Grimoldi, M. Binda, M. Caironi, D. Natali, M. Sampietro, “Fully inkjet-printed organic photodetectors with high quantum yield”, Adv. Mater., Vol. 25, pp. 201303473, 2013.

[4] Y. Zhang, B. Zhu, Y. Liu, G. Wittstock, “Hydrodynamic dispensing and electrical manipulation of attolitre droplets”, Nat. Commun., Vol. 7, pp. 12424, 2016.

[5] Y. Zhang, D. Li, Y. Liu, G. Wittstock, “Inkjet printing in liquid environments”, Small, Vol. 14(27), pp. 1801212, 2018.

CONTACT

* Yanzhen Zhang, yanzhenzhang@swin.edu.au

COMPARISON OF PLANAR AND HALBACH PERMANENT MAGNET SYSTEMS FOR MOBILE MICROFLUIDIC NMR APPLICATIONS

Yannick Philippe Klein [1], *Leon Abelmann[1,2], Jankees Hogendoorn[3], Han Gardeniers[1]*
[1] Mesoscale Chemical Systems, University of Twente, Enschede, The Netherlands
[2] KIST Europe, Saarland University, Saarbrücken, Germany
[3] KROHNE Nederland B.V., Dordrecht, The Netherlands

ABSTRACT

We optimized the magnetic field inhomogeneity of a simple cuboid and a more complex Pseudo-Halbach configuration for mobile microfluidic NMR-applications. Next to the influence of the sample length, general design guidelines will be presented. For a fair comparison the sensitive length of the sample has been chosen to be the same as the gap size between the magnets to ensure enough space for the transmitting and receiving unit, as well as basic electric shimming components around the complete magnet configuration. Keeping the compactness of the final device in mind, a box with an edge length 5 times the gap size has been defined in which the complete magnet configuration should fit. With the chosen boundary conditions, the simple parallel cuboid configuration reaches the best inhomogeneity without active shimming ($0.5B_s$, 41 ppm), while the Pseudo-Halbach configuration has the highest field strength ($0.9B_s$, 994 ppm).

KEYWORDS

mobile NMR, permanent magnets, magnetic field homogeneity

INTRODUCTION

Low-field and low-cost mobile microfluidic nuclear magnetic resonance (NMR) sensors are very suitable for applications in chemical process industry and in research, for example chemical analysis, biomedical applications or flow measurements [1] [2] [3]. The design of a permanent magnet for NMR-sensors requires both a strong magnetic field and a high field homogeneity within a defined volume of interest. In NMR, a high external magnetic field B_s results in a high spectral resolution and detection sensitivity. However, inhomogeneities of B_s compromise the spectral resolution. In literature several magnet shapes for mobile NMR-sensors have been reported. U-shaped single-sided magnets and magnets with specially shaped iron pole magnets, have been used to explore surfaces, mobile Pseudo-Halbach configurations and two cylindrical magnets have been applied for solid and liquid NMR measurements [4]. Comparing the reported mobile NMR sensors it stands out that there is no obvious relation between the size of the sensor and the choice of the magnet configuration. To achieve more insight in the magnet design guidelines, in this work a modelling study has been performed from which the homogeneity and field strength at specific locations in the gap of the magnet configuration is derived numerically.

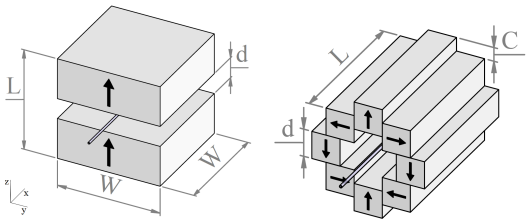

Figure 1: Left: Schematic view of the cuboid configuration Right: Schematic view of the Pseudo-Halbach configuration The arrows indicate the magnetization of each individual magnet.

To compare planar and Halbach permanent magnet systems for such devices the following boundary conditions have been chosen: The sensitive length of the channel (s) has been chosen to be the same as the gap size (d) between the magnets to ensure enough space for the transmitting and receiving unit, as well as for basic electric shimming components around the channel. Keeping the compactness of the final device in mind, a box with an edge length (L) 5 times the gap size has been defined in which the whole configuration should fit. For example: In case a maximal magnet size of 5 cm x 5 cm x 5 cm is required, the gap size and the channel length results to be 1 cm. All dimension specifications are scalable and will be normalized with the gap length, scaling the dimensions bigger or smaller will result in an increased or decreased sample volume while the magnetic properties within the region of interest will stay the same. The magnetic field has been normalized to the saturation magnetization of the used magnetic material.

METHODS

Computational method

The simulations have been done using CADES simulation software, completely described by Delinchant et al. [5]. Magnetic interactions are modelled with the MacMMems tool, which uses the Coloumbian equivalent charge method to generate a semi-analytic model.

$$\mathbf{H}(\mathbf{r}) = \iint_S \frac{\sigma_S \cdot (\mathbf{r} - \mathbf{r'})}{|\mathbf{r} - \mathbf{r'}|^3}\, ds + \iiint_V \frac{\sigma_V \cdot (\mathbf{r} - \mathbf{r'})}{|\mathbf{r} - \mathbf{r'}|^3}\, dv$$

$$\sigma_S = \mathbf{M} \cdot \mathbf{n}$$

$$\sigma_V = -div(\mathbf{M})$$

with **H** as the magnetic field intensity. **r** and **r'** define the observation point and its distance to the elementary field source enclosed by ds and dv, σ_S and σ_V are the surface and volume charge, **n** a vector normal to surface and **M** the magnetisation .

The CADES framework, including component generator, component calculator and component optimizer generated the final equations which are used by to calculate and optimize the designs.

Design

To optimize magnet configurations, the field inhomogeneity of its z-component was defined as the root mean square of the difference of the mean field and the field along the sample with the length (s), B_{mean} respectively B_0, related to the mean field:

$$\frac{\frac{1}{s}\int_0^s \sqrt{(B_0 - B_{\text{mean}})^2}dx}{B_{\text{mean}}} \qquad (1)$$

For better understanding of the different magnet configurations, we start with a description of the cuboid case. The cuboid configuration can be found in fig. 1. The field strength is symmetric, showing a valley in the middle and two peaks in direction of the edges. After those maxima the field is decreasing with the distance to the magnet.

Fig. 2 shows how the field homogeneity develops with increasing the sample size while keeping the previously optimized parameter-set constant. Three regions

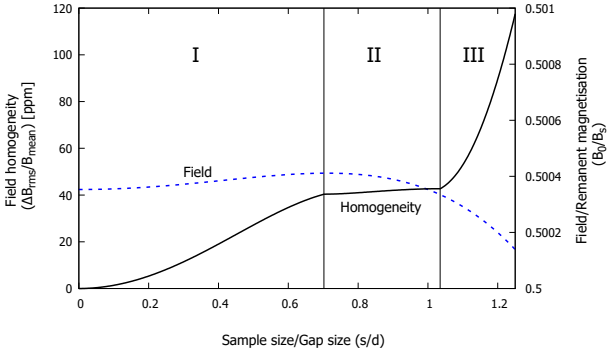

Figure 2: Field inhomogeneity and field as a function of the sample size for the cuboid configuration. The homogeneity has been optimized for a sample size equal to the gap. With increasing the sample size both the field and the field inhomogeneity increases theoretically (region I). The field reaches a local maximum of 0.5004$\mathrm{B_s}$ at a distance of 0.71d from the center. Above this distance the homogeneity of the sample stays approximately the same (region II). When the sample size increases more than 1.1 times the gap size, the inhomogeneity strongly increases (region III). Hence, to optimize the homogeneity of cuboid magnet configuration the field difference between the center and the sample edge needs to be minimized.

can be seen. In the first one the field is rising from $0.50035\mathrm{B_s}$ to $0.50041\mathrm{B_s}$, which means that the minimal field of $0.50035\mathrm{B_s}$ stays the same while the maximum field is increasing till it reaches its global maximum, hence the inhomogeneity is also increasing. In the second region the inhomogeneity stays almost constant. In the third region the field is dropping below the previous minimum which results in a drastic increase of the inhomogeneity. Because of that the lowest inhomogeneity between two points can be either reached keeping the sample as short as possible or when the field difference at the sample edges and the middle are the same. This information is important for the following optimization processes. High stray fields raise a safety issue due to attraction of the magnet by larger magnetic objects causing its uncontrollable movements; hence next to the homogeneity, the stray field has been simulated at a distance of d from the configuration surface is $0.24\mathrm{B_s}$.

RESULTS AND DISCUSSION

Optimization

The cuboid configuration (fig. 1) consists out of two parallel cuboid magnets, the length (L) of the whole configuration has been chosen to be five times the gap size (d). The width (W) was used to tune the field in between the magnets. This subsection will show how to optimize a cuboid configuration using its width to tune the field-homogeneity. From the previous section we know that we have to find a width, for which the field in the center and at the sample edge is the same.

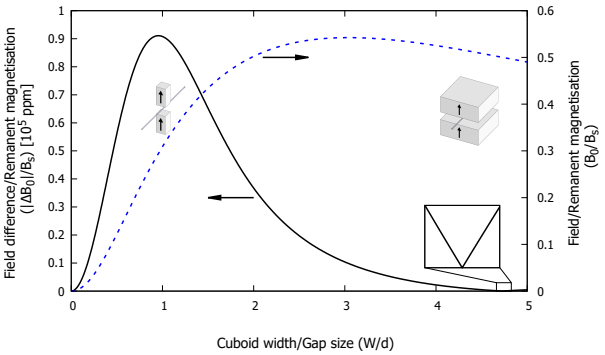

Figure 3: Field strength in the middle of the configuration and difference of the field center and the edge of the sample, both as function of cuboid width over length ratio. Field increases up to 0.54 B_s *at cuboid width 3.0375 times the gap size. The inset shows the field difference dropping to zero at a width/gap ratio of 4.72.*

Fig. 4 shows that the magnetic field in the center is rising up to its maximum of $0.54B_s$ at a width of $3.0375d$. Increasing the width further results in a reduction of the magnetic field, caused by the higher distance from the magnet edges to the center. The difference of the magnetic field in the center and the sample edge is rising till it reaches a maximum at a width/gap ratio of 1. From this point the difference is decreasing till it reaches a minimum at width/gap = 4.72. Its stray field at a distance d is 0.24 B_s.

The Pseudo-Halbach configuration (fig. 1) consists out of eight magnets, arranged in such a way that the field in the bore becomes enhanced while the stray-field is minimized. The magnets have a fixed dimension ($d \times d \times 5d$). To tune the homogeneity, the position of the magnets in the corners stay the same, while the other magnets get spread, illustrated with a spread parameter C. The width starts at W = 3d to ensure a minimum bore width of d and ends at W = L, due to the previously chosen boundary conditions.

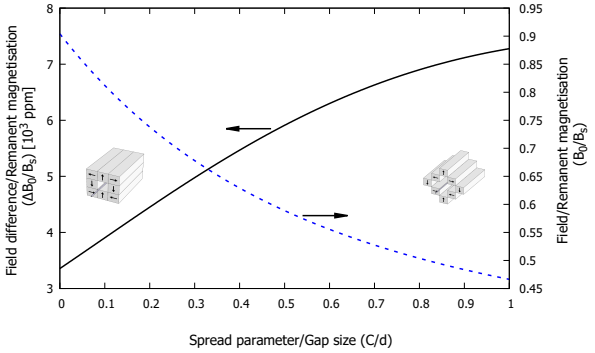

*Figure 4: Spreading the middle magnets has been used to change the normalized field strength and field difference. At a spread parameter C = 0, a minimal field difference of 3365 ppm and a field strength of 0.90*B_s *can be reached.*

With spreading the configuration, the distance of the middle magnets increase which results in a decreased magnetic field strength (fig. 4). With this configuration the convex field profile has no chance to change to a concave profile - a minimum can not be reached. With the most compact magnet arrangement, a field of $0.9B_s$ and a field difference of 3365 ppm can be achieved. The stray field is at a distance d from the surface is $0.07B_s$.

Comparison

Table 1 compares the major specifications of the two configurations.

Table 1: Comparison of magnetic and mechanic properties of different magnet configurations.

	B_{max} [B_s]	B_{stray} [B_s]	$\Delta B_{rms}/B_{mean}$ [ppm]
Cuboid	0.5	0.24	41
Pseudo-Halbach	0.9	0.07	994

The Pseudo-Halbach configuration reaches 0.9 B_s, a 1.8 times higher field as the Cuboid configuration, while the stray-field at a distance of d from the magnet surface is with $0.07B_s$ 3.4 times lower. In terms of homogeneity the Cuboid configuration reaches a homogeneity of 41 ppm, which is compared to the Pseudo-Halbach configuration 24.2 times better.

CONCLUSIONS

In this paper a cuboid and a Pseudo-Halbach configuration have been compared regarding their field strength, field homogeneity and stray field. We have shown that for our boundary conditions (sample size equal gap size, max. magnet edge length equal five times gap size) the magnetic field drops strongly for a sample size longer than the gap. The field inhomogeneity increases for a sample size above 70% of the gap size, and remains constant up to 103%. Thus, to reach the best homogeneity for a 1D sample using a cuboid configuration the field difference in the center and the edge of the sample needs to be equal (fig. 2). The width of the cuboid magnets can be used to tune the field homogeneity. For our boundary conditions a minimal field difference can be found with a width over gap size ratio of 4.72. With this ratio, the field in the center reaches $0.5B_s$ (fig. 3).
Regarding the Pseudo-Halbach configuration, the distance of the mid-positioned magnet has been chosen to tune the field homogeneity. We have shown that with decreasing the distance, the field strength in the center increases (up to $0.9B_s$ for the gap size equals the sample size), while the homogeneity decreases (fig. 4). The pseudo-Halbach configuration has a 64% lower external stray field, which reduces interference with the environment, but is more difficult to assemble than the cuboid due to the 4 times larger amount of magnets (tab. 1).

REFERENCES

[1] J. Mitchell, L.F. Gladden, T.C. Chandrasekera, and E.J. Fordham. "Low-field permanent magnets for industrial process and quality control". Progress in Nuclear Magnetic Resonance Spectroscopy, 76:160, jan 2014.

[2] Dirk Kreyenschulte, Eva Paciok, Lars Regestein, Bernhard Blumich, and Jochen Buchs. "Online monitoring of fermentation processes via non-invasive low-field NMR. Biotechnology and Bioengineering", 112(9):18101821, may 2015.

[3] Morten K. Srensen, Ole Jensen, Oleg N. Bakharev, Tavs Nyord, and Niels Chr. Nielsen. NPK NMR sensor: "Online monitoring of nitrogen, phosphorus, and potassium in animal slurry". Analytical Chemistry, 87(13):6446 6450, jun 2015.

[4] Vasiliki Demas and Pablo J. Prado. "Compact magnets for magnetic resonance". Concepts in Magnetic Resonance Part A, 34A(1):4859, jan 2009.

[5] B. Delinchant, D. Duret, L. Estrabaut, L. Gerbaud, H. Nguyen Huu, B. Du Peloux, H.L. Rakotoarison, F. Verdiere, and F. Wurtz. "An optimizer using the software component paradigm for the optimization of engineering systems". COMPEL - The international journal for computation and mathematics in electrical and electronic engineering, 26(2):368379, 2007.

CONTACT

* Y.P. Klein, y.p.klein@utwente.nl

ATOMIZATION OF FLUIDS WITH ULTRASOUND

P. Dunst[1], P. Bornmann[2], T. Hemsel[1], W. Littmann[2], and W. Sextro[1]*
[1] Paderborn University, Chair of Dynamics and Mechatronics, Paderborn, Germany
[2] ATHENA Technologie Beratung GmbH, Paderborn, Germany

ABSTRACT

In a variety of industrial applications, liquids are atomized to produce aerosols for further processing. Example applications are the coating of surfaces with paints, the application of ultra-thin adhesive layers and the atomization of fuels for the production of combustible dispersions. In this publication different atomizing principles (standing-wave, capillary-wave, vibrating-mesh) are examined and discussed. Using an optimized standing-wave system, tough liquids with viscosities of up to about 100 Pas could be successfully atomized.

KEYWORDS

atomization, ultrasound, standing-wave, capillary-wave, vibrating-mesh

INTRODUCTION

Since the individual applications differ greatly considering to the properties of the liquid, their intended use, the required throughputs and the desired properties of the dispersion, the atomizing systems must be customized to fulfil the requirements of the respective process with high technical and economical efficiency. The relevant parameters of the atomizing process are the flow rate of the liquid, the required droplet diameter (mean diameter and diameter distribution), viscosity and surface tension of the liquid and the permissible velocity of the droplets. Standard atomizing systems like pressure and pneumatic nozzles or mechanical atomizers typically produce sprays at high volume but mean variation of the droplet size is often unwanted high. As well, spray velocity is rather high and the technical effort raises if fluids with higher viscosity shall be dispersed.

Atomizing fluids by ultrasound is well known since decades, but its common use is rather limited yet. The ultrasound systems can generate comparatively low spray velocity, but are either only suitable for small volume flows or can only atomize low-viscosity fluids. This contribution reports on three basic principles for atomizing fluids using ultrasound (capillary-wave, standing-wave and vibrating-mesh atomization). The limitations are investigated and improvements are made using model based optimization. In conclusion, the advantages and disadvantages of the three systems are worked out in order to be able to give recommendations for different application scenarios.

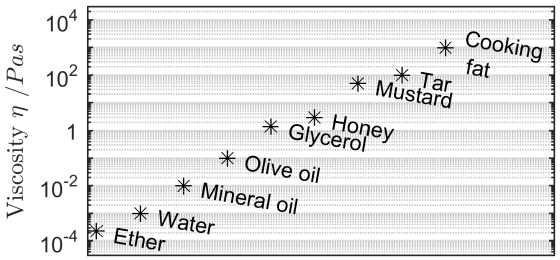

Figure 1: Viscosities of common fluids.

Figure 1 shows a compilation of common fluids and their viscosities, to classify the viscosity values mentioned in this publication. Experiments were done on glycerol-water solutions and silicone oils with different viscosities.

STANDING WAVE ATOMIZATION

Ultrasound standing-wave systems consist of a piezoelectric Langevin transducer, which generates a sound wave. Using a reflector which is arranged opposite to the transducer a standing wave is generated and the sound pressure is increased. The atomization happens in the sound pressure node of the standing wave and depends on many parameters like the sound pressure level of the adjacent sound pressure maxima, the viscosity and surface tension of the fluid and also dimensions and velocity of the inflow [1].

At present, there is no standing-wave system commercially available for atomization. However, literature reports the atomization of fluids with viscosities of up to 10 Pas [7], which is an outstanding result for atomizers and would e. g. allow for the dispersion of adhesives. To further move that limit, the maximum sound pressure in the standing wave field must be increased, which is possible by geometry optimization.

The standing-wave condition is to be fulfilled for all emitted and reflected sound waves and no sound waves should leave the space between the transducer and the reflector to achieve an optimum. In order to meet these conditions, the distance between the transducer and the

reflector as well as the reflector shape were optimized [2]. The optimization was performed on a linear two-dimensional finite-element-model. For the validation of the model results, pressure sensors as well as a scanning refracto-vibrometry, [4, 5] were used.

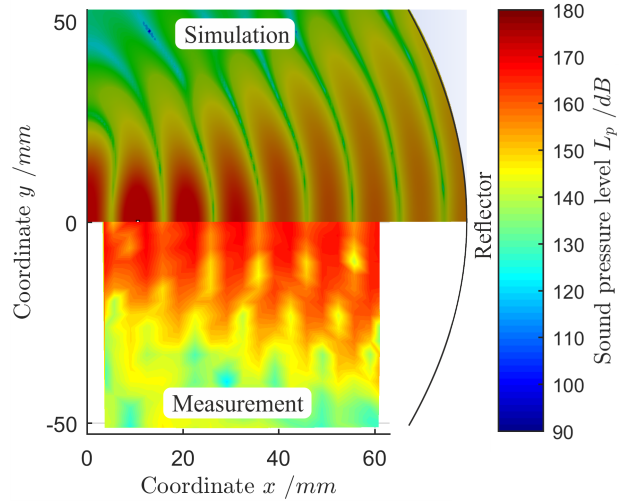

Figure 2: Comparison of measurement and simulation of a standing-wave system with concave reflector at a distance of $L = 4\lambda$, $f = 21.4\ kHz$, $\hat{v} = 2.55\ m/s$

Figure 2 shows a comparison of the simulated and measured sound pressure in an optimized standing-wave system. Although the results of the linear model show much higher sound pressure levels, the sound pressure distribution is in very good agreement. By using a concave reflector at the optimal distance, the maximum sound pressure level could be increased more than 10 times compared to a plain reflector.

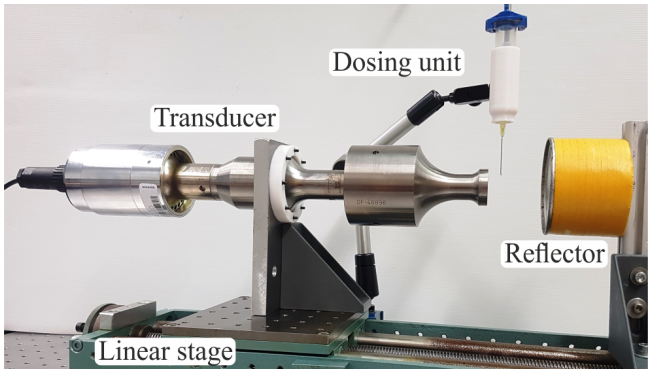

Figure 3: Standing-wave system, consisting of ultrasonic transducer, reflector and dosing unit.

With a vibration amplitude of $\hat{v} = 17.5\ m/s$ at the tip of the transducer (frequency $f = 20\ kHz$ a sound pressure level of $L_p = 182\ dB$ was reached.Figure 3 shows the correcponding standing-wave system, consisting of a transducer on a linear stage, an optimized reflector and a dosing unit.

To evaluate the efficiency of the optimized system, silicone oils with different viscosities were atomized. Figure 4 shows the atomization of silicone oil with a viscosity of $1,000\ cSt$ (about $960 mPas$). At the flow rate of $2.5\ ml/s$, which is relatively high for atomization of fluids with high viscosity, a complete atomization is achieved.

Figure 4: Standing-wave atomization of silicone oil with viscosity of $1,000\ cSt$ $(960\ mPas)$ *at a mass flow of* $2.5\ ml/s$

At a lower flow rate of a few ml/min, silicone oil with a viscosity of up to 100,000 cSt (about 96 Pas) could be atomized.

CAPILLARY WAVE ATOMIZATION

Capillary wave atomizers produce fine droplets by generating surface acoustic waves on a thin liquid film using ultrasonic vibration. They are used to atomize low-viscuos fluids, e. g. in oil combustion systems, and can produce high volume flows of up to about $30\ ml/s$. The surface acoustic waves are generated by an ultrasound transducer that operates in a frequency range between 20 and $800\ kHz$. The droplet diameter depends on the frequency of the ultrasonic excitation and fluid parameters like surface tension and viscosity. However, according to literature this process is limited to viscosities up to $20\ mPas$ [1].

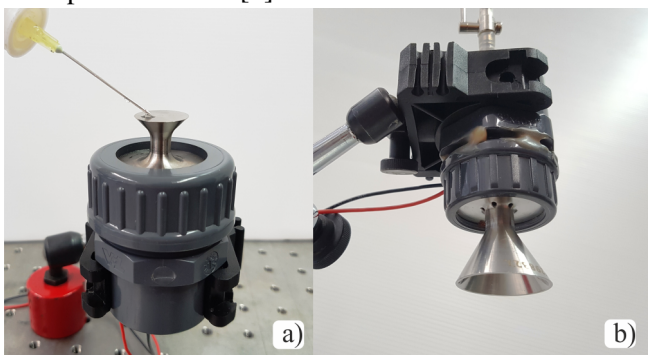

Figure 5: Systems for capillary-wave atomization on plain surface a) and on conical surface b).

Figure 5 shows two different types of capillary-wave atomizers. Figure 5a) shows a transducer with plain surface, whereupon the fluid is supplied, generating an axial nebulization. In figure 5b) the fluid is supplied through holes in the transducer onto a vibrating conical surface, which generates a mostly radial nebulization.

Own studies have shown that fluids with viscosities of up to 50 mPas can be atomized. Figure 6 shows the capillary-wave atomization of silicone oil with a viscosity of 50 cSt (48 $mPas$) at a frequency of 20 kHz.

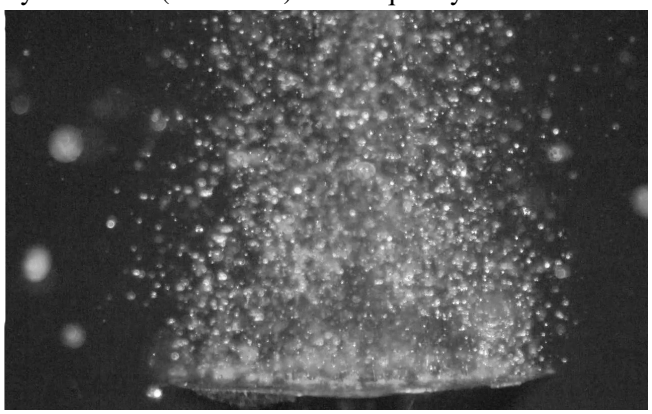

Figure 6: Capillary-wave atomization of silicon oil with viscosity of 50 mPas.

Depending on viscosity and surface tension of the fluid and vibration frequency, there is a minimum vibration amplitude needed to start the atomization. Figure 7 shows the critical amplitude for glycerol-water solutions with different viscosities and almost constant surface tension.

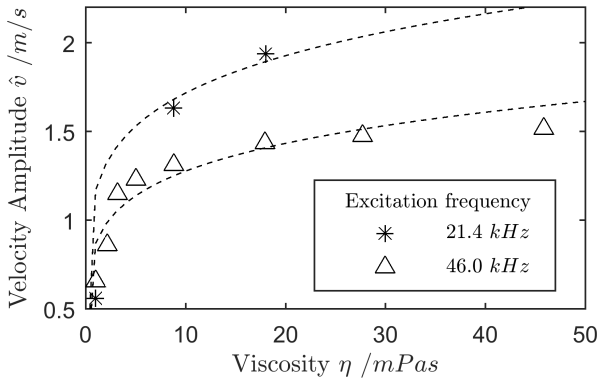

Figure 7: Required minimum amplitude for atomization of glycerol-water mixtures with different viscosities.

According to [1] the critical amplitude is proportional to $(\eta/\rho)^{1/6}$ with dynamical viscosity η and density rho. The dashed lines in figure 7 show a fitted function with proportionality to $(\eta/\rho)^{1/6}$. The experimental results are in good accordance to that.

VIBRATING MESH ATOMIZATION

A relatively young technology of atomizing liquids are vibrating-mesh nebulisers, which generate a fine aerosol by pushing the liquid through a mesh at frequencies of about 100 kHz (see figure 8). Benefits of this technology are the simple design and the ability to set drop diameters by adjusting the size of the holes in the mesh. Typically, the atomizers consist of a piezoelectric ring, which is adhered to a membrane with holes. The fluid is kept on one side of the atomizer and is atomized on the other side during the process. Figure 8 shows the cross-section of a vibrating-mesh atomizer and a photograph of the mesh and the piezoelectric ring.

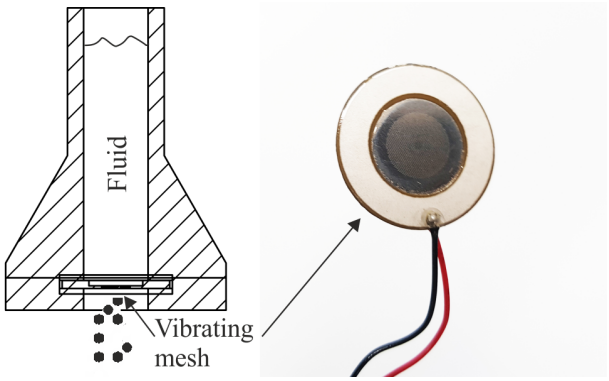

Figure 8: Vibrating-mesh nebulizer for atomization of low-viscosity fluids.

Publications show applications only, in which water-equivalent liquids with low viscosity are atomized [6]. In a series of experiments, the flow rate of a vibrating-mesh atomizer was measured for different excitation amplitudes.

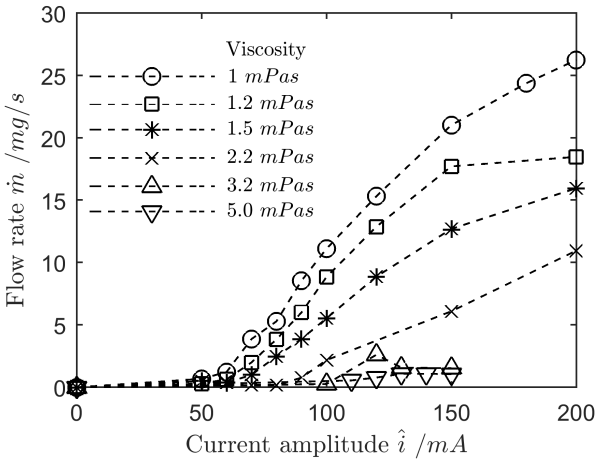

Figure 9: Flow rate of a glycerol-water solution over the excitation amplitude for a vibrating-mesh atomizer with a hole diameter of 5 μm.

Figure 9 shows the flow rate of glycerol-water solutions with different viscosities over the current ampli-

tude at the piezoelectric ceramics of the vibrating mesh, which is proportional to the vibration amplitude of the mesh. For all fluids the flow rate increases with increasing current amplitude. The flow rate is higher for fluids with lower viscosity. The absolute limit for atomization with a vibrating-mesh atomizer was about 10 $mPas$, but at very low and unstable flow rates.

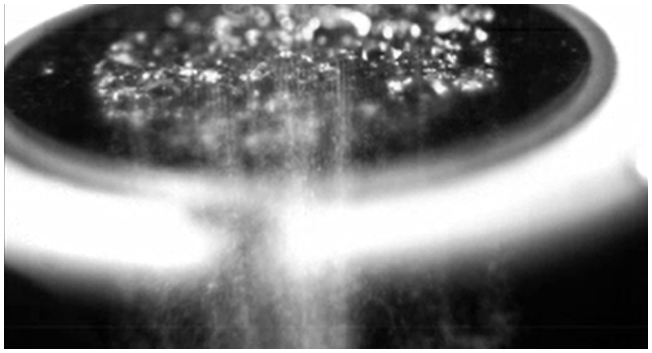

Figure 10: Vibrating-mesh atomization of water with viscosity of 1 mPas.

Using a high-speed camera the atomizing process of a vibrating-mesh atomizer was examined. During atomization three different mechanisms occur: 1) a bubble-jet atomization, where single drops are blown out of a hole 2) a capillary-wave atomization from bigger drops, that are formed on the outlet side of the vibrating mesh 3) at very low excitation amplitude drops grow on the outlet side and block the whole process if they do not fall down.

CONCLUSIONS

Measurements on vibrating-mesh atomizers showed a direct dependency between the excitation amplitude of the vibrating mesh and the flow rate. Although vibrating-mesh atomizers are only suitable for fluids with very low viscosities, they are increasingly used in the mass market, due to their simple design and compactness. Current applications include humidifiers and inhalers.

The capillary wave atomization is suitable for atomizing fluids with viscosities of up to about 50 $mPas$. Atomization results depend also on the surface tension of the fluid. However, the effects of surface tension are low for fluids with higher viscosity and were not considered in this publication. The capillary wave atomization is mainly used in humidifiers, vacuum dryers and powder generators for materials with low melting point [1].

Using an optimized standing-wave system, fluids with viscosities of up to about 100 Pas can be atomized. However, the maximum flow rate decreased with increasing viscosity of the fluid. There is no clear critical sound pressure level, at which the atomization works. Instead, the diameters of droplets increase with decreasing excitation amplitude and increasing flow rate. The ultrasonic standing-wave atomization is suitable for fluids with low viscosity as well as liquids with very high viscosity. An advantage is also the contactless atomization. Therefore, it is especially suitable for spraying hot metal melts, but also highly viscous adhesives.

REFERENCES

[1] E. G. Lierke, “Techniken und Anwendungen der Ultraschallzerstäubung – ein Rückblick auf 35 Jahre Forschung und Entwicklung”, Chemie Ingenieur Technik 70, 1998, pp. 815-826.

[2] P. Dunst, T. Hemsel, P. Bornmann, W. Littmann, W. Sextro, “Modellbasierte und experimentelle Charakterisierung von intensiven Ultraschall-Stehwellenfeldern für die Zerstäubung hochviskoser Flüssigkeiten”, DAGA 2019 proceedings, pp. 1037-1040.

[3] P. Dunst, P. Bornmann, T. Hemsel, W. Littmann, W. Littmann, “Vibration Assisted Dosing, Mixing and Transport of Dry Fine Powders”, ACTUATOR 2018, 16th International Conference on New Actuators

[4] L. Zipser, H. Franke, “Laser-scanning vibrometry for ultrasonic transducer development”, Sensors and Actuators A ’110, 2004, pp. 264-268

[5] W. Littmann, “Refracto-vibrometry”, Infocus ’1, 2010

[6] J. S. Lass, A. Sant, M. Knoch, “New advances in aerosolised drug delivery: vibrating membrane nebuliser technology”, Expert Opinion on Drug Delivery, 3:5, 2006, pp. 693-702

[7] O. Andersen, S. Hansmann, K. Bauckhage, “Production of Fine Particles from Melts of Metals or Highly Viscous Fluids by Ultrasonic Standing Wave Atomization”, Particle and Particle Systems Characterization, ’13, 1996, pp. 217-223

CONTACT

* Paul Dunst, paul.dunst@uni-paderborn.de

NO HEATED WALL EVAPORATOR: AN INNOVATIVE WAY TO REDUCE FOULING IN A MINIATURE EVAPORATOR SYSTEM

C.M. Rops[1], M. Del Hoyo Arroyo[2] , J.W. van de Geest[3] and R.M.C. Mestrom[2]

[1] TNO Science and Industry, High tech campus 21, The Netherlands
[2] Eindhoven university of Technology, PO Box 513, 5600 MB Eindhoven, The Netherlands
[3] Bronkhorst High-Tech BV, Ruurlo, The Netherlands

ABSTRACT

An innovative strategy for evaporation is the application of bulk heating using electromagnetic (EM) waves instead of hot walls. These hot walls are considered a root-cause for molecule degradation, precipitation and thus fouling. Fouling strongly impacts the reliability and robustness of miniature devices. To design a miniature EM evaporator, the interaction between the EM field and the fluid is investigated in this study. A measurement setup to test the proof-of-concept miniature evaporator has been constructed to determine the EM power input and the energy used for fluid heating. In initial tests, it was possible to heat up the water more than 10 Kelvin, absorbing almost 20% of the total power. The results are encouraging and evaporative tests with water will give further insights regarding the feasibility of this concept.

KEYWORDS

Electromagnetic heating, miniature/compact evaporator, flow boiling.

INTRODUCTION

Over the last decades, the development of microfluidic devices has shown extraordinary growth. Its main drivers are that small sized fluidic systems allow for better control of process conditions, faster response times, and functionality integration [1]. Due to the significantly reduced cost price, their availability has increased significantly. For example, in atomic layer deposition (ALD) and chemical vapour deposition (CVD) processes, micro evaporators could have added value, given their low flow rate, controllability and serviceability.

A challenge, however, is that small channel diameters require extra care on **fouling**, **reliability** and **thermo-mechanical** management. Fouling and reliability of a micro system are obviously determined by the deposition and entrainment rates of particles at the wall. In addition, the heated wall of the micro evaporator may act as a catalyst leading to undesired reactions which accelerate fouling. This may lead to uncontrolled behavior and ultimately clogging of the micro evaporator over time [2].

An innovative strategy to realise the phase transfer is the application of bulk heating using electromagnetic (EM) waves instead of hot walls. The interaction of the fluid with the EM field depends on the media properties. The electric field in the fluid scales inversely proportional to the dielectric constant, ε'. Additionally, the heat dissipation caused by this electric field depends on the loss factor (or electric conductivity) of the fluid [3]. These fluid properties depend on the frequency of the EM wave, on the fluid temperature and, of course, on the fluid itself.

Another advantage of applying EM waves is that the energy input will stop immediately as soon as the EM field is turned off. Therefore, no evaporation delay is present due to acting thermal capacities. Also, if the walls are made from good conductors, negligible bulk heat is generated in the walls. Therefore the wall temperature will not exceed the temperature of the fluid and the liquid can not become overheated and disintegrate. To prevent fluid disintegration by the EM wave, the EM should not interact with the internal structures of the molecules or atoms. This requirement poses an upper bound in frequency (or a lower bound on the wavelength). Together with cost considerations, this limits the allowed frequencies typically below 10 GHz, see Fig. 1.

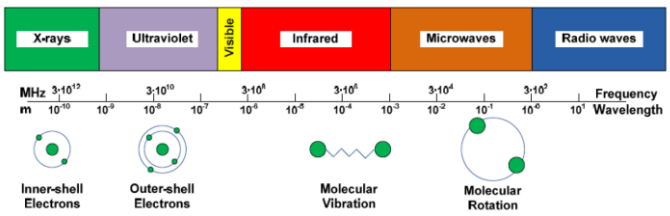

Figure 1: Interaction scale of EM waves with molecules and atoms [4].

In this investigation, we report on a feasibility study based on EM waves as an energy source in a continuous-flow micro evaporator. To design a miniature and compact EM evaporator the field-fluid interaction is studied first. Next, a measurement setup to test the proof-of-concept miniature evaporator has been designed. Finally, a test setup has been constructed for initial testing to determine the EM power input and the energy used for fluid heating

THEORETICAL BACKGROUND

In literature (and industry) the concept of a microwave chamber around a tube has already been explored [4, 5]. Typically the EM radiation is produced by a microwave antenna and is led towards the chamber in which the sample or tube is present using a wave guide. The electromagnetic waves interact with the fluid molecules. Therefore the energy is absorbed by the sample or liquid in the tube, which results in its temperature increase. However, this approach is difficult to realize in a miniature and compact EM evaporator design.

The electromagnetic interaction with the fluid is explained in further detail below. A fluid may contain molecules and/or atoms which are charged (ions). In an electric field the positive ions move along the field towards the negative potential and the negative ions in opposite direction. This field-induced transport causes friction and thus heat. On the other hand molecules that are neutral may have a polar nature, which is a small off-set between the center of the positive and negative charges (a so-called dipole moment). Under influence of a changing electric field, the molecules tend to reorient. This movement induces friction and thus heat as well. Finally, the dipole can be induced as a response of the electrons around the nuclei in the electric field (electronic polarisation) or the relative displacement of unequal charged atomic nuclei in the molecule (atomic polarisation) [6, 7].

The dipole moment, $\boldsymbol{\mu}$, of a particle is given by

$$\boldsymbol{\mu} = q\,\boldsymbol{x}, \tag{1}$$

where q is the charge and $\boldsymbol{x}$ is the charge separation distance. Gauss's law states that the flux through a closed surface is determined by its enclosed charges. The total charge of a system is related to the electric flux density vector, $\boldsymbol{D}$, which, in vacuum, is given by

$$\boldsymbol{D}_{vacuum} = \varepsilon_0 \boldsymbol{E}. \tag{2}$$

However the interaction of possible dipoles present in the medium introduces a polarization field, $\boldsymbol{P}$, which adds to the total flux density. The difference between the two vectors $\boldsymbol{P}$ and $\boldsymbol{D}$ gives the remaining free charges in a real medium.

$$\boldsymbol{D} = \varepsilon_0 \boldsymbol{E} + \boldsymbol{P}. \tag{3}$$

where ε_0 is the dielectric constant of vacuum. Therefore, the charge density can also be given by:

$$\boldsymbol{D} = \varepsilon_0 \varepsilon_r \boldsymbol{E}, \tag{4}$$

where ε_r is the relative dielectric constant. This relative dielectric constant attains a complex form:

$$\varepsilon_r = \varepsilon_r' - j\,\varepsilon_r'', \tag{5}$$

in which the imaginary part, ε_r'', is referred to as the loss factor. This naming can be better understood on assuming time-harmonic electric field variations, $\boldsymbol{E} = \tilde{\boldsymbol{E}}\exp(j\omega t)$. The total current density $\boldsymbol{J}$ is linearly proportional to the electric field ($\boldsymbol{J} = \sigma \boldsymbol{E}$) and the time derivative of the charge density, $\boldsymbol{D}$. Inserting (4) in time-harmonic form and with inserting (5), we get:

$$\boldsymbol{J} = \sigma \boldsymbol{E} + j\omega\varepsilon_0\varepsilon_r \boldsymbol{E} = (\sigma + \omega\varepsilon_0\varepsilon_r'')\boldsymbol{E} + j\omega\varepsilon_0\varepsilon_r' \boldsymbol{E}. \tag{6}$$

As can be seen from and (6), the imaginary part of the relative dielectric constant has the same effect as the (real) direct current (DC) electric conductivity, σ. On the other hand the (real) DC conductivity can be regarded as a type of frequency dependent loss factor for the effective relative dielectric constant:

$$\varepsilon_{effective}(\omega) = \varepsilon_r''(\omega) + \frac{\sigma}{\omega\varepsilon_0}. \tag{7}$$

This shows that for increasing frequencies the contribution of the DC conduction losses decreases. Other dielectric losses, $\varepsilon_r''(\omega)$ depend on the frequency, due to e.g. ionic translation, reorientation of dipoles, which behave frequency dependent. These strongly depend on the (internal) structure of the atoms and molecules of which the fluid consists. It is important to add that microwave heating of gases (and vapour) is hardly possible with frequencies up to 10 GHz. The distance between the rotating and/or translating molecules is too wide to cause heating up via friction.

Even though the loss factor may be more optimal for higher frequencies (>10 GHz), these frequencies do interact with smaller structures of the molecules/atoms. This possibly breaks the bonds at that level, and thus alters/degrades the fluid properties. Additionally, this allows the vapour to be heated substantially as well, needlessly bringing the fluid temperature significantly above its boiling temperature. Therefore the frequencies above 10 GHz are not considered within this investigation.

Dielectric properties of a fluid play an important role in microwave heating. The ratio of the loss factor ε_r'' to the real dielectric constant ε_r' is called the loss tangent ($\tan\delta = \varepsilon_r''/\varepsilon_r'$). The loss tangent determines the ability of any liquid to convert microwave energy into heat. In general, liquids can be classified based on this ability as high ($\tan\delta > 0.5$), medium ($0.1 < \tan\delta < 0.5$), and low ($\tan\delta < 0.1$) microwave absorbing fluids.

Liquids with different dielectric properties, when exposed to microwave radiation, have different responses to it. Liquids with very low dielectric constant and loss factors cannot absorb microwave energy efficiently, which makes them "transparent" to microwave radiation. The potential for applying microwave heating commercially depends on the dielectric properties of the fluid to be heated. Knowledge of how electromagnetic material properties depend on frequency is quite poor and has only been well-documented for water. Therefore, water will be used in this investigation, see Fig.2 .

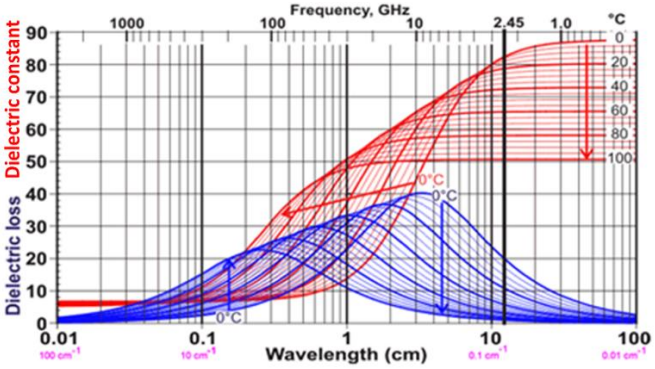

Figure 2: Dielectric constant and dielectric loss of water between 0 °C and 100 °C [8].

For the frequencies between 500-1000 MHz water has a typical loss tangent 0.01-0.1 depending on the frequency and temperature. Therefore water is a 'low' microwave absorbing fluid. However, we still consider this a useful range, because commercial fluids that need to be evaporated in the micro-evaporator are expected to have a low loss tangent as well.

EXPERIMENTAL SETUP

In order to validate the above premises, an experimental EM evaporator setup has been constructed. Although the actual liquid evaporation chamber is kept compact, as desired from performance point of view, its periphery is not fully integrated. Using readily available and individual components allows for a swift assembly of the test setup and allows to operate at a wide range of test parameters.

An overview of the measurement setup is given in Figure 3. The electromagnetic wave source for the evaporator consists of several pieces of equipment. A waveform generator is used to generate electrical waveforms over a wide range of frequencies. It is able to create various waveforms ranging from frequencies to 10 kHz to 2.45 GHz, with a maximum output power of 1 mW. Next, a power amplifier is used to increase the magnitude of power of a given input signal. The applied device can process signals up to 1 GHz. The power that can be supplied to the evaporator chamber can be up to 10 W. A directional coupler is used for measurement and monitoring of power and prevents reflected power reaching the amplifier. Two power meters are used, one measures the input signal to the evaporator, and another measures and dissipates the reflected power. The power meters measure the power in dB, which can be related to Watts.

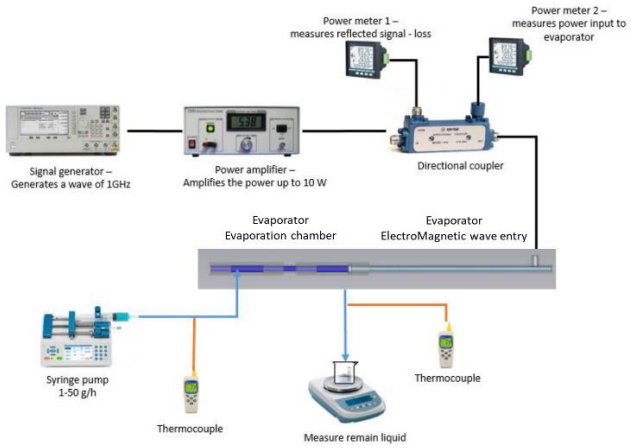

Figure 3: Schematic overview of the experimental setup.

In order to have little wave reflection at the entry of the evaporator setup, good electromagnetic coupling must be ensured by impedance matching. Therefore, a conventional RF connector is used. The reflected power may damage the amplifier and the possible resistance induces power losses leading to local (over)heating and thus performance loss.

The fluid handling system consists of the following components: a syringe pump that is able to deliver liquid from 1 to 50 grams per hour of water; A weighting scale to measure the water that remains liquid after going through the evaporator cavity. This liquid mass measurement at the exit allows an estimation on the amount of evaporation; A thin thermocouple (type K) to measure the temperature difference between the entrance and exit of the evaporator chamber.

EXPERIMENTAL RESULTS

First the absorption of the electromagnetic waves is investigated. This is done by filling the evaporation chamber with stagnant water and connecting to the EM source generating a harmonic wave. A frequency sweep is performed between 800-1000MHz, see Figure 4. By measuring the reflected signal, the absorbed power of the evaporator can be estimated, which is a measure of the energy deposited into the liquid. However, it must be noted that the absorbed power evaporator is not uniquely used for heated the liquid, since energy losses in the connections and EM waves leaking out of the setup may occur as well.

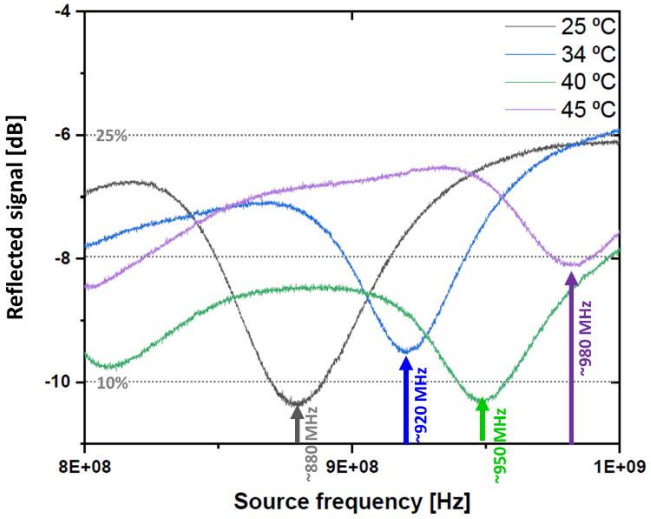

Figure 4: Relative strength of the reflected EM signal from the evaporation chamber filled with stagnant water at 4 temperatures.

In Figure 4 the relative strength of the reflected signal is shown for water at 4 different temperatures. For increasing temperatures the frequency increases at which the reflection dip (i.e. the resonance peak for absorption) occurs. Even though the reflected signal varies over the frequencies and is different for the four temperatures, the levels of absorption are always between 75% and 90% (-8 to -10.5 dB). These are promising values for heating up water in our evaporation chamber.

Next, the test of heating up water using EM waves in our compact evaporation chamber is carried out. The flow of water is set to 20 g/h, the power input is set to 1.85 W and the input frequency is set at 900 MHz. After the experiment reached steady state (all the signals – water temperatures, power input, and power reflected – are constant) the difference between the inlet and outlet temperature was measured.

The reflected power signal is about -4 dB (40%), which corresponds to about 0.75 W. The difference in temperature between the inlet and outlet stream of the evaporation chamber is 14 Kelvin. This corresponds to an absorbed power of about 0.3 W. The remainder (0.8 W) relates to power losses. As mentioned above, these power losses can be addressed to power losses in the conventional RF connector and electromagnetic power losses in the metal walls.

CONCLUSIONS

This investigation shows that it is possible to construct a compact evaporation chamber while using electromagnetic micro waves as a heating source. The compact evaporator is able to heat up water, at 1 bar by applying 900 MHz electromagnetic waves of 1.8 W. A temperature increase of 14 K is achieved for a water flow rate of 20 g/h. This result proves the concept that the liquid flow is able to absorb electromagnetic micro wave energy in a compact space. The results are encouraging and evaporative tests with water will give further insights regarding the feasibility of this concept.

REFERENCES

[1] P. Tabeling, Introduction to microfluidics. Oxford university press, 2006.

[2] J.F. Perry, Fouling in silicon microchannel designs used for IC chip cooling and its mitigation, *Dissertation*, Rochester Institute of Technology, 2008.

[3] Introduction to Electrodynamics, D.J. Griffiths, Pearson Education, 4th edition, 2013

[4] N.G. Patil, Integration of microwave heating with continuously operated milli-reactors for fine chemical synthesis, *dissertation*, Eindhoven University of Technology, 2012.

[5] N.E. Leadbeater, H.M. Torenius, A study of the ionic liquid mediated microwave heating of organic solvent, *J. Org. Chem*. vol.67(9), pp. 3145-3148, 2002.

[5] E. Vinogradova, Electromagnetic plane wave scattering by arbitrary two-dimensional cavities: Rigorous approach, *Wave motion*, vol.70, pp. 47-64, 2016.

[6] A.C. Metaxas, R.J. Meredith, Industrial microwave heating, Peter Peregrinus, 1983.

[7] D.J. Griffiths, Introduction to electro-dynamics. Prentice Hall, 3rd edition 1999, 1981.

[8] "Water and microwaves." [Online]. Available: http://www1.lsbu.ac.uk/water/microwave_water.html. [Accessed: 07-Nov-2018].

CONTACT

* C.M. Rops, cor.rops@tno.nl

TOPOLOGICAL OPTIMIZATION OF HEATING RESISTORS FOR CONTROLLING TEMPERATURE IN A MICROFLUIDIC CAVITY

T. Mabit[1], M.-C Jullien[2] and H. Ben Ahmed[1]
[1] SATIE, ENS Rennes, CNRS, av. Robert Schuman, Bruz 35170, France
[2] IPR UMR 6251, Univ. Rennes1, CNRS, av. Général Leclerc, Rennes 35000, France

ABSTRACT

We propose a numerical technique allowing to determine a priori the topology of heating resistances in order to control the shape of the temperature profile within a cavity on fixed dimensions. The tool is based on a genetic algorithm and the approach is supported by experimental results. We show that complex heating profile can be performed successfully. We believe this work opens new perspectives for applications in biotechnology or chemistry. Furthermore, we provide a numerical open-source tool that embeds the presented method.

KEYWORDS

Temperature control, topological optimization, genetic algorithm.

INTRODUCTION

Integrating temperature control within a microsystem is in itself a difficulty. Among the different heating techniques, the Joule effect allows a simple integration in microsystems [1]. The general idea is to integrate an optimized electrical circuit placed below the zone whose temperature one wishes to control, see Fig. 1.

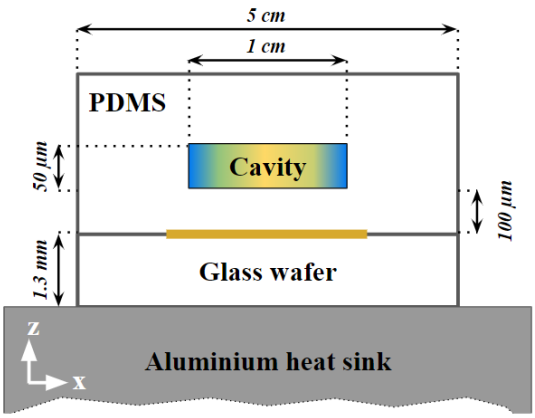

Figure 1: Fluidic system in a cross-sectional view. The heating circuit, which is below the cavity, is located on a glass wafer.

By control we mean its shape and its magnitude. In a previous work, an optimization was made on the local slope of the resistors which does not allow generating complex temperature profile [2]. Depending on the shape of the electrical circuit and how it's powered, the observable temperature profile can be tuned. Fig. 2 gives an example of heating resistors leading to a 3D double cosine temperature shape.

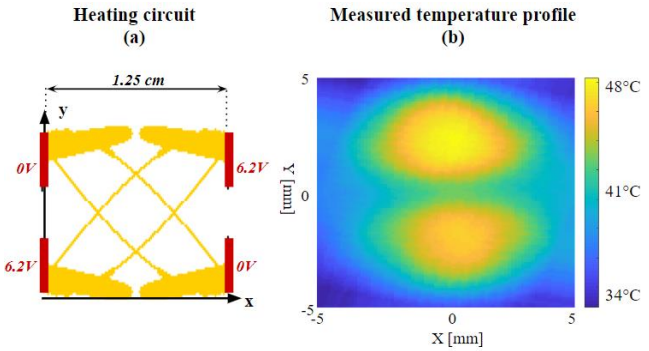

Figure 2: Example of heating circuit leading to a 3D double cosine temperature shape on the upper face of the fluidic layer.

When the temperature profile is an input and the heating circuit the output, the problem becomes an inverse problem. It is therefore a question of designing the most suitable circuit topology to generate a thermal profile in a microsystem.

THEORY

Topological optimization

The inverse problem can be solved by means of a genetic algorithm operating a topological optimization. The optimization procedure is shown schematically in Fig. 3. The algorithm uses routines inspired by the theory of evolution of populations (selection, crossing, etc.) [3]. The selection phase is based on the evaluation of each individual (circuit topology) to keep only the best circuits in terms of temperature that is output from the given topologies. The difference between the profile that is output from the optimization and the one that is given as the input of the problem constitutes the quantity allowing to discriminate the circuits. Thus, the genetic algorithm aims to find a vector X^* that contains all the parameters of the system, i.e. geometrical and electrical, that outputs the required temperature profile. The vector X^* is then obtained by the minimization of the objective function F, which experimentally would correspond to the thermal output of each vector X given by the genetic algorithm:

$$X^* = \underset{X=(x_1 \dots x_{N+7M})}{argmin}\, F(X)\ , \quad \begin{cases} 0 < x_1 \dots x_N < U_m \\ 0 < x_N \dots x_{N+7M} < 1 \end{cases} \qquad (1)$$

where x_1 to x_N contain different powering voltages of the circuit and values x_{N+1} to x_{N+7M} are used to describe the topology of the circuit. The F function compute a mark for the input circuit X based on its ability to reach the targeted temperature profile. X^* is further the optimal topology.

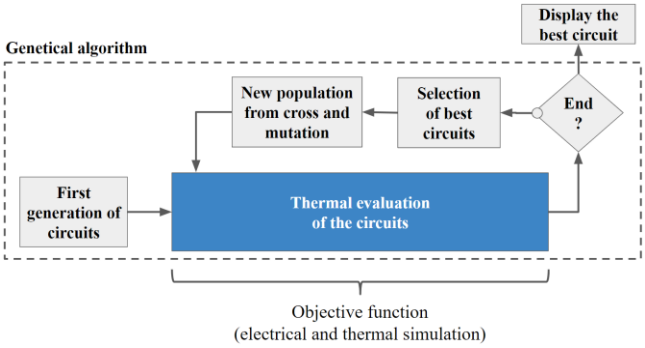

Figure 3: Algorigram describing the genetic algorithm optimization process.

Bézier formalism

As explained above, the topology of a circuit is described with the 7M first components of the vector that describe circuits. These components are used to define M Bézier curves, and an equal amount of polynomial functions.

Bézier curves are defined with 3 control points (second-order Bézier curves). The first two come from circuit's powering boundaries in order to define a line. A third control point allow the line to becomes distorted. Since the set of coordinates available for the first two points are homeomorphic to a segment, only two values are needed to define them. The third point can be placed in the whole of the circuit area. In fact, a Bézier curve can be described with 4 real numbers. To obtain a conductive surface from this curve, it is necessary to complete the curve with a resistor width that can vary along the latter.

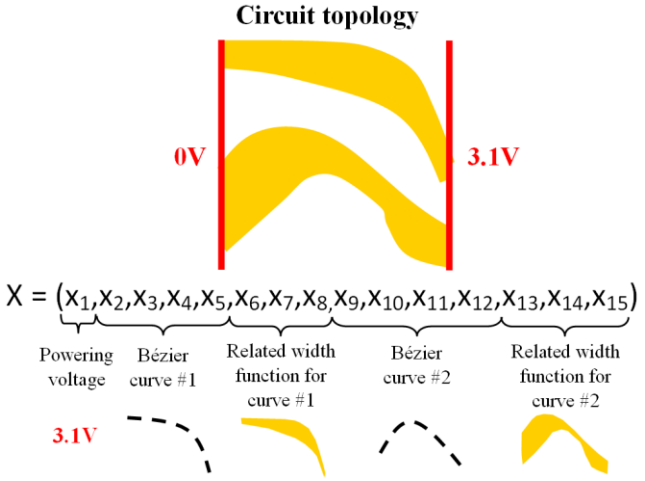

Figure 4: Example of the introduced Bézier formalism for a circuit described with 2 Bézier curves.

For that purpose, a second-order polynomial, described with 3 more real numbers, is used as a width function. An example is given in Fig. 4.

Thermal and electrical simulation

The temperature profile generated by each circuit is then simulated by a home-made numerical tool. The computation first calculates the thermal power dissipated by the electrical circuit. The temperature profile at the fluidic layer is further computed in a second step. Both simulations are based on using an equivalent circuit described in Fig. 5.

For the thermal simulation, the whole system (different material layers) is discretized in parallelepipedic volumes at homogeneous temperature $\theta_{i,j,k}$. Thermal transfers between adjacent volumes are governed by Fourier's law in 1D and modeled with an equivalent resistor [4]. Each other boundary condition for lone volume's sides, which can be convection (with air), temperature-fixed (with the heat sink) or heat source (by the heating circuit), constitute a specific equation.

For the electrical simulation, the layer of chromium is discretized in parallelepipedic volumes at homogeneous electrical potential $\theta_{i,j}$. Current flow between adjacent volumes are governed by Ohm's law. Each other boundary condition for lone volume's sides, which can be no current flow or settled potential, constitute a specific equation.

Such approach leads to a system of invertible equations relating to the temperatures in each discretized volume. Notice that increasing the amount of volumes is needed to improve result accuracy but it will also increase the computing time.

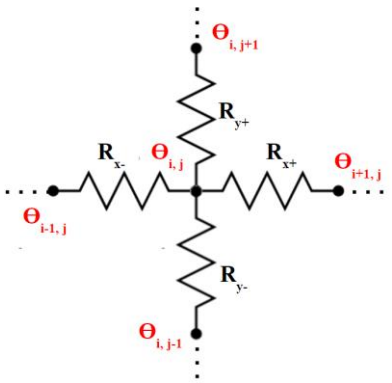

Figure 5: Part of the equivalent scheme used to model the electrical circuit (in 2D). Model for the whole system for thermal (in 3D) is very similar.

Ranking process

The quadratic difference between the temperature profile obtained by the simulation and the one that is reached constitutes the quantity associated with the evaluation of the circuit:

$$F(X) = \sqrt{\sum_{i,j} T_{i,j}(X)^2 - T_{i,j}^{*2}} \qquad (2.1)$$

Where $T_{i,j}$ is the function that give for a circuit X the temperature of the volume i,j of the fluidic layer. $T^*_{i,j}$ is the reached temperature at the volume i,j of the fluidic layer. This quantity is directly exploited to guide the selection of circuits by the genetic algorithm.

EXPERIMENTAL

Different circuit topologies were generated using the introduced method for cosine, Gaussian and parabola temperature shapes. Each optimized circuit was experimentally tested in the fluidic system introduced in Fig. 1. Heating resistors are composed of a chromium layer of 15 nm thickness manufactured by standard lithography technologies. Parameters of the optimization are given in Table 1. The Fig. 6 shows all generated circuits. For practical convenience, experiments have been performed on cavity of cm width.

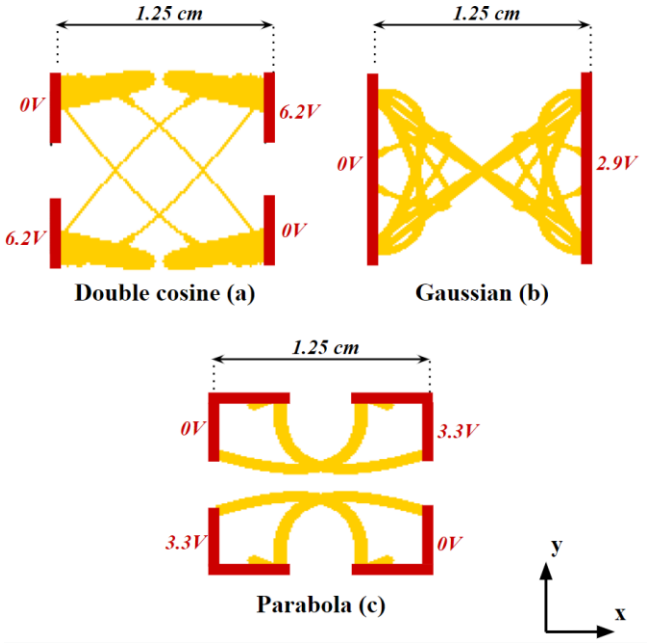

Figure 6: Generated circuits and their powering parameters.

Table 1: Parameters used for the optimization process.

Electrical conductivity of chromium ($\sigma_{Chromium}$)	$7.74e6\ S.m^{-1}$
Thermal conductivity of PDMS (λ_{PDMS})	$0.2\ W.m^{-1}.K$
Thermal conductivity of Water (λ_{Water})	$0.6\ W.m^{-1}.K$
Thermal conductivity of Glass (λ_{Glass})	$1.2\ W.m^{-1}.K$
Heat transfer coefficient with air (h_{Air})	$5\ W.m^{-2}.K$

The temperature mappings are processed using an Infra-Red camera (Fluke TiS45). The whole experimental setup is presented in Fig. 7. Notice that the IR measure is performed at the substrate interface, i.e. with only the PDMS layer of 100 µm thickness. The surface is covered with an adhesive tape as a black body instead of the cavity covered with PDMS. The heat sinks prevent from a global temperature increase of the system.

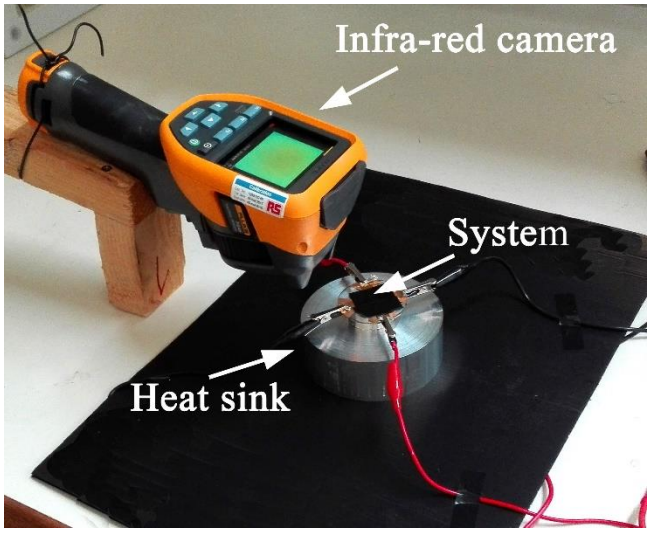

Figure 7: Experimental setup.

RESULTS AND DISCUTION

The different experiments allowed us to validate the optimization method as a whole. The difference between the measured profiles and those announced at the end of optimization are on the order of few Kelvin. A comparison between temperature profile measured and goal is given in Fig. 8 for a Gaussian profile.

Discrepancies stem from the fact that the spatial resolution of the heating resistors has to be in adequacy with the required temperature profile, given thermal diffusion. We are currently working on the open access code to solve this point automatically.

Even though experimentation were made with macro system (cavity width of 1 cm), the method can operate with a micro system (cavity with of some µm).

The level of detail of the electrical circuit (mesh refinement) and the thickness of PDMS between the heating layer and the bottom of the cavity lead the complexity of the temperature profile: increasing the thickness of the PDMS layer will homogenize the temperature at the fluidic layer.

Fig. 9.1, Fig. 9.2 and Fig. 9.3 show measured temperature profiles for the 3 presented circuits in Fig. 6.

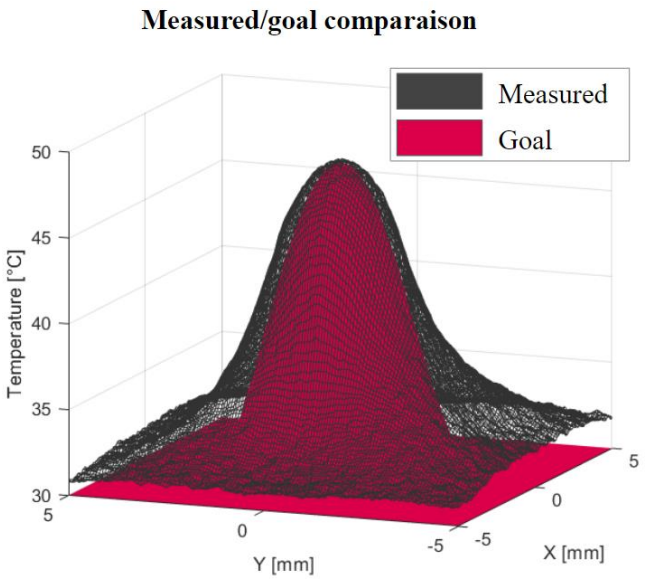

Figure 8: Comparison of temperature profile between the goal profile and the one measured with the infra-red camera.

CONCLUSION

This work revealed the interest of using a formalism based on Bézier curves, in a genetic algorithm. This approach generates circuit geometries leading to controlled temperature profile.

Improvements will be further provided by defining a condition of feasibility, because of the diffusion that limit the accuracy of the required temperature profile (typically a sharp step cannot be performed).

A numerical tool, of free access and open-source, has been developed and can be used without having to master the domain (https://microheat.ppaduc.fr).

REFERENCES

[1] V. Miralles, A. Huerre, F. Malloggi and M.-C. Jullien, A review of heating and temperature control in mi-crofluidic systems: techniques and applications, Diagnostics 3 (1), 33-67 (2013).

[2] Selva, B.; Mary, P.; Jullien, M.-C. Integration of a uniform and rapid heating source into microfluidic sys-tems. Microfluid. Nanofluid. 2010, 8, 755–765.

[3] Jonathan Denies. Métaheuristiques pour l'optimisation topologique : application à la conception de disposi-tifs électromagnétiques. Autre. École normale supérieure de Cachan - ENS Cachan, 2013.

[4] Henrik Bruus, Theoretical Microfluidics, Oxford University Press, 2008.

CONTACT

* H. Ben Ahmed, phone: +33299059330, hamid.benahmed@ens-rennes.fr

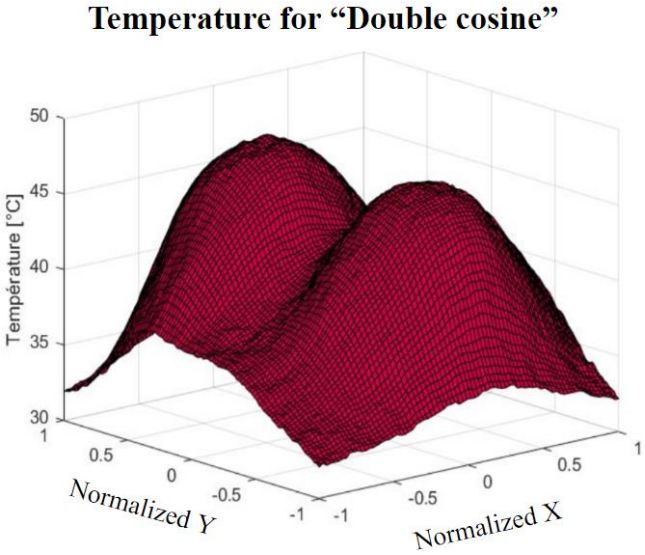

Figure 9.1: Measured temperature profile for "Double cosine" circuit.

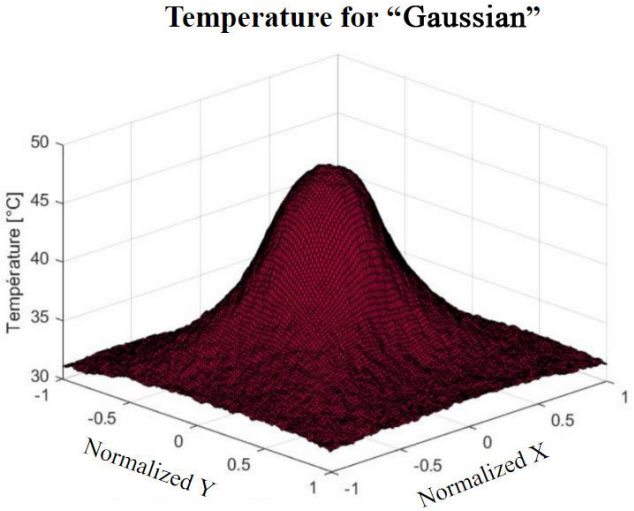

Figure 9.2: Measured temperature profile for "Gaussian" circuit.

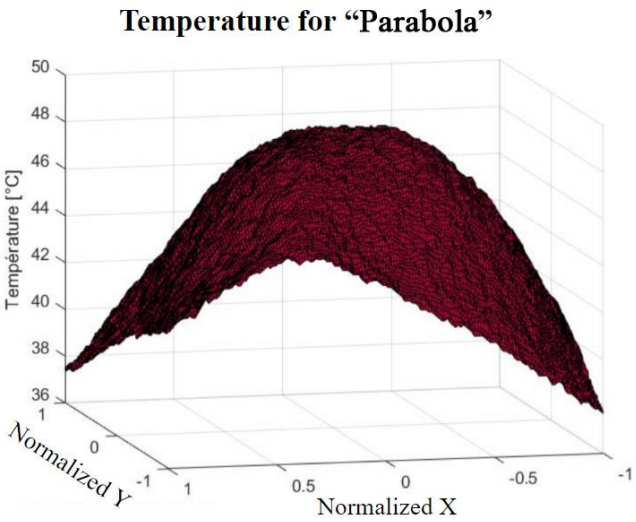

Figure 9.3: Measured temperature profile for "Parabola" circuit.

USING GALLIUM AS A PROTECTIVE LAYER DURING A SOLVENT BONDING PROCESS FOR LAB-SCALE POLYMER BASED MICROFLUIDIC DEVICE FABRICATION

M.A. Hintermüller and B. Jakoby*
Johannes Kepler University Linz, Institute for Microelectronics and Microsensors, Linz, Austria

ABSTRACT

A fabrication process for polymeric microfluidic devices using a solvent bonding technique is presented. Liquid gallium is filled into the channels beforehand, in order to keep their structural integrity intact during the bonding process. Due to its melting point just above room temperature, gallium features several advantages compared to other materials used in a similar fashion. The proposed method does not require special equipment and is especially suitable for rapid prototyping on a small academic lab scale.

KEY WORDS

Polymer microfluidics; solvent bonding; microfluidic device fabrication; gallium

INTRODUCTION

Over the last few years, the use of polymeric microfluidic devices was established as a worthwhile alternative to the classic approach using silicone or glass, due to the wide variety of available polymer materials, which can be used for different applications, easy fabrication of microfluidic devices and affordable costs [1], [2].

While methods for pattering of the microfluidic channel features are readily available, bonding of microfluidic chips can still be a challenging task [3]. Polymeric microfluidic devices can be sealed by, e.g., adhesive [3], thermal [4] or solvent bonding techniques [5]. Solvent bonding is of particular interest, as no special equipment is required to perform the process and the sealing performances are outstanding.

In this contribution, a fabrication method for polymeric microfluidic chips is presented, which utilizes solvent bonding for sealing the devices. In order to prevent the microchannels from distorting and clogging during the bonding process, the channels are temporarily sealed and filled with liquid gallium beforehand. After freezing the gallium, it forms a protective layer which prevents the channel geometry from altering. Compared to previously reported materials used in a similar manner, gallium features distinct advantages due to its unique melting point [6].

To demonstrate the feasibility of this approach, demonstrator devices were fabricated, each posing different challenges for the proposed process. The flow focusing device possesses very intricate channel features, whereas the chemical gradient generator has multiple serpentine channels and the herringbone mixer is three dimensionally structured inside the channel.

MATERIALS AND METHODS

Fabrication

The whole fabrication process of a microfluidic chip using the presented method is schematically depicted in Fig. 1. First, the microfluidic channels are patterned into a blank sheet of PMMA using a CO_2-laser engraver (Trotec Speedy 300 flexx, Fig. 1a). Also, holes for the inlet and outlet ports are cut out. Next, threads are cut into the holes of the inlet and outlet ports using a mechanical thread cutter to enable fast and leak-proof connection using threaded Luer adapters (Fig. 1b).

During laser engraving, the PMMA blank is exposed to pulsed laser light, which causes the material to periodically heat up and cool down in a short amount of time. This induces thermal stresses in the material. During the bonding process the surfaces come in contact with solvents, which soften up the top surfaces and therefore releasing tension caused by the thermal stresses, which in turn gives rise to the creation of small cracks around the laser engraved parts. This effect is often referred to as stress crazing [7], [8]. In order to relax the workpieces after engraving, an annealing process (Fig. 1c) should be performed to circumvent the forming of these cracks. To this end, the engraved workpieces are put in a box oven which is slowly heated up to about 75°C (the annealing temperature should be below the glass transition temperature of the polymer) and held at this temperature for about 1–2 h. Then the oven is turned off, allowing the workpieces to slowly cool off back to room temperature. Figure 2 highlights the mending effect of the annealing process. Figures 2 (1a–1c) show untreated and (2a–2c) show annealed engraved test pieces after getting in contact with different solvents of PMMA. Clearly, all the untreated test pieces exhibit cracks in the engraved area, whereas no cracks appear in the annealed ones.

After the annealing process the microfluidic channels are temporarily sealed by clamping the engraved piece channel side down to another PMMA blank or glass slide with a thin polymer film in between using spring clamps (Fig. 1d). Metal gallium

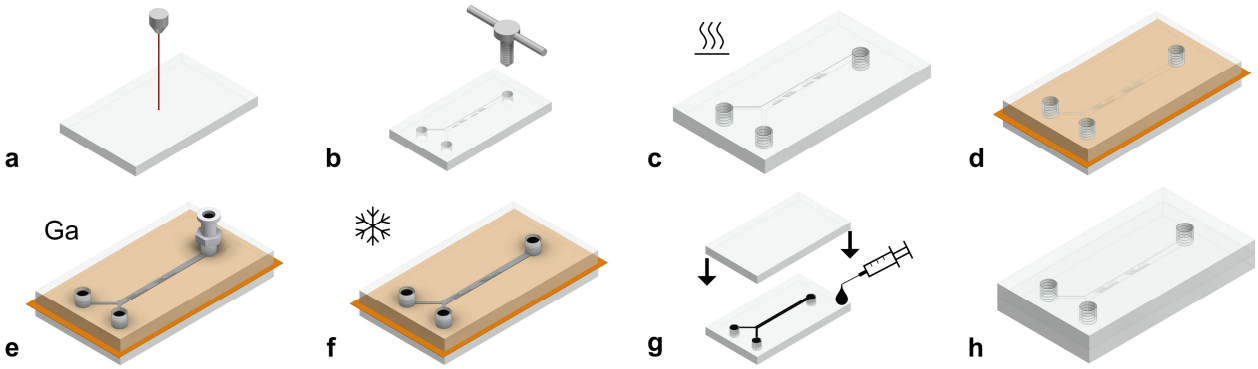

Figure 1: Fabrication process. (a) Laser engraving the channel geometry. (b) Inlets and outlet thread cutting for easy connection via threaded Luer fittings. (c) Annealing for 1–2 h at 75°C. (d) Temporarily sealing by clamping together two PMMA parts with a thin polymer film in between. (e) Filling the channels with liquid gallium. (f) Freezing to solidify the gallium inside the channels at -10°C. (g) Applying solvent and pressing the parts together. (h) Flushing the gallium from the channels.

is then put on a hotplate at about 60°C for 5 min in order to melt it. Using a syringe the liquid gallium is gently filled into the microchannels (Fig. 1e) and put into a freezer for about 5–10 min at -10°C in order to solidify it again (Fig. 1f), therefore forming a protection layer during the subsequent solvent bonding process. As gallium is prone to supercooling, it is best to put a little piece of solid gallium (which acts as a seeding crystal) in one of the inlet/outlet ports to speed up the freezing process. Since gallium expands by about 3.2 vol% when frozen [9], the channel geometry is not compromised by any shrinkage effects; the inlet and outlet ports provide sufficient room for expansion.

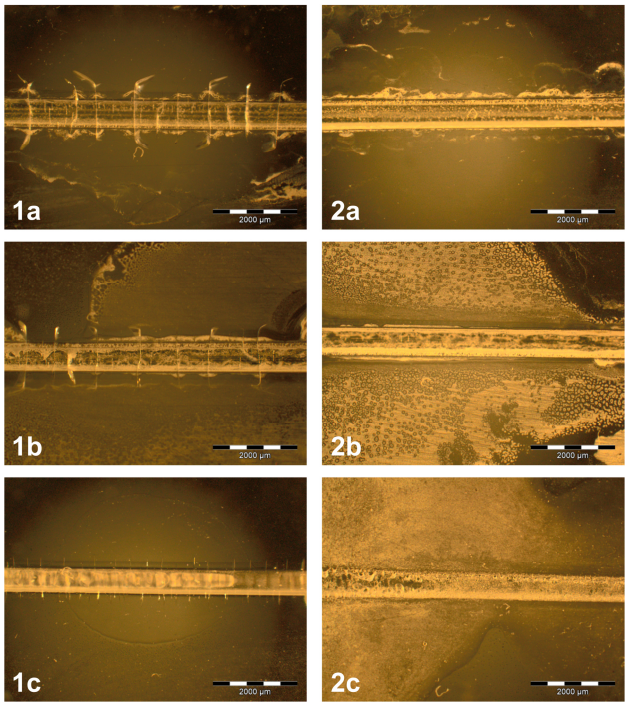

Figure 2: Effect of stress crazing. Photographs 1a–1c show untreated, 2a–2c annealed workpieces. Solvents: (a) Acetone, (b) tetrahydrofuran, (c) dichloromethane. No cracks form after the annealing process.

After removing the parts from the freezer, the engraved part with the protective gallium filling is bonded to another piece of PMMA by means of a solvent bonding process. To this end a suitable solvent (dichloromethane in our case) is put on top of one of the parts (or alternatively the part is dipped into the solvent) then aligned and clamped to the corresponding part using a single-handed quick release bar clamp for about 5 min (Fig. 1g).

In the last step the bonded microfluidic chip is submerged in warm water to melt the gallium inside the channels again, which is subsequently flushed from the device. Gallium quickly forms an oxide skin on its surface due to atmospheric oxygen. This oxide layer tends to stick to many surfaces [10], which is advantageous during the filling of the channels, as it helps to line the whole channel with the gallium, but hampers the cleaning process, as residuals may adhere to channel walls. Fortunately, this oxide layer can be easily removed using bases or acids [9]. Therefore the channels are initially flushed using sodium hydroxide (NaOH) in order to remove the oxide layer. This causes the gallium to bead up, which helps releasing it from the channel walls. The removed gallium can be collected and reused again. Afterwards the device is cleaned by flushing it with water and air, leaving the finished microfluidic device (Fig. 1h).

Testing

The three demonstrator devices were tested as follows:

The flow focusing device was tested using water mixed with a small amount of dishwashing detergent, colored with black ink as the continuous phase and air as the dispersed phase, to create uniform air bubbles in the continuous phase.

Water mixed with yellow and blue ink was used

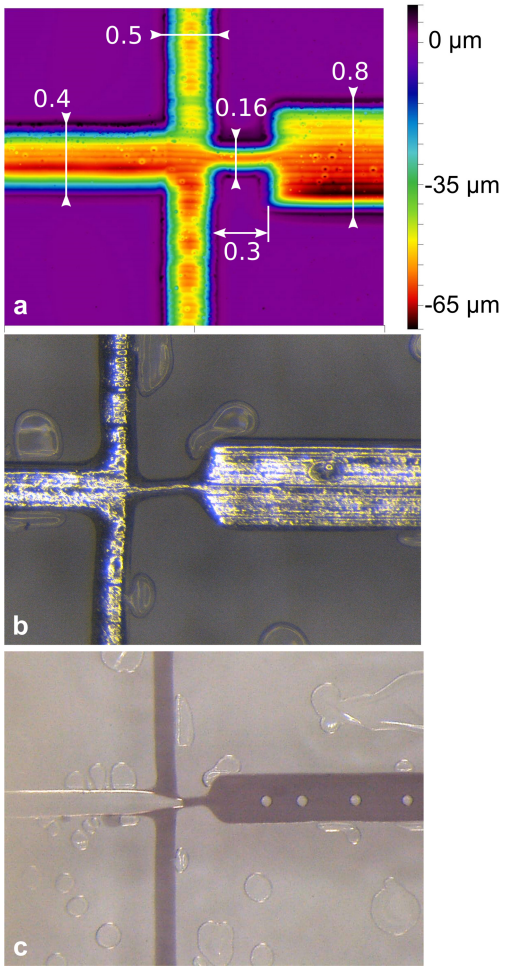

Figure 3: Fabricated flow focusing device. (a) Profile scan and dimensions in mm. (b) Channels filled with solid gallium. (c) Device testing.

for the chemical gradient generator. Five different gradations of these two colors can be expected at the outlet.

The herringbone mixer was tested using water colored with ink (pink and cyan this time) to easily detect the mixing of the two colors with the eye.

RESULTS AND DISCUSSION

Figure 3 shows the fabricated flow focusing device. In Fig. 3a a surface profile scan is shown to display the dimensions and the depth of the channel. Figure 3b shows a photograph of the microchannels filled with solid gallium after bonding and Fig. 3c shows the working device, creating uniformly sized air bubbles in the continuous water phase.

Figure 4a shows the chemical gradient generator and Fig. 4c a magnified view of the outlet. The five distinct bands of different concentrations can be seen. The photograph in Fig. 4b shows one of the meander shaped channel parts filled with gallium; also dimension are shown here.

Finally, Fig. 5 shows the test results of the herringbone mixer. Figure 5a shows a surface profile scan of one of the mixing stages, Fig. 5b again the channel feature with the solidified gallium. The photograph in Fig. 5c shows the mixing capabilities of the design.

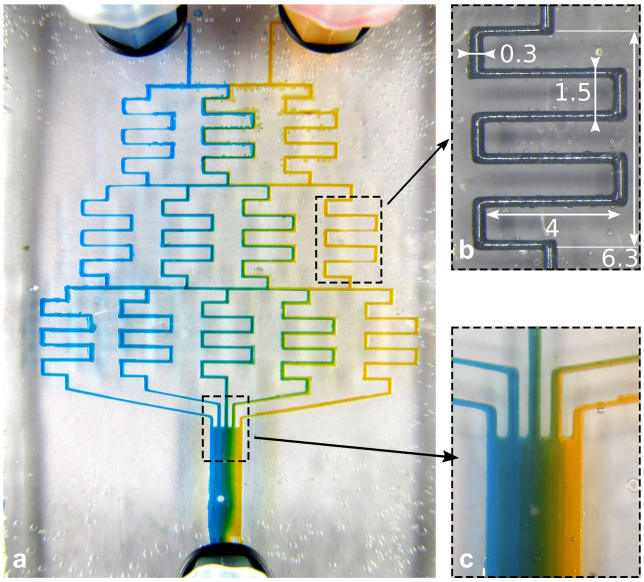

Figure 4: Fabricated gradient generator. (a) Device testing (channel height is 200 µm). (b) Gallium filled channel and dimensions of one meander in mm. (c) Zoom of outlet while testing.

The main advantage of the proposed method using gallium as the protective layer, compared to previously reported materials such as paraffin wax [11] and water/ice [12] is its special melting point, which allows for easier handling at room temperature. Table 1 compares the three different materials at four crucial fabrication steps during manufacturing. The proposed method using gallium is superior in every category.

Table 1: Comparison of different protective materials.

Process step	Wax	Ice	Gallium
Time available for filling the channels	Short	Long*	Long*
Shrinkage while cooling	Yes	No*	No*
Time available for bonding process	Long*	Very short	Long*
Cleaning after bonding	Moderate	Good*	Good*

*Preferred

CONCLUSIONS

A method for fabrication of polymer microfluidic devices using gallium as a protective layer during a solvent bonding process was presented. As demonstrated, the proposed method is capable of

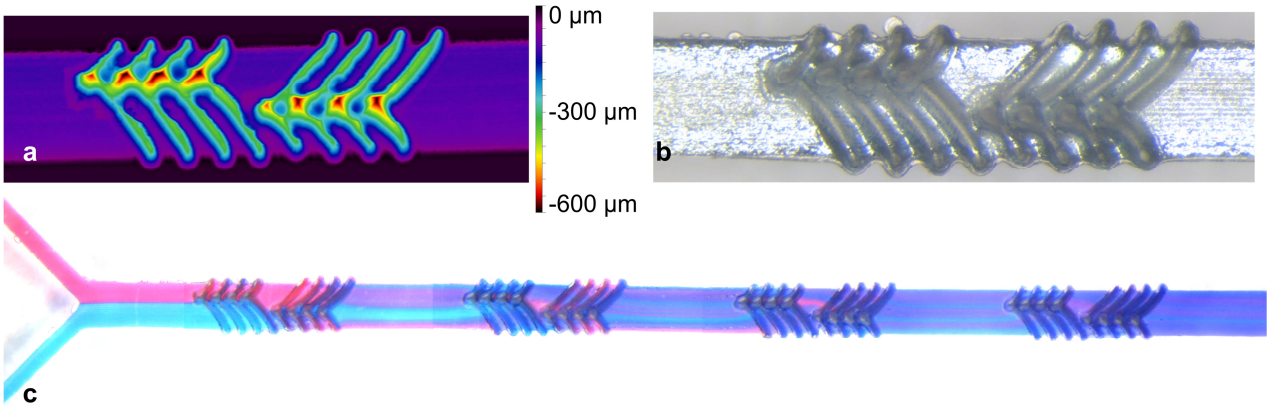

Figure 5: Fabricated herringbone mixer. (a) Surface scan of one mixing stage. (b) Channel filled with solid gallium after bonding. (c) Device testing.

handling different kinds of channel geometries with no problem. Compared to previously reported materials used for protecting the channel integrity, the method using gallium features longer processing time at room temperature, no shrinkage and easy cleaning, enabling fast and simple prototyping of microfluidic devices on a small academic lab-scale, without the need of special equipment.

ACKNOWLEDGMENTS

This work has been supported by the COMET-K2 "Center for Symbiotic Mechatronics" of the Linz Center of Mechatronics (LCM) funded by the Austrian Federal Government and the Federal State of Upper Austria.

REFERENCES

[1] C.-W. Tsao, "Polymer Microfluidics: Simple, Low-Cost Fabrication Process Bridging Academic Lab Research to Commercialized Production," *Micromachines*, vol. 7, no. 12, p. 225, Dec. 2016.

[2] K. Ren, J. Zhou, and H. Wu, "Materials for Microfluidic Chip Fabrication," *Acc. Chem. Res.*, vol. 46, no. 11, pp. 2396–2406, Nov. 2013.

[3] Y. Temiz, R. D. Lovchik, G. V. Kaigala, and E. Delamarche, "Lab-on-a-chip devices: How to close and plug the lab?," *Microelectron. Eng.*, vol. 132, pp. 156–175, Jan. 2015.

[4] X. Wang *et al.*, "Low-pressure thermal bonding," *Microelectron. Eng.*, vol. 88, no. 8, pp. 2427–2430, Aug. 2011.

[5] M. Svoboda, Z. Slouka, W. Schrott, P. Červenka, M. Přibyl, and D. Šnita, "Fabrication of plastic microchips with gold microelectrodes using techniques of sacrificed substrate and thermally activated solvent bonding," *Microelectron. Eng.*, vol. 87, no. 5–8, pp. 1590–1593, May 2010.

[6] M. A. Hintermüller and B. Jakoby, "Lab-scale prototyping of polymer based microfluidic devices using gallium as phase-changing sacrificial material," *Microelectron. Eng.*, vol. 211, pp. 50–54, Apr. 2019.

[7] J. Powell, "Cutting Non-metals," in *CO2 Laser Cutting*, London: Springer London, 1998, pp. 91–115.

[8] D. Doran and B. Cather, *Construction Materials Reference Book*. Routledge, 2013.

[9] M. D. Dickey, "Emerging Applications of Liquid Metals Featuring Surface Oxides," *ACS Appl. Mater. Interfaces*, vol. 6, no. 21, pp. 18369–18379, Nov. 2014.

[10] K. Doudrick *et al.*, "Different shades of oxide: From nanoscale wetting mechanisms to contact printing of gallium-based liquid metals," *Langmuir*, 2014.

[11] R. T. Kelly, T. Pan, and A. T. Woolley, "Phase-Changing Sacrificial Materials for Solvent Bonding of High-Performance Polymeric Capillary Electrophoresis Microchips," *Anal. Chem.*, vol. 77, no. 11, pp. 3536–3541, Jun. 2005.

[12] M. T. Koesdjojo, Y. H. Tennico, and V. T. Remcho, "Fabrication of a Microfluidic System for Capillary Electrophoresis Using a Two-Stage Embossing Technique and Solvent Welding on Poly(methyl methacrylate) with Water as a Sacrificial Layer," *Anal. Chem.*, vol. 80, no. 7, pp. 2311–2318, Apr. 2008.

CONTACT

* M.A. Hintermüller, Tel.: +43-732-2468-6266,
E-mail: marcus.hintermueller@jku.at.

TOWARDS 3D PRINTED MICROFLUIDIC DEVICES IN α-ALUMINA

H.-W. Veltkamp[1], Y. Zhao[1], R.G.P. Sanders[1], R.J. Wiegerink[1], and J.C. Lötters[1,2]
[1] MESA+ Institute for Nanotechnology, University of Twente, Enschede, The Netherlands
[2] Bronkhorst High-Tech BV, Ruurlo, The Netherlands

ABSTRACT

3D-printing in microfluidics is a relatively new approach. However, most of the applications are printed in polymeric material, limiting the use in high temperature applications. This paper describes the first steps towards a 3D printed microfluidic device in α-alumina. This material could potentially be used in applications with temperatures up to 1000 °C. In this paper we shortly discuss the history of 3D printing and microfluidics, the material properties of α-alumina, the theory on membrane deflection, and proposed structures to test this theory, gas-tightness, metal adhesion properties of α-alumina.

KEYWORDS

Laminated object manufacturing, 3D printing in α-alumina, high temperature microfluidics

INTRODUCTION

3D printing

After the Second (electricity and assembly line manufacturing) Industrial Revolution the world was mainly based on Fordism, a concept of mass production originally based on the large-scale manufacturing of cars. However, the demand for customized goods is increasing, goods that no longer can be made with conventional methods. Additive manufacturing (AM) is, in contrast to subtractive (e.g. milling, turning, grinding) and equivalent manufacturing (e.g. casting, forging), a relatively new field (roughly 40 years compared to centuries), and sometimes referred to as the third industrial revolution[1]. It is defined by the American Society for Testing and Materials (ASTM) as the "process of joining materials to make objects from 3D model data, usually layer upon layer, as opposed to subtractive manufacturing methodologies"[2].

One major technique in AM, and often used as a synonym for AM, is 3D printing. Though the first patent is from almost 10 years earlier[3], this technique emerged in the early 1980s with a patent on the first commercial stereolithography (SLA) machine[4]. After SLA, the field of 3D printing evolved and matured, making that more 3D printing techniques were developed. With the expiration of the first patents, 3D printing became open-source, which greatly reduced the costs and boosted the development of each printing technique and even hybrid techniques. A 2010 Gartner's Hype Cycle Report[5] identified 3D Printing as a transformational technology in the Technology Trigger phase of the Hype Cycle[6]. According to the ASTM F42 subcommittee on Additive Manufacturing Technologies, established in 2009, the field encompasses 7 distinct printing methods[2], which are nowadays used in all kinds of industries, ranging from aerospace to automotive and medical equipment. This makes the prediction that it was only 5 to 10 years away from mass adoption, back in 2010[5] a quite valid prediction. The seven distinct 3D print methods are listed in table 1 together with a reference to their first patent.

Table 1: The seven distinct 3D printing techniques with their corresponding first patents and date of filing.

3D printing technique	U.S. patent no.	Date of filing
Material extrusion[3]	4,078,229	Jan. 27, 1975
Directed energy deposition[7]	4,323,756	Oct. 29, 1979
Material jetting[8]	4,665,492	Jul. 2, 1984
Vat photopolymerication[9]	4,575,330	Aug. 8, 1984
Sheet lamination[10]	4,752,352	Apr. 17, 1987
Powder bed fusion[11]	5,121,329	Oct. 30, 1989
Binder jetting[12]	5,204,055	Dec. 8, 1989

Microfluidics

Another relatively new field is microfluidics. Starting in the 1950s with the development of modern ink-jet printing technology[13]. The real revolution came when the first miniaturized gas chromatograph was realized in 1979 by Terry *et al.*[14]. Manz *et al.* extended this principle to the concept of micro total analysis system in 1990[15] (nowadays known as lab-on-a-chip devices). With the support of the Defense Advanced Research Projects Agency (DARPA) of the US Department of Defence, the development of field-deployable microfluidic systems that can be used for the detection of chemical and biological threats was boosted[16]. The next revolution in microfluidics came with the development of soft lithography[17]. However, this method uses molds/stamps which are

often fabricated using a microfabrication line and the used materials are not industry compatible, preventing large-scale manufacturing[18].

3D printing in microfluidics

With 3D printing no molds/stamps are required and more complex 3D structures can be fabricated. Since 2012, this is being used for direct manufacturing of microfluidic reaction-ware[19]. Although, the efficiency of the microfluidic device depends largely on the chosen 3D printing method[18], all reported applications in microfluidics lack the possibility for being used at high temperatures and in harsh chemical conditions. This is solved by using α-alumina. In table 2 a comparison between α-alumina and two commonly used materials in (high temperature) micro-electro mechanical systems, i.e. silicon and silicon-rich silicon nitride (SiRN), is given.

Table 2: Comparison α-alumina with traditional MEMS materials.

Property [unit]	Si	Si_xN_y	α-Al_2O_3
Density [$g\,cm^{-3}$]	2.28-2.38	2.37-3.25	3.00-3.98
Thermal conductivity [$W\,m^{-1}\,K^{-1}$]	84-100	10-43	12-38.5
Heat capacity [$J\,kg^{-1}\,K^{-1}$]	668-715	673-1100	451-955
Thermal expansion [$10^{-6}\,K^{-1}$]	7-8	1.4-3.7	4.5-10.9
Melting temperature [K]	1700-1723	2661-2769	2277-2369
Young's modulus [GPa]	140-180	297	215-413
Poisson's ratio [-]	0.265-0.275	0.28	0.21-0.33
Resistivity [$10^{-8}\,\Omega\,m$]	10^{6}-10^{10}	10^{16}-10^{21}	10^{18}-10^{24}

α-Alumina can be printed by using a patented technique based on digital light processing (DLP) and laminating object manufacturing (LOM)[20]. In this LOM technique, photosensitive resin mixed with α-alumina particles (i.e. the 'slurry') is transported to the building platform using a foil roll. The building stage is pressed onto the foil and is patterned with DLP. Repeating this, allows layers to be built on top of each other, as is shown in figure 1. In subsequent post-processing the resin is evaporated and the α-alumina particles are sintered.

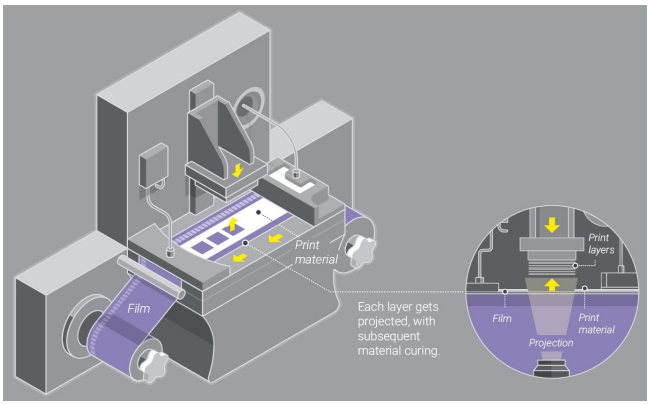

Figure 1: Working principle of the patented DLP-LOM printing method for ceramics[20]. Picture taken from Admaflex 130 flyer of Admatex[21].

PROPOSED EXPERIMENTAL WORK

The use of α-alumina and this printing technique is a new approach in microfluidics. Therefore, there are still quite some unknowns in the development of a microfluidic device. Examples of these unknowns are:

1. How good is the leak-tightness of the printed material after sintering as function of wall thickness;
2. What is the maximum operating pressure as function of wall thickness;
3. How good is the adhesion between sintered α-alumina and glue when tubing/capillaries are glued into the inlets;
4. How good is the adhesion between sintered α-alumina and deposited thin-film resistive metal tracks for heaters/temperature sensors;
5. What is the surface roughness of sintered α-alumina;
6. What is the optical transparency of sintered α-alumina;
7. How to incorporate heaters in a 3D printed system;
8. How to incorporate temperature sensors in a 3D printed system.

Unknowns 1, 2, 3, and 5 can all be examined with one test structure, shown in figure 2. This test structure has cylindrical chambers with a diameter of 1 cm with varying top and bottom wall thicknesses (0.5 mm, 1.0 mm, 1.5 mm, and 2.0 mm) and an inlet channel on the long side of the cylinder for an $1/16$ inch tubing, which can be glued into this channel. Schematics of the chambers are shown in figure 2. These chambers will be printed both parallel and perpendicular to the printing direction. He-leakage tests will be performed in order to check the porosity of different wall thicknesses

and the adhesion of glue between the α-alumina and the tubing. As final tests on these chambers, the maximum operating pressure will be determined, while monitoring the deflection of the thin α-alumina wall. The deflection of this wall can be approximated by the deflection of a thin clamped circular plate loaded by a uniform pressure (see also figure 3)[22]:

$$w(r) = \frac{P}{64D}(a^2 - r^2)^2 \qquad (1)$$

where, $w(r)$ is the deflection under pressure P at point r of radius a. D is the flexural rigidity, and is given by $Eh^3/(12(1-\nu^2))$, where E is Young's modulus, h the membrane thickness, and ν Poisson's ratio.

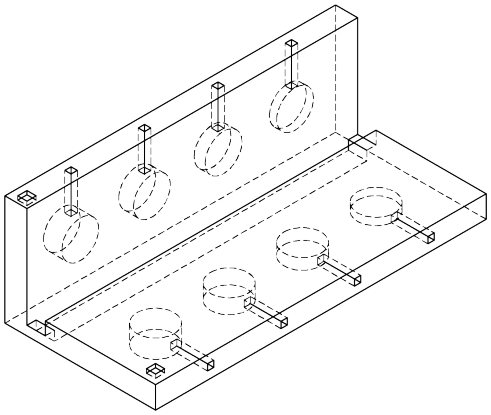

Figure 2: Designed pressure chambers for He leakage tests and failure pressure tests. The chambers are 1 cm in diameter.

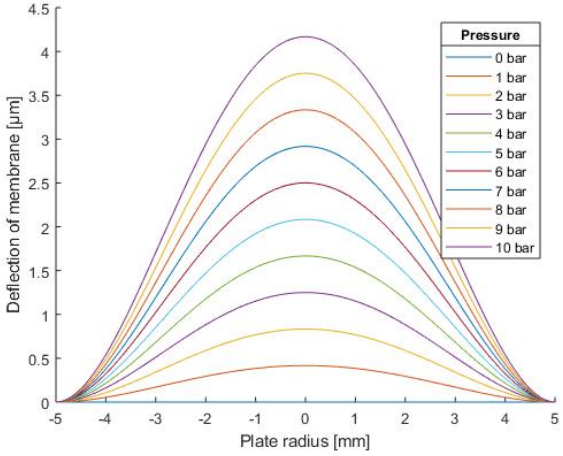

Figure 3: Deflection of a 0.5 mm thick membrane with a radius of 1 cm, a Young's modulus of 215 GPa and a Poisson's ratio of 0.21 according to the clamped thin circular plate with uniform pressure theory[22].

Unknown number 4 can be investigated using the same device. Metal can be deposited using either DC magnetron sputtering or e-beam physical vapor deposition (evaporation). Metals of interest are, for example, Au and Pt, which are commonly used metals in microfluidics[23]. Adhesion properties can be studied using the Scotch tape test[24], and the resistance versus temperature behavior in the range 20 °C – 1000 °C.

CONCLUSION

All above mentioned experiments are purely conceptual. The printing of the test structures did not proceed yet, as there are a lot of design rules for sintering. However, once these results are obtained, it becomes evident whether 3D printing of α-alumina is an applicable method for the fabrication of high temperature microfluidic structures.

ACKNOWLEDGMENTS

This work is part of the research program Integrated Wobbe Index Meter under project number 13952 which is co-financed by the Netherlands Organization for Scientific Research (NWO).

REFERENCES

[1] B. Lu, D. Li, and x. Tian. Development trends in additive manufacturing and 3d printing. *Engineering*, 1(1):85–89, 2015. doi: 10.15302/J-ENG-2015012.

[2] American Society for Testing and Materials Committee F42 on Additive Manufacturing Technologies. Standard terminology for additive manufacturing technologies. (ASTM standard F2792-10), June 2010. doi: 10.1520/F2792-10.

[3] S.S. Crump. Apparatus and method for creating three-dimensional objects. (U.S. Patent 5,121,329), Oct. 30, 1989. URL `https://patents.google.com/patent/US5121329A/en`. [Last accessed: Jun. 5, 2019].

[4] C.W. Hull. Apparatus for production of three-dimensional objects by stereolithography. (U.S. Patent 4,575,330), Aug. 8, 1984. URL `https://patents.google.com/patent/US4575330A/en`. [Last accessed: Jun. 5, 2019].

[5] J. Fenn. Hype cycle for emerging technologies, 2010. URL `http://www.eircomictdirect.ie/docs/whitepapers/HypeCycle_EmergingTechnologies2010.pdf`. [Last accessed: Sep. 18, 2019].

[6] J. Fenn. *Mastering the hype cycle: how to choose the right innovation at the right time*. Harvard Business School Press, Cambridge, MA, USA, 1st edition, 2008. ISBN 9781422121108.

[7] C.O. Brown, E.M. Breinan, and B.H. Kear. Method for fabricating articles by sequential layer deposition. (U.S. Patent 4,323,756), Oct. 29, 1979. URL `https://patents.google.com/patent/US4323756A/en`. [Last accessed: Jun. 5, 2019].

[8] W.E. Masters. Computer automated manufacturing process and system. (U.S. Patent 4,665,492), Jul. 2, 1984. URL `https://patents.google.com/patent/US4665492A/en`. [Last accessed: Jun. 5, 2019].

[9] W.K. Swanson and S.D. Kremer. Three dimensional systems. (U.S. Patent 4,078,229), Jan. 27, 1975. URL https://patents.google.com/patent/US4078229A/en. [Last accessed: Jun. 5, 2019].

[10] M. Feygin. Apparatus and method for forming an integral object from laminations. (U.S. Patent 4,752,352), Apr. 17, 1987. URL https://patents.google.com/patent/US4752352A/en. [Last accessed: Jun. 5, 2019].

[11] C.R. Deckard. Method and apparatus for producing parts by selective sintering. (U.S. Patent 4,863,538), Oct. 17, 1986. URL https://patents.google.com/patent/US4863538A/en. [Last accessed: Jun. 5, 2019].

[12] E.M. Sachs, J.S. Haggerty, M.J. Cima, and P.A. Williams. Three dimensional printing techniques. (U.S. Patent 5,204,055), Dec. 8, 1989. URL https://patents.google.com/patent/US5204055A/en. [Last accessed: Jun. 5, 2019].

[13] N. Convery and N. Gadegaard. 30 years of microlfuidics. *Micro and Nano Engineering*, 2(1):76–91, 2019. doi: 10.1016/j.mne.2019.01.003.

[14] S.C. Terry, J.H. Jerman, and J.B. Angell. A gas chromatographic air analyzer fabricated on a silicon wafer. *IEEE Transactions on electron devices*, 26(12):1880–1886, 1979. doi: 10.1109/T-ED.1979.19791.

[15] A. Manz, N. Graber, and H.M. Widmer. Miniaturized total chemical analysis systems: a novel concept for chemical sensing. *Sensors and actuators B: Chemical*, 1(1–6):244–248, 1990. doi: 10.1016/0925-4005(90)80209-I.

[16] G.M. Whitesides. The origins and future of microfluidics. *Nature*, 442(7101):368–373, 2006. doi: 10.1038/nature05058.

[17] Y. Xia and G.M. Whitesides. Soft lithography. *Annual Review of Materials Science*, 28(1):153–184, 1998. doi: 10.1146/annurev.matsci.28.1.153.

[18] N.P. Macdonald, J.M. Cabot, P. Smejkal, R.M. Guijt, B. Paull, and M.C. Breadmore. Comparing microfulidic performance of three-dimensional (3D) printing platforms. *Analytical Chemistry*, 89(7):3858–3866, 2017. doi: 10.1021/acs.analchem.7b00136.

[19] M.D. Symes, P.J. Kitson, J. Yan, C.J. Richmond, G.J.T. Cooper, R.W. Bowman, T. Vilbrandt, and L. Cronin. Integrated 3D-printed reactionware for chemical synthesis and analysis. *Nature Chemistry*, 4(5):349–354, 2012. doi: 10.1038/nchem.1313.

[20] P.A.J.M. Kuijpers and M.A.J. van Antwerpen. Additive manufacturing device for manufacturing a three dimensional object. (U.S. Patent 2018/0200948 A1), Jul. 13, 2016. URL https://patents.google.com/patent/US20180200948A1/en. [Last accessed: Jun. 5, 2019].

[21] Admaflex Additive Manufacturing Technologies. Admaflex 130: Experience 3D printing ceramics and metals in one exceptional way. URL https://admateceurope.com/site/wp-content/uploads/2017/08/Introducing-the-ADMAFLEX-130.pdf. [Last accessed: Jun. 5, 2019].

[22] S. Timoshenko and S. Woinowsky-Krieger. *Theory of plates and shells*. McGraw-Hill Book Company, 2nd edition, 1987. ISBN 0-07-064779-8.

[23] V. Miralles, A. Huerre, F. Malloggi, and M. C. Jullien. A review of heating and temperature control in microfluidic systems: techniques and applications. *Diagnostics*, 3(1):33–67, 2013. doi: 10.3390/diagnostics3010033.

[24] I. F. Silvera, K. R. Stewart, G. M. Whitesides, H. P. Godfried, and F. Silvera. Improved adhesion of thin conformal organic films to metal surfaces. *Review of Scientific Instruments*, 57 (7):1381–1383, 1986. doi: 10.1063/1.1138605.

CONTACT

Henk-Willem Veltkamp, h.veltkamp@utwente.nl

TOWARDS DESIGN AUTOMATION FOR MICROFLUIDIC DEVICES

G. Fink[1], *M. Hamidović*[2], *W. Haselmayr*[2] and *R. Wille*[1]
[1] Johannes Kepler University, Institute for Integrated Circuits, Linz, Austria
[2] Johannes Kepler University, Institute for Communications Engineering and RF-Systems, Linz, Austria

ABSTRACT

Microfluidics is a prospective field which provides technological advances to the life sciences and is an enabling technology when it comes to, e.g., biological cell studies, high throughput drug development, and diagnostic screenings. However, the design process of microfluidic devices is still in its infancy and usually accomplished entirely by hand so far–frequently resulting in a "trial-and-error" scheme. In order to overcome this "trial-and-error" approach, we provide a selection of design automation tools as well as simulation methods in this work, which allow for deriving the design, for validating the functionality of the design, and for exploring alternative designs, without the need of an actual fabricated and costly prototype.

KEYWORDS

microfluidics, design automation, simulation

INTRODUCTION

Microfluidics deals with the control and manipulation of small amounts of fluids (in the order of few micro- to pico-liters) and provides technological advances to the life sciences. It is an enabling technology when it comes to, e.g., biological cell studies, high throughput drug development, and diagnostic screenings. Corresponding devices are called Lab-on-a-Chip (LoC), which minimize, integrate, automate, and parallelize typical laboratory operations such as mixing heating, incubation, etc. on a single chip. This has several advantages compared to conventional methods, since it requires significantly less reagent and sample volumes (e.g. relevant for restricted samples or costly reagents), facilitates shorter reaction times and, hence, higher throughput of numerous laboratory activities. This eventually provides affordable, accessible, sensitive, specific, easy-to-use, and robust healthcare for both developed and developing countries.

Despite these promises, the design and layout process of such microfluidic devices is still in its infancy and far away from the standards, which e.g. is taken for granted in the "traditional" chip/semiconductor industry. In fact, the current design process is usually accomplished entirely by hand so far, which is particularly critical, since the design process is a rather complex task where a huge number of physical parameters need to be considered, e.g., the dimensions of the channels, flow rates, the applied liquids, etc., which all depend and affect each other. As a result, designers often rely on their expert knowledge and derive the design based on manual calculations, simplifications, as well as assumptions. However, such a design process can be very error-prone and frequently results in a "trial-and-error" scheme, as sketched in Fig. 1. That is, a prototype of the current design gets fabricated and, then, physical experiments are conducted to test its functionality. If the prototype does not show the intended behavior (which frequently is the case, particularly in first iterations), the designer has to revise the design, repeat the production and test its functionality again. Even for simple microfluidic devices, this can lead to multiple iteration loops, yielding a time-consuming and rather costly design and production process. In order to overcome this "trial-and-error" approach, design automation tools as well as simulation methods (utilizing different abstraction levels to cope with complexity) can be employed (cf. Fig. 1). These tools and simulation methods allow for deriving the design, for validating the functionality of the design, and for exploring alternative designs, without the need of an actual fabricated and costly prototype. Furthermore, these tools can help to make microfluidics more accessible, in particularly for end-users, i.e., biologists, chemists, or medical experts, which usually have no expertise in designing mi-

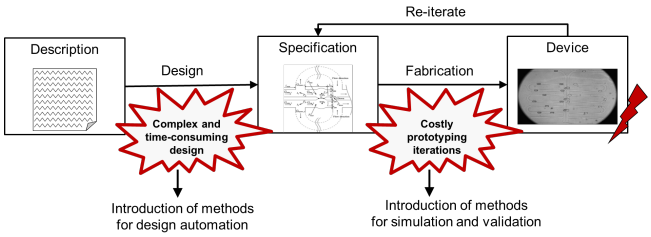

Figure 1: Thus far, microfluidic devices are often designed manually – a complex and time-consuming task. This frequently results in designs which, once fabricated, do not work as intended and, hence, have to be revised in re-iterations. Methods for design automation as well as simulation and validation can help here.

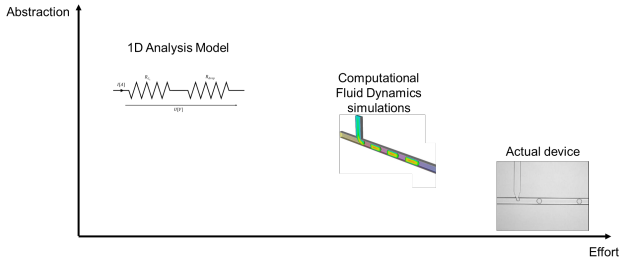

Figure 2: Design automation tasks can be conducted on different abstraction levels. If more physical details are needed, CFD simulations provide a good abstraction level, but also require more setup and computational efforts. In contrast, many design tasks can also be conducted on the more abstract 1D analysis model, which is easier to set up and fast to execute.

crofluidic devices. In this work, we provide a selection of corresponding design automation methods.

ABSTRACTION LEVELS

In order to develop corresponding design automation tools and simulation methods, a physical model which describes the behavior of microfluidics is needed. Here several physical models can be utilized, where each model can be seen as a different abstraction level (sketched in Fig. 2).

These levels can be categorized by their abstraction (plotted on the y-axis) and the respectively required effort/costs (plotted on the x-axis). Lower abstractions (e.g., CFD simulations [2]) consider more physical details and, hence, allow, e.g., more precise simulations. But they also result in higher costs with respect to setup and computation time. In contrast, higher abstractions (e.g., the one-dimensional (1D) analysis model [7]), need fewer requirements and, hence, can be applied early in the design process for deriving the specification of the design, for initially validating the functionality by using simulation, and also for design exploration.

SIMULATOR

One example of a corresponding method is the simulator proposed in [5], which utilizes the 1D analysis model and can be used to simulate droplet-based microfluidic devices. In such droplet-based devices, small amounts of fluids, so-called droplets, flow through closed micro-channels inside a second immiscible fluid which acts as a carrier for the droplets. These droplets usually contain biological or medical samples which can then be mixed, reacted, heated, incubated, etc. and found great applications, e.g., for DNA sequencing, cell analysis, organism analysis, and drug screening.

The simulator captures the behavior of a microfluidic network in five steps:

1. *Initialization:* In order to simulate a droplet-based microfluidic network, the designer has to initialize the simulation first. This means, the designer has to provide the following specifications:
   - Dimensions of all channels (i.e. their length, width, and height)
   - Structure of the network (i.e. how the channels/pumps are connected with each other)
   - Pressure or volumetric flow rate of the supply pumps
   - Properties of the continuous and dispersed phase (viscosity, density, interfacial-tension)
   - Droplet volumes and their injection times

   After passing these specifications to the simulator, the actual simulation process can start and the following steps are performed in a loop.
2. *Compute flow state:* The simulator converts the channels and droplets into their equivalent hydrodynamic resistances and derives a linear equation system that captures the physical behavior. This equation system is then used to determine the instantaneous flow state (i.e. pressure drops and flow rates in all channels) inside the microfluidic network. With the obtained flow rates, it is possible to determine the droplet velocities, which are required for the next step.
3. *Compute next event-time:* An event is basically an incident, which changes the current flow state of the microfluidic network and can be triggered by
   - injecting a droplet into the network,
   - a droplet flowing into another channel, or
   - a droplet leaving the network.

   Therefore, the simulator computes the time when the next event gets triggered, which is achieved by using the previously computed droplet velocities.
4. *Update system state:* The simulator updates the system state (i.e. droplet positions and their resistances in the channels) accordingly to the occurred events and droplet velocities.
5. *Termination condition:* If a termination condition is reached (e.g. all droplets left the network), the simulation stops, otherwise, the simulator continues with Step 2 and computes the flow state again. Because the simulator stores each system state at every time step, the paths of the droplets as well as the flow states of all time steps can be easily obtained.

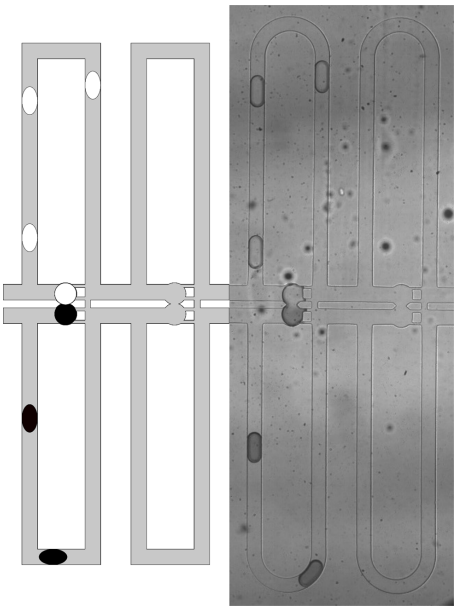

Figure 3: Comparison of the simulation output (left-hand side) to the actual physical realization (right-hand side) of the microfluidic device proposed in [1]. Even at this high abstraction (the 1D analysis model is employed), rather precise simulations can be conducted. The simulator is freely available at http://iic.jku.at/eda/research/microfluidics_simulation/.

Overall, after initializing the simulator, it always recalculates the flow state of the network, when the old one becomes invalid due to an occurrence of an event. A huge advantage of such an event-based simulation compared to CFD-Simulations tools like COMSOL Multiphysics, Ansys, or OpenFOAM (such as proposed in [2, 8]) is that the computational time is much lower and, therefore, allows to simulate even large microfluidic networks in negligible runtime.

With the help of this simulator, it was possible, e.g., to significantly improve the design of a device which is able to screen drug compounds that inhibit the tau-peptide aggregation [1] (cf. Fig. 3). The original design of this device took a whole month, required six different prototypes, and produced costs of about $1200. Using simulations (rather than a "trial-and-error" approach), these efforts could be reduced to a single day, one prototype, and costs of $200 only [3].

DESIGN AUTOMATION

When designing a microfluidic device, designers often have to conduct tasks entirely by hand–resulting in time consuming and labor-intensive processes. Design automation tools for microfluidic devices address this problem, by providing the designer with methods and means to automatically generate proper designs.

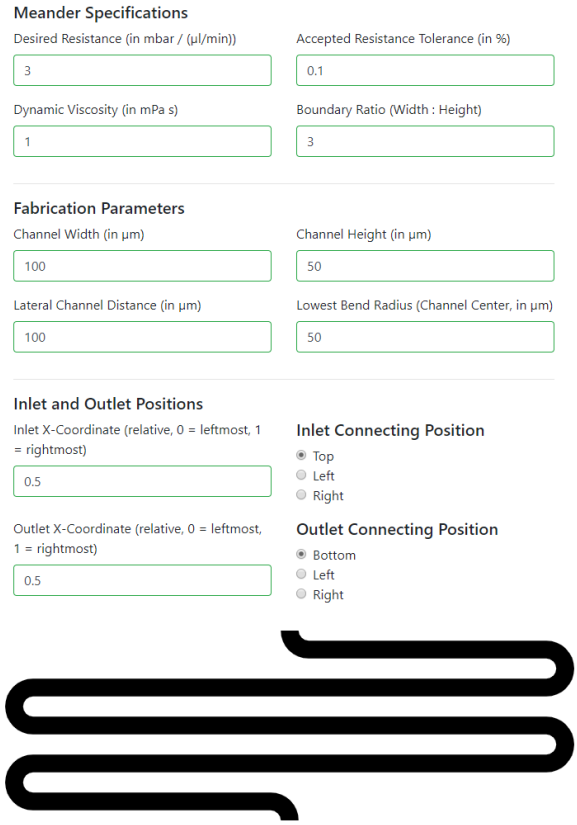

Figure 4: Once corresponding parameters such as the desired fluidic resistance, fabrication parameters, as well as the positions of the inlets and outlets are provided (see top part of the figure), a meander design satisfying these parameters is automatically generated (see bottom part of the figure). The tool is freely available at http://iic.jku.at/eda/research/meander_designer/.

Meander-Designer

Meander channels are a central microfluidic component which are often integrated in many different platforms such as pressure driven, droplet-based, and paper-based microfluidics. However, even for this frequently re-occurring component, designers still have to manually draw the meander channel for their respective application and design rules. The online-tool *Meander-Designer* (proposed in [4] and found under the link http://iic.jku.at/eda/research/meander_designer/) addresses this issue and automates this tedious task, while still retaining the full control over the design. More precisely, the designer only has to provide corresponding parameters such as the desired hydrodynamic resistance, fabrication parameters, as well as the positions of the inlets and outlets (cf. the input mask shown in Fig. 4). Based on that, a design satisfying these parameters is automatically generated, as shown in the bottom of Fig. 4.

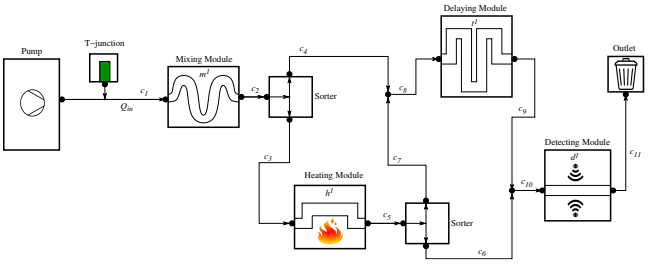

Figure 5: In order to design a droplet microfluidic network, all used components have to be properly chosen, such as the pumps, modules, sorters, and channels. Especially the dimensioning of the channels between the components constitutes a significant challenge. A corresponding method is proposed in [6].

Dimensioning of channels

In order to design a droplet microfluidic network as shown in Fig. 5, all used components have to be properly chosen, such as the pumps, modules, sorters, and channels. The specifications of all components and how they are connected determine the flow of droplets. Especially the specification of channels (i.e. their resistances) can be varied in a broad bandwidth and, by this, their dimensioning constitutes a significant challenge. In fact, improper specifications can cause

- the flow in channels/modules to be in the wrong direction or
- the time a droplet requires to pass a channel/module to be too long/short.

However, for dimensioning a microfluidic network, a huge number of constraints and dependencies have to be considered and already slightly changing e.g. the resistance of a single channel may change the behavior of the entire microfluidic system.

In the work proposed in [6], these problems are addressed by introducing automatic methods that aid designers in the specification of droplet microfluidic networks—especially in the dimensioning of channels. More precisely, methods are proposed which automatically allow to (1) validate whether a manually derived specification indeed works as intended, i.e. fulfills certain objectives as well as (2) conduct the dimensioning to obtain a proper specification.

CONCLUSIONS

This work provided a brief selection of automatic methods for important tasks in the design of microfluidic devices. We strongly believe those may provide the basis for comprehensive and elaborated design automation flows to be established in the near future.

*

References

[1] X. Chen and C. L. Ren. A microfluidic chip integrated with droplet generation, pairing, trapping, merging, mixing and releasing. *RSC Adv.*, 7(27):16738–16750, 2017.

[2] T. Glatzel, C. Litterst, C. Cupelli, T. Lindemann, C. Moosmann, R. Niekrawietz, W. Streule, R. Zengerle, and P. Koltay. Computational fluid dynamics (CFD) software tools for microfluidic applications–a case study. *Computers & Fluids*, 37(3):218–235, 2008.

[3] A. Grimmer, X. Chen, M. Hamidović, W. Haselmayr, C. L. Ren, and R. Wille. Simulation before fabrication: a case study on the utilization of simulators for the design of droplet microfluidic networks. *RSC Advances*, 8:34733–34742, 2018.

[4] A. Grimmer, P. Frank, P. Ebner, S. Häfner, A. Richter, and R. Wille. Meander designer: Automatically generating meander channel designs. *Micromachines – Journal of Micro/Nano Sciences, Devices and Applications*, 9(12), 2018.

[5] A. Grimmer, M. Hamidović, W. Haselmayr, and R. Wille. Advanced simulation of droplet microfluidics. *Journal on Emerging Technologies in Computing Systems*, 2019.

[6] A. Grimmer, W. Haselmayr, and R. Wille. Automated dimensioning of Networked Labs-on-Chip. *Trans. on Computer-Aided Design of Integrated Circuits and Systems*, 2018.

[7] K. W. Oh, K. Lee, B. Ahn, and E. P. Furlani. Design of pressure-driven microfluidic networks using electric circuit analogy. *Lab on a Chip*, 12(3):515–545, 2012.

[8] M. Wörner. Numerical modeling of multiphase flows in microfluidics and micro process engineering: a review of methods and applications. *Microfluidics and Nanofluidics*, 12(6):841–886, 2012.

DEVELOPMENT OF FRONT-END ELECTRONICS FOR LOW-FIELD NMR APPLICATIONS

E. Aydin[1] and K. A. A. Makinwa[1]
[1] Delft University of Technology, Delft, The Netherlands

ABSTRACT

This paper describes some first steps toward the realization of a miniature Nuclear Magnetic Resonance (NMR) system intended for use in micro-flow measurements and chemical analysis applications. The designed system is used together with a bench-top NMR measurement device (Drive-L) and bench-top measurement equipment. The implemented front-end has 50 Ω input impedance and 1.2 dB noise figure, while its gain can be tuned between 29.5 dB to 77 dB. The designed system is tested with single-shot Free Induction Decay (FID) experiments and with complex pulse sequences using a solenoidal detection coil with a 40 Q, 6 µL $CuSO_4$ sample and a 507 mT permanent magnet.

KEYWORDS

NMR, analog-front-end, pulse sequence, flow measurement

INTRODUCTION

NMR is used in several fields such as analytical chemistry, bio-sensing, medicine, oil-gas industry, and geosciences. However, it is typically an expensive and bulky technique, since superconducting magnets are often used to generate the high magnetic fields required. Recently, these have started to be replaced by low-field permanent magnets, thus reducing the size and cost of NMR analysis [1]–[3]. But this is accompanied by a significant decrease in signal levels, which makes the design of the front-end electronics challenging.

As a first step toward the realization of a low-field NMR system, an analog front-end has been realized. It was tested together with a 507 mT (21.7 MHz) magnet and a benchtop NMR control/measurement unit (Pure Devices, Drive-L) for pulse control (TX/RX) and sample excitation. The sample excitation and pulse control for simple FID experiments are provided by a signal generator.

This paper is organized as follows. The basic NMR principle, the timing diagram of NMR systems and the complex pulse sequence used for testing are explained briefly. Next, the specifications of the front-end electronics and the designed system are explained in detail. After presenting the test results, the paper is finalized with the conclusion.

NMR PRINCIPLE

The term NMR refers to the resonant interaction between an RF magnetic field and nuclei in the presence of a static magnetic field (B_0). The magnetic moments of protons will then align themselves with B_0. The alignment will be disturbed by the application of an RF signal perpendicular to B_0 at the so-called Larmor frequency, (f_{Larmor}), given by:

$$f_{Larmor} = \gamma B_0 \quad (1)$$

where γ is the gyromagnetic ratio and is a material-dependent parameter. For Hydrogen (H), γ is equal to 42.58 MHz/T. The excitation duration determines the angle of misalignment. To have the maximum signal magnitude, this angle should be 90°. This excitation frequency is called as $T_{90°}$ and is calculated as shown in Equation 2.

$$T_{90°} = \frac{\pi}{\gamma B_1} \quad (2)$$

where B_1 is the oscillating magnetic field generated by the RF excitation. When the RF signal is removed, the magnetic moments will re-align themselves with B_0 and emit the NMR signal. The decay time constant of the NMR signal depends on the spin-spin relaxation (T_2) mechanism and the inhomogeneity (T_2^*) of B_0. The NMR principle is illustrated in Figure 1.

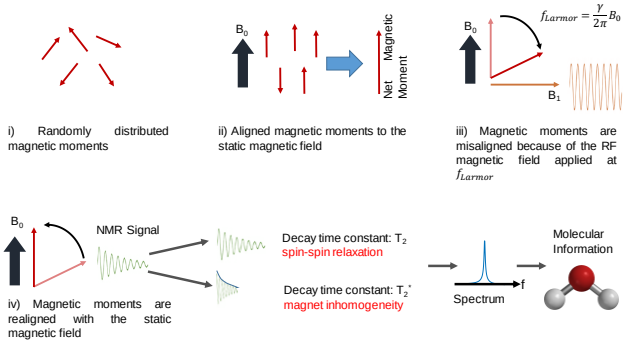

Figure 1. Principle of NMR

T_2 depends on the sample and concentration of the solution. For pure water, T_2 is typically around 1 s. T_2^* is the decay time due to the inhomogeneity ΔB_0 of the static magnetic field. If the static magnetic field has a gradient, the resulting NMR signal includes all Larmor frequencies corresponding to the magnetic field interval. That means signal bandwidth increases as a result of the static magnetic field inhomogeneity. T_2^* is calculated as shown in Equation 3. The measured decay time T_{decay} is the geometric mean of T_2 and T_2^*. Even in a slightly inhomogeneous magnetic field T_2^*

becomes the dominant decay mechanism. For example, under a static field having ΔB_0=50 μT in the sample volume, $T_2{}^*$ is calculated as 75 μs. Therefore, for inhomogeneous magnetic fields, $T_{decay} \approx T_2{}^*$.

$$T_2{}^* = \frac{1}{2\pi\gamma\Delta B_0} \quad (3)$$

NMR TIMING AND PULSE SEQUENCE

To further understand the specifications of the electronics, the timing of an NMR system will be explained. The timing diagram is shown in Figure 2. The SW signal is used to switch between the transmitter and receiver. When SW is high (+5 V), the transmitter applies an RF excitation signal that misaligns the magnetic moment of protons with respect to the static magnetic field. When SW goes low (-5 V), the receiver picks-up the NMR signal emitted from the sample.

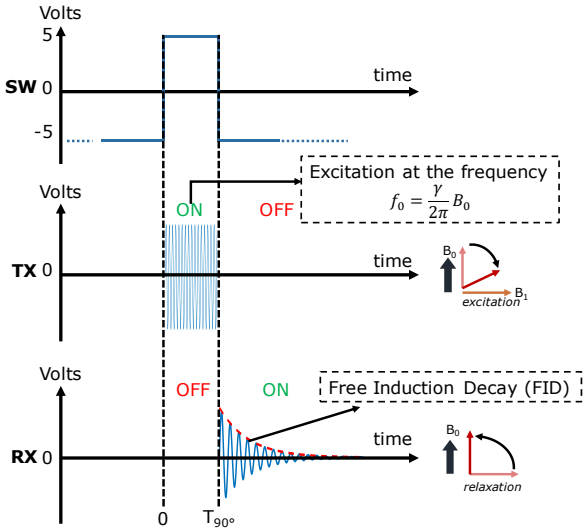

Figure 2. The timing diagram of an NMR system

By appropriately programming the SW signal, the transition between TX and RX can be continuously realized and complex pulse sequences can be implemented to obtain further information about the sample. One of these complex pulse sequences is the Carr-Purcell-Meiboom-Gill (CPMG) pulse sequence that is used to extract T_2 under inhomogeneous magnetic fields [4]. The CPMG pulse sequence involves the periodic excitation of the sample by 180° pulses (with a period T) after a 90° pulse. By measuring the peaks of the echo signal after each excitation, the T_2 decay can be interpolated. *Figure 3* illustrates the CPMG pulse sequence, and the $T_2{}^*$ and T_2 decay. The designed system is intended to use the CPMG pulse sequence to reach T_2 time constant of the sample, in addition to single shot FID experiments.

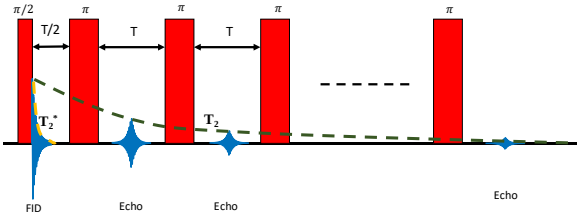

Figure 3. Illustration of CPMG pulse sequence, T_2 and $T_2{}^*$

FRONT-END ELECTRONICS

Figure 4 shows the basic schematic of the designed system. It consists of a coil to excite the sample and pick up the NMR signal, a transmitter to excite the coil and a receiver to acquire the NMR signal received by the coil. A TX/RX switch enables the transition between transmitting and receiving. Moreover, an impedance matching network is used to match the impedance of the coil to 50 Ω at the frequency of interest.

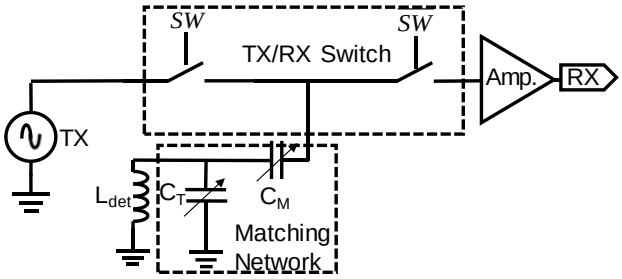

Figure 4. The schematic of the transceiver of the designed system

A more detailed schematic of the system is shown in Figure 5. It employs a solenoidal coil (Q_{coil}=40 at 21.7 MHz) for both excitation and detection. The coil impedance is tuned to 50 Ω by using a capacitive impedance matching network. Its resonance frequency is tuned by trimming C_T, while C_M is used to match the network to 50 Ω. A TX/RX switch is implemented using anti-series PIN diodes. The resistors R_{bias} set the operating point of diodes, while L_D and C_D are used to separate the low frequency (≈ 1 Hz) SW and high frequency (≈ 22 MHz) RF signals from each other. By using two switches, and reversing the polarity of the diodes in each switch, a single DC bias can be used. The operating point of the diodes is determined by considering the speed, insertion loss, and power consumption of the switch. Each switch draws 1 mA and has 0.5 dB insertion loss and 5 μs dead time.

Since the amplitude of the NMR signal at the coil output varies from 100 nV to 10 μV, a low noise amplifier (LNA) is required. Therefore, an LNA with 1.1 dB noise figure (NF) and 22 dB gain is utilized as the first stage. Since the gain of the LNA is quite high, the noise of the following stages has been suppressed.

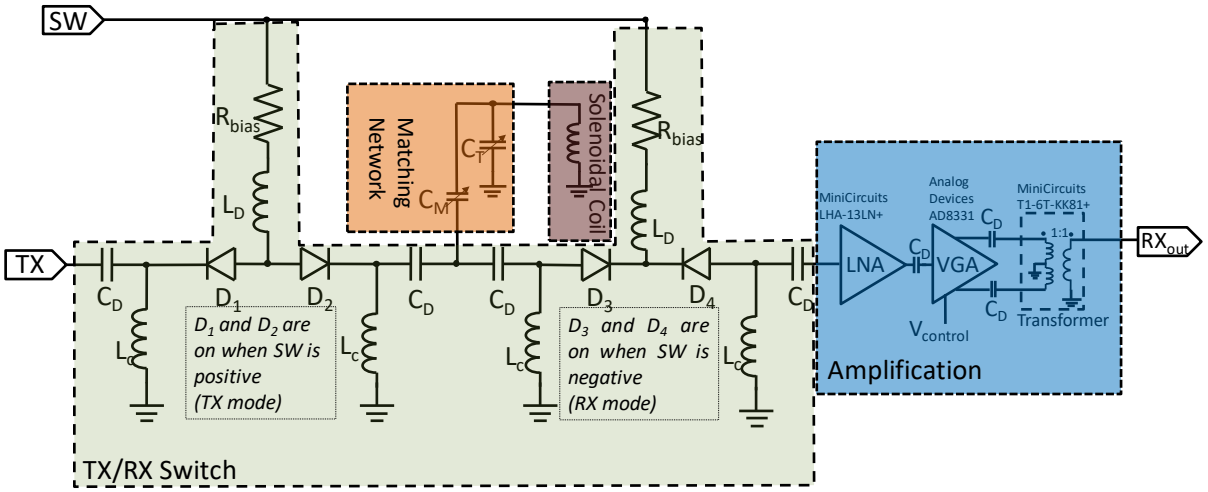

Figure 5.The detailed schematic of the NMR system

Normally, high-Q coils provide passive amplification of both the signal and the noise, with a gain equal to the Q of the coil. The noise figure (NF) of this process is 0 dB [2]. However, the Q of the coil is reduced by the input resistance of the (LNA). As a result, the benefit of the passive amplification is degraded by the input resistance of the LNA. So it would be beneficial to use an LNA with a high input resistance, which can be realized in a custom ASIC. However, commercially-available LNAs usually have 50 Ω input resistance. Therefore, in this design, an LNA with 50 Ω input resistance is used.

Depending on the shape and the dimensions of the coils, the signal amplitude can vary significantly. To prevent the receiver from saturating, a variable gain amplifier (VGA) with a gain range between 7.5 dB and 55 dB is used as the second amplification stage. Its gain is controlled by a control voltage $V_{control}$. Finally, a transformer is used to convert the differential output of the VGA into a single-ended signal.

The NF of the overall receiver system is calculated as 1.2 dB and its gain can be adjusted between 29.5 dB and 77 dB.

TEST RESULTS

To show the functionality of the system, a 507 mT magnet is used with the designed front-end electronics. A 6 µL, 17 mM $CuSO_4$ water solution was used in all experiments. First, CPMG experiments and simple FID experiments were performed. The CPMG experiment results are shown in Figure 6 and T_2 is measured as 29 ms. The obtained results have been verified by repeating the same experiment with the benchtop Drive-L system.

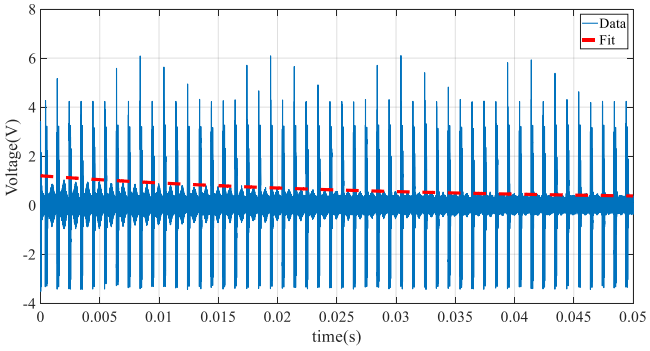

Figure 6. The CPMG pulse sequence test results

The FID experiments were first performed as shown in *Figure 7*. $T_{90°}$ was experimentally found as 48 µs. After exciting the sample the NMR signal is acquired with the help of an oscilloscope. The decay time constant (T_2^*) is measured as 150 µs in both experiments that correspond to the 50 ppm ($\Delta B_0/B_0$) static magnetic field inhomogeneity.

After obtaining the signal, FFT of the FID signal was obtained using MATLAB as shown in Figure 8. Q of the signal was measured as 6500. Inhomogeneity of the static magnetic field can clearly be seen from the FFT of the signal. The flat region corresponds to the static magnetic field mapping on the coil.

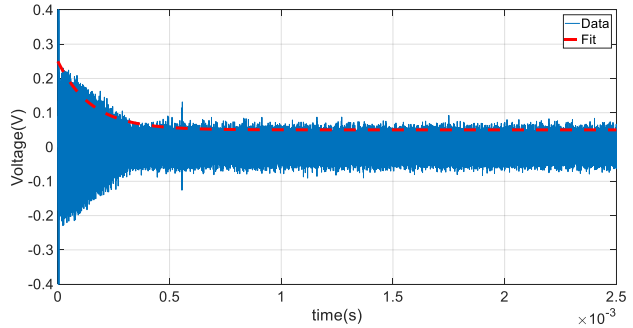

Figure 7. The FID signal obtained from the designed system

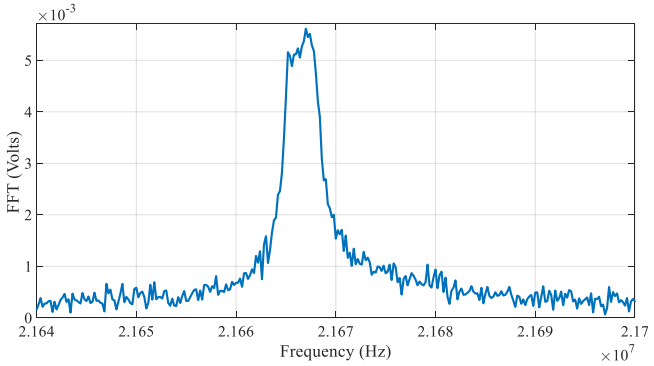

Figure 8. The FFT signal of the obtained NMR signal

CONCLUSION

In this paper, the design of an analog front-end was presented as the first step towards implementing a complete micro-NMR based flowmeter. The designed system has 1.2 dB NF with a gain that can be tuned between 29.5 dB and 77 dB. With the designed front-end, it is achieved to measure NMR signals using commercial electronics laboratory instruments or a benchtop NMR machine. A 6 µL sample was used to perform a single shot FID experiments and more complicated CPMG pulse sequences.

In the future, an IQ demodulator will be employed to further limit the signal band and relax the requirements of a succeeding ADC.

REFERENCES

[1] K.-M. Lei, P.-I. Mak, M.-K. Law, and R. P. Martins, "A µNMR CMOS Transceiver Using a Butterfly-Coil Input for Integration With a Digital Microfluidic Device Inside a Portable Magnet," IEEE J. Solid-State Circuits, vol. 51, no. 10, pp. 2274–2286, Oct. 2016.

[2] N. Sun, Y. Liu, H. Lee, R. Weissleder, and D. Ham, "CMOS RF Biosensor Utilizing Nuclear Magnetic Resonance," IEEE J. Solid-State Circuits, vol. 44, no. 5, pp. 1629–1643, May 2009.

[3] N. Sun, T.-J. Yoon, H. Lee, W. Andress, R. Weissleder, and D. Ham, "Palm NMR and 1-Chip NMR," IEEE J. Solid-State Circuits, vol. 46, no. 1, pp. 342–352, Jan. 2011.

[4] H. Y. Carr and E. M. Purcell, "Effects of Diffusion on Free Precession in Nuclear Magnetic Resonance Experiments," Phys. Rev., vol. 94, no. 3, pp. 630–638, May 1954.

CONTACT

* E. Aydin, e.aydin@tudelft.nl

DESIGN CONSIDERATIONS FOR A MEMS CORIOLIS MASS FLOW SENSING SYSTEM

A. C. de Oliveira[1], T. Schut[2], J. Groenesteijn[3], Q. Fan[1], R. Wiegerink[2] and K. A. A. Makinwa[1]
[1]Electronic Instrumentation Laboratory, Delft University of Technology, Delft, The Netherlands
[2]MESA+ Institute for Nanotechnology, University of Twente, Enschede, The Netherlands
[3]Bronkhorst High-Tech BV, Ruurlo, The Netherlands

Recently, several MEMS Coriolis mass flow sensors have been reported [1–3]. However, they are typically readout by bulky and expensive bench-top equipment. To achieve further size and cost reductions, dedicated readout electronics is required. This should perform two functions: 1) drive the sensor at its resonance frequency; and 2) detect and process its output signals. This paper briefly discusses the considerations involved in the design of the readout electronics for a compact MEMS Coriolis mass flow sensor [4–6]. Based on its measured, target specifications for future designs intended for ultra-low flow applications are defined and compared to a state-of-the-art Coriolis mass flow sensor [7].

The operating principle of a MEMS Coriolis mass flow sensor is illustrated in Fig. 1 [3]. The flow of interest is passed through a MEMS sensing element, which consists of a silicon nitride resonating tube and two capacitive sense electrodes with which the motion of the tube can be sensed. Together with an external magnetic field (B), the tube can be driven at its twist-mode resonance frequency ω_T by passing an AC-current through a metal track on the tube. Fluid flow through the tube gives rise to a Coriolis force that excites the tubes swing-mode at the drive frequency (ω_T). As a result, the phase-shift between C_1 and C_2 is proportional to the Coriolis force and, consequently, is a direct measurement of mass flow.

A simplified block diagram of the MEMS Coriolis mass flow sensing system is shown in Fig. 2. It consists of a drive path that detects and amplifies the drive (twist) motion, and a sense path that detects both the twist and swing motions. A phase-shifter ensures that the phase requirements for oscillation are satisfied. Both twist and swing mode motions are required to extract the mass flow information, and thus both are detected by the integrated capacitive sense electrodes (Fig. 1(a)). As a result, conventional capacitance-to-voltage (C/V) conversion methods can be applied in the sense path, which means that the sensing performance is limited by the non-idealities (alignment, co-planarity etc) of the sense electrodes. Finally, the drive and sense signals are processed by a phase (mass flow) and frequency (density) readout.

While the sensor's mass flow resolution is mainly limited by the resolution with which the sense capacitance can be readout, the noise in the drive loop can also degrade the systems resolution (such as its density resolution) due to sensor non-idealities. Therefore, a drive signal with a high signal-to-noise ratio (SNR) is desired. Here, we discuss the implementation of the current drive-loop, as implemented with bench-top equipment (Fig. 3, [4]) as well as an alternative solution that can be integrated and which should achieve better performance (Fig. 4).

In the current drive loop, , the tubes twist motion is detected by sensing the induced electromotive force (EMF) generated in a pick-up coil on the tube. Since this is a single-turn coil, the resulting drive signal is quite small, and the drive-to-EMF transfer can than -85 dB (V/V) [4], resulting in a low-SNR drive signal. The drive-loop can also be implemented by means of a phase-locked loop (PLL) as in [5]. Although the EMF-based PLL implementation based on the EMF is beneficial due to its flexible implementation, it achieves a frequency stability of more than 140 mHz, which is still around $2\times$ more than that of the drive-loop in [4].

Alternatively, the drive signal can be obtained by measuring the difference between the two capacitive signals (Fig. 1(b)). In this drive-loop, the capacitor electrodes are AC-biased. Even though additional demodulators and low-pass filters are necessary, low-noise levels can be achieved since the signal is up-modulated and operates well above the flicker-noise corner of the C/V converters. Measurement results of such implementation are presented in [6], where it achieved a drive frequency stability of 1 mHz during a one hour measurement. This is a $80\times$ improvement when compared to previous EMF-based drive-loop implementations [4, 5].

Based on the discussion presented in this paper, the target specifications for an improved system are defined. A comparison between a state-of-the-art commercially-available Coriolis mass flow sensor [7] and the target specifications are pre- sented in Table 1.

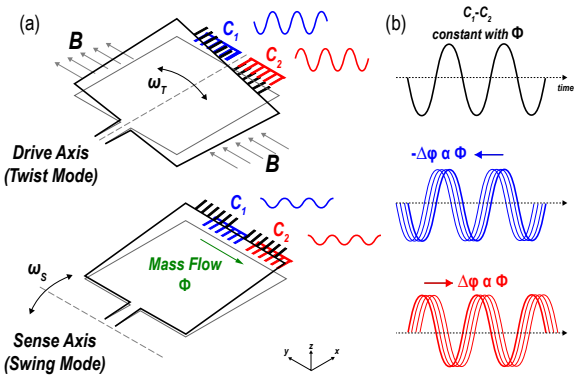

Figure 1: MEMS Coriolis mass flow sensor (a) operation principle and (b) capacitive signals in the time-domain.

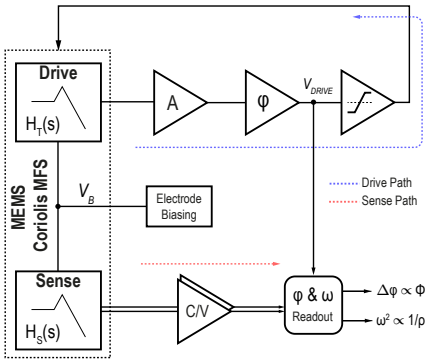

Figure 2: MEMS Coriolis mass flow sensing system overview.

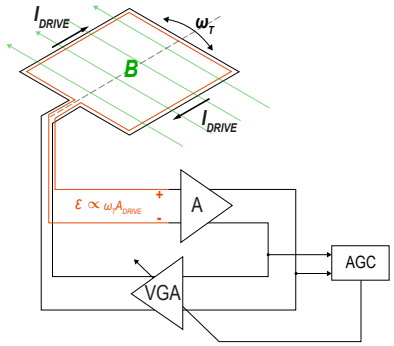

Figure 3: Induced EMF-based drive-loop.

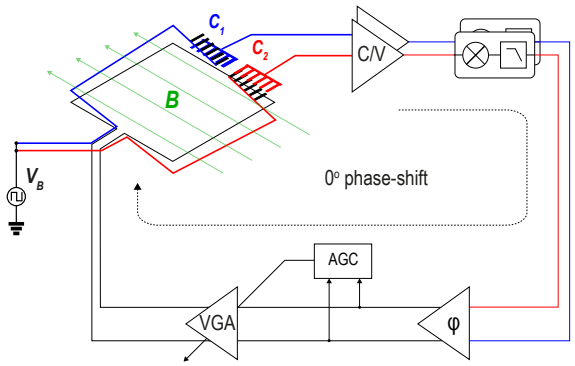

Figure 4: Drive Loop based on the sense signals.

Target Specifications for a MEMS Coriolis Mass Flow Sensing System

	ML120	**Target**
Technology	Stainless Steel	**MEMS**
Max. Flow Range	5 g/h	**5 g/h**
Zero Stability (ZS)	±10 mg/h	**< ±2 mg/h**
Density Stability	±5 kg/m^3	**< ±1 kg/m^3**
Temperature Range	0 - 70 °C	**0 - 70 °C**
Bandwidth	-	**1 - 10 Hz**
Power Consumption	3 W	**< 20 mW**

REFERENCES

[1] P. Enoksson, G. Stemme, and E. Stemme, "A Silicon Resonant Sensor Structure for Coriolis Mass-Flow Measurements," *Journal of Microelectromechanical Systems*, vol. 6, no. 2, pp. 119–125, June 1997.

[2] R. Smith, D. R. Sparks, D. Riley, and N. Najafi, "A MEMS-Based Coriolis Mass Flow Sensor for Industrial Applications," *IEEE Transactions on Industrial Electronics*, vol. 56, no. 4, pp. 1066–1071, April 2009.

[3] D. Alveringh, R. J. Wiegerink, and J. C. Lötters, "Integrated Pressure Sensing Using Capacitive Coriolis Mass Flow Sensors," *Journal of Microelectromechanical Systems*, vol. 26, no. 3, pp. 653–661, June 2017.

[4] J. Groenesteijn, M. Dijkstra, T. Lammerink, J. C. Lötters, and R. Wiegerink, "A compact micro Coriolis mass flow sensor with flow bypass for a monopropellant micro propulsion system," *2nd Conference on MicroFluidic Handling Systems (MFHS)*, Oct 2014.

[5] D. Alveringh, T. Schut, R. Wiegerink, and J. C. Lotters, "Coriolis mass flow and density sensor actuation using a phase-locked loop," *3nd Conference on MicroFluidic Handling Systems (MFHS)*, Oct 2017.

[6] A. C. de Oliveira, T. Schut, J. Groenesteijn, Q. Fan, R. Wiegerink, and K. Makinwa, "A MEMS Coriolis Mass Flow Sensing System with Combined Drive and Sense Interface," *2019 IEEE Sensors Conference*, Oct 2019.

[7] Bronkhorst, "mini CORI-FLOW™ ML120V21 datasheet," 2018.